

UNIVERSIDAD POLITÉCNICA DE CARTAGENA

Department of Thermal and Fluid Engineering



**MULTIDIMENSIONAL MODELLING OF MULTIPHASE  
REACTIVE MIXTURES**

**Caracterización de la movilización y combustión de mezclas bifásicas de gases y  
partículas en procesos transitorios**

**Doctoral Thesis**

**RAMÓN ANTONIO OTÓN MARTÍNEZ**

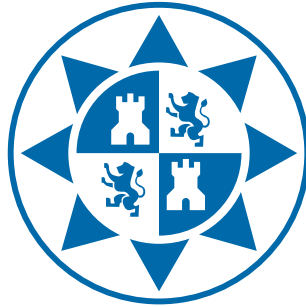
2014



# TESIS DOCTORAL

UNIVERSIDAD POLITÉCNICA DE CARTAGENA

Departamento de Ingeniería Térmica y de Fluidos



## MULTIDIMENSIONAL MODELLING OF MULTIPHASE REACTIVE MIXTURES

Caracterización de la movilización y combustión de mezclas bifásicas de gases y  
partículas en procesos transitorios

PRESENTADA POR:

**Ramón Antonio Otón Martínez**

DIRIGIDA POR:

**Dr. José Ramón García Cascales**

Presentada para la obtención del grado de  
**Doctor con Mención Europea**  
en el Programa de Doctorado de  
*Energías Renovables*

Cartagena, noviembre de 2014

Ramón Antonio Otón Martínez: *Multidimensional modelling of multi-phase reactive mixtures*, Doctoral Thesis. UNIVERSIDAD POLITÉCNICA DE CARTAGENA © 2014



**CONFORMIDAD DE SOLICITUD DE AUTORIZACIÓN DE DEPÓSITO DE  
TESIS DOCTORAL POR EL/LA DIRECTOR/A DE LA TESIS**

D. José Ramón García Cascales, Director de la Tesis doctoral “**Caracterización de la movilización y combustión de mezclas bifásicas de gases y partículas en procesos transitorios. (*Multidimensional modelling of multiphase reactive mixtures*)**”,

**INFORMA:**

Que la referida Tesis Doctoral, ha sido realizada por D/D<sup>a</sup>. Ramón Antonio Otón Martínez, dentro del programa de doctorado de ENERGÍAS RENOVABLES, dando mi conformidad para que sea presentada ante la Comisión de Doctorado para ser autorizado su depósito.

La rama de conocimiento en la que esta tesis ha sido desarrollada es:

- Ciencias
- Ciencias Sociales y Jurídicas
- Ingeniería y Arquitectura

En Cartagena, a 14 de julio de 2014.

EL/LA DIRECTOR/A DE LA TESIS

Fdo.: JOSE R. GARCIA CASCALES

**COMISIÓN DE DOCTORADO**



**CONFORMIDAD DE DEPÓSITO DE TESIS DOCTORAL  
POR LA COMISIÓN ACADÉMICA DEL PROGRAMA**

D/D<sup>a</sup>. Antonio Urbina Yeregui, Presidente/a de la Comisión Académica del Programa de Doctorado de Energías Renovables,

**INFORMA:**

Que la Tesis Doctoral titulada, “**Caracterización de la movilización y combustión de mezclas bifásicas de gases y partículas en procesos transitorios. (*Multidimensional modelling of multiphase reactive mixtures*)**”, ha sido realizada, dentro del mencionado programa de doctorado, por D. Ramón Antonio Otón Martínez, bajo la dirección y supervisión del Dr. José Ramón García Cascales.

En reunión de la Comisión Académica de fecha 17 de Junio de 2014, visto que en la misma se acreditan los indicios de calidad correspondientes y la autorización del Director de la misma, se acordó dar la conformidad, con la finalidad de que sea autorizado su depósito por la Comisión de Doctorado.

La Rama de conocimiento por la que esta tesis ha sido desarrollada es:

- Ciencias
- Ciencias Sociales y Jurídicas
- Ingeniería y Arquitectura

En Cartagena, a 14 de Julio de 2014.

EL PRESIDENTE DE LA COMISIÓN ACADÉMICA DEL PROGRAMA



Fdo:--Antonio Urbina Yeregui

**COMISIÓN DE DOCTORADO**



## ABSTRACT

---

This Doctoral Thesis is devoted to the study, and implementation in a computational code, of different phenomena related to mobilisation and violent reaction of particles in reactive atmospheres, involving shock waves and/or detonation. The resulting computational code is intended to provide reliable predictions about explosions of two-phase systems in closed spaces, what could be directed, among many other applications, towards security assessments on nuclear power generation. In particular, the code is developed within the framework of a collaboration between IRSN (Institut de Radioprotection et Sûreté Nucléaire, France) and UPCT (Universidad Politécnica de Cartagena, in Spain). The objective of the research project is to develop an accurate and strong tool which is able to perform predictions and give valuable data for safety analysis, based on different reference scenarios specified in the ITER project technical basis [94].

The problem we have focused on is the case of Loss of Vacuum Accident (LOVA), whose conditions are detailed in the Safety Specifications of the ITER project [95]. It consists of an air ingress causing a pressurisation of the vacuum vessel and a shock wave. The increased temperature causes generation of hydrogen which can react violently with air. Simultaneously, certain amounts of beryllium powder, carbon and tungsten, present inside the reactor, can explode causing deflagration or detonation. Other complex phenomena could be involved on this process (e.g., Deflagration to Detonation Transition, or DDT).

As a first step in the present thesis, a comprehensive literature survey is done on mathematical models of equations. Different options are brought to comparison in order to find the model which best suited our multiphase reactive problem. In addition, an extensive state of the art is gathered in quest of closure laws for the systems of equations, including combustion chemical models for the species involved in LOVA scenario (hydrogen, carbon monoxide, beryllium dust, tungsten dust, carbon particles and aluminium dust). From this search, chemical kinetics laws have been selected from different validated scientific works available in literature and implemented into the system of conservation equations of the problem.

After this mainly theoretical study, numerical methods have taken a large portion of the work developed in this thesis. The choice of the numerical approach is not a trivial issue. Most general purpose numerical methods used on the resolution of systems of partial differential equations, become unstable in the presence of discontinuities, as shock waves. Chemical reaction and the interaction with particles

only aggravates this situation, making the problem really demanding with the numerical method. As a consequence, various methods have been implemented and tested, including first and second order finite-volume methods. Approximate Riemann solvers (AUSM+, Roe, Rusanov, VLH) are also tested for both gas and particles phases. Then, the solution of source terms is addressed in detail. The use of splitting methods has proven to be more reliable, but even those approaches may fail if the source-term problem becomes stiff due to chemical reaction and particle interaction. Thus, a new methodology for numerical treatment of source terms is developed and tested, working as a relaxation model, which allows to find a suitable solution for adverse conditions of the problem.

The implementation of all these advances in the computational code are validated through various two-phase explosion problems tested with the code. These analyses are performed by considering trustworthy experimental data from literature. Among these tests, we focus on closed-vessel experiments which are first reproduced in 1D (shock-tube tests, combustion tubes), and later extended to 2D and 3D problems (multi-dimensional tubes and spheric combustion vessels). Finally, the LOVA scenario is analysed under the real geometry of ITER. Dust mobilisation by a leading shock is successfully simulated under expected normal operational conditions of the fusion reactor. Results about the mobilised dust fraction from three-dimensional computations are reported.

## RESUMEN

---

La presente Tesis Doctoral está dedicada al estudio de los fenómenos relacionados con la movilización de partículas y su reacción de forma violenta en atmósferas reactivas, así como la implementación de estos fenómenos en un código computacional capaz de simular ondas de choque y detonaciones. Se pretende que este código pueda proporcionar, con suficiente fiabilidad, predicciones sobre explosiones en sistemas bifásicos cerrados, que pudieran ser empleadas en estudios de evaluación de seguridad en centrales nucleares. Este código, en particular, se desarrolla en el marco de un programa de colaboración entre el IRSN (Institut de Radioprotection et Sûreté Nucléaire, de Francia) y la Universidad Politécnica de Cartagena, en España. El objetivo de esta colaboración es desarrollar una herramienta de simulación sólida y precisa, con el fin de proporcionar datos para el análisis de seguridad del reactor de fusión nuclear ITER, basándose en determinados eventos de referencia estipulados en las bases técnicas del proyecto [94].

A partir de aquellos eventos de referencia, el problema en que nos centramos es el caso de una pérdida de vacío en la vasija del reactor

(o LOVA por sus siglas en inglés), cuyos detalles se describen en las Especificaciones de Seguridad del proyecto ITER [95]. Este supuesto considera un ingreso de aire en la vasija del reactor, provocando una presurización del mismo y una onda de choque. A consecuencia del súbito incremento de temperatura, se generaría hidrógeno, que podría reaccionar de forma violenta con el aire. De forma simultánea, ciertas cantidades de polvo de berilio, carbono y wolframio, presentes en el interior del reactor, podrían reaccionar en forma de una deflagración o detonación.

Por lo tanto, como primer paso en esta Tesis Doctoral, se ha realizado un estudio bibliográfico exhaustivo acerca de modelos matemáticos, buscando el modelo de ecuaciones que más se adapta al problema multifásico y reactivo que queremos estudiar. Además, se ha reunido un compendio de leyes de cierre para los sistemas de ecuaciones, incluyendo leyes de combustión para las especies químicas presentes en el problema (hidrógeno, monóxido de carbono y polvo de berilio, wolframio, carbono y aluminio). A partir de esta búsqueda se han seleccionado modelos de cinética química que han sido implementadas en el sistema de ecuaciones de conservación.

Después de este estudio mayoritariamente teórico, se dedica una porción importante de esta tesis al estudio de los métodos para la resolución numérica del problema. La elección del método numérico no es un asunto trivial, pues la mayoría de las aproximaciones normalmente utilizadas en la resolución de sistemas en derivadas parciales se vuelven inestables en presencia de discontinuidades, tales como ondas de choque. En consecuencia, varios métodos numéricos son aquí analizados. Basándonos en el método de volúmenes finitos de primer y segundo orden, se ha testeado un conjunto de esquemas de Riemann aproximados (AUSM+, Roe, Rusanov, VLH), tanto para la fase gaseosa como la de las partículas. A continuación, se trata en detalle la resolución de los términos fuente. A este respecto, el uso de métodos de resolución por separado han resultado ser muy acertado, pero incluso estas aproximaciones fallan si el problema se vuelve numéricamente rígido. Por consiguiente, se ha desarrollado una nueva metodología para el tratamiento de estos términos en condiciones numéricamente adversas.

La implementación de estos avances en el código se ha validado con diferentes test bifásicos mediante su comparación con datos experimentales publicados en la bibliografía. Entre estos test, nos centramos en experiencias realizadas en sistemas cerrados, que se han reproducido en 1D y se han extendido posteriormente a 2D y 3D. Finalmente, en un dominio computacional 3D, que reproduce fielmente la geometría de la vasija del reactor ITER, se ha simulado la movilización de partículas bajo el supuesto de LOVA y se proporcionan resultados de la fracción de polvo movilizada.



*En cuanto a vosotros, no os hagáis llamar "maestros", porque no tenéis más que un Maestro y todos vosotros sois hermanos. No os dejéis llamar tampoco doctores, porque solo tenéis un doctor, que es el Mesías. El que quiera ser grande que se haga vuestro servidor.*

(Matthew 23, 8-11)

## ACKNOWLEDGMENTS

---

Esta Tesis Doctoral se engloba en un proyecto de investigación que se enmarca en una serie de contratos de colaboración mantenidos entre el Institut de Radioprotection et de Sûreté Nucléaire (Francia) y la Universidad Politécnica de Cartagena. Quiero agradecer, en primer lugar, al Dr. José Ramón García Cascales por haberme dado la oportunidad de participar en este interesante proyecto, por su constancia y dedicación, así como por la inolvidable experiencia de mi estancia pre-doctoral en el centro de Fontenay-aux-Roses (Paris). A este respecto, agradezco a los doctores Ahmed Bentaib, Nicolas Meynet y Alexandre Bleyer por su buena acogida y su ayuda en la investigación.

Un reconocimiento especial a los profesores Francisco Vera García y Francisco Javier Sánchez Velasco. Gracias por vuestro apoyo y consejo a lo largo de este periodo. Igualmente, doy las gracias a mis compañeros doctorandos del Departamento de Ingeniería Térmica y de Fluidos, por la cercanía, la amistad, y los buenos momentos compartidos.

Nunca podré agradecer suficientemente a mi familia, ya que ellos son la base sobre la que he podido construir mi presente y mi futuro, con su ejemplo y su constante aliento. Pero mi principal agradecimiento es para ti, Elena, que has sido la mejor compañera con tu cariño y comprensión en los buenos y malos momentos. A ti va dedicado este trabajo. Contigo, esta es sólo una pequeña meta, de las muchas que superaremos juntos en nuestras vidas.

Gracias a Dios. En él vivimos, en él nos movemos y existimos. Que todo nuestro trabajo y esfuerzo sea en gloria y alabanza suya.



# CONTENTS

---

<b>I</b>	<b>THEORETICAL STUDY</b>	<b>1</b>
<b>1</b>	<b>INTRODUCTION</b>	<b>3</b>
1.1	Industry interest in particle mobilisation and explosion problems	3
1.2	The International Thermonuclear Experimental Reactor (ITER) project	5
1.2.1	Safety issue in ITER project	7
1.2.2	Mathematical modelling for the analysis of Reference Events	11
1.3	Thesis objectives and setting out	12
1.3.1	Main objectives of this Thesis	12
1.3.2	Thesis setting out	13
<b>2</b>	<b>STATE OF THE ART</b>	<b>15</b>
2.1	Models for the analysis of gas-particle mixtures	15
2.2	Combustion of dust	17
2.2.1	Chen et al. (1996)	20
2.2.2	Detonation in gaseous explosive mixtures with aluminium particles in suspension	21
2.2.3	Detonation phenomena in dense particle beds. Deflagration to Detonation Transition	26
2.3	Review of models for unsteady, two-phase flow	31
2.3.1	Baer and Nunziato model for laden mixtures	31
2.3.2	Hoffman and Krier model of equations	34
2.3.3	Models of equations by Powers, Stewart and Krier	35
2.3.4	Veyssi�re- Khasainov model	37
2.3.5	Chen and Fan	40
2.3.6	The Warsaw model	42
2.4	State of the Art on Closure Laws	46
2.4.1	Force balance model	46
2.4.2	Particle interfacial forces	47
2.4.3	Interfacial heat transfer	51
2.4.4	Equations of state for the two-phase system	54
2.4.5	Gas-phase combustion in reactive atmospheres	58
2.4.6	Literature review on the oxidation of carbon particles	62
2.4.7	Tungsten combustion laws	72
<b>3</b>	<b>PHYSICAL MODELS FOR REACTIVE TWO-PHASE MIXTURES</b>	<b>81</b>
3.1	Hyperbolic Systems of Conservation Equations	81
3.1.1	Exact solution of the Riemann problem for a linear hyperbolic system	84

3.1.2	Non-linearities and shock formation	85
3.2	Euler equations for a mixture of gases	88
3.3	Governing Equations for Unsteady, Two-Phase Flow	91
3.3.1	Hyperbolicity of the system	92
3.4	Definition of the Source Terms in the model	93
3.4.1	Drag force on particles and interfacial heat transfer	93
3.4.2	Modelling of combustion	93
4	NUMERICAL METHODS	101
4.1	Conservative Method for Hyperbolic Equations	103
4.1.1	Domain discretisation for the Conservative Scheme	105
4.2	Conservative Upwind Methods	107
4.3	Convective Flux Evaluation	110
4.3.1	First-order Upwind Method by Godunov	111
4.3.2	Approximate Riemann Solvers	112
4.4	Source terms solution	121
4.4.1	First step: friction terms	122
4.4.2	Second step: heat transfer terms	124
4.4.3	Third step: integration of the reactive source terms	125
4.4.4	Fourth step: rest of source terms (gravity)	126
4.4.5	Time step modelling for the case of combustion of multiple species	126
4.5	Boundary Conditions	129
II	NUMERICAL STUDY	133
5	RESULTS FOR MOBILISATION TESTS	135
5.1	Mobilisation of dust induced by a 1D shock wave	135
5.1.1	Description of the test	135
5.1.2	Sensitivity Study Numerical results: influence of the thermodynamic variables on the wave structure	136
5.1.3	Results for Shock Tube Problem under numerically adverse source-term conditions	138
5.1.4	Grid convergence study for the one-dimensional shock-wave simulations	144
5.2	2D and 3D Dust Mobilisation due to Rarefaction Waves	144
5.2.1	Description of the Test	145
5.2.2	Numerical results on validation of the numerical source term treatment proposed	147
5.2.3	Results for the rarefaction wave problem under numerically adverse source term conditions	148
5.3	Analysis of 3D Dust Mobilisation Problems Inside of ITER	150
6	RESULTS FOR COMBUSTION TESTS	155

6.1	Shock Wave Induced by Combustion of Particles in Suspension: Chen Test	155	
6.1.1	Initial conditions and test configuration	155	
6.1.2	One-dimensional and multi dimensional grids for this test	157	
6.1.3	Computational implementation	157	
6.1.4	Numerical results	158	
6.1.5	Discussion of results for the multi-dimensional cases	161	
6.1.6	Grid convergence study for dust combustion simulations	163	
6.2	Detonation Induced by Combustion of Hydrogen and Solid Particles	166	
6.2.1	Veyssi�re Test geometry and spatial discretisation	166	
6.2.2	Test specifications	167	
6.2.3	Numerical results	168	
6.3	W-Dust Combustion in a Reacting Multicomponent Atmosphere	176	
6.3.1	Description of the Test	176	
6.3.2	Results for low concentration test	176	
6.3.3	Results for high concentration test	178	
6.4	Graphite Combustion in Reactive Atmosphere	183	
6.4.1	Implementation of graphite combustion models	183	
6.4.2	Definition of Orleans tests	187	
6.4.3	Mesh analysis	188	
6.4.4	Analysis of different initiation sequences	193	
6.4.5	Analysis on the influence of particle concentration	197	
6.4.6	Simulation of graphite experiments at CNRS Orleans	198	
6.5	3D Simulation of Tungsten combustion inside a sphere	203	
6.5.1	Simulation of tungsten experiments at CNRS Orleans	203	
7	CONCLUSIONS AND PERSPECTIVES	209	
III	APPENDIX	215	
A	IMPLEMENTATION IN CAST3M	217	
A.1	The code Cast3M and its philosophy	217	
A.1.1	Programming languages: Gibiane and Esope	218	
A.1.2	Operators and their structure	221	
A.2	Application into fluid dynamics, compressible flow simulations	222	
A.2.1	Different approaches for numerical flux evaluation (implemented schemes)	227	

A.2.2	Detonations in Cast3M. FLAM and DETO operators.	228
A.3	Implementation of the solid phase	229
A.3.1	Operators being modified	232
A.3.2	FUENTE operator: friction and heat transfer	241
A.4	Modifications undertaken for combustion	246
BIBLIOGRAPHY		253

## LIST OF FIGURES

---

Figure 1.1	Section of the overview of ITER scheme.	7
Figure 1.2	Photography inside the JET tokamak.	8
Figure 2.1	Variation with time of spatial distribution of two-dimensional detonation.	19
Figure 2.2	Outline of Chen's horizontal combustion tube.	20
Figure 2.3	Typical pressure histories in combustion of pentane in a suspension of particles [20].	21
Figure 2.4	Veyssiere's Detonation tube.	22
Figure 2.5	Detonation structure according to Veyssi�re et al. [133].	22
Figure 2.6	Pressure profile in detonation of mixture H-1. Source: Veyssi�re [130].	23
Figure 2.7	Pressure profile in detonation of mixture H-1 with Al particles, at two points [130].	24
Figure 2.8	Pressure profile in detonation of mixture H-2 with Al particles, at two points [130].	24
Figure 2.9	Forces acting on a single sphere at rest on a wall with a steady, fully developed flow.	47
Figure 2.10	Laws for $C_d$ from literature, as a function of Re number.	50
Figure 2.11	Two laws for Nusselt number from literature, as a function of $Re_p$ number.	53
Figure 2.12	Rate coefficients in Arrhenius form [11].	62
Figure 2.13	Chemical kinetics data for heterogeneous oxidation of some coals [1].	65
Figure 2.14	Elementary reaction rates from [18].	69
Figure 2.15	Variation of burning rates and surface temperatures with particle size (source [17]).	71
Figure 2.16	Ignition temperatures of tungsten vs. oxygen concentration [74].	74
Figure 2.17	Reaction rate of reaction W-1 as a function of pressure and temperature.	78
Figure 2.18	Reaction rate of reaction W-2 as a function of pressure and temperature.	79
Figure 3.1	Structure of the solution of a linear Riemann problem.	85
Figure 3.2	Characteristic curves for hyperbolic equations at the initial time.	86
Figure 3.3	Characteristic curves for discontinuous data leading to a shock or rarefaction wave.	87

Figure 4.1	Discretisation of the 1D domain $[0,L]$ into $M$ finite volumes. 104
Figure 4.2	Data piece-wise distribution, at time level $n$ . 106
Figure 4.3	Outline of the time stepping strategy for multiple reactions. 128
Figure 4.4	Flowchart of the computational loop on combustion time stepping. 129
Figure 4.5	Boundary conditions in a 1D domain. Ghost cells outside the computational domain. 130
Figure 5.1	Shock tube problem geometry. 135
Figure 5.2	Laws for CD from literature, as a function of Re number. 136
Figure 5.3	Comparison of 1D shock-tube problem for single and two-phase flow. 137
Figure 5.4	Influence of particle diameter ( $\mu\text{m}$ ) on gas and particle variables. 139
Figure 5.5	Influence of particle concentration on gas and particle variables. 140
Figure 5.6	Results with both the conventional and the ASTT methods for ITER conditions. 141
Figure 5.7	Results obtained for the modified problem with W. 142
Figure 5.8	Results from the modified problem with W at different times. 143
Figure 5.9	Grid convergence analysis for the 1D mesh with Miura & Glass test. 145
Figure 5.10	Dust mobilisation problem geometry. 146
Figure 5.11	2D mesh for the analysis of dust mobilisation provoked by rarefaction waves. 146
Figure 5.12	3D mesh for the analysis of dust mobilisation problem by rarefaction waves. 147
Figure 5.13	Klemens Test. Particle concentration distribution in the tube. 1 <sup>st</sup> order. 147
Figure 5.14	Klemens Test. Particle concentration distribution in the tube. 2 <sup>nd</sup> order. 148
Figure 5.15	Klemens Test. Particle concentration distribution with a finer mesh. 148
Figure 5.16	Particle concentration at different times, different positions and different particle diameters. 149
Figure 5.17	ITER VV mesh for the study of the mobilisation problem. 151
Figure 5.18	Evolution of dust concentration ( $\text{kg}/\text{m}^3$ ) during the mobilisation of particles inside ITER (from $t = 0$ to $t = 45.0$ ms). 152
Figure 6.1	Smooth tube geometric model for Chen Test. 156

- Figure 6.2 2D and 3D grids for multi-dimensional Chen Test. 158
- Figure 6.3 Chen Test: Pressure history over time for 1D and 2D computations. 159
- Figure 6.4 Chen test: 1D and 2D-3D results. Dashed line: results from 1D model, continuous line: 2D and 3D model outcomes. 160
- Figure 6.5 2D Chen Test outcomes: Contours of particles velocity (m/s) at every 0.001 s. 161
- Figure 6.6 3D Chen Test outcomes. Top: Contours of pressure (Pa), bottom: velocity of particles (m/s) at every 0.001 s. 162
- Figure 6.7 1D Chen test with adapted kinetic parameters. 164
- Figure 6.8 Pressure history for the 1D Chen test. Computations with varying grid resolutions. 165
- Figure 6.9 Pressure history for the 1D Chen test with adapted parameters. Computations with varying grid resolutions. 165
- Figure 6.10 Smooth duct model for Veyssi re Test. 167
- Figure 6.11 2D grid for numerical resolution of Veyssi re Test. 167
- Figure 6.12 Distribution of variables along the vertical combustion tube for 1D Veyssi re- Test H1. 169
- Figure 6.13 Mass fractions of species in Veyssi re Test H1, at  $t = 0.6$  ms. 170
- Figure 6.14 Pressure history of the detonation in Veyssi re Test H1, at 1.195 m from the ignition point. 171
- Figure 6.15 Distribution of variables for 2D Veyssi re Test H1. 173
- Figure 6.16 Distribution of variables for 2D Veyssi re Test H1. 174
- Figure 6.17 Flame propagation (m) vs. time (ms) for the H<sub>2</sub>-Al detonation. 2D Veyssi re Test. 174
- Figure 6.18 2D Veyssi re Test outcomes: Contours of gas velocity (m/s) at every 0.1176 ms. 175
- Figure 6.19 Smooth duct model for W-combustion Test. 176
- Figure 6.20 Results of W combustion Test for low concentration. 179
- Figure 6.21 Results of W combustion Test for low concentration. 180
- Figure 6.22 Results of W combustion Test for high concentration. 181
- Figure 6.23 Results of W combustion Test for high concentration. 182

- Figure 6.24 Implementation in 2D *DUST* code of combustion models from literature: horizontal 2D tube at 24 ms. 185
- Figure 6.25 Spatial distributions at 2.5 ms in the CNRS Orleans sphere. Combustion models from literature. 186
- Figure 6.26 Graphite combustion laws from literature. History of absolute pressure in 3D Orleans. 187
- Figure 6.27 Simplified geometry of the CNRS Orleans experiment. 188
- Figure 6.28 Two different approaches to mesh a spherical sector: constant thickness (left) and constant volumes (right). 189
- Figure 6.29 3D grid of spherical sector with  $\alpha = 0.36^\circ$ . 190
- Figure 6.30 Cell detonation sizes for different fuel-air mixtures. 192
- Figure 6.31 Grid convergence in the 3D CNRS Orleans sphere with graphite. Gauge pressure at the wall. 194
- Figure 6.32 3D CNRS Orleans sphere with three different solid angles. History of gauge pressure at the wall. 194
- Figure 6.33 3D Orleans with graphite. Overpressure at the sphere's wall for different ignition strategies. 197
- Figure 6.34 Influence of  $\sigma$  in the combustion. Transient evolution of temperature distributions for various particle concentrations. 198
- Figure 6.35 3D Orleans with graphite. Overpressure at the sphere's wall for different particle concentrations. 199
- Figure 6.36 Experimental results of gauge pressure vs. time in the CNRS Orleans sphere with graphite [104]. 200
- Figure 6.37 Result of 3D numerical simulations for graphite Orleans tests. 201
- Figure 6.38 3D Orleans tests with graphite. Numerical errors vs. time for every test simulated from EXP1 to EXP4. 202
- Figure 6.39 Experimental gauge pressure in the sphere vs. time for Tungsten Orleans tests. 205
- Figure 6.40 Gauge pressure at the wall vs. time for simulations. Mesh of 60 cells. Tungsten Orleans tests. 206
- Figure 6.41 Gauge pressure at the wall vs. time for simulations. Mesh of 600 cells. Tungsten Orleans tests. 206
- Figure A.1 File structure of FLAM operator. 230

Figure A.2	Flow chart of a general solution strategy in Cast3M. <a href="#">231</a>
Figure A.3	Diagram on the structure of KONV operator in Cast3M. <a href="#">233</a>
Figure A.4	Diagram on the structure of KONV operator in Cast3M. <a href="#">235</a>
Figure A.5	Diagram on the structure of PRET operator in Cast3M. <a href="#">239</a>
Figure A.6	Diagram on the structure of PRET operator in Cast3M. <a href="#">239</a>
Figure A.7	Diagram on the structure of PRIM operator in Cast3M. <a href="#">241</a>
Figure A.8	Diagram on the structure of PRIM operator in Cast3M. <a href="#">241</a>
Figure A.9	File structure of FUEN operator: PHASEIN1 and PHASEIN2. <a href="#">243</a>
Figure A.10	File structure of FUEN operator. <a href="#">247</a>
Figure A.11	File structure constructed for 'COMBUSTC' and 'COMBUSTW'. <a href="#">249</a>
Figure A.12	General flowchart of a two-phase problem in Cast3M. <a href="#">252</a>

## LIST OF TABLES

---

Table 1.1	Fundamental aspects addressed in dust explosion research. <a href="#">4</a>
Table 1.2	Detailed list of Reference Events analysed in the project. <a href="#">9</a>
Table 2.1	CO oxidation kinetic laws proposed by literature (Desroches-Ducarne et al., 1998). <a href="#">60</a>
Table 2.2	Non-porous graphite reaction mechanism Chelliah [17]. <a href="#">71</a>
Table 2.3	Porous graphite reaction mechanism Chelliah [17]. <a href="#">71</a>
Table 5.1	Shock tube problem initial conditions. <a href="#">136</a>
Table 6.1	Initial parameters for 1D W-combustion Tests. <a href="#">177</a>
Table 6.2	Grid convergence analysis for Orleans tests. <a href="#">195</a>
Table 6.3	Orleans tests. Energy parameters for different initiation strategies. <a href="#">196</a>
Table 6.4	Numerical errors for the Orleans Tests. <a href="#">202</a>
Table 6.5	Initial parameters for tungsten combustion tests in CNRS Orleans sphere. <a href="#">204</a>

Table A.1	Succinct description of the types of object in Cast3M. <a href="#">220</a>
Table A.2	A variety of CFD tests already studied with Cast3M. <a href="#">223</a>
Table A.3	Finite elements and finite volumes for the Navier-Stokes and Euler formulations, respectively. <a href="#">224</a>

Part I

THEORETICAL STUDY



## INTRODUCTION

---

### 1.1 INDUSTRY INTEREST IN PARTICLE MOBILISATION AND EXPLOSION PROBLEMS

Solid particles and gas mixtures are encountered in many scientific and industrial fields such as combustion, pollutant dispersion, filter technology, ventilation systems or fluid catalytic crackers. Reactive gas-particle interaction is also a key process nowadays in the field of Renewable Energies, because of its key role in fluidised bed combustors and biomass fuel blends [106]. In certain fields like agricultural, chemical, metallurgical or nuclear industry, special interest has been paid to these mixtures because of safety reasons. Problems related to dust mobilisation or dust combustion have become primordial issues due to the existing risks for population and other nearby facilities .

Dust explosion hazards represent a constant threat to process industries that manufacture, use and/or handle powders or dusts of combustible materials. Table 1.1 summarises some fundamental research topics addressed in dust explosion research over the years.

Research on dust explosions has been a very active field for a long time. There are registered accidents from more than a century. Nearly 140 years ago, in 1878, R. Weber, one of the pioneers of dust explosion research, stressed the importance of accounting for dust cohesion and dust dispersibility when considering the possibility of generation of explosive dust clouds. It is suggested that two large dust explosion disasters, one in Szczecin (Poland) and one in Munich (Germany), were mainly due to the high dispersibility of the flours [31]. One of the main areas of development of combustion models of mixtures of flammable dusts and gases is the combustion of explosive coal dust. Pressure waves, for example those induced by a combustible gas inside a coal mine, disperse coal dust from walls of the mine into the gas stream and forms an explosive dust cloud, which may make initial explosion sustained by itself and propagated on a long distance. Situations like these could be very hazardous because a weak primary explosion can initiate a strong one in a whole area, where the dust deposit is present. A typical example of such situation is a coal mine with a high risk of methane explosion. Weak explosion of methane-air mixture can generate a pressure wave which may disperse the deposited dust. The combustion of methane can cause the ignition of the dust-air mixture and then a strong pressure wave can be generated which intensifies the dust dispersion process and finally causes a powerful explosion [63].

## INTRODUCTION

---

### 1.1 INDUSTRY INTEREST IN PARTICLE MOBILISATION AND EXPLOSION PROBLEMS

Solid particles and gas mixtures are encountered in many scientific and industrial fields such as combustion, pollutant dispersion, filter technology, ventilation systems or fluid catalytic crackers. Reactive gas-particle interaction is also a key process nowadays in the field of Renewable Energies, because of its key role in fluidised bed combustors and biomass fuel blends [106]. In certain fields like agricultural, chemical, metallurgical or nuclear industry, special interest has been paid to these mixtures because of safety reasons. Problems related to dust mobilisation or dust combustion have become primordial issues due to the existing risks for population and other nearby facilities .

Dust explosion hazards represent a constant threat to process industries that manufacture, use and/or handle powders or dusts of combustible materials. Table 1.1 summarises some fundamental research topics addressed in dust explosion research over the years.

Research on dust explosions has been a very active field for a long time. There are registered accidents from more than a century. Nearly 140 years ago, in 1878, R. Weber, one of the pioneers of dust explosion research, stressed the importance of accounting for dust cohesion and dust dispersibility when considering the possibility of generation of explosive dust clouds. It is suggested that two large dust explosion disasters, one in Szczecin (Poland) and one in Munich (Germany), were mainly due to the high dispersibility of the flours [31]. One of the main areas of development of combustion models of mixtures of flammable dusts and gases is the combustion of explosive coal dust. Pressure waves, for example those induced by a combustible gas inside a coal mine, disperse coal dust from walls of the mine into the gas stream and forms an explosive dust cloud, which may make initial explosion sustained by itself and propagated on a long distance. Situations like these could be very hazardous because a weak primary explosion can initiate a strong one in a whole area, where the dust deposit is present. A typical example of such situation is a coal mine with a high risk of methane explosion. Weak explosion of methane-air mixture can generate a pressure wave which may disperse the deposited dust. The combustion of methane can cause the ignition of the dust-air mixture and then a strong pressure wave can be generated which intensifies the dust dispersion process and finally causes a powerful explosion [63].

DUST CLOUD FORMATION PROCESSES	DUST CLOUD IGNITION PROCESSES	FLAME PROPAGATION PROCESSES IN DUST CLOUDS	BLAST WAVES GENERATED BY BURNING DUST CLOUDS
Inter-particle forces in dust deposits (cohesion). Entrainment of particles from dust deposits by shock waves passing across the deposit surface. Entrainment of particles from dust deposits by turbulent gas flows. Transport of dust particles in turbulent gas flows. Measurement and characterisation of turbulence in dust clouds. Measurement and characterisation of spatial distribution of particles in dust clouds.	Ignition of single particles and clouds. Ignition by smouldering combustion in dust layers or deposits. Ignition by hot surfaces. Ignition by flying burning metal particles. Ignition by electric sparks and arcs. Ignition by electrostatic discharges. Ignition by hot gas jets. Ignition by shock waves. Ignition by hot-spots from focused light beams. Influences on dust cloud ignition sensitivity of cloud properties.	Microscopic aspects (Single-particle ignition) and combustion in hot oxidiser gas. Laminar and turbulent flames in dust clouds. Mechanisms of heat transfer (conduction, convection, radiation). Limit conditions for flame propagation in dust clouds (particle properties, dust conc., oxygen conc., geometry). Acceleration of flames in dust clouds by turbulence mechanisms. Detonation phenomena in dust clouds.	Blast wave properties as a function of properties of burning dust clouds. Effects of blast waves on humans and mechanical structures. Ability of blast waves from dust explosions to transform dust layers into explosive dust clouds (coupled to first column of table).

Table 1.1: Fundamental aspects addressed in dust explosion research.

On coal dust explosion, Cybulski [25] reports explosions in an experimental gallery in which pressures of up to six or seven atmospheres were observed. But, in smaller ducts, it appears to be much more difficult to initiate such explosions. However, an understanding of flame propagation in confined dust/air mixtures is also needed for the safe design of industrial pneumatic conveying systems and with that aim, Pickles [91] develops a theoretical model for coal dust explosion propagating in small ducts. describing the flow pattern along the duct generated by the explosion. He concludes that the finite particle burning time restricts the development of explosions in small ducts.

Clark and L.D. [21] presented, some years later, a model describing the turbulent coal dust flame propagation and acceleration based on the transient macroscopic equations of change. Turbulent flame velocity was obtained by a simple correlation technique that combines chemical and turbulent effects.

One of the most important determining factors in the spontaneous explosion of organic dust is the inflammation of volatiles. This has a strong effect on coal dust explosions, but especially in the case of peat dust, where the concentration of volatiles can reach 70 weight percent of dry matter. Kjaldman [59] reported a numerical model for peat dust deflagration, based on the experiments done in a closed

spherical vessel. The model included drying and pyrolysis of the particles, and combustion of the devolatilised gases.

Regarding the ignition of metal solid particles, an early work by Medvedev et al. [77] dealt with the mathematical description of the flow of a mixture of gas and solid particles, with the ignition and combustion of them when the temperature conditions of the gas phase is sufficiently high. The combustion model, based on a general Arrhenius equation, did not specify parameters for a given metal. Soon after, Boiko et al. [10] showed the results of an experimental and theoretical study of the movement and ignition of solid particles behind shock waves. They described the drag coefficient found for the particles and the effects of the volume concentration of particles on the acceleration in the supersonic flow. They proposed both mathematical and numerical models to describe the ignition of particles and compared the experimental results for the case of magnesium particles.

On **nuclear safety** [43], a detailed understanding of those gas-particle processes is especially important not only in the analysis of accident sequences in nuclear fission power plants [127], but also in fusion facilities such as *tokamaks* [76], as in the International Thermonuclear Experimental Reactor (ITER) [110]. As mentioned (and later developed in Section 1.3), this work is devoted to the modelling of some certain accident scenarios in the context of ITER operation safety analysis. In the next Section, a few paragraphs are added aiming to contextualise the present development of the project and nuclear fusion as a new, profitable source of energy.

## 1.2 THE INTERNATIONAL THERMONUCLEAR EXPERIMENTAL REACTOR (ITER) PROJECT

Development of nuclear fusion as a practical energy source could provide great benefits. This fact has been widely recognised and fusion research has enjoyed a high level of international co-operation.

Fusion power plants are expected to have high gains, that is, producing more energy than required to ignite the reaction, after 60 years of design improvements and scientific progress. In fact, a high energy payback ratio ( $Q \geq 10$ ) is expected for a standard reactor. For example, from 50 MW of input power, the ITER machine is designed to produce 500 MW of fusion power [48]. This will hopefully tend a way to reconcile the constantly growing demand of energy with the environmental hazards resulting from the present energy supply. Currently, the expected gradual depletion of fossil fuels and environmental concerns about emissions of greenhouse gases are urging the development of new “alternative” sources of large-scale, clean energy. In this sense, nuclear fusion is presented as a strong and hopeful re-

sponse to the energy challenge that current and future generations are facing.

Twentieth-century fusion science has identified the most efficient fusion reaction to reproduce in the laboratory setting: the reaction between two hydrogen (H) isotopes deuterium (D) and tritium (T). The D-T fusion reaction produces the highest energy gain at the “lowest” temperatures. It requires nonetheless temperatures of  $150,000,000^{\circ}$  Celsius to take place—ten times higher than the H-H reaction occurring at the Sun’s core. At such extreme temperatures, electrons are separated from nuclei and a gas becomes a plasma.

Building upon the experiments on nuclear transmutation by E. Rutherford in the early 1930s, the fusion of hydrogen isotopes in laboratory was first accomplished by M. Oliphant in 1932. During the remainder of that decade, the steps of the main cycle of nuclear fusion in stars were worked out by H. Bethe.

Research into developing controlled thermonuclear fusion for civil and non-violent purposes began in earnest in the 1950s, and it continues to this day. This process has been full of extreme scientific and technological challenges, what has led into progress. Due to the extreme conditions that must be met to result in a fusion reaction, throughout history the use of this energy has proved to be unworkable. Also the absence of known materials capable of withstanding such high temperatures makes this purpose a feat of engineering.

The Joint European Torus (JET) in Culham, U.K., in operation since 1983, is a first step in this direction. In 1991, the JET tokamak achieved the world’s first controlled release of fusion power. The Japanese JT-60 achieved the highest value of fusion triple product—density, temperature, confinement time—of any device to date. Meanwhile, US fusion installations have reached temperatures of several hundred million degrees Celsius.

In this context of technical achievements, the development of the International Experimental Thermonuclear Reactor is started. After a initial phase of conceptual design (1988-1990), and the subsequent Engineering Design Activities, a final document was signed in 2001 by the four parties (EU, Russia, Japan and USA). The results from this process, were gathered in the ITER technical basis [94], where design specification, operation, safety issues and the project costs were detailed.

A critical issue for fusion-plasma research was the erosion of the first wall of plasma facing components due to impulsive heating from repetitive instabilities known as ‘edge-localized modes’ (ELMs). This key problem was resolved in 2006 by Evans et al. [33]. They shown that the addition of small resonant magnetic field perturbations completely eliminates ELMs while maintaining a steady-state high-confinement plasma. The solution was based on the use of a reactor with a *Tokamak* design (Figure 1.1), in which the plasma is

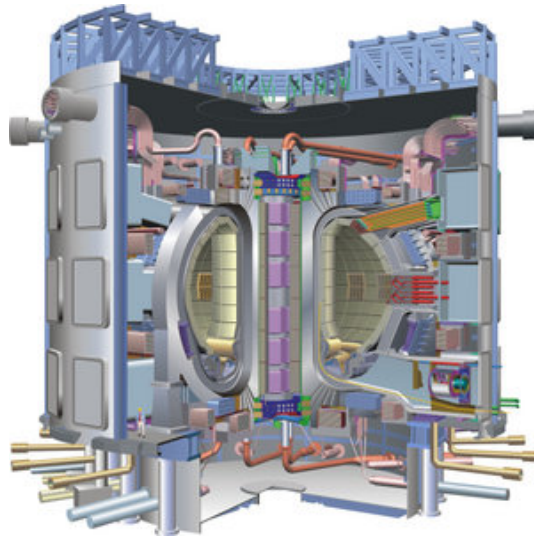


Figure 1.1: Section of the overview of ITER scheme.

contained in a doughnut-shaped vacuum vessel with toroidal magnetic confinement devices.

In May 2006, the ITER project partners signed the release of the reactor, which would be built in Cadarache (France), using the Tokamak design. Construction costs were estimated at 4,570 million Euros and duration of construction in 10 years.

#### 1.2.1 *Safety issue in ITER project*

Safety is a top-priority issue for ITER. The technical specifications [94] are concerned about the safety of the project, staff and workers on site, the local population and the environment. French nuclear regulations have been applied throughout the design phase of the project, and shall continue to be applied during construction, operation, and decommissioning. The IRSN (Institut de Radioprotection et de Sûreté Nucléaire) is the French public service expert in nuclear and radiation risks, nuclear reactor safety and the prevention of major accidents. Thus, they emerge as a competent authority on ITER safety assessments.

The ITER installation is classed as a "basic nuclear installation" by French authorities. In a tokamak fusion device, the quantity of fuel present in the vessel at any one time is sufficient for a few-seconds burn only. It is difficult to reach and maintain the precise conditions necessary for fusion; any disruption in these conditions and the plasma cools within seconds and the reaction stops; there is no danger of run-away reaction or explosion. In addition, ITER's tokamak is being made of specially reinforced concrete, and will rest upon bearing pads, specially designed to withstand earthquakes.

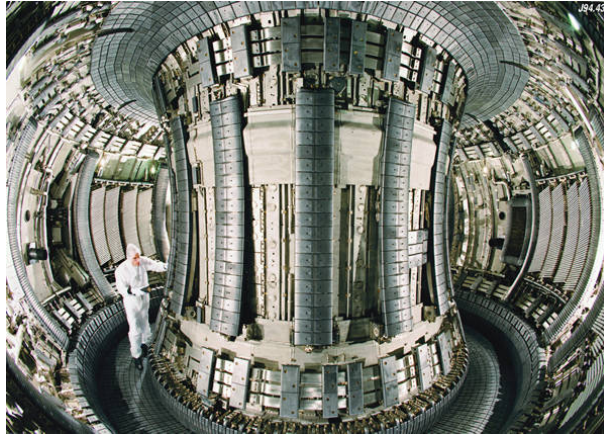


Figure 1.2: Photography inside the JET tokamak.

Furthermore, based on feedback from the European tokamak JET (Figure 1.2), the most modern and efficient safety measures for the handling of tritium have been incorporated into the ITER design. Tritium is a radioactive substance that also has applications in medicine and technology; the techniques for the safe storage and handling of tritium are well developed. ITER has been designed to protect against tritium release and against workers' exposure to radioactivity.

#### 1.2.1.1 Reference Events analysis

A comprehensive analysis of off-normal events has been performed to assess the effectiveness of the implementation of the safety requirements and functions in the ITER design (see [94]). The analyses must include conservative assumptions of initial facility operating and off-normal conditions and thoroughly examine possible ways for tritium, activated corrosion products in coolants, and neutron-activated tokamak dust, to be released to the environment. The evaluation for all of these *reference events* (Table 1.2) must show that radioactive releases are well below the project release guidelines, so that they would result in no significant risk to the general public from postulated accidents.

In the safety analyses, events and plant conditions are categorised as follows:

- **Normal operation** events and plant conditions are planned and required for normal operation, including some faults and events which can occur as a result of the experimental nature of ITER;
- **Incidents** are deviations from normal operation, event sequences or conditions not planned but likely to occur one or more times during the life of the plant as the result of components failures (excluding normal operation events);

- **Accidents** are event sequences or conditions not likely to occur during the plant life but are postulated to demonstrate the safety of the facility.

The basic principle in relating design requirements to each of the conditions is that the most probable occurrences should yield the least radiation exposure to the public, and those conditions having the potential for the greatest exposure to the public should be those least likely to occur.

Table 1.2 shows the 25 different reference events that have been analysed in-depth with their respective categories. These were selected to cover the major systems, the radioactive inventories distributed amongst these systems, and initiator types that have the potential to cause releases.

Event Family	Events
Plasma events	Loss of plasma control/exceptional plasma behaviour (i,a)
Loss of electrical power	Loss of off-site power for up to 1 h (i)
	Loss of off-site power for up to 32 h (a)
	Loss of off-site power and on-site class III power for 1 h (a)
In-vessel events	In-vessel first wall pipe or coolant channel leak (i)
	Multiple first wall pipe or coolant channel damage (a)
	Loss of vacuum through a vacuum vessel penetration line (a)
Ex-vessel HTS events	Loss of heat sink in divertor HTS (i)
	Pump trip/loss of flow in divertor HTS (i)
	Pump seizure in divertor HTS (a)
	Vacuum vessel HTS break (a)
	Large ex-vessel divertor HTS break (a)
	Heat exchanger leakage (i)
Tritium plant and fuel cycle events	Heat exchanger tube rupture (a)
	Tritium process line leakage (i)
	Transport hydride bed mishandling (a)
	Isotope separation system failure (a)
Maintenance events	Fuelling line with impaired confinement (a)
	Stuck divertor cassette in transport cask (a)
Magnet events	Maintenance accident on vacuum vessel (a)
	TF short. (a)
Cryostat event	Magnet arc (a)
	Air ingress (a)
Hot cell events	Water/air/helium ingress (a)
	Failure of confinement (a)

Table 1.2: Detailed list of Reference Events analysed in the project.

Hereinafter, we will focus on two specific reference events: (i) first wall pipe or coolant channel damage and (ii) loss of vacuum accident (LOVA) through a penetration line of the vacuum vessel. These are outlined below:

- (i) **Coolant Leakage:** During plasma operation, a double-ended pipe rupture of the largest pipe ( $0.4 \text{ m}^2$  flow area) is postulated to occur in the ex-vessel section of a coolant loop. Coolant is discharged at a high rate into the containment volume. The fusion power is terminated by both active and passive methods to avoid overheating of components. Even if the plasma is terminated, there is a possibility that the in-vessel cooling channels could be damaged. That would lead to a high rising of in-vessel pressure, that must remain lower than  $0.2 \text{ MPa}$ . The pressure peak transports radioactive material through the broken pipe. The corrosion products, dust and tritium in the vault may leak to the environment before the vault pressure is restored to sub-atmospheric pressure within 24 hours after the event.
- (ii) **Loss of Vacuum:** Although vacuum vessel penetrations are designed with care to provide two confinement barriers, the large number of these penetrations suggests that failure of a penetration line should be investigated to demonstrate the tolerance of the design to such failures. A loss of vacuum event results from this. The penetration line ( $0.02 \text{ m}^2$  cross-sectional area) is assumed in the analysis to be connected to the gallery with air atmosphere. Air ingress into the plasma chamber terminates the plasma with a disruption. The shock-wave generated mobilises tritium and dust (Beryllium, Tungsten and steel) initially at rest in the divertor (the lower side of the vacuum vessel). Dust may also violently react with air and water vapour, generating  $\text{H}_2$ , causing in turn a detonation. Radioactivity could be then transported out of the vacuum vessel into the atmosphere.

Substances inside the tokamak, of which emissions may be composed, are tritium used in the reactor, activated products (gases, dust and corrosive substances) and unactivated powder. With regard to the origin of this last, one of the most critical technical challenges of the ITER project is the design of plasma facing components in the reactor's vacuum vessel (VV): the blanket and the divertor. A good resistance to high temperatures and an adequate thermal conductivity are required. Because of these requirements, materials containing Carbon, Beryllium and Tungsten were chosen to cover the first wall in both components [94].

Despite the problem of ELMs was successfully solved [33], as previously commented, some subatomic particles from the plasma break out of the confinement magnetic fields. The high-energy neutron fluxes erode the plasma facing materials generating small loose particle agglomerates ranging from nanometres to millimetres, usually referred to as "dust" [16, 102, 101].

Particulate filters with an efficiency of better than 99.9%, would maintain effluents to very low levels. It is estimated that a few tens

of kg of beryllium dust could be present, which would lead to a discharge below 0.1 g/a.

### 1.2.2 *Mathematical modelling for the analysis of Reference Events*

In order to assess the reference events, mathematical tools are needed to analyse the different scenarios. In this sense, quantitative models are being used, as well as integrated system simulation codes, with a certain degree of accuracy. One can find many options to simulate severe accident scenarios: MELCOR (a product of Sandia National Laboratories), L-3 MAPPs, etc. The potential emissions, calculated by these models, must be below the values outlined in the project's safety specifications.

However, an even more realistic approach is pursued in the present work in order to obtain more reliable assessments. It must implement selected physical models which are able to reproduce complex physical phenomena taking place at hypothetical accident scenarios, i.e., transient detonation, combustion (that means phase exchanges and thermodynamic transformations), dust suspension-mobilisation, particle interaction, and so on. In addition, the convoluted geometry at ITER's VV requires a code with a good geometrical versatility.

For that reason, the IRSN raised the development of a multiple-phase Computational Fluid Dynamics (CFD) code. Indeed, CFD has emerged in the last decades as a valuable tool for problems involving complex flow [128], including phase interaction phenomena and chemical reactions. The progressive improvement of computational capabilities has provided the technical substrate for the scientific progress on this field.

In the last decade, many mathematical models have been developed for the analysis of mixtures of gas and particles. They study the set of non-linear conservation equations for each phase with complex source terms. Most of them lie between two different approximations: Eulerian-Eulerian (E-E) or Eulerian-Lagrangian (E-L). E-E methods treat solid phase as a continuum, they are not suitable for large and heavy particles [118]. The use of an E-E approach, while economical and suited to dense mixtures with two-way coupling, requires good phenomenological models, usually based on kinetic theories for granular flows [66].

In this context, *DUST* is a finite-volume code for 3D simulation of gas-particle interaction which has been developed in close collaboration between IRSN and the UPCT, on the basis of the CAST<sub>3</sub>M code developed at the CEA (Commissariat à l'Énergie Atomique, France) [13, 36, 37, 38]. The code permits the analysis of transient dust spatial distribution, re-suspension and entrainment, as well as explosion, to be carried out in the cases of laden and high dilute mixtures. In addition, the code allows multidimensional problems in unstructured

grids to be studied. It is based on a Eulerian-Eulerian finite-volume approximation where the numerical fluxes at each element interface are evaluated explicitly.

In some cases, such as in ITER accident sequences, the type of dust mobilisation problems being analysed become very complex as they may involve very low initial pressure and a high concentration of dense particles with small diameters. Under these conditions, source terms in the system of balance equations become so stiff that a reformulation of the finite-volume method is needed. The use of splitting methods with an implicitisation of the source terms is proven to help circumvent these difficulties [115, 69].

A new approach is proposed in this work for the treatment of source terms, which delivers physical solutions from the system of equations, even when the source terms become stiffer. This new option is presented as an alternative in numerical calculation of problems with adverse conditions that are too demanding with conventional upwinding methods, such as thermodynamic conditions encountered in the simulation of air ingress in ITER fusion reactor.

### 1.3 THESIS OBJECTIVES AND SETTING OUT

#### 1.3.1 *Main objectives of this Thesis*

This Doctoral Thesis falls within the scope of the safety assessment studies for the future experimental ITER facility. The analysis focuses on the risk of explosion of dust in the vacuum chamber of this facility. The object of the study is to improve and consolidate the currently available modelling of dust mobilisation and explosion.

Therefore, the general objective of this Doctoral Thesis is to build up a consistent numerical code, based on the general equations of Fluid Dynamics, for two-phase, reactive mixtures of particles and gases. The code is intended to provide transient, physically consistent solutions, which are validated with external experimental results. This task must be addressed after a comprehensive literature survey on mathematical models of governing equations these multi-phase mixtures. The sort of model which fits best with the features of the problem under study will be determined through this study on the governing equation in the literature.

The main goal is to develop a suitable tool which is able to compute the ITER hypothetical accident scenarios, such as the aforementioned LOVA event.

The mathematical approach adopted for the numerical resolution of the model must be able to deal with complex phenomena, such as shock wave, detonation, chemical reaction, phase changes, gas-particle interaction, external forces acting on particles and dust explosion. A review on numerical models shall be performed.

Next, the numerical results provided by the code need to be validated by experimental test. These tests will be faced in two major groups:

- (i) those aiming to validate the models for dust mobilisation, and
- (ii) those intended to validate the reaction models.

### 1.3.2 Thesis setting out

This Doctoral Thesis is arranged in three phases, in accordance with the previously established objectives, and the order of milestones that have been followed during the various stages of this research work:

1. Literature survey on physical models: in [Chapter 2](#) a extensive review is presented about published work on mathematical models for the analysis of gas and particle mixtures, with a special emphasis on those works dedicated to particle combustion ([Section 2.2](#)), detonation of particles in suspension ([Section 2.2.2](#)), and detonation on dense mixtures ([Section 2.2.3](#)). Next, a review is addressed on mathematical models of governing equations, from the more general to the more particular models aimed at specific two-phase mixtures. At the end of the chapter, a literature survey is done on closure laws, including physical laws for particle drag force, interfacial heat transfer, equations of state, and combustion mechanisms.

Later, in [Chapter 3](#), some theoretical considerations are given to the hyperbolic systems and the Riemann problem for linear or non-linear systems of equations. Then, in [Section 3.3](#), the system of governing equations for unsteady, two-phase flow which is employed in the numerical calculations of this Thesis is presented.

2. Investigation on numerical methods and schemes for two-phase flow: the numerical approximation of this Thesis is focused on Conservative Methods for Hyperbolic Equations. In [Chapter 4](#), particularities about these methods are expounded. Since the numerical approach implemented on the computational code is based on *splitting* methods, schemes for convective flux evaluation ([Section 4.3](#)) and for the source terms resolution ([Section 4.4](#)) are presented separately. A special emphasis has to be done to the numerical schemes for the evaluation of the particle subsystem of equations, and also to the so-named *Advanced Source-Term Treatment*, a numerical solution developed for the nonhomogeneous problem with the source terms, which acts as a relaxation method in those cases where the test conditions make the problem numerically stiff.

- 
- 
3. Numerical results for reference tests are reported with a focus on both particle mobilisation ([Chapter 5](#)) and combustion of dust in reactive atmospheres ([Chapter 6](#)).

## 2.1 MODELS FOR THE ANALYSIS OF REACTIVE AND NON-REACTIVE GAS AND PARTICLE MIXTURES

In [Section 1.1](#) an overview is given on the interest of industry in mobilisation and combustion processes involving mixtures of particles and gases. The analysis of those phenomena is specially important when dealing with safety assessments.

The way of modelling these problems depends on the application considered, the type of particles, their size, the interaction between the phases, the internal reactions, the problem geometry, and so forth. Even the sort of problem faced in each case will be determinant to choose one model or another.

In last decades, great efforts have been made in order to find proper physical models capable to characterise each particular dust and gas mixture. Most models lay between two different approximations: Eulerian-Eulerian (E-E) or Eulerian-Lagrangian (E-L) approximations. As mentioned above, Eulerian methods treat solid phase as a continuum and they are not suitable for large and heavy particles [118]. Instead, in the Lagrangian approximations, the trajectories of individual particles are pursued and can be applied to any particle size, even particle with large inertia. Particle-to-wall interaction and particle to particle interaction can be taken into account based on the physical properties of the materials concerned.

Lagrangian and Eulerian approaches are compared in many recent works. Turbulent dispersion and coalescence of droplets are simulated within a spray in (Nijdam et al. 2006). They report that the Lagrangian formulation is more practical in terms of the range of applicability and ease implementation. In the Eulerian model, the gaseous and droplet phases are treated as separate interpenetrating continua, with the transport of both phases being modelled in an Eulerian framework. In this work, the Simonin model is used to simulate the turbulent dispersion of the droplet (Simonin, 1991). A standard  $k - \epsilon$  turbulence model is used to predict the turbulent motion of the gas phase. It should be remarked that the Eulerian model described in this paper is specially developed to model the coalescence of droplets in gas flow.

According to Kosinski et al. (2007a), in the E-L approach, the particles are tracked in the computational domain. This kind of model is physically more correct than the E-E models. It makes much easier the implementation of phenomena like particle-particle and particle-

wall interactions, and some particle-fluid interactions (like the lift force, for example). The use of the E-E approach, while economical and suited to dense mixtures with two-way coupling requires good phenomenological models, usually based on kinetic theories for granular flows. Kosinski (2007b) carries out a numerical analysis of the interaction between a shock wave and a cloud of particles in a channel. He proposes an Eulerian-Lagrangian technique so the particle-particle and particle-wall interactions are modelled directly. According to him, the drawback of this approach is that in the real applications, the number of the particles is too large to consider the behaviour of all of them. In order to overcome this problem, he groups the particles in “virtual particles” or clusters, so the number of particles can be reduced. This type of approximations was formerly studied by other authors as Tanaka et al. (1995) and is included in codes as Gasflow (Xu et al., 2006). The drag force is calculated for a single particle and assumed for a cluster with a defined number of the particles. Solving the transient balance equations with a dynamic time stepping procedure, new values of the particle parameters are obtained (linear velocity and temperature). As velocity is linear, the later positions of the particles can be found. If the results corresponding to two particles coincide the particle will collide and the colliding equations will be calculated in order to update the values of linear velocity.

The E-L approach treats the particles as points, whose motion is the result of the influence of the gas phase. The main drawback of the method is that in real industrial applications the number of the particles is too large to consider the behaviour of all of them. In order to overcome the problem, a number of particles are often grouped to form “virtual particles” with the same parameters, so that the number of the particles to be considered may be reduced. During the last years, many interesting studies using or comparing these formulations have appeared in the existing literature. Some of them are briefly described in what follows. Many of them are total or partially Lagrangian.

Apte et al. (2003a, 2003b, 2008) calculates the behaviour of particles and droplets in flows. His work is dedicated to study complex geometries in high fast processes (injection and/or combustion processes). Apte et al. (2003a) describes a stochastic subgrid model for Large-Eddy Simulation (LES). This model is mainly used in spray and liquid atomisation. The parameters of the model are dynamically obtained by relating them to the local Weber number with two-way coupling between the gas and liquid phases. They also describe a new numerical algorithm capable of simultaneously simulating individual droplets as well as a group of droplets with similar properties commonly known as parcels. The numerical algorithm is computationally efficient to capture the complex fragmentary process of liquid

atomisation. Apte (2003b,2007) offers the results of a LES model over a mixture of air and lightly loaded, spherical, glass-particles with a prescribed size-distribution enters. The incompressible, spatially filtered Navier-Stokes equations are solved on unstructured grids to compute the turbulent gas phase. A Lagrangian formulation and an efficient particle-tracking scheme on unstructured meshes is developed to compute the dispersed phase. The particles are treated as point sources and influence the gas only through momentum-exchange terms. The mean and turbulent quantities for the gas and particle phases are compared to experimental data obtained a good agreement.

Hu & Celik (2008), use an E-L model experimented a unsteady two phase flow using gas-liquid bubbly. The simulation that they explained in their article was made by means of LES in combination of Lagrangian tracking with two ways coupling. For the backward momentum coupling they used the concept of “particle-source-in-ball” (PSI-ball), which in essence is a generalisation of the conventional particle-source-in-cell (PSI-cell) method using by Apte and Kosinski in their articles.

On other hand, Pialat et al. (2007) develop a hybrid E-L method to simulate the dispersed phase in turbulent gas-particle flows. The paper presents a methodology to combine stochastic Lagrangian approach and continuum model to simulate the dispersed phase in gas particle turbulent flows. In order to joint both methods they use the fact that both methods are based on the same Boltzmann-like kinetic equation governing the joint fluidparticle a Probability Density Function (PDF).

## 2.2 COMBUSTION OF DUST

Our main concern is to analyse the combustion of mixtures of dust and gases. As discussed above, many works are found in the existing literature, related to the combustion of corn powder, peat, metal powders, and so on. Unlike in the case of solid fuel pellets, when the dust is in suspension, diffusion of hot gases is not the cause of particles ignition. By contrast, particles may burn when hit by a pressure and temperature wave front.

According to Kauffman et al. [55], a shock wave can cause ignition of a dust particle and can initiate the detonation mode of combustion in powder mixtures. Many organic dusts or metallic materials can be ignited by a shock wave, some even more easily than gas mixtures. The size and structure of the dust particles strongly affect the ignition. There is an optimum size diameter for the particles that favours the ignition, for a given material. The relatively short delay in the ignition of many dust particles is due to the peculiar behaviour of them behind an incident shock wave. When a dust particle is subject

to an existing supersonic flow behind the shock wave, a bow shock associated particle is produced. The high temperature gases existing between the arc and the particle cause the rapid warming of the particle surface. Simultaneously, the aerodynamic drag causes the particle to be accelerated, thereby reducing the gas temperature in the region between the bow shock and the particle and, consequently, the rate of convective heating of the particle. Ignition occurs when the surface temperature increases over the critical value necessary for the rapid surface chemical reaction, leading to the combustion of the particle.

The warming rate of the particle depends on its diameter and properties. Very small particles may heat faster than large ones, but smaller particles are accelerated faster to convective flow velocity, so that the high temperature region remains very short time. On the contrary, larger particles are accelerated more slowly, but they absorb more heat before the ignition. Therefore, one concludes that there is an optimum size of particle diameter that provides the best conditions for ignition. Experimental data and calculations confirm these conclusions [55].

In the late nineties, Klammer et al. [60] studied the dust ignition, combustion, and detonation in gases. In their paper, two problems based on a 2D flat gallery are modelled by analytical (Catastrophe model) and numerical methods (finite differences). The mathematical model considers no interaction between particles and the volume fraction of the solid phase is neglected. The gas phase is supposed to behave according to the equation of state of ideal gases. The model used is the set of Navier-Stokes equations for viscous laminar flow and includes the mass flow due to diffusion in the gas phase. The reaction model includes three terms, the solid phase combustion, the solid volatilisation, and the volatilised gas combustion. Therefore, the reaction rate is divided into three different terms:  $\dot{R}$ , which describes the combustion of volatiles under the law of Arrhenius,  $\dot{W}$  the rate of volatiles release, and  $\dot{K}$ , which corresponds to the combustion of the particles and can be calculated as:

$$\dot{K} = A_d (R_s^{-1} + R_d^{-1})^{-1} \quad (2.1)$$

where  $R_s$  is the surface reaction rate and  $R_d$  is the diffusion reaction rate. The parameter  $A_d$  is a shape factor.

Two 2D problems are discussed in this work, which can be adapted for 1D geometry:

- i a detonation initiation by a supersonic inflow, and
- ii ignition of the gas/particle mixture near hot closed end of the tube.

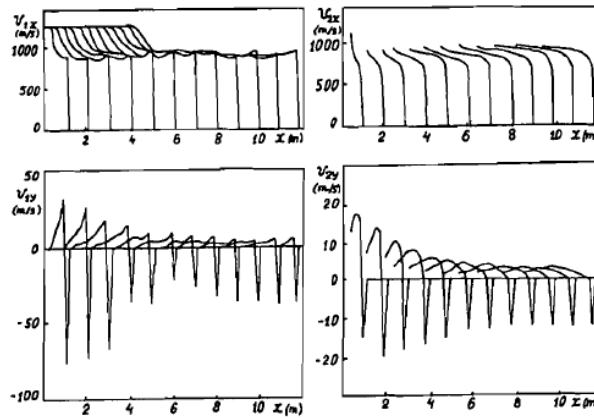


Figure 2.1: Variation with time of spatial distribution for velocity vector components in the case of formation of two-dimensional detonation [60].

Regarding the first problem, they study a bi-dimensional tube (channel). At the initial time, air begins to enter with a supersonic velocity at the position  $x = 0$ . The tube is filled in by air which occupies the volume above a layer of coal dust/air heavy laden mixture with volatile gases. Such distribution simulates the situation which takes place in real coal mine galleries. Formation of two-phase and two-dimensional detonation in the tube is numerically studied at  $t > 0$  in the frame of the mixture flow model adopted.

The propagation of the detonation is illustrated in Figure 2.1. In this figure, the velocity vector components ( $v_{ix}$ ,  $v_{iy}$ ) for the gas phase ( $i = 1$ ) and solid phase ( $i = 2$ ) are shown along the dusty layer at the distance  $y = h/2$  from the bottom wall of the tube. The shock wave is formed in the tube, which destroys the dusty layer causing the particles go up away from the bottom wall.

The second problem studied (ignition of the mixture near hot closed end of a tube) is important for determination of combustion beginning. The difference between this problem and the previous one is only in the boundary conditions at the left end of the tube, which is considered as closed with the temperature of 1500 K keeping for the first 0.8 ms. Figure 2.1 illustrates some results of these calculations for the case of uniform distribution of particles across the tube, where spatial distributions along the tube for the temperature  $T$ , the gas velocity  $v_1$  the pressure  $P$ , and the density of combustion products are given at several time moments for the initial stage of the process.

The model of governing equations presented by Klammer et al. [60] in their study of ignition of coal particles with air, was later employed by Korobeinikov et al. [65] in a study of mine explosions. This model was completed by that introduced by Oleszczak and Klemens [86], for the study of mitigation of dust combustion. Again, they consider three processes in the reaction process:

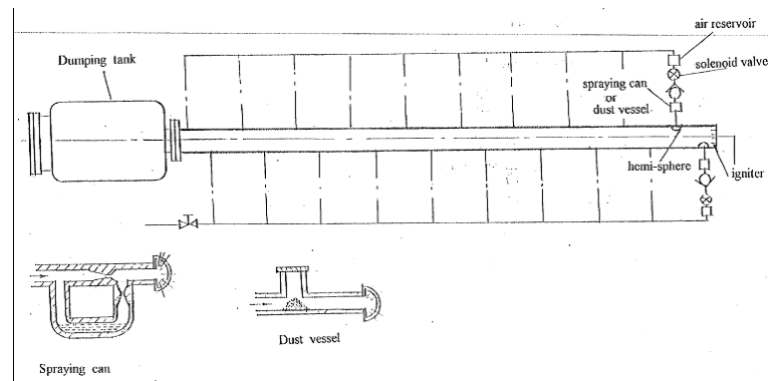


Figure 2.2: Outline drawing of the horizontal combustion tube employed in the study by Chen et al. [20].

- Emission of volatiles,
- Combustion of volatiles,
- Combustion of coke remains.

#### 2.2.1 Chen et al. (1996)

Chen et al. [20] presented an experimental study on the ignition and flame acceleration of a mixture of air and Al particles or sprays in a shock tube. They present an installation consisting of a horizontal combustion tube which creates a homogeneous suspension of aluminium particles and pentane or propane spray.

Chen's first work is dedicated, in short, to explain in detail the facility used and present some experimental results. A schematic representation of the horizontal combustion tube is shown in [20]. It is 12 m long, 0.14 m internal diameter and has 20 devices for the dispersion of dust.

Experiences with the horizontal combustion tube under normal pressure and temperature conditions, show a typical pressure history at different measurement points at distances  $x = 4.05, 4.95, 5.85, 6.75, 7.65$  and  $8.55$  m (Chen et al., 1996). In Figure 2.2 we can see the shock wave induced by the turbulent combustion of a vapour cloud (right: pentane combustion) and a dust and air mixture (left: Al combustion).

In a second work, Chen and Fan [19] numerically study the process of combustion, expansion, and turbulence inside the tube. The problem was solved by using the SIMPLE numerical method. The combustion model is taken from Ogle et al. [85], which can be found in Section 3.4.2.3 and the experimental data comes from the installation introduced previously.

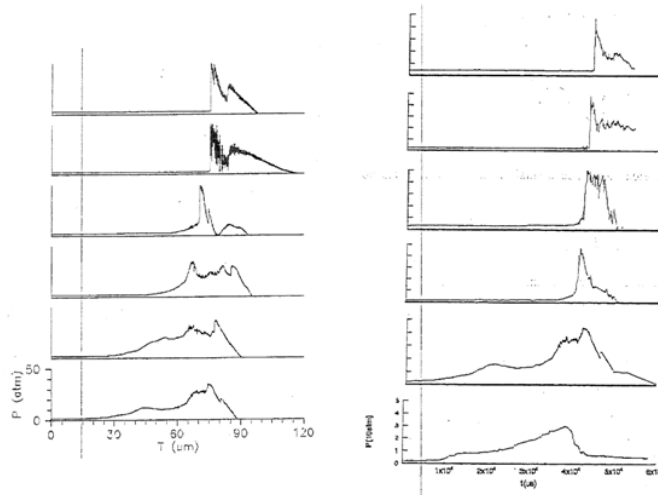


Figure 2.3: Typical pressure histories in combustion of pentane (left) and a suspension of particles and pentane (right). Source: Chen et al. [20].

### 2.2.2 Detonation in gaseous explosive mixtures with aluminium particles in suspension

In the existing literature on the ignition of solid particles in gaseous fuel mixtures one can emphasise the fruitful experimental research carried out by Veyssi re and co-workers [133, 129, 130]. They mostly studied the combustion of aluminium particles in a gaseous detonation, paying attention to the combustion mechanism and the double front detonation (DFD) structure that sometime appears when a metal ignites in some sorts of gaseous fuel mixtures. These works show that the detonation of two-phase media consisting of solid particles suspended in a gaseous mixture cannot be analysed generally by the classical Chapman-Jouget (CJ) theory because the time of particle burning is usually by one or more orders of magnitude larger than that of reaction between gaseous species. This particular feature leads to a non-instantaneous and often non-monotonic heat release process.

Veyssi re et al. [133] present a facility constructed for the study of these phenomena. It is a vertical detonation tube of 6 m long (Figure 2.4). They present and analyse experimental results corresponding to the combustion of Al in mixtures of  $C_2H_4$ ,  $O_2$  and  $N_2$ . Two different effects are reported: (a) The presence of Al (at certain concentration) leads to a decrease of about 3% in detonation velocity when there is no reaction and solid particles remain chemically inert. (b) On the other hand, the reaction of Al with gaseous detonation products occurs intensively only behind the detonation front after some “ignition delay”.

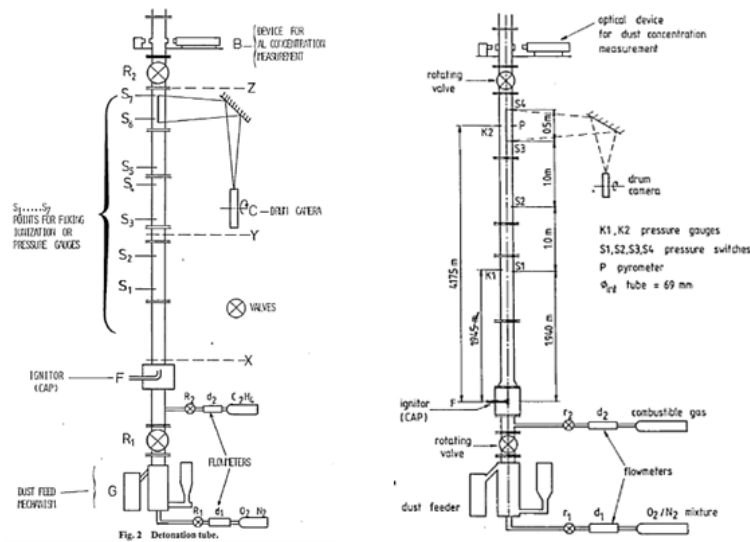


Figure 2.4: Detonation tube (left: Veyssiere, 1981) - more detailed version (right, Veyssiere, 1984).

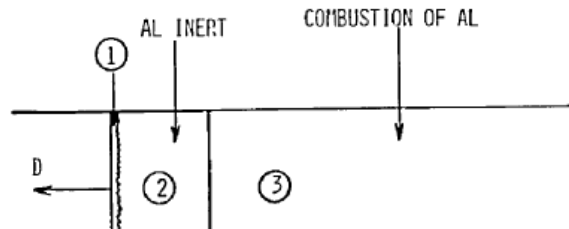


Figure 2.5: Detonation structure according to Veyssi re et al. [133].

Considering these results, they imagine the structure of the detonation wave in gaseous mixtures containing Al particles in suspension as the juxtaposition of three zones:

- i A narrow one, which is the front where the shock initiates the gaseous reactions.
- ii A second zone between the front and the D part (Figure 2.5) where the gases only react at a fast rate.
- iii The third part is beyond D. This is where Al reacts intensively with the gaseous products of zone 2.

Later, Veyssi re [129] studies whether the ignition mechanism of Al follows the pattern suggested by other authors through which the ignition of the particle occurs when the temperature of the surface exceeds the melting point of  $\text{Al}_2\text{O}_3$  (2310 K). He states that, in certain manner, this temperature difference justifies the double detonation effect that happens when Al is added to a gaseous fuel mixture.

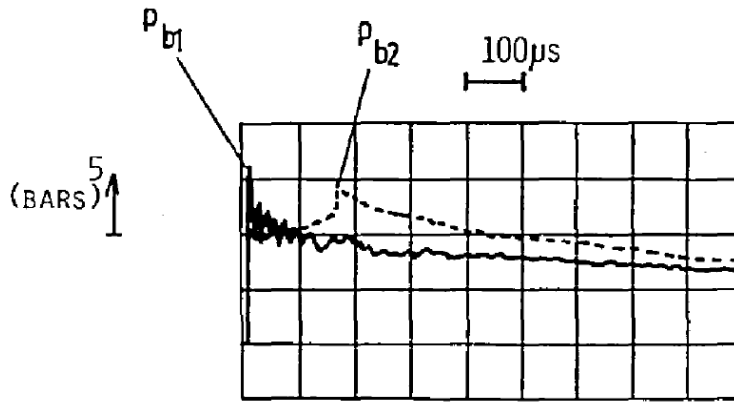


Figure 2.6: Pressure profile in detonation products of mixture H-1 without Al particles (solid), and with Al particles (dashed line). Source: Veyssi re [130].

After these two works, the author carries out new experiments, but now with  $H_2$  [130]. He shows that this double detonation front is more significant in the case of  $H_2$  than in the case of ethylene ( $C_2H_6$ ). This is depicted in Figure 2.6 (mixture A: ethylene). Three mixtures of  $H_2 + XO_2 + ZN_2$  are studied, which are characterised by

- Test H-1:  $Z/X = 3.76$  and  $r = 0.78$ ,
- Test H-2:  $Z/X = 3.76$  and  $r = 1.06$ ,
- Test H-3:  $Z/X = 2.2$  and  $r = 0.75$  (H-3).

Concentration of Al during the experiments was  $\sigma = 65 \pm 15 \text{ g/m}^3$ . The place where the pressure transmitters are located is shown in Figure 2.4 (right).

Two detonations are reported when studying the combustion of  $H_2$  and the Al particles. One is due to the gas combustion front and another one delayed, when the Al ignites (Figure 2.7 and 2.8). The author states this is restricted to the experimental configuration of their installation and the influence of the detonation tube may be of great importance (it may depend on the tube's diameter, the tube's length, and so on).

The detonation problem of  $H_2$  and Al was studied numerically by Khasainov and Veyssi re [56], Veyssi re and Khasainov [131, 132]. In [56], they describe a "quantitative" numerical model for studying the DFD structure (Section 2.3.4). It is based on the theory of two-phase flows in one-dimensional configuration with energy losses to the walls, and on an empirical burning law of aluminium particles. They show computations performed for hydrogen-air mixtures with aluminium particles show that DFD may exist only for an appropriate range of mass concentration of particles, and a sufficient amount

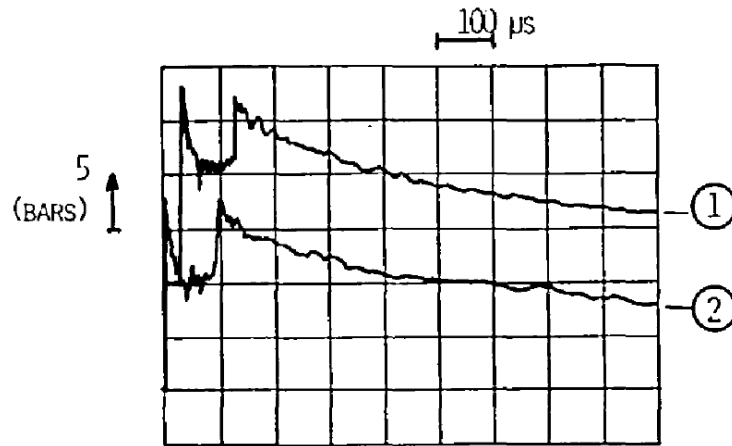


Figure 2.7: Pressure profile of the detonation in mixture H-1 with Al particles, at 1.945 m (1) and at 4.175 m (2) from the ignition point. Source: Veysière [130].

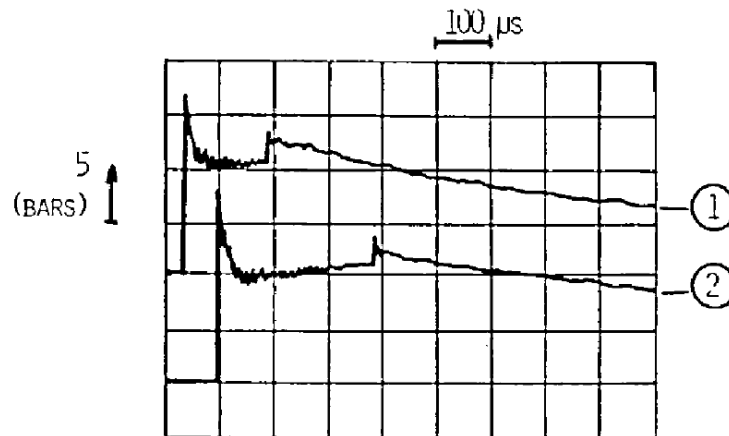


Figure 2.8: Pressure profile of the detonation in mixture H-2 with Al particles, at 1.945 m (1) and 4.175 m (2) from the ignition point. Source: Veysière [130].

of energy losses to the walls. They consider a steady state model of equations to conclude that the existence of momentum and energy losses to the tube walls is a necessary condition for the steady DFD structure to exist.

In the early 1990s, Veyssi re and Khasainov [131] improved the numerical model to find the steady propagation regimes and continued with the investigation on their structure. They considered the one-dimensional time-independent set of Euler equations. The structure of the leading detonation wave is described by the ZND model of detonation with losses to the lateral boundaries. They observe three different propagation regimes:

- Pseudo-gas detonation (PGD). When the particles react behind the CJ plane, the detonation is supported only by heat release from gaseous reactions, which is a pseudo-gas detonation.
- Single-front detonation (SFD). The detonation supported by both gaseous reactions and reactions between particles and gases in a unique large reaction zone is the single-front Detonation.
- Double-front detonation (DFD). As described above, in some cases, there may exist two fronts, the first one is supported by gaseous reactions, the second one by reactions between particles and gases.

After the definition of these three regimes [131], they made a detailed analysis of each one in [132], also addressing the influence of different parameters on them. The approximate numerical model is improved to analyse the characteristics and structure of steady, plane, non-ideal detonation regimes in hybrid two-phase mixtures. They centre their interest in the profiles of flow parameters between the shock front and the CJ point of the detonation wave.

For modelling the gaseous reactions, the two-step scheme (an induction zone followed by a reaction zone) of Korobeinikov et al. (1972) is chosen. Hence, after the beginning of the reactions:  $Q_{gas} = \rho_g Q_g d\beta/dz$ , with  $Q_g$  being the thermal effect of gaseous reactions, and  $\beta$  the fraction of decomposed gaseous explosive ( $\beta = 0$  during induction period). The empirical burning law used to model the regression rate of aluminium particles is due to Price (1984), who reported a sequence of possible behaviours of the aluminium combustion.

Finally, they analyse the dependence of the detonation structure on the fundamental parameters, as well as the influence of concentration, particle diameter, heat losses, and gas mixture composition. They found DFD is replaced by SFD when the tube diameter increases. On the opposite, for smaller tube diameter DFD is replaced by PGD.

### 2.2.3 *Detonation phenomena in dense particle beds. Deflagration to Detonation Transition*

A fruitful research topic on mathematical models for predicting two-phase reactive flows is that associated with the accelerating deflagration wave in a porous medium of reactive solid propellant.

The hazard of DDT (deflagration-to-detonation transition) in solid propellants, especially solid propellants burning in rocket motor environments, is usually not considered as a possibility. However, It may be that under certain situations (for example, a grain structure failure) the solid motor may crack and form regions of granular or porous propellant. When flame from the surface-deflagrating propellant reaches this seam of porous material it will accelerate into this medium and be supported by convective heat transfer from the burned gas into the unignited porous region. If, in addition to this, the product gases are confined to a finite volume, the accelerating deflagration could transit into a detonation.

A number of scientists associated with the University of Illinois have been investigating, since before 1980, on DDT in porous explosives or solid fuels. One of the earliest works from this group was developed by Hoffman and Krier [44]. They studied the fluid mechanics processes that characterise the DDT in granular beds of high-energy solid fuel. They presented a mathematical model for two phase mixtures including an equation of state for the solid phase, needed to fully describe the flow.

According to their experiments, the spontaneous transition from deflagration to detonation can be explained as follows: During combustion of a granulated explosive, the pressure front (still not a shock wave) is behind the flame front. This state is called deflagration phase. Due to the rapid generation of gases of combustion by the burning propellant, the pressure front is simultaneously increased in magnitude, steepened in its gradient, and accelerated towards the flame front. The point at which the pressure front overtakes the flame front is called the transition point. From that point, the flame front, now preceded by the pressure front, moves down the bed of particles in self-sustaining detonation wave at a speed greater than the deflagration wave.

Referring to the mechanism that causes the transition, Hoffman and Krier [44] state that a detonation can be said to have begun when the very strong pressure front precedes the flame front and both move along the bed of particles at a speed that is characteristic of a detonation wave for the type of propellant and initial porosity used. Another important contribution of this paper is the inclusion of a state equation for the solid phase. According to the authors, the inclusion of this equation is crucial to truly represent the DDT in granular fuels. As described, a packed bed placed under a compressive load can be

further compacted. However, there is a force which resists this compaction that depends on the stress-strain relationship of the particle lattice. The resultant force on the particles will be a function of the porosity, the porosity gradient, and possibly other factors. Thus, they artificially imposed the constraint that the normal stress follows a functional relation that resists compaction below a porosity of 0.2595 (solid volume fraction).

Few years later, Butler et al. [12] analysed the DDT process by solving the model of equations previously developed. The numerical resolution model was carried out by using Lax-Wendroff finite-difference scheme. Their analyses indicate the effect of the propellant physical and chemical parameters on the predicted run-up length to detonation. Predictions of this length to detonation are presented as a function of propellant chemical energy, burning rate, bed porosity, and granulation size.

As found in this study, the propellants with a high chemical energy per unit mass, which are able to rapidly generate gases due to their high rate of reaction, are more likely to undergo DDT.

Hot gases generated from the propellant surfaces are driven forward into the unburned solid matrix by the pressure gradient developed at the ignition front. Heat transfer from the hot gases to the unignited propellant particles, dependent on the velocity of the gas relative to the particles and several gas properties, transports energy from the gas to the solid phase. Subsequent ignition of particles further down the bed is assumed to occur when a critical solid phase internal energy is reached. As time progresses, the gas pressure behind the ignition front increases due to the confinement of the gases from the closed rear boundary and the pressure-dependent rate of mass generation in the gas phase.

In order to numerically model the DDT in two-phase flow, Butler et al. [12] consider various assumptions retaining the physics of the problem:

1. Both the solid and gas phases are independently treated as continua requiring their own conservation relations.
2. Each phase interacts with the other. This is modelled by the mass, momentum, and energy interaction terms in the conservation equations.
3. Propellant is monodisperse, all particles are spheres of the same diameter.
4. Ignition of a propellant particle is obtained when a critical energy, expressed as a particle temperature, is transferred to the solid.
5. Both ends of the bed are closed allowing no gases to escape.

6. All the product gases obey an assumed non-ideal equation of state.
7. At some initial time, a “narrow” region at one end is ignited, burning at the low pressure prescribed.
8. The volume of particles varies with time. That will affect its drag coefficient, interfacial heat transfer and the rate of reaction.
9. When the solid phase in a given  $x$  coordinate, displays a volume of particles less than one tenth of its original size, it is burned suddenly and no product of reaction is generated thereafter. This is necessary to prevent singularities when the radius of the particle tends to zero.
10. The solid particles are compressible, without heating, obeying an equation of state.

According to the authors, these are important assumptions: the use of models for incompressible solid phase provides some reasonable answers, as for instead on the burning velocity, but does not indicate adequately the peak pressure during acceleration from deflagration. Since the peak pressures are precursors of the final detonation solutions, accurate calculations are needed. Thus, compressible solid models are more suitable for that purpose.

At the early nineties, Powers et al. [92] published a theoretical work which is a revision of the mathematical models by Baer-Nunziato (BN) and the model developed by the University of Illinois (PSK, Powers-Stewart-Krier). The authors developed a more general model which is a combination of the two previous ones. A rigorous theoretical approach is outlined to demonstrate that the new model satisfies the second law of thermodynamics. It is shown that this and previous models do not satisfy the second law under all circumstances. In a second paper, in the same Journal, the authors solved numerically the model.

The two-phase model in [92] is a generalisation of the BN model and the PSK model. The governing equations of the model presented in Section 2.3.3 consider conservation of mass, momentum and energy for both phases (6 equations). The peculiarities of the model are a dynamic compaction equation:

$$\frac{\partial \phi_2}{\partial t} + u_2 \frac{\partial \phi_2}{\partial x} = \frac{\phi_1 \phi_2}{\mu_c} [P_2 - f_2 - (P_1 - f_1)] + a_2 / \rho_2 \quad (2.2)$$

and an equation for the number evolution:

$$(1 - \delta_c) \left[ \frac{\partial n}{\partial t} + \frac{\partial}{\partial x} (u_2 n) \right] = (1 - \delta_c) F(P_1, \rho_1, P_2, \rho_2, \phi_2) \quad (2.3)$$

In these equations, subscripts “1” and “2” denote the gas and solid phase, respectively. The variable  $\rho$  represents the material density; the variable  $\phi$  stands for the volume fraction of each phase. Velocities are denoted by the variable  $u$ , pressure by  $P$ , and the number density of spherical particles:

$$n = \frac{3\phi_2}{4\phi r^3} \quad (2.4)$$

The variable  $\delta_c$  is used in these equations to describe either the BN formulation or the PSK formulation.

The use of the dynamic compaction equation is not standard. They argue that this equation allows volume fractions to change without affecting the bulk motion of the mixture and thus is able to model microstructural details in some way. For this model it is assumed that the particles are spherical. Assumption, that is not valid under all circumstances, especially when local deformation due to solid compaction is considered.

The number evolution equation allows for the total number of particles to change in response to the general forcing function  $F$ . For  $F < 0$ , particle agglomeration is predicted, and for  $F > 0$  particle breakup is predicted. For  $F = 0$ , the number of particles is conserved. According to the authors, such an equation is a necessity for models that describe the burning of moving particles.

Although the model is admittedly complicated, when compared to many other models, it is more compact. If one’s goal is to match experimental data under a wide variety of flow conditions, then this model is inadequate.

As mentioned, the model by Powers et al. [92] was solved numerically by the authors in an additional paper, but also by other researchers (i.e. Gonthier and Powers [40] who used that model to predict the evolution of detonation in a granulated reactive material). Combustion is initiated due to compression of the material by a moving piston. The numerical method used to approximate solution to the two-phase Riemann problem at each interface was based on Godunov’s method. In particular, this study demonstrates the existence of a Shock to Detonation Transition (SDT) event which gives rise to a steady two-phase Chapman-Jouguet detonation structure consisting of a single lead shock in the gas and an unshocked solid.

There are three different tests which could be reproduced in [92]:

- A. A biphasic inert shock tube,
- B. The evolution of a compression wave in response to movement of the piston, and
- C. The evolution of the detonation wave in response to movement of the piston.

In 1999, Bdzil et al. [7] made a critical examination of the two-phase mixture model developed by Baer-Nunziato to study the problems of DDT in granular explosives. They reviewed the fundamentals of the theory of continuous mixtures and energetic phenomena occurring at grain size scales. It clarifies the nature of the approximations in the formulation of the constitutive terms and its application range. Attention is paid to certain gaps and inconsistencies in the derivation and some improvements to the model are suggested.

Kapila et al. [52] proposed two reduced models to eliminate the stiffness of the source terms associated with the model of Baer-Nunziato, when using small time scales. These reduced models are hyperbolic and are mechanically as well as thermodynamically consistent with their parent model. However, they cannot be written in conservative form and thus require an adjustment in order to fully specify the jump conditions across shock waves.

### 2.3 REVIEW OF MODELS OF GOVERNING EQUATIONS FOR UNSTEADY, ONE DIMENSIONAL, TWO-PHASE FLOW

In what follows, the systems of equations proposed by the different works analysed in this *state of the art* are briefly described.

#### 2.3.1 Baer and Nunziato model for laden mixtures

Baer & Nunziato two-phase model for gas and particles is one of the most referenced in the existing literature. The paper in 1986 presents a theory of two-phase mixtures describing the deflagration to detonation transition (DDT) in reactive granular materials [4]. The theory is based on the continuous theory of mixtures made and includes both phase compressibility and compaction of granular material. Specific expressions for the exchange of mass, momentum and energy are proposed, which are consistent with known empirical models.

The model is applied to describe the combustion processes associated with DDT in a pressed column of HMX. Numerical results seem to predict the transition to detonation run distances in accordance with experimental observations. In addition, certain calculations are performed to demonstrate the effect of particle size and porosity and compaction of the material studied by varying the viscosity of the explosive. According to this work, the process of DDT in a column essentially consists of four regimes: conductive burning, convective burning, compressive burning, and detonation. As a result of rapid gas pressurisation, detonation occurs when pressure disturbances in the combustions regions focus and reinforce each other.

Baer and Nunziato [4] made an analysis of different approaches to develop two-phase flow equations (averaged methods of mass or volume, continuum mixture theory, and so on). The authors state that a complete treatment of reactive two-phase flow (total non-equilibrium) leads to a closure problem. This problem results from including the volume fraction of a phase as an independent kinematic variable and can be seen by comparing the set of unknowns to the set of known relationships. For each phase there are 5 quantities to be determined during flame spread (pressure, temperature, density, velocity and volume fraction); a total of 10 unknowns. The conservative laws (three for each phase), the state relation (one for each phase) and the volume constraint (sum of the volume fractions of all phases must be one) only result on 9 equations, and hence, the problem is undetermined.

Several different approaches have been used to achieve closure. Some models consider the solid phase to be incompressible, considering a finite sound speed in that phase in such way that a solid equation of state is not compatible in that case. Another type of constraint

assumes pressure equilibrium between phases, which produces a coupling between both phases' sound speeds. Another approach, used by Krier and the Illinois research group, consider different pressures for both phases, but the pressure in the solid phase is defined in terms of the configurations changes of the granular material.

The model finally proposed was developed in the context of the continuum theory of multiphase mixtures. They made two important assumptions:

- Each phase behaves as if it were a single material except when it is interacting and hence exchanging mass, momentum and energy with the other phase;
- The conservation equations for the mixture are also the same as those for a single material and follow from summing the conservation equations for individual constituents over all constituents.

If  $a$  stands for either phase solid or gas and with and we use  $'$  to refer to the material time derivative of a variable, the system of conservation equations for each phase is given by

$$\rho_a' = -\rho_a \frac{\partial v_a}{\partial x} + c_a^+ \quad (2.5a)$$

$$\rho_a v_a' = -\frac{\partial \pi_a}{\partial x} + \rho_a b_a + m_a^+ - c_a^+ v_a \quad (2.5b)$$

$$\rho_a e_a' = -\pi_a \frac{\partial v_a}{\partial x} - \frac{\partial q_a}{\partial x} + \rho_a r_a + e_a^+ - m_a^+ v_a - c_a^+ \left( e_a - \frac{1}{2} v_a^2 \right). \quad (2.5c)$$

where

- $\rho$ : phase density,
- $v$ : phase velocity,
- $c_a^+$  mass exchanged between phases due to chemical reactions,
- $\pi$  pressure,
- $b$  external body forces (e.g. gravitational forces),
- $m^+$  momentum transferred from one phase to another (i.e. drag) and the momentum associated with the appearance (or disappearance) of phase  $a$ ,
- $e$ : specific internal energy for each phase,
- $q$ : conduction heat transfer,
- $r$  external heat sources (i.e. radiation),
- $e^+$  energy associated with momentum transfer and the energy associated with the appearance (or disappearance) of a phase.

It is required that the interaction terms  $c_a^+$ ,  $m_a^+$  and  $e_a^+$  satisfy the following summing rules:

$$\sum_a c_a^+ = 0; \quad \sum_a m_a^+ = 0; \quad \sum_a e_a^+ = 0.$$

In addition, Baer and Nunziato give an own definition for specific internal energy, as a function of the Helmholtz free energy  $\psi_i$  (see [Section 2.4.4](#), about the Equations of State). Then, as a consequence of the entropy inequality:

$$e_i = \psi_i - T_i \frac{\partial \psi_i}{\partial T_i} \quad (2.6)$$

The sum of the systems of equations for each phase should provide a system for a single component (equations of the mixture). Performing this cumbersome work, the following system is obtained:

$$\dot{\rho} = -\rho \frac{\partial v}{\partial x} \quad (2.7a)$$

$$\rho \dot{v} = -\frac{\partial P}{\partial x} + \rho b \quad (2.7b)$$

$$\rho \dot{e} = -P \frac{\partial v}{\partial x} - \frac{\partial q}{\partial x} + \rho r \quad (2.7c)$$

where

$$\begin{aligned} P + \rho v^2 &= \sum (\pi_a + \rho_a v_a^2) \\ \rho b &= \sum \rho_a b_a \\ \rho \left( e + \frac{1}{2} v^2 \right) &= \sum \rho_a \left( e_a + \frac{1}{2} v_a^2 \right) \\ q + P v + \rho \left( e + \frac{1}{2} v^2 \right) v &= \sum \left[ q_a + \pi_a v_a + \rho_a \left( e_a + \frac{1}{2} v_a^2 \right) v_a \right] \\ \rho (r + b v) &= \sum \rho_a (r_a + b_a v_a) \end{aligned}$$

which are the so-called summing rules for the mixture.

The introduction of dissipation considerations lead to a friendly system of equations which is finally used in their work for the analysis of DDT [4]. The implemented numerical test consists of modelling the combustion and the subsequent detonation of an explosive column. Side effects are neglected, so a one-dimensional model is considered. In the end where ignition occurs ( $x = 0$ ) a reflection boundary condition and zero heat flux are set. At the opposite end

( $x = L$ ), with  $L$  the total length of the column), zero gradients on the dependent variables are assumed, so that the material can flow freely. Initially, the gas and solid velocities are zero. Over a short distance  $L_1$ , they assume a linear variation of gas pressure and initial temperature in the bed of particles:

$$p_G(x, 0) = \begin{cases} (p_G)_1 \left(1 - \frac{x}{L_1}\right) & \text{if } 0 \leq x \leq L_1 \\ 0 & \text{if } L_1 < x \leq L \end{cases} \quad (2.8)$$

$$p_G(x, 0) = \begin{cases} (T_g)_1 \left(1 - \frac{x}{L_1}\right) & \text{if } 0 \leq x \leq L_1 \\ T_0 & \text{if } L_1 < x \leq L \end{cases} \quad (2.9)$$

where  $T_0$  is the reference temperature for the bed (300 K).

### 2.3.2 Hoffman and Krier model of equations

The approach taken by Hoffman and Krier [44] for the conservation equations assumes that there are two distinct continua, one for solids and one for the gas, each moving through its own control volume. Owing to this approach, the sum of these two volumes must represent an average mixture volume, while at the same time, the equations which describe the two continua must account for the effect that one flow has on the other.

In order to uniquely describe the properties of the two-phase flow, the following nine variables must be determined:  $\rho_g$ ,  $\rho_p$ ,  $u_g$ ,  $u_p$ ,  $T_g$ ,  $T_p$ ,  $P_g$ ,  $P_p$  and  $\phi$ . For these nine unknowns, nine equations must be supplied. Six of those equations are determined by the conservation of mass, momentum and energy equations for both phases:

$$\frac{\partial}{\partial t} (\phi_g \rho_g) + \frac{\partial}{\partial x} (\phi_g \rho_g u_g) = a \quad (2.10a)$$

$$\frac{\partial}{\partial t} (\phi_p \rho_p) + \frac{\partial}{\partial x} (\phi_p \rho_p u_p) = -a \quad (2.10b)$$

$$\frac{\partial}{\partial t} (\phi_g \rho_g u_g) + \frac{\partial}{\partial x} (\phi_g \rho_g u_g^2) + \phi_g \frac{\partial P_g}{\partial x} = a u_p - b \quad (2.11a)$$

$$\frac{\partial}{\partial t} (\phi_p \rho_p u_p) + \frac{\partial}{\partial x} (\phi_p \rho_p u_p^2) + \phi_p \frac{\partial P_g}{\partial x} = -a u_p + b \quad (2.11b)$$

$$\begin{aligned} \frac{\partial}{\partial t} (\phi_g \rho_g E_g) + \frac{\partial}{\partial x} \left( \phi_g \rho_g u_g \left( E_g + \frac{P_g}{\rho_g} \right) \right) = \\ a \left( E_{\text{chem}} + \frac{u_p^2}{2} \right) - b u_p - c \end{aligned} \quad (2.12a)$$

$$\begin{aligned} \frac{\partial}{\partial t} (\phi_p \rho_p E_p) + \frac{\partial}{\partial x} \left( \phi_p \rho_p u_p \left( E_p + \frac{P_g}{\rho_g} \right) \right) = \\ -a \left( E_{\text{chem}} + \frac{u_p^2}{2} \right) + b u_p + c \end{aligned} \quad (2.12b)$$

Phase porosities (or volume fractions) are defined as follows:

$$\phi_g = \frac{V_g}{V_T}; \quad \phi_p = \frac{V_p}{V_T} \quad (2.13)$$

and must satisfy that  $\phi_g + \phi_p = 1$ .

Total internal energy:

$$E_g = e_g + \frac{u_g^2}{2} = c_{p,g} T_g + \frac{u_g^2}{2} \quad (2.14)$$

$$E_p = e_p + \frac{u_p^2}{2} = c_{p,s} T_p + \frac{u_p^2}{2} \quad (2.15)$$

Here specific heats are assumed averaged constants, independent of temperature:  $c_{p,g} = 1.269$  kJ/kg·K and  $c_{p,s} = 1.777$  kJ/kg·K.

The seventh and eighth equations needed to close the system are the Equations of State associated with each phase. For the gas, a Nobel-Able type of non-ideal equation of state is used (see [Section 2.4.4](#)).

### 2.3.3 Models of equations by Powers, Stewart and Krier

The model proposed in [92] and further discussed in [93] is a generalisation of the Baer-Nunziato model and the Illinois model. The governing equations in conservative form are given below:

$$\frac{\partial}{\partial t} (\rho_1 \phi_1) + \frac{\partial}{\partial x} (\rho_1 \phi_1 u_1) = a_1 \quad (2.16)$$

$$\frac{\partial}{\partial t} (\rho_2 \phi_2) + \frac{\partial}{\partial x} (\rho_2 \phi_2 u_2) = a_2 \quad (2.17)$$

$$\frac{\partial}{\partial t} (\rho_1 \phi_1 u_1) + \frac{\partial}{\partial x} (\rho_1 \phi_1 u_1^2 + P_1 \phi_1) = a_1 u_2 + b_1 + \delta_a P_1 \frac{\partial \phi_1}{\partial x} \quad (2.18)$$

$$\frac{\partial}{\partial t} (\rho_2 \phi_2 u_2) + \frac{\partial}{\partial x} (\rho_2 \phi_2 u_2^2 + P_2 \phi_2) = a_2 u_2 + b_2 - \delta_a P_1 \frac{\partial \phi_1}{\partial x} \quad (2.19)$$

$$\begin{aligned} \frac{\partial}{\partial t} \left( \rho_1 \phi_1 \left( e_1 + \frac{u_1^2}{2} \right) \right) + \frac{\partial}{\partial x} \left( \rho_1 \phi_1 u_1 \left( e_1 + \frac{u_1^2}{2} + \frac{P_1}{\rho_1} \right) \right) = \\ a_1 \left( e_2 + \frac{u_2^2}{2} \right) + b_1 u_2 + c_1 + \delta_a P_1 u_2 \frac{\partial \phi_1}{\partial x} \\ + \delta_b (P_2 - f_2) [P_2 - f_2 - (P_1 - f_1)] \frac{\phi_1 \phi_2}{\mu_c} \end{aligned} \quad (2.20)$$

$$\begin{aligned} \frac{\partial}{\partial t} \left( \rho_2 \phi_2 \left( e_2 + \frac{u_2^2}{2} \right) \right) + \frac{\partial}{\partial x} \left( \rho_2 \phi_2 u_2 \left( e_2 + \frac{u_2^2}{2} + \frac{P_2}{\rho_2} \right) \right) = \\ a_2 \left( e_2 + \frac{u_2^2}{2} \right) + b_2 u_2 + c_2 - \delta_a P_1 u_2 \frac{\partial \phi_1}{\partial x} \\ - \delta_b (P_2 - f_2) [P_2 - f_2 - (P_1 - f_1)] \frac{\phi_1 \phi_2}{\mu_c} \end{aligned} \quad (2.21)$$

$$\frac{\partial \phi_2}{\partial t} + u_2 \frac{\partial \phi_2}{\partial x} = \frac{\phi_1 \phi_2}{\mu_c} [P_2 - f_2 - (P_1 - f_1)] + \frac{a_2}{\rho_2} \quad (2.22)$$

$$(1 - \delta_c) \left[ \frac{\partial n}{\partial t} + \frac{\partial}{\partial x} (u_2 n) \right] = (1 - \delta_c) F(P_1, \rho_1, P_2, \rho_2, \phi_2) \quad (2.23)$$

In these equations, the subscripts “1” and “2” denote the gas and solid phase, respectively. The variable  $\rho$  represents the material density, the variable  $\phi$  represents the volume fraction of each phase. Velocities are denoted by the variable  $u$ , pressure by  $P$  and the number density of spherical particles:

$$n = \frac{3\phi_2}{4\pi r^3} \quad (2.24)$$

The variable  $\delta$  is used in these equations to describe either the BN formulation ( $\delta_a = \delta_b = \delta_c = 1$ ) or the PSK formulation ( $\delta_a = \delta_b = \delta_c = 0$ ). For  $\delta_a = 1$ , an additional term proportional to the product of gas pressure and volume fraction gradient is included as a phase interaction term in the momentum and energy equations. For  $\delta_b = 1$  a work term, known as compaction work, is included as an energy phase interaction. For  $\delta_c = 0$  a number evolution relation is enforced; for  $\delta_c = 1$  such a relation is not enforced.

The term  $f$  represents the configurational stress as used by BN:  $f_i = \rho_i \phi_i (\partial \psi_i / \partial \phi_i)$ , where the Helmholtz free energy of phase  $i$  is defined as  $\psi_i = e_i - T_i \eta_i$ , with  $\eta_i$  the entropy of phase  $i$  (see [Section 2.4.4](#), about the Equations of State).

The terms  $a_i$ ,  $b_i$ , and  $c_i$  are constitutive functions representing the inter-phase mass, momentum, and energy transport, respectively. The combustion model is contained in the term  $a_i$ , which specifies the rate of mass transfer per unit time per unit volume. It is assumed that  $a_i$ ,  $b_i$ , and  $c_i$  can be functions of all of the flow variables.

It is noted that the mass, momentum, and energy of each constituent are not conserved but change in response to the forcing functions terms  $a_i$ ,  $b_i$ , and  $c_i$ . It is required, however, for the mixture

that mass, momentum, and energy be conserved. To ensure that this holds, Truesdell's axioms of balance for mixtures require that

$$a_1 + a_2 = 0; \quad b_1 + b_2 = 0; \quad c_1 + c_2 = 0$$

Equations in the model represent, respectively, the gas and solid mass conservation equations (2.16 and 2.17), the gas and solid momentum equations (2.18 and 2.19), the gas and solid energy equations (2.20 and 2.21), the dynamic compaction equation (2.22).

The use of the dynamic compaction equation (2.22) is not standard. Passman et al. (1984) argue that this equation allows volume fractions to change without affecting the bulk motion of the mixture and thus is able to model microstructural details in some way. For this model it is assumed that the particles are spherical. This assumption is probably not valid under all circumstances, especially when local deformation due to solid compaction is considered.

The number evolution equation (2.23) allows for the total number of particles to change in response to the general forcing function  $F$ . For  $F < 0$ , particle agglomeration is predicted, and for  $F > 0$  particle breakup is predicted. For  $F = 0$ , the number of particles is conserved. According to the authors, such an equation is a necessity for models that describe the burning of moving particles.

#### 2.3.4 *Veyssière- Khasainov model*

As described above, Veyssière and Khasainov (1995) study the steady propagation of detonation in hybrid two-phase mixtures by considering a one-dimensional time-independent Eulerian approach.

Different assumptions are made about their model of equations:

- i It has been developed for treating steady propagation of plane, one-dimensional, and non-ideal detonations in a mixture of gaseous explosive with reactive solid particles.
- ii Particles are assumed incompressible, not interacting between each other.
- iii Particle volume fraction is negligible.
- iv Temperature gradients are neglected inside particles. They state that characteristic time for conduction heat transfer inside a particle is negligible as compared to other characteristic times (for particles with  $d_p < 50\mu\text{m}$ ).
- v Velocities and temperatures are assumed to be different for particles and gases, mass, momentum, and heat exchanges between particles and gases are taken into account.

vi The detonation is described following the ZND model (i.e. a shock thermally initiating chemical reactions, but with viscous and thermal losses to the tube walls allowed behind the shock wave).

Based on these assumptions, they consider a time-independent set of Euler equations written in coordinates linked to the leading front. The balance equations of the solid discrete phase for mass, momentum, energy and number of particles may be written as:

$$\frac{\partial}{\partial z}(\sigma_{p,i}u_{p,i}) = -J_i, \quad i = 1, \dots, N \quad (2.25)$$

$$\frac{\partial}{\partial z}(\sigma_{p,i}u_{p,i}^2) = f_i - J_i u_{p,i}, \quad i = 1, \dots, N \quad (2.26)$$

$$\frac{\partial}{\partial z}(\sigma_{p,i}u_{p,i}e_{p,i}) = q_i - J_i e_{p,i}, \quad i = 1, \dots, N \quad (2.27)$$

$$\frac{\partial}{\partial z}(N_{p,i}u_{p,i}) = 0, \quad i = 1, \dots, N \quad (2.28)$$

where  $z$  is a characteristic coordinate defined as  $z = D_{CJ}t - x$ , with  $t$  and  $x$ , time and axial coordinate, respectively; the internal energy of particles is calculated as  $e_{p,i} = c_{p,i}T_{p,i} + Q_{Al}$ . Also the following variables are defined:

- $i = 1, \dots, N$ : indicate the different fractions of particles of discrete diameter,
- $\sigma_{p,i}$ : mass concentration of the  $i$ -th fraction of particles,
- $u_{p,i}$ : velocity of the  $i$ -th fraction of particles,
- $N_{p,i}$ : the total number of solid particle species;
- $J_i$ : mass exchanges between particles and gases,
- $f_i$ : momentum exchanges between particles and gases,
- $q_i$ : heat exchanges between particles and gases,
- $C_p$ : heat capacity of particles,
- $T_{p,i}$ : temperature of the  $i$ -th fraction of particles,
- $Q_{Al}$ : effective heat effect of the global reaction between particles and oxidising gases (see Veyssi re and Khasainov, 1991a).

Regarding the gaseous phase, the balance equations for mass, momentum and energy may take the form:

$$\frac{\partial}{\partial z}(\rho_g u_g) = \sum_{i=1}^N J_i \quad (2.29)$$

$$\frac{\partial}{\partial z}(\rho_g u_g^2 + p) = \sum_{i=1}^N (J_i u_{p,i} - f_i) + 4 \frac{\tau_w}{D_w} \quad (2.30)$$

$$\begin{aligned} \frac{\partial}{\partial z} \left( \rho_g u_g \left( e_g + \frac{u_g^2}{2} \right) \right) &= Q_{gas} + 4 \frac{\tau_w}{D_w} D_{CJ} - 4 \frac{q_w}{D_w} \\ &+ \sum_{i=1}^N \left[ J_i \left( e_{p,i} + \frac{u_{p,i}^2}{2} \right) - f_i u_{p,i} - q_i \right] \end{aligned} \quad (2.31)$$

where

- $\gamma = C_p/C_v$ : heat capacity ratio of the gas
- $\rho_g$ : density of the gas phase,
- $u_g$  velocity of the gas phase,
- $e_g$ : internal energy of the gas phase;
- $\tau_w$  viscous stress to the walls,
- $q_w$  heat flux to the walls,
- $D_{CJ}$  detonation velocity,
- $D_w$ : hydraulic diameter of the tube,
- $Q_{gas}$ : heat release from gaseous reactions (not very clearly explained for this model).

Veyssière and Khasainov's is a high dilute model in which each solid component is treated individually, with its own system of equations. The meaning of the conservation equation for the number of particles is that number will not change, even though those particles oxidise.

Interactions between solid particles and gases are taken into account by means of coupling source terms from mass exchange, momentum and heat transfer. The empirical burning law used to model the regression rate of aluminium particles is due to Price (1984), who reported a sequence of possible behaviours of the aluminium combustion. We can find that the mass exchange due to chemical reaction is modelled with a term:

$$J_i = 3\sigma_{p,i} \left( \frac{\dot{d}}{d} \right)_i (1 + 0.275Re_i) \quad (2.32)$$

which is activated only if temperature of particles is greater than the ignition temperature,  $T_{\text{ign}} = 2310$  K. If  $d$  is considered as the diameter of particles, and  $\dot{d}$  the rate of variation of  $d$ , the combustion rate can be modelled as a function of the particle burning time:

$$\left(\frac{\dot{d}}{d}\right)_i = -\frac{1}{t_{p,i}} \quad (2.33)$$

$$t_{p,i} = k \frac{d_{p0}^n}{\phi^{0.9}} \quad (2.34)$$

where  $K$  and  $n$  are empirical constants, and  $\phi$  is the volume fraction of the sum of oxidising species. To find out the empirical constants one must look into Price (1984), where  $K = 7.3 \times 10^{-6}$  and  $n = 1.75$ .  $d_{p0}$  is the initial diameter of particles.

Expressions for the drag force and heat exchange between gases and particles are given for this model in [131]. Those expressions can be consulted in Section 2.4.2 and Section 2.4.3, respectively.

Also both source terms are included to account for the interaction with walls: wall friction,  $\tau_w$ , and heat exchange with walls,  $q_w$ :

$$\tau_w = \frac{\lambda_w}{8} \rho_g (D_{CJ} - u_g)^2 \quad (2.35)$$

$$q_w = \frac{\lambda_w}{8} \rho_g (D_{CJ} - u_g) c_{pg} (T_g - T_0) \quad (2.36)$$

with  $T_0$  is the wall temperature and the wall friction coefficient  $\lambda_w = [1.74 - 2 \log(2h_0/d_w)]^{-2}$  is a function of the wall roughness height,  $h_0$  and the tube diameter  $d_w$ .

### 2.3.5 Chen and Fan

Based on the two-fluid model and  $k-\varepsilon$  model, a set of conservation equations is derived by Chen and Fan [19] to describe two-phase turbulent combustion flow.

For the **gaseous phase**:

$$\frac{\partial}{\partial t}(\rho) + \frac{\partial}{\partial x_j}(\rho u_j) = S \quad (2.37a)$$

$$\frac{\partial}{\partial t}(\rho u_i) + \frac{\partial}{\partial x_j} \left( \rho u_i u_j - \mu_c \frac{\partial u_i}{\partial x_j} \right) = \frac{\partial P}{\partial x} + \frac{\partial}{\partial x_j} \left( \mu_c \frac{\partial u_j}{\partial x_i} \right) + u_i S + \frac{\rho_p f(u_{p,i} - u_i)}{\tau_\Gamma} \quad (2.37b)$$

$$\frac{\partial}{\partial t}(\rho T) + \frac{\partial}{\partial x_j} \left( \rho u_j T - \frac{\mu_c}{\sigma_T} \frac{\partial T}{\partial x_j} \right) = n_p (\beta Q_c - Q_r + Q_p) + c_p T S \quad (2.37c)$$

$$\frac{\partial}{\partial t}(\rho Y_s) + \frac{\partial}{\partial x_j} \left( \rho u_j Y_s - \frac{\mu_c}{\sigma_Y} \frac{\partial Y_s}{\partial x_j} \right) = \beta_S R_{fu} + \alpha_S S \quad (2.37d)$$

$$\frac{\partial}{\partial t}(\rho k) + \frac{\partial}{\partial x_j} \left( \rho u_j k - \frac{\mu_c}{\sigma_k} \frac{\partial k}{\partial x_j} \right) = G - \rho \varepsilon \quad (2.37e)$$

$$\frac{\partial}{\partial t}(\rho \varepsilon) + \frac{\partial}{\partial x_j} \left( \rho u_j \varepsilon - \frac{\mu_c}{\sigma_\varepsilon} \frac{\partial \varepsilon}{\partial x_j} \right) = \frac{k}{\varepsilon} (C_1 G - C_2 \rho \varepsilon) \quad (2.37f)$$

Where:

$$\mu_c = \mu + \mu_T,$$

$$\mu_T = C_\mu \rho \frac{k^2}{\varepsilon},$$

$$S = -n_p \dot{m}_p,$$

$$\dot{m}_p = \frac{dm_p}{dt},$$

$$\tau_\Gamma = (d_p^2 \rho_p) / 18 \mu,$$

$$\beta = 1 - \left( \frac{d_p}{d_{p0}} \right)^3 \left( 1 - \frac{T_p}{T} \right),$$

$$f = 1 + 0.15 \text{Re}_{ep}^{2/3},$$

$$\text{Re}_{ep} = \rho |u - u_p| d_p / \mu.$$

The generation rate of turbulence,  $G$ , consists of three parts: the first part  $G_R = 2Sk$  is related to mass transfer between gas and particles due to combustion, the second part,  $G_k$ , is about the shear flow:

$$G_k = \mu_T \left[ \left( \frac{\partial u_i}{\partial x_j} \right) + \left( \frac{\partial u_j}{\partial x_i} \right) \right] \left( \frac{\partial u_j}{\partial x_i} \right)$$

and the last part represents the interaction between two-phase turbulent fields:

$$G_p = \sum \frac{\rho_p}{\tau_\Gamma} \left[ \left( C_k \sqrt{k k_p} - 2k \right) - \frac{u_{p,i} - u_i}{n_p} \frac{v_p}{\sigma_p} \frac{\partial n_p}{\partial x_i} \right]$$

For the **solid phase**:

$$\frac{\partial n_p}{\partial t} + \frac{\partial}{\partial x_j} (n_p u_{p,j}) = \frac{\partial}{\partial x_j} \left( \frac{v_p}{\sigma_p} \frac{\partial n_p}{\partial x_j} \right) \quad (2.38a)$$

$$\frac{\partial}{\partial t} (n_p m_p) + \frac{\partial}{\partial x_j} (n_p m_p u_{p,j}) = \frac{\partial}{\partial x_j} \left( \frac{m_p v_p}{\sigma_p} \frac{\partial n_p}{\partial x_j} \right) + n_p \dot{m}_p \quad (2.38b)$$

$$\begin{aligned} \frac{\partial}{\partial t}(n_p u_{p,i}) + \frac{\partial}{\partial x_j} \left( n_p u_{p,i} u_{p,j} - n_p v_p \frac{\partial u_{p,i}}{\partial x_j} \right) = \\ (u_i - u_{p,i}) \left( \frac{f}{\tau_r} + \frac{\dot{m}_p}{m_p} \right) n_p + \frac{\partial}{\partial x_j} \left[ n_p v_p \left( \frac{\partial u_{p,i}}{\partial x_j} + \frac{\partial u_{p,j}}{\partial x_i} \right) \right] \\ + \frac{v_p}{\sigma_p} \left( u_{p,j} \frac{\partial n_p}{\partial x_j} + u_{p,i} \frac{n_p}{x_i} \right) \end{aligned} \quad (2.38c)$$

$$\begin{aligned} \frac{\partial}{\partial t}(n_p T_p) + \frac{\partial}{\partial x_j} \left( n_p u_{p,j} T_p - \frac{n_p v_p}{\sigma_p} \frac{\partial T_p}{\partial x_j} \right) = \frac{n_p}{m_p C} [m_p (1 - \beta) Q_c \\ - Q_p + (C_p T - C T_p) \dot{m}_p] + \frac{\partial}{\partial x_j} \left( \frac{v_p}{\sigma_p} \frac{\partial (n_p T_p)}{\partial x_j} \right) \end{aligned} \quad (2.38d)$$

The value of the particulate turbulent viscosity  $v_p$  is chosen from experiments or through a complementary analysis, but the selection for a given application has to be dependent on experimental validation.

The convective heat transfer per particle,  $Q_p$  can be expressed as:

$$Q_p = \frac{\pi d_p^2}{4} h_t (T_p - T_t) \quad (2.39)$$

The radiant energy emitted by one particle is given by the Stefan-Boltzmann law:

$$q_r = \frac{\pi d_p^2}{4} \tilde{\epsilon} \sigma T_p^4 \quad (2.40)$$

where  $\tilde{\epsilon}$  is the emissivity and  $\sigma$  is Boltzmann's constant.

### 2.3.6 The Warsaw model

What we call the Warsaw model is, in fact, the model of conservation equations proposed by Klammer et al. [60] and Korobeinikov et al. [65], which was later completed by Oleszczak and Klemens [86] for the study of mitigation of dust combustion.

If NGSP is number of species in the gas phase and NSSP is number of species in the solid phase, the model is formed by a number of  $(4 + \text{NGSP} + \text{NSSP})$  conservation equations:

$$\frac{\partial}{\partial t} \rho_1 + \vec{\nabla} \cdot (\rho_1 \vec{u}_1) = \vec{\nabla} \cdot \vec{J} + \Gamma_c \quad (2.41a)$$

$$\frac{\partial}{\partial t} (\rho_1 \vec{u}_1) + \vec{\nabla} \cdot (\rho_1 \vec{u}_1 \otimes \vec{u}_1) + \vec{\nabla} \cdot (\mathbf{p}) = -\vec{F} + \vec{\nabla} \cdot \vec{T}_1 + \Gamma_c \vec{u}_2 \quad (2.41b)$$

$$\begin{aligned} \frac{\partial}{\partial t}(\rho_1 E_1) + \vec{\nabla} \cdot [(E_1 + p)\vec{u}_1] = & -\vec{\nabla} \cdot (\vec{q}_{1,T} + \vec{q}_{1,R}) - \vec{F} \cdot \vec{u}_2 \\ & - Q_T - Q_R + \Gamma_c E_2 + (1 - \alpha)Q_c + \vec{\nabla} \cdot (\tilde{T}\vec{u}_1) \end{aligned} \quad (2.41c)$$

$$\frac{\partial}{\partial t}(\rho_1 Y_{1,k}) + \vec{\nabla} \cdot (\rho_1 Y_{1,k}\vec{u}_1) = \dot{\omega}_{1,k}; \quad k = 1, \dots, \text{NGSP} - 1 \quad (2.41d)$$

$$\frac{\partial}{\partial t}\rho_2 + \vec{\nabla} \cdot (\rho_2\vec{u}_2) = -\Gamma_c \quad (2.41e)$$

$$\frac{\partial}{\partial t}(\rho_2\vec{u}_2) + \vec{\nabla} \cdot (\rho_2\vec{u}_2 \otimes \vec{u}_2) = \vec{F} - \Gamma_c\vec{u}_2 \quad (2.41f)$$

$$\begin{aligned} \frac{\partial}{\partial t}(\rho_2 E_2) + \vec{\nabla} \cdot (E_2\vec{u}_2) = & -\vec{\nabla} \cdot \vec{q}_{2,R} + \vec{F} \cdot \vec{u}_2 + Q_T + Q_R \\ & -\Gamma E_2 + \alpha Q_c \end{aligned} \quad (2.41g)$$

$$\frac{\partial}{\partial t}(\rho_2 Y_{2,k}) + \vec{\nabla} \cdot (\rho_2 Y_{2,k}\vec{u}_2) = -\dot{\omega}_{2,k}; \quad k = 1, \dots, \text{NSSP} - 1 \quad (2.41h)$$

where, according to Korobeinikov's notation:

- $\vec{j}$ : mass flux due to diffusion in the gas phase,
- $\dot{\omega}$ : mass source of components due to reactions in the gas and solid phases, and extraction of volatiles from the particles,
- $\vec{F}$ : interface forces ( $\vec{f}_v$ : interfacial friction, FM: Magnus force,  $f^*$ : Saffman force, near walls and gravity forces),
- $d$ : particle diameter,
- $E_k$ : total energy of phase  $k$ :  $E_k = \rho_k e_k + \rho_k |\vec{u}_k|^2 / 2$ ,
- $H$ : total enthalpy:  $H = h + |\vec{u}|^2 / 2$ ,
- $e$ : specific internal energy for each phase,
- $n$ : number of particles per unit volume,  $n = \sigma/m$ ,
- $m$ : mass of a particle,
- $\vec{q}$  is the heat flux vector,
- $Q_c$ : chemical energy due to burning of particles,
- $Q_T$ : interfacial heat exchanged by convective mechanism,
- $Q_R$ : is the heat transferred by radiation,
- $\tilde{T}$ : stress tensor,
- $\vec{u}$ : phase velocity,
- $\rho$ : density,
- $\Gamma_c$ : total mass exchange between phases.

Subscripts:

- 1: gas phase,
- 2: solid phase,
- c: combustion,
- vol: volatiles.

This model includes a high-dilute mixture modelling assumption as the effect of pressure on the solid phase is neglected. The authors using this model consider the solid mixture is comprised of coke (C) and volatiles (vol), so that  $\text{NSSP} = 2$ , and

$$\frac{\partial}{\partial t}(\sigma Y_{2,C}) + \vec{\nabla} \cdot (\sigma Y_{2,C} \vec{u}_2) = -\dot{\omega}_{2,C} \quad (2.42)$$

where

$$\Gamma_c = \sum_{k=1}^{\text{NPSP}} \dot{\omega}_{2,k} = - \sum_{k=1}^{\text{NGSP}} \dot{\omega}_{1,k} \quad (2.43)$$

The interfacial forces (drag and Magnus forces), the heat transfer by both convection and radiation are modelled by a set of closure laws which are detailed in [Section 2.4.2](#).

The emission of volatiles is computed by means of an Arrhenius-type equation and considering the mass exchange between phases. They affirm that the emitted volatiles constitute a mixture of gases including  $\text{N}_2$ ,  $\text{O}_2$ ,  $\text{CO}_2$ ,  $\text{CH}_4$ ,  $\text{H}_2$ ,  $\text{H}_2\text{O}$  and others. They also include a one-step reaction mechanism to account for the combustion of methane, which is not specified here. The combustion of coke, on the contrary, is modelled by a more compelling mechanism based in two coefficients, one for the influence of kinetics in the global reaction rate, and a second one for the influence of diffusion.

The equations of the Warsaw model are completed by the following thermodynamics relationships:

$$E_1 = \frac{1}{2} \rho_1 \vec{u}_1^2 + \sum_{k=1}^{\text{NG}} \rho_{1,k} e_{1,k} \quad (2.44)$$

$$E_2 = \frac{1}{2} \rho_2 \vec{u}_2^2 + \sum_{k=1}^{\text{NS}} \rho_{2,k} e_{2,k} \quad (2.45)$$

with

$$e_{1,k} = c_{1,k} T_1, \quad e_{2,k} = c_{2,k} T_2, \quad p = \sum_{k=1}^{\text{NG}} \rho_{1,k} R_{1,k} T_1$$

$$h_{1,k} = e_{1,k} + R_{1,k} T_1, \quad k = 1, \dots, \text{NG}$$

The mass flux due to diffusion in the gas phase is defined as follows:

$$\vec{J}_k = \rho_1 D_{1,k} \vec{\nabla}(X_{1,k}), \quad k = 1, \dots, \text{NGSP}, \quad (2.46)$$

where  $D_{1,k}$  is the diffusion coefficient for  $k$ -th species and  $X_{1,k}$  is the mole fraction.

## 2.4 STATE OF THE ART ON CLOSURE LAWS FOR REACTIVE TWO-PHASE MODELS

Different equations are considered in order to close the system of equations when modelling the behaviour of a gas and particle mixtures. These correlations accounts for many physical phenomena such as gravity, viscous and non-viscous friction, lift, buoyancy, and so on. Special care must be taken when re-entrainment and re-suspension of particles are present.

Among them, we should also include other interactions that are modelled as a coupling between phases: such as interfacial heat transfer, phase change or energy generation due to chemical reaction. Chemical processes can be classified as homogeneous (gas phase) or heterogeneous (gas-solid) reactions. The former include heat generation and species transport, whilst reactions involving several phases imply exchanges of mass, momentum and energy between phases. Some approximations from literature, to characterise these processes, are introduced in the following sections.

### 2.4.1 *Force balance model*

In the study of re-suspension of particles from a surface when a turbulent flow passes by and interacts with these particles three theories are considered:

- Force balance
- Momentum balance
- Energy balance

The first two approximations consider the forces acting on a particle by means of either the force or the momentum balance; the interaction between fluid and particle is enough to provoke the re-entrainment of the particle. The third approximation is based on the energy transferred to a particle by the fluid which is balanced with the adhesion energy of the particle to the surface. Unlike, the other approaches, this model considers the particle oscillating in an equilibrium position. So, in re-suspension process, the particle leaves the energy *well* where it is when the accumulated energy exceeds the adhesion potential.

In the case of the force balance, two types of forces are basically considered: Aerodynamic and attractive forces. Aerodynamic forces are mainly drag and lift forces. Lift forces elevate the particle by introducing it in the fluid stream. Attractive forces instead, tend to avoid the re-entrainment. The momentum balance methodology is quite similar to the previous one, but this includes the action of external

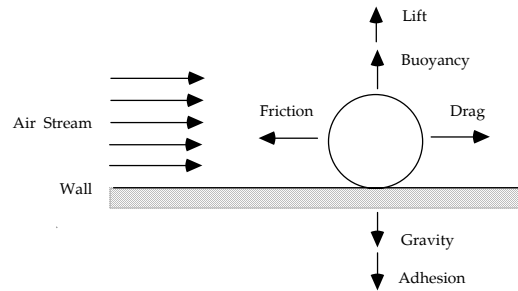


Figure 2.9: Forces acting on a single sphere at rest on a wall with a steady, fully developed flow.

momentums applied to the contact point between particle and surface. Moreover, certain particle deformation is sometimes assumed in different re-entrainment mechanisms proposed in the literature. Finally, in energy balance models, the statistical nature of the process is taken into account. There are several developments; some of them implicitly retain the force balance philosophy and others consider that the re-entrainment only occurs when the particle gains enough turbulent energy [97]. The different forces acting on the particles must be included in the balance equations which characterise the behaviour of the gas and particle mixture.

The Force Balance model is rather utilised due to its simplicity. The approximations based on this model consider that particle re-entrainment takes place depending on the resultant force from the force balance considered on this particle. In order to describe it, let us consider the forces acting on a particle, which can be classified as horizontal and normal forces: horizontal forces are the fluid-drag force and the frictional force, this last one is the product of the normal forces and the coefficient of friction. Normal forces are adhesion, gravitational, buoyant and lift forces as Figure 2.9 shows for a specific case of a particle on a horizontal surface. For the case of vertical surfaces, the gravitational and buoyant forces are tangential to the surface.

To identify each force and the force acting on each control volume, one must know the number of particles in the domain, calculated by means of averaged void fraction and solid concentration.

#### 2.4.2 Particle interfacial forces

In a two-phase gas and particles flow, the force interaction between the two phases can characterised by means of several effects, including the particle drag force, the Magnus force or the Saffman force. The steady-state drag, accounting for the interfacial friction, is defined as the drag force which acts on the particle in a uniform pres-

sure field when there is no acceleration of the relative velocity between the particles and the conveying fluid.

In general, the drag coefficient depends on the particle shape and orientation with respect to the flow as well as on the flow parameters such as Reynolds number, Mach number, intensity of turbulence, etc.

Since contradictions are found among the reported experimental results, it seems reasonable to apply as a standard the drag formula for steady processes on a single sphere [89, 81]:

$$\vec{F}_d = \frac{1}{2} \rho_g C_d A |\vec{u}_g - \vec{u}_p| (\vec{u}_g - \vec{u}_p) \quad (2.47)$$

where  $C_d$  is the drag coefficient which is a function of the Reynolds number for particles and  $A$  is a representative area of the particle [24]. For spherical particles, considering the number of particles  $\sigma/m_p$ , and  $m_p$  the mass of a particle, Equation 2.47 can be expressed as:

$$\vec{F}_d = \frac{3\sigma}{4d_p \rho_p} \rho_g C_d |\vec{u}_g - \vec{u}_p| (\vec{u}_g - \vec{u}_p) \quad (2.48)$$

Many expressions can be found in the existing literature for the drag coefficient of a particle. Otterman and Levine [89] proposed an expression that was later used by Miura and Glass [81] in their work:

$$C_d = 0.48 + 28Re_p^{-0.85} \quad (2.49)$$

where the Reynolds number for particles is given by

$$Re_p = \frac{\rho_g d_p |\vec{u}_g - \vec{u}_p|}{\mu_g} \quad (2.50)$$

and the gas viscosity (in this case air) is given by a Sutherland formula:  $\mu_g = 1.71 \cdot 10^{-5} (T_g/273)^{0.77}$  (N·s/m<sup>2</sup>) [15]. Applications involving large changes in temperature (such as transient combustion or detonation problems) require that sort of viscosity definitions as a function of temperature.

For larger particles, Rogue et al. [100] addressed an experimental study on unsteady two phase flow in a vertical shock tube. They obtained the experimental trajectories of the various particles as a function of the time and they adjusted the value of the drag coefficient into an analytical expression. For a Reynolds number ranging from 5,000 to 120,000 (Mach number varying from 0.2 to 0.6), they measured the drag coefficient for different types of particles, including nylon and glass balls from 1 to 2 mm wide. The expression proposed to obtain the drag coefficient is [100]:

$$C_d = 0.38Re^{0.0539} \quad (2.51)$$

On other hand, as Crowe et al. [24] postulated, when the Reynolds number is little, the drag coefficient appears to vary inversely with

it (that is known as *Stokes flow regime*). When  $Re$  increases, the drag coefficient approaches to a nearly constant value of 45.0 (*Newton's law*). For the range of  $Re$  between 750 and  $3.5 \times 10^5$ ,  $C_d$  varies only about 13% from the constant value. Finally, there is a critical Reynolds number for which  $C_d$  suddenly decreases, i.e.  $Re = 3.0 \times 10^5$ . All this can be summarised as follows:

- (1) For  $Re < 1$  (Stokes' law):  $C_d = 24/Re$ ,
- (2) For  $Re > 5$ ,  $C_d = \frac{24}{Re} (1 + 0.1875Re)$ ,
- (3) For  $750 < Re < 3.5 \times 10^5$  (Newton's law),  $C_d = 0.45$ ,
- (4) For  $Re > 3.5 \times 10^5$ , there is a sudden decrease in  $C_d$ .

Other experimental studies gave a wide variety of expressions. Ingebo [47], on combustion experiments, reported that  $C_d = 28Re^{-0.84}$ . Schiller and Neumann [109] used

$$C_d = \frac{24}{Re} (1 + 0.15Re^{0.687}) \quad (2.52)$$

for  $Re$  greater than 800, while Putnam [96] proposed two expressions for different flow regimes:  $C_d = \frac{24}{Re} (1 + 0.16Re^{0.6})$  with  $Re < 10^3$  and  $C_d = 0.4392$  with  $10^3 < Re < 3 \times 10^5$ .

For most cases with spherical particles, the Schiller-Neumann law is more than adequate for general use in multiphase calculations with  $Re < 1000$ . Notwithstanding, for the complete sub-critical  $Re$  number range a general expression was developed by Cliff and Gauvin [22], which is an extension of Schiller-Neumann law:

$$C_d = \frac{24}{Re} \left( 1 + 0.15Re^{0.687} + \frac{0.0175Re}{4.25 \times 10^4 Re^{-1.16}} \right) \quad (2.53)$$

Also Combe and Hérard [23] used a very similar formula for  $Re < 800$  that inevitably recalls the Schiller-Neumann approach:  $C_d = \frac{24}{Re} (1 + 0.15Re^{0.7})$ , and  $C_d = 0.44$  for higher Reynolds.

Meanwhile, in numerous works, Klemens [61, 62] considered the general law by Schiller and Neumann, for the case of isolated particles. However, when dealing with dense mixtures, the following expression was used:

$$C_d = \frac{24}{Re} \left( 0.0972Re - 8.33 \frac{\alpha}{\alpha - 1} \right), \quad (2.54)$$

where  $\alpha$  is the volume fraction of the solid phase. A complete approach by Tu and Fletcher [123] consist in the following piece-wise formula:

$$C_d = \begin{cases} \frac{24}{Re} (1 + 0.15Re^{0.687}) & \text{for } 0 < Re \leq 200, \\ \frac{24}{Re} (0.914Re^{0.282} + 0.0135Re) & \text{for } 200 < Re \leq 2500, \\ 0.4008 & \text{for } 2500 < Re. \end{cases}$$

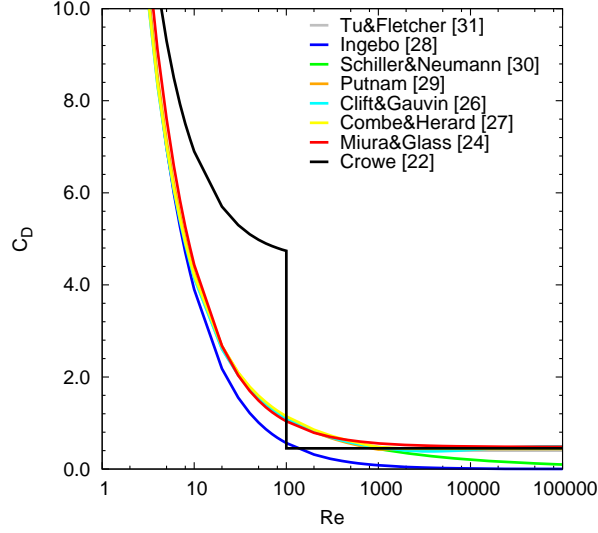


Figure 2.10: Laws for  $C_d$  from literature, as a function of Re number.

(2.55)

All these expressions have been gathered and depicted in [Figure 2.10](#), so that they can be compared.

Mean while, Veyssi re and Khasainov for their model ([Section 2.3.4](#)) assume the momentum exchange between phases due to drag force is modelled by an expression like [Equation 2.48](#). And the drag coefficient would be correlated with the Reynolds number as follows:

$$C_d = \frac{24}{Re_p} + 4.4Re_p^{-0.5} + 0.42 \quad (2.56)$$

$$Re_p = \rho_g d_p |u_g - u_p| / \mu_g \quad (2.57)$$

Other authors like Klammer et al. [[60](#)] and Korobeinikov et al. [[65](#)], using the Warsaw model, consider the total interfacial force as a combination of drag and Magnus force.

They propose that the following relationship holds for the interfacial friction:

$$\vec{F}_d = n \frac{\pi d_p^2}{8} C_d \rho_1 |\vec{u}_g - \vec{u}_p| (\vec{u}_g - \vec{u}_p) \quad (2.58)$$

with  $n$  the number of particles, and  $C_d$  the drag force coefficient:

$$C_d = \frac{24}{Re} \left( 1 + \frac{Re^{2/3}}{6} \right) \quad (2.59)$$

In addition to the drag force, the Magnus force, which is caused by the rotation of particles, is also considered in that model. This force is suggested to explain the mechanism of particle entrainment and dispersion from layered wall-adjacent dust. They assume the Magnus force can be computed as:

$$\vec{f}_M = K_M \frac{d^3}{8} \rho_1 [(\vec{u}_1 - \vec{u}_2) \times \text{rot } \vec{u}_1], \quad (2.60)$$

where  $K_M$  is a non-dimensional coefficient, whose value can not be derived analytically and should be instead assessed by experimental methods. However, some estimations obtained by computational experiments show that this value varies with the limits of several units to several tenth [65].

Although the Saffman force might be also important for the particle lift process, this is not taken into account neither in [60] or in [65].

### 2.4.3 Interfacial heat transfer

The heat transferred from the gas to the particle at its surface  $S$  is given by

$$Q = - \int_{cs} \mathbf{q} \cdot \hat{\mathbf{n}} dS \approx -\bar{q}S \quad (2.61)$$

where  $q$  is the heat transferred per unit area and per unit time to the particle. Considering that we have  $\sigma/m_p$  particles per unit volume, the total heat exchanged between the gas and the particles is given by:

$$Q_g = -\frac{\sigma}{m_p} Q \quad (2.62)$$

If the particle is assumed to be spherical then, the heat exchanged by convection mechanism is:

$$Q = -\pi d_p^2 h_g (T_g - T_p) \quad (2.63)$$

If the Nusselt number is defined as  $Nu = h_g/d_p k_g$ , Equation 2.63 can be written as:

$$Q = -\pi d_p k_g (T_g - T_p) Nu \quad (2.64)$$

Considering that the Prandtl number is  $Pr = (\mu_g c_{pg})/k_g$ , and the thermal conductivity in the case of air is  $k_g = 0.028 + 0.04/60(T_g - 303.15)$  W/(m·K), Equation 2.64 can be written as:

$$Q = \pi d_p \mu_g c_{pg} Pr^{-1} (T_g - T_p) Nu \quad (2.65)$$

And therefore,

$$Q_g = -\frac{\sigma}{m_p} \pi d_p \mu_g c_{pg} Pr^{-1} (T_g - T_p) Nu \quad (2.66)$$

where the Nusselt number can be calculated by means of the expression:

$$\text{Nu} = 2 + 0.6\text{Pr}^{1/3}\text{Re}^{1/2} \quad (2.67)$$

This formula for Nusselt (Equation 2.67) is valid for  $\text{Re} \leq 50000$  according to Crowe et al. [24]. It was originally proposed by Knudsen and Katz [64] and implemented by Otterman and Levine [89], and Miura and Glass [81], and in the Warsaw model [60, 65], among others.

Rogue et al. [100] proposed for laden mixtures the expression posed by Butler et al. [12]:

$$Q = -\pi d_p^2 (1 - \alpha) \frac{k_g}{d_p} \text{Pr}^{0.33} \text{Re}^{0.7} (T_g - T_p), \quad (2.68)$$

so that the heat exchanged between the gas phase and the particles in the control volume is

$$Q_g = -\frac{\sigma}{m_p} \pi d_p (1 - \alpha) k_g \text{Pr}^{0.33} \text{Re}^{0.7} (T_g - T_p), \quad (2.69)$$

which is similar to Equation 2.66, but with a Nusselt number given by

$$\text{Nu} = 0.65\text{Pr}^{0.33}\text{Re}^{0.7} \quad (2.70)$$

In Figure 2.11, both expressions for the Nusselt number are compared. Certainly, the difference between them is important. It is worth noting that Butler et al. [12] obtained their expression from experiments on TDD during DDT combustion. In addition, Rogue et al. [100] forgot to include the coefficient 0.65 in the paper.

Notwithstanding, many authors assume that radiation transfer plays a role in heat transfer which cannot be neglected in combustion problems with elevated temperatures. For instance, Klammer et al. [60] and Korobeinikov et al. [65] calculate the radiation part of the interface heat flux  $Q_R$  in a simple way as:

$$Q_R = \sigma_E \varepsilon_1 T_1^4 + q_{1e} \quad (2.71)$$

where  $\varepsilon \in (0, 1)$  is an empirical coefficient and  $q_{1e}$  is the radiant flux due to external sources (hot walls, sparks, etc.). However, when  $T_1 \leq 1000\text{K}$ ,  $Q_R$  can be neglected.

For the sake of simplicity Klammer et al. [60] use the diffusion approximation, and they split the total radiation flux into two different parts, one of which is for the gas phase,  $\bar{q}_{1,R}$ , and the other for the particle medium,  $\bar{q}_{2,R}$ . For the first, the Plank approximation for grey body is considered, while for the second, it is assumed the Rosseland

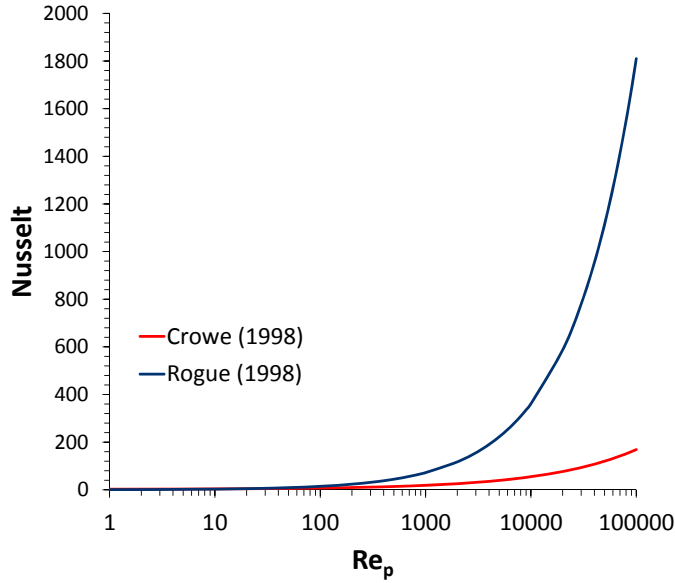


Figure 2.11: Two laws for Nusselt number from literature, as a function of  $Re_p$  number.

approximation for optically thick grey body. That means these parts are taken as follows:

$$\vec{\nabla} \cdot \vec{q}_{1,R} = 4\sigma_E K_p T_g^4, \quad (2.72)$$

$$\vec{q}_{2,R} = -\frac{16\sigma_E T_p^3}{3K_2} \vec{\nabla}(T_p), \quad (2.73)$$

where  $K_p$  is the Plank absorption coefficient for the gas phase, and the Rosseland approximation is assumed for the solid phase with the coefficient  $K_2$  ranging from 0.01 to 1 in the CGS system of units. For the coefficient  $K_p$  a mean value of  $10^{-4} \text{ cm}^{-1}$  can be adopted [65].

In the same vein, according to the model by Veyssi re and Kha-sainov, which was previously described in Section 2.3.4, the heat ex-change between phases can be modelled as:

$$Q_g = \frac{6\sigma}{\rho_p d_p} \left[ \frac{\text{Nu} \lambda_g (T_g \cdot T_p)}{d_p} + \epsilon \sigma_E (T_g^4 - T_p^4) \right] \quad (2.74)$$

where  $\epsilon$  is the emissivity of aluminium,  $\sigma_E$  is the Stefan-Boltzmann constant,  $\lambda_g$  is the gas conductivity, and  $\text{Nu}$  the number of Nusselt, calculated as:

$$\text{Nu} = 2 + 0.6 \text{Re}_p^{0.5} \left( \frac{c_{p,g} \mu_g}{\lambda_g} \right)^{1/2} \quad (2.75)$$

#### 2.4.4 Equations of state for the two-phase system

Equations of state are required by governing models of equations in order to characterise the behaviour of the materials of which the different phases in the system are constituted. In two-phase models, generally speaking, each phase should come with its respective equations of state. That would mean each phase could behave in a different way against pressure or temperature, and not only the gas phase but also if one of them is constituted by solid particles, due to compressibility phenomena.

Thus, a general conception of the behaviour of a two phase system, would lead to models like BN (see [Section 2.3.1](#)), in which pressure equilibrium between phases is not assumed, i.e. a different pressure is considered, respectively, for each of the phases. The thermodynamic state of the phase is then independently calculated by means of its own equation of state. In particular, for the phase  $\alpha$ , they introduce the Helmholtz free energy [4]:

$$\psi_\alpha = e_\alpha - T_\alpha \eta_\alpha \quad (2.76)$$

with  $e_\alpha$  the specific internal energy and  $\eta_\alpha$  the entropy of phase  $\alpha$ . Then, for the solid phase, a thermoelastic description of the Helmholtz free energy is used:

$$\begin{aligned} \psi_s(\gamma_s, T_s) = c_p^s \left\{ (T_s - T_s^0) \left[ 1 + \Gamma_s \gamma_s \left( \frac{1}{\gamma_s^0} - \frac{1}{\gamma_s} \right) \right] + T_s \ln \left( \frac{T_s}{T_s^0} \right) \right\} \\ + \frac{K_T}{\gamma_s^0 N(N-1)} \left[ \left( \frac{\gamma_s}{\gamma_s^0} \right)^{N-1} - (N-1) \left( 1 - \frac{\gamma_s^0}{\gamma_s} \right) - 1 \right]. \end{aligned} \quad (2.77)$$

The constants in this description are obtained from Hugoniot and thermophysical data (see [4]). For the combustion product gas, an equation of state is employed that can describe the highly-expanded to the very-dense thermodynamic states, i.e., the Jones-Wilkins-Lee equation of state.

A number of equations of state for solid phases can be collected from the literature. Among others, Hoffman and Krier [44] presented an equation of state for the solid phase, needed to fully describe the flow at very high pressures, by assuming that the particles are compressible. A modified Tait equations is proposed:

$$\rho_p = \rho_{0p} \left[ \frac{3P}{K_0} + 1 \right]^{1/2}, \quad (2.78)$$

where a value for the constant is given ( $K_0 = 1.38\text{GPa}$ ). Note that, in order to conserve the particle mass as the density increases, the particle size must decrease instead.

On other hand, the hypothesis of incompressible solid is incompatible with a solid equation of state since an infinite sound speed is

implied [4]. As mentioned above, according to Butler et al. [12], the use of compressible equations of state for the solid phase might be of great importance in some specific cases when solid compression is not negligible: despite its simplicity, the use of models for incompressible solid phase [41, 111] provides some reasonable answers, as for instead on the burning velocity, but does not indicate adequately the peak pressure during acceleration from deflagration. Since the peak pressures are precursors of the final detonation solutions, accurate calculations are needed and, thus, compressible solid models are more suitable for detonation calculations. Then, they assume the solid particles are compressible, without heating, obeying an equation of state.

As a further approximation, simpler than the BN model, both pressures at gas and at solid can be assumed to be related each other. In some cases, it has been proposed that this relationship can be modelled as an algebraic expression which accounts for the intergranular stress. Some authors using those kind of approaches, as Krier and co-workers [44, 92, 93, 12], consider the pressure in the solid phase is defined in terms of the configuration changes of the granular material. In particular, as described by Hoffman and Krier [44], a packed bed of particles placed under a compressive load can be further compacted. However, there is a force which resists this compaction that depends on the stress-strain relationship of the particle lattice, which is not necessarily the same as that of a homogeneous solid made from the same material. The compressive load on the bed will be split between the two phases in proportion to the porosity. So the resultant force on the particles will be a function of the porosity, the porosity gradient, and possibly other factors. There can be a variety of formulations used to relate this particle-particle interaction through a stress (see, for instead, [44, 41, 111]).

It is worth noting these cited works address the modelling of the two-phase flow in very dense mixtures where particle interaction becomes crucial, as for instead columns of pressed hi-explosive grains, such as HMX. However, when dealing with polydisperse, highly diluted mixtures [20, 65, 60] authors tend to assume that particle-particle interaction as negligible. So pressure would only affect to the gaseous phase, the solid can be considered as incompressible, and no equation of state is needed for its characterisation.

Regarding the equation of state for the gas, the authors are divided between those accepting the ideal-gas equation of state [60, 20, 131], and others who use equations accounting for the co-volume of the gas. Of the latter, Hoffman and Krier [44] or Gough and Zwarts [41] propose an equation of Nobel-Able type that can be expressed with Hoffman and Krier's notation as:

$$P_g = \frac{\rho_g R_g T_g}{1 - \rho_g B_\phi} \quad (2.79)$$

The co-volume  $B_\phi$ , a term that is a function of the gas density, has been described as a parameter which takes into account the physical size of the molecules and any intermolecular forces created by their proximity one to another.

#### 2.4.4.1 *Ideal-gas equations of state for an equilibrium mixture of gases*

The ideal-gas model of gases is by far the most used due to its simplicity and relative accuracy in a wide variety of situations. At states where the pressure,  $p$  is small relative to the critical pressure of the gas,  $p_c$  and/or the temperature  $T$  is large relative to the critical temperature,  $T_c$ , the compressibility factor,  $Z = pv/RT$ , is approximately 1. At such states, we can assume with reasonable accuracy that  $Z=1$ , or

$$pv = RT \quad (2.80)$$

where  $v$  is the gas specific volume and the constant  $R = R_u/W$ , being  $W$  the atomic or molecular weight. An alternative form of the same basic relationship among pressure, specific volume, and temperature are obtained as follows, with  $v = V/m$ :

$$p = \rho RT \quad (2.81)$$

The specific internal energy and enthalpy of gases generally depend on two independent properties. As proven [82], for any gas whose equation of state is given exactly by Equation 2.80, the specific internal energy depends on temperature only. The ideal gas equation of state does not provide an acceptable approximation at all states. Accordingly, whether the ideal gas model is used depends on the error acceptable in a given calculation.

If heat capacities,  $c_p(T)$  and  $c_v(T)$  are considered to be temperature independent, with the Mayer's relation ( $R = c_p - c_v$ ) and the definition of the adiabatic constant,  $\gamma$ , we can express Equation 2.80 as:

$$p = \left( \frac{\gamma - 1}{\gamma} \right) \rho e \quad (2.82)$$

where  $e$  is the internal energy of the gas. However, this assumption is a very strong one, especially when combustion is present. Furthermore, it can lead to non-physical solutions as discussed later in Section 3.2.

A more general approach accounts for the dependence of heat capacities with temperature. In fact, for a gas obeying the ideal gas model, specific internal energy depends only on temperature. Hence, the specific heat  $c_v$  is also a function of temperature alone, i.e.,

$$c_v(T) = \frac{de}{dT} \quad (2.83)$$

By separating variables we get  $de = c_v(T)dT$ . And, similarly, since the enthalpy depends only on temperature,  $dh = c_p(T)dT$ . These expressions require the ideal gas specific heats as functions of temperature. These functions are available for gases of practical interest in various forms, including graphs, tables, and equations. In particular, useful polynomial expressions can be found in the open-access NIST data base [83], as well as tabular specific heat data. Those easily integrable expressions have the form:

$$\frac{\bar{c}_p}{\bar{R}} = A + BT + CT^2 + DT^3 + E/T^2 \quad (2.84)$$

in molar basis. Values for  $A$ ,  $B$ ,  $C$ ,  $D$ , and  $E$  are taken from [83]. It is worth noting that, due to its definition, also the adiabatic coefficient depends only on temperature:  $\gamma(T) = c_p(T)/c_v(T)$ .

Hence, by using those temperature dependent expressions, a more general form of the equation of state 2.82 is needed, namely,

$$p = \left( \frac{\gamma(T) - 1}{\gamma(T)} \right) \rho c_v(T) T \quad (2.85)$$

Finally, using the equation of state 2.85 together with the thermodynamic definition of speed of sound, we get:

$$c_s = \sqrt{\left( \frac{\partial p}{\partial \rho} \right)_s} = \sqrt{\frac{\gamma p}{\rho}} \quad (2.86)$$

For the multicomponent case, having neglected the intermolecular forces, we can state that for simple system consisting in a mixture of ideal gases the total energy and the total entropy are the sum of the energies and the entropies of the single components as they occupy alone the total volume  $V$  at the equilibrium temperature  $T_g$  of the mixture (Gibbs theorem). In that general case, the internal energy of the mixture of gases,  $e_g$ , is defined as:

$$e_g(T) = \sum_i Y_i \left( h_i^0 + \int_0^{T_g} c_{v,i}(\alpha) d\alpha \right) \quad (2.87)$$

with  $Y_i$  the mass fraction of the component  $i$  of the mixture. And therefore, the equation of state can be written as:

$$p = \rho_g \left( \sum_i Y_i \frac{R_u}{W_i} \right) T_g = \rho_g R(\mathbf{Y}) T_g \quad (2.88)$$

where  $R(\mathbf{Y})$  is the gas constant of the mixture, as a function of the vector of mass fractions  $\mathbf{Y}$ . Then, the speed of sound is determined by

$$c_{s,g}^2 = \gamma(T_g, \mathbf{Y}) R(\mathbf{Y}) T_g \quad (2.89)$$

with

$$\gamma(T_g, \mathbf{Y}) = \frac{\sum_i Y_i c_{p,i}(T_g)}{\sum_i Y_i c_{v,i}(T_g)} = \frac{c_v(T_g, \mathbf{Y}) + R(\mathbf{Y})}{c_v(T_g, \mathbf{Y})} = \frac{c_p(T_g, \mathbf{Y})}{c_v(T_g, \mathbf{Y})} \quad (2.90)$$

$$c_{p,i}(T_g) = c_{v,i} + \frac{R_u}{W_i} \quad (2.91)$$

#### 2.4.5 Gas-phase combustion in reactive atmospheres

A comprehensive research has been done within literature in order to find the most appropriate kinetic model of CO oxidation for our purposes. Since we are dealing with modelling of strong detonation flames, a great amount of computational resources are necessary to get the solution, so among the different approaches, we will choose those which allow lower computing times, trying not to sacrifice the accuracy of the solution.

Because of limitations on computer capabilities, there is a need for detailed chemical-kinetic mechanisms for combustion that are not too large. Several detailed mechanisms are now available for accurate description of the combustion process under conditions of practical interest. However, because of the relatively large number of chemical species and elementary rates appearing in these detailed mechanisms, their use in computations of high-Reynolds-number flows is still prohibitively expensive, given the present computational capabilities. Reduced mechanisms, systematically derived from detailed chemical schemes by introduction of steady states for intermediate species, represent an attractive alternative to shorten computational times, while providing sufficient accuracy to yield reliable computational results [11]. These are called skeletal mechanisms and they constitute an option which provides a good balance between computing resources consumed and accuracy of the solution.

There is another simple option that is appropriate to be used with numerical methods for high Reynolds numbers, and that can be taken as a first approximation, more or less accurate: it is a global reaction mechanism. The commonly accepted one-step reaction mechanism for moist carbon monoxide oxidation consists of the overall chemical equation,



with with the reaction rate for CO disappearance defined as:  $-d[\text{CO}]/dt = k_{ov}[\text{CO}]^a[\text{H}_2\text{O}]^b[\text{O}_2]^c$ . Typically, the overall specific rate constant is expressed in Arrhenius form as:

$$k_{ov} = A_{ov} \exp(-E_{ov}/RT) \quad (2.93)$$

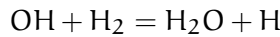
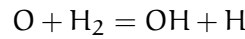
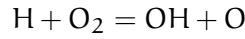
Since first postulated in 1956, the global parameters,  $A_{ov}$ ,  $E_{ov}$ ,  $a$ ,  $b$ , and  $c$ , of this model have been empirically derived by numerous research groups from various experiments [45].

#### 2.4.5.1 Global reaction mechanisms for moist CO oxidation

A four equations reaction model is presented in Howard et al. [45] for CO combustion in the presence of hydrogen. The goal of that work is to develop a global expression for the reaction rate of CO combustion. The reported expression is compared and validated against data from a two-stage combustor experiment at 1 atm. According to Howard et al. [45], in the reaction system the effect of temperature and concentration and the approach to equilibrium are in approximate agreement with a mechanism based on rate control by the forward and reverse steps of the reaction:



equilibration of the reactions:



and three-body recombinations.

The resulting global reaction rate equation is:

$$-\frac{d[\text{CO}]}{dt} = k_0[\text{CO}][\text{O}_2]^{1/2}[\text{H}_2\text{O}]^{1/2} \exp\left(-\frac{E}{RT}\right), \quad (2.95)$$

with the following parameters:  $k_0 = 1.3 \cdot 10^4 \text{ (ml}\cdot\text{mol}^{-1}\cdot\text{s}^{-1})$  and  $E = 30 \text{ (kcal}\cdot\text{mol}^{-1})$ .

Although a single, simple equation cannot describe all the reaction details, such as the varying order in oxygen concentration, the agreement of the equation with data representing different types of burners and reactors, different fuels, equivalence ratios, pressures, and temperatures over the range 840-2360 K is found to be good. However, the study from Howard et al. (1973) presents some drawbacks for our purpose, namely, its validity is restricted to atmospheric pressure (for higher pressures we should go to [112]). The experimental data are measured in post flame gases but, in fact, the high temperatures reached in those situations are not too elevated compared with those in detonation fronts.

A compilation of different global reaction mechanisms is found in [29]. This paper, the second part of a work on co-combustion of coal and urban biomass, explores the inhibition of CO oxidation with HCl.

REFERENCES	$k_0$	E/R	a	b	c
Howard et al.	$1.3 \cdot 10^8$	15106	1	0.5	0.5
Hottel et al.	$1.9 \cdot 10^6$	8056	1	0.3	0.5
Dryer et al.	$1.3 \cdot 10^{10}$	20141	1	0.25	0.5
Yetter et al.	$7.2 \cdot 10^{14}$	34743	1	0.5	0.5
Hannes	$1 \cdot 10^7$	15106	1	0.5	0.5
Jensen et al.	$3.25 \cdot 10^7$	15098	1	0.5	0.5

Table 2.1: CO oxidation kinetic laws proposed by literature (Source: Desroches-Ducarne et al. [29]).

The reaction mechanism is based in a global model as in Eq. 2.93. The different kinetic parameters from literature are gathered in Table 2.1.

An experimental validation of Howard’s one-step reaction with kinetic parameters by Jensen and Johnsson [51] was reported by Heikkinen et al. [42] in the framework of research about co-combustion of chicken droppings with carbon. The CFD results seemed to match quite well with results from experiments.

#### 2.4.5.2 Detailed reaction schemes for CO oxidation

As a matter of fact, the Howard’s expression and the other one-step reaction mechanisms are commonly used in combustion problems when simplified chemistry is needed. In order to define their limitations, the reasons why the models could fail and how to correct it, Yetter et al. [137] carried out a discussion by comparing the results obtained from both a one-step reaction mechanism and a detailed kinetic model, based on a set of 11 chemical species and 27 reversible reactions. The detailed model was set as a benchmark, due to its proven validity. The parameters for the global reaction mechanism were determined from the detailed calculations with that detailed model. Regarding the global expression (Eq. 2.93), the authors suggest that if the global parameters of the one-step mechanism are evaluated at a specific operating point (i.e., specific temperature, pressure, equivalence ratio, mixture composition), significant errors can result in predictions at operating points other than where the model was originally calibrated. The most significant error would occur in a system with a large change in temperature. Furthermore, the specific rate constant  $k_{ov}$  does not exhibit an Arrhenius dependence over the complete temperature range studied (770-2500 K). The global model, unlike the detailed model, does not have induction time kinetics. This complication is commonly remedied by introducing an

induction time also in global form with another set of global parameters:

$$\tau = B[\text{CO}][\text{H}_2\text{O}]^{0.5}[\text{CO}]^{0.25} \exp(F/RT) \quad (2.96)$$

where the parameters B and F were determined by the least squares analysis, by using values of the reaction rate at different times. Finally, if the variations in the global parameters are to be eliminated from the current model, it is clear that the functional form of  $k_{ov}$ , and  $\tau$  must be altered. The non-linearity in combustion kinetics equations makes this a particularly difficult task.

The truth is that even the more detailed schemes suffer a loss of accuracy when we move outside the range of application for which they were designed. Hence, Kim et al. [58] presented a revision of the comprehensive CO/H<sub>2</sub>/O<sub>2</sub> reaction mechanism by Yetter et al. [137]. Experimental data from a variable pressure flow reactor were used to calibrate the model, in order to make it suitable for high pressure (1-9.6 atm) and high temperature (960-1200 K) conditions, considering an equivalence ratio from 0.33 to 2.1. The model consists of a set of 28 reactions. Later, in 2005, Davis et al. proposed a comprehensive kinetic model for H<sub>2</sub>/CO combustion, basing on the thermodynamic, kinetic, and species transport updates then available to get a reaction model of 14 species and 30 reactions. This kinetic model was tested against a wide range of experimental data, according to the authors. Other detailed models specifically adapted for high pressures and temperatures were reported by Saxena and Williams [108], paying attention to temperatures above 1000 K, pressures below 100 bar and equivalence ratios below 3 (resulting sub-mechanism still consists of 30 reactions and 12 species), and model proposed by Sivaramakrishnan et al. [112] based on Davis et al. [27]. The last includes an experimental study in a high pressure shock tube containing a system of CO-H<sub>2</sub>-H<sub>2</sub>O-O<sub>2</sub>. Inside the tube, the combustion of diluted mixtures of CO, doped with H<sub>2</sub>, was studied behind reflected shock waves.

#### 2.4.5.3 Skeletal models for CO oxidation

Those detailed mechanisms remain too exhaustive to be implemented in a finite-volume code due to the high number of species interacting with each other. An intermediate choice to avoid an excess of species but also keeping a good level of accuracy is the use of skeletal models. Boivin et al. [11] reported a reduced (four-step) reaction mechanism for Syngas combustion. The Syngas mixture contains significant amounts of CO and H<sub>2</sub> as the main reactive species along with diluents such as N<sub>2</sub>, CO<sub>2</sub> and H<sub>2</sub>O. The skeletal mechanism is formulated from a 21-step detailed mechanism which is later reduced to a reasonably accurate 16-step mechanism, after extensive tests and computations. By introducing steady-state assumptions, the chemistry for CO/H<sub>2</sub> oxidation reduces to the four global steps:

Rate coefficients in Arrhenius form  $k = AT^n \exp(-E/RT)$  for the skeletal mechanism.

Reaction		$A^a$	$n$	$E^a$		$A^a$	$n$	$E^a$	
1	$H+O_2 \rightleftharpoons OH+O$	$k_f$	$3.52 \times 10^{16}$	-0.7	7142	$k_b$	$7.04 \times 10^{13}$	-0.26	0.60
2	$H_2+O \rightleftharpoons OH+H$	$k_f$	$5.06 \times 10^4$	2.67	2632	$k_b$	$3.03 \times 10^4$	2.63	2023
3	$H_2+OH \rightleftharpoons H_2O+H$	$k_f$	$1.17 \times 10^9$	1.3	1521	$k_b$	$1.28 \times 10^{10}$	1.19	7825
4	$H+O_2+M \rightarrow HO_2+M^b$	$k_0$	$5.75 \times 10^{19}$	-1.4	0.0	$k_\infty$	$4.65 \times 10^{12}$	0.44	0.0
5	$HO_2+H \rightarrow 2OH$		$7.08 \times 10^{13}$	0.0	1.23				
6	$HO_2+H \rightleftharpoons H_2+O_2$	$k_f$	$1.66 \times 10^{13}$	0.0	344	$k_b$	$2.69 \times 10^{12}$	0.36	23186
7	$HO_2+OH \rightleftharpoons H_2O+O_2$		$2.89 \times 10^{13}$	0.0	-208				
8	$H+OH+M \rightleftharpoons H_2O+M^c$	$k_f$	$4.00 \times 10^{12}$	-2.0	0.0	$k_b$	$1.03 \times 10^{23}$	-1.75	496.14
9	$2H+M \rightleftharpoons H_2+M^d$	$k_f$	$1.30 \times 10^{18}$	-1.0	0.0	$k_b$	$3.04 \times 10^{17}$	-0.65	433.09
10	$2HO_2 \rightarrow H_2O_2+O_2$		$3.02 \times 10^{12}$	0.0	5.8				
11	$HO_2+H_2 \rightarrow H_2O_2+H$		$1.62 \times 10^{11}$	0.61	100.14				
12	$H_2O_2+M \rightarrow 2OH+M^e$	$k_0$	$8.15 \times 10^{23}$	-1.9	207.62	$k_\infty$	$2.62 \times 10^{19}$	-1.39	214.74
13	$CO+OH \rightleftharpoons CO_2+H$	$k_f$	$4.4 \times 10^6$	1.5	-3.1	$k_b$	$2.41 \times 10^{13}$	0.22	10460
14	$CO+HO_2 \rightleftharpoons CO_2+OH$		$6.03 \times 10^{13}$	0.0	96.0				
15	$HCO+M \rightleftharpoons CO+H+M^f$	$k_f$	$1.86 \times 10^{17}$	-1	71.13	$k_b$	$3.51 \times 10^{16}$	-0.77	5.35
16	$HCO+H \rightarrow CO+H_2$		$5.0 \times 10^{13}$	0.0	0.0				

<sup>a</sup> Units are mol, s, cm<sup>3</sup>, kJ, and K.

<sup>b</sup> Chaperon efficiencies are 2.5 for H<sub>2</sub>, 16.0 for H<sub>2</sub>O, 1.2 for CO, 2.4 for CO<sub>2</sub>, 0.7 for Ar and He and 1.0 for all other species; Troe falloff with  $F_2 = 0.5$ .

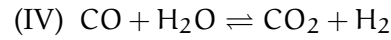
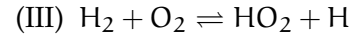
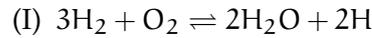
<sup>c</sup> Chaperon efficiencies are 2.5 for H<sub>2</sub>, 12.0 for H<sub>2</sub>O, 1.9 for CO, 3.8 for CO<sub>2</sub>, 0.38 for Ar and He and 1.0 for all other species.

<sup>d</sup> Chaperon efficiencies are 2.5 for H<sub>2</sub>, 12.0 for H<sub>2</sub>O, 1.9 for CO, 3.8 for CO<sub>2</sub>, 0.5 for Ar and He and 1.0 for all other species.

<sup>e</sup> Chaperon efficiencies are 2.0 for H<sub>2</sub>, 6.0 for H<sub>2</sub>O, 1.5 for CO, 2.0 for CO<sub>2</sub>, 0.4 for Ar and He and 1.0 for all other species;  $F_2 = 0.265 \exp(-7.94 K) + 0.735 \exp(-T/1756 K) + \exp(-5182 K/T)$ .

<sup>f</sup> Chaperon efficiencies are 1.9 for H<sub>2</sub>, 12.0 for H<sub>2</sub>O, 2.5 for CO, 2.5 for CO<sub>2</sub> and 1.0 for all other species.

Figure 2.12: Rate coefficients in Arrhenius form. Source: Boivin et al. [11].



with rates given in terms of the different elementary reaction rates by the expressions:

$$\omega_I = \omega_1 + \omega_{5f} + \omega_{10f} + \omega_{11f} + \omega_{14f}$$

$$\omega_{II} = \omega_{4f} + \omega_8 + \omega_9 - \omega_{10f} - \omega_{11f} - \omega_{15}$$

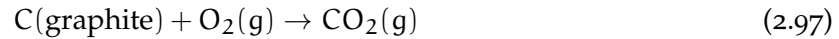
$$\omega_{III} = \omega_{4f} - \omega_{5f} - \omega_6 - \omega_{7f} - 2\omega_{10f} - \omega_{11f} - \omega_{14f}$$

$$\omega_{IV} = \omega_{13} + \omega_{14}$$

The different elementary reaction rates from the reduced (16 steps) mechanism are in turn calculated according to Arrhenius type laws, following the coefficients in Figure 2.12.

#### 2.4.6 Literature review on the oxidation of carbon particles

Graphite is reactive with atmospheric oxygen and oxidises at above 970 K. The global oxidation reaction for graphite with oxygen can be defined as:



The thermochemistry of this reaction can be found in not few places, from student textbooks to more advanced scientific works. The total enthalpy variation for the complete reaction is  $\Delta H = -94.052$  (kcal·mol<sup>-1</sup>) [5]

If the working temperature range is small, normally the variation of the heat capacity with temperature can be neglected, this approach is clearly acceptable for mono-atomic ideal gases. But if one needs to

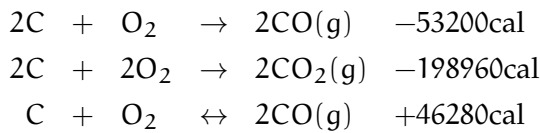
take into account the dependence, an empirical expression that gives good results is:

$$C_p(\text{J K}^{-1}\text{mol}^{-1}) = a + bT + \frac{c}{T^2} \quad (2.98)$$

Parameters  $a$  and  $b$  are temperature-independent. For carbon in graphite phase the following values are given:  $a = 16.86$ ,  $b = 4.77 \cdot 10^{-3} \text{ K}^{-1}$ ,  $c = -8.54 \cdot 10^5 \text{ K}^2$  [5].

As evident, a very extensive literature is available on carbon oxidation, as it is one of the most common reactions in nature, and dozens of kinetic laws can be found. However, chemical kinetics for carbon oxidation is strongly influenced by its geometry (i.e. filament, rod, block or particles) and the allotrope of carbon (they are graphite, diamond, and amorphous carbon). We look only for reaction mechanisms of graphite particles oxidation.

According to [46], if the amount of oxygen supplied is large enough, the product is carbon dioxide, but if the amount of oxygen is insufficient, then carbon dioxide and carbon monoxide are simultaneously produced, following chemical equilibrium:



The overall reaction process of graphite consists of transportation of gaseous reactants to the surface, adsorption of the gas to the surface (or even undergoing dissociative adsorption), stabilisation of the surface intermediates so formed with, some undergoing surface migration, desorption of the intermediates to form gaseous products and subsequent transport of the products away from the surface. Under quiescent, atmospheric pressure conditions, the transport of reactants and products through the boundary layer is governed by molecular diffusion. In the case of graphite particles, the mass diffusion rate of the products and reactants depends on the particle size, while the adsorption-desorption rates are strongly coupled to the surface temperature [17].

On char particles combustion, ignition, flame spread and extinction, many works by Annamalai and Durbetaki were released in the period 1974-1979. In particular, [2] deals with an observed phenomenon which is a maximum erosion rate at a particular temperature.

Unlike the combustion of liquid droplets where the rate governing process is essentially diffusion, for the case of small particles (less than about 200  $\mu\text{m}$ ) the rate controlling process, to a significant level, is the chemical kinetics. However, the peak burning rate is sandwiched between the limiting diffusion rates of CO and CO<sub>2</sub> production at the surface [2].

The authors describe the combustion process as a coupled effect of both heterogeneous reaction at the particle's surface (where carbon is

oxidised to CO) and a homogeneous gas phase reaction (where CO oxidation produces CO<sub>2</sub>). A relatively fast heterogeneous reaction followed by a slow gas phase oxidation can lead to a peak burning rate. Two oxidation regimes exist, one at the surface where the carbon oxidises to CO and one in the gas phase where the CO oxidises the CO<sub>2</sub>. Oxygen diffuses to both oxidation zones. Carbon dioxide from the gaseous oxidation regime diffuses both towards the solid surface and away into the oxidising atmosphere. An assumption have been done by which all surface reactions including the reduction of solid carbon produce only CO at high temperatures.

Expressions for reaction kinetics are reported, with a set of differential equations for species and energy transport. At the particle surface, due to oxidation reaction:  $C(s) + 1/2O_2 \rightarrow CO$ ,

$$(\dot{\omega}_{CO})_1 = A_{w,1}(1 + \nu_1) \exp(-E_{w,1}/RT_w)C_O \quad (2.99)$$

and due to reduction:  $C(s) + CO_2 \rightarrow 2CO$ ,

$$(\dot{\omega}_{CO})_2 = A_{w,2}(1 + \nu_2) \exp(-E_{w,2}/RT_w)C_{CO_2} \quad (2.100)$$

In the gas phase:

$$\dot{\omega}_{CO} = A_g \exp\left(-\frac{E_g}{R}\right) C_{CO}^{n_{CO}} C_O^{n_O} C_{H_2O}^{n_{H_2O}} \quad (2.101)$$

As a method of solution they use a modified initial value method, with Adams-Moulton integration formula [2]. The values given for reaction kinetics parameters are valid for the combustion of brown coal or coal chars, but it is not clear if they would be useful even for graphite oxidation.

A second work by Annamalai [1] focused on ignition of coal particles in normal operation regimes of coal fired power plants. More specifically, the study centres on the critical conditions of oxygen concentrations, temperatures and particle sizes for which particles cannot be ignited. Very small particles unable to make up the heat loss, even take external heat input (from larger particles) to equilibrate with the ambient thermal condition. Sometimes the required temperature for ignition of small particles may be so high that raising the furnace temperature for ignition may melt the ash to form a slag around the particle. The smaller particles, on the other hand, exhibit rapid heating and hence less time to attain the furnace temperature.

Extinction limits are studied in that work and some expressions are given for the threshold temperature and the lean limit which can be reached by supplying a large number of smaller sized particles or by a smaller number of large sized particles.

According to the authors [1], at the time of ignition, the heat generation rate is equal to heat loss rate and rate of change of generation with temperature is equal to the rate of change of heat loss

Coal No.	Coal Type	$Q_h$ J/g	$E_h$ KJ/mole	$A_{w,h}$ <sup>†</sup> g cm/mole s	$(D_{O_2})^a$	$\bar{\nu}_s$	Reference
1	Bituminous	20842	124.0	$61.0 \times 10^6$	380.0	1.72	[25]
2	Lignite	10468	83.7	$9.2 \times 10^6$	85.0	.885	[25]
3	Anthracite	25164	140.2	$76 \times 10^6$	418.0	1.885	[25]
4	Brown	9492 <sup>a</sup>	56.7	$3.2 \times 10^6$	43.0	1.333	[14]
5	Petroleum Coke	9492 <sup>a</sup>	76.2	$2.3 \times 10^6$	23.0	1.333	[8]
6	Anthracite Char	9492 <sup>a</sup>	69.9	$1.2 \times 10^6$	13.0	1.333	[8]
7	Bituminous Char	9492 <sup>a</sup>	67.0	$1.0 \times 10^6$	11.0	1.333	[8]
8	Brown Coal Char	9492 <sup>a</sup>	67.8	$1.1 \times 10^6$	12.6	1.333	[26]

<sup>a</sup> assumed that CO is the only product of oxidation.  
<sup>†</sup> The kinetic schemes for heterogeneous oxidations differ as far as the dependence on oxygen concentration is concerned. The schemes were brought to the following format:  

$$\dot{m}^* = A_{w,h} \frac{P}{RT_w} \exp\left[-\frac{E_{w,h}}{RT_w}\right] Y_{O_2,w}$$
 Then the pre-exponent factors  $A_{w,h}$  were computed.

Figure 2.13: Chemical kinetics data for heterogeneous oxidation of some coals [1].

with temperature. So, at critical ignition conditions there is equilibrium between heat generation and heat loss. That is valid for non-gasifying fuel; for partially gasifying solid fuels ignitions occurs in the gas phase. Formulations are given for gas-phase and heterogeneous ignition. For the last one, due to stoichiometry, oxygen flux consumed by coal oxidation

$$\dot{\omega}_O = \bar{\nu}_s A_{w,h} \frac{P}{RT} \exp\left(-\frac{E_{w,h}}{R_0 T_w}\right) Y_{O_2,w} \tag{2.102}$$

Regarding the model constants for the chemical reaction, different kinetic schemes are gathered for various sorts of solid fuels, from lignite to anthracite char (Figure 2.13).

Following with the ignition and extinction of solid char particles, Phuoc and Annamalai [90] used a very simple model for burning of carbon. They considered a unique reaction ( $C + O_2 = CO_2$ ), and the rate  $\dot{r}_c$  (kg of carbon/m<sup>2</sup>·s) was expressed in terms of an Arrhenius equation:

$$\dot{\omega}_c = \rho_{g,s} Y_{O_2,s} A \exp(-E/RT_s) \tag{2.103}$$

where  $A = 3020.75$  (m/s) is the frequency factor;  $E = 100.9$  (MJ/kmol) is the activation energy;  $\rho_{g,s}$  is the gas density at the particle surface;  $R$  is the gas constant; and  $T_s$  is the particle temperature.

Shortly after, in 1980, Vatikiotis [126] addressed the problem of a porous graphite fibre plate subject to combustion. In [126], a transient one-dimensional model is converted into a set of mass and heat transfer equations on the graphite and air, which are solved by a Galerkin formulation of the finite element method and a number of computer analysis results are presented. Regarding the reaction scheme, a global, idealised treatment of the reaction is taken, with the one-step reaction:  $C + O_2 \rightarrow CO_2$  (although they recognise the actual reaction is more complex, yielding various concentrations of carbon dioxide and carbon monoxide, depending on temperature).

As specified in [126], a relation derived from a previous work by Parker and Hottel in 1936 was used to predict the combustion rate of graphite fibres,  $\dot{\omega}$  ( $\frac{\text{lbm}}{\text{ft}^3 \cdot \text{hr}}$ ):

$$\dot{\omega} = 4.014 \times 10^7 R_{O_2} T_g^{1/2} S_v [O_2]^n \exp\left(-\frac{39.883}{T_g}\right) \quad (2.104)$$

where  $R_{O_2}$  is the gas constant for  $O_2$  and  $[O_2]$  is the oxygen concentration. The combustion is characterised as an  $n$  order reaction, where  $n$  is in the range  $1/3$  to  $2/3$  (they chose  $n = 1/2$  for their analysis).

The previous expression by Parker and Hottel is a function of oxygen partial pressure and is independent of the graphite shape:

$$\dot{\omega} = 9.55 \times 10^6 \frac{P_{O_2}}{T_g^{1/2}} \exp\left(-\frac{44000}{RT_g}\right) \quad (2.105)$$

in units ( $\frac{\text{gm}}{\text{cm}^2 \cdot \text{sec}}$ ). Vatikiotis transformed this last formula with an expression of  $P_{O_2}$  as a function of  $T_g$  for standard air, and also by introducing the surface-volume ratio of the fibres ( $S_v$ ) and converting into imperial units system.

Although forgotten by most authors who seek detailed models, it is possible to find some simple burning models in the early literature. The work by Libby and Blake [70] focuses on the dynamic behaviour of single carbon particles in a hot oxidising ambient. Both the direct oxidation of carbon via the reaction  $C + \frac{1}{2}O_2$  (identified as R1) and the indirect oxidation via the reaction  $C + CO_2$  (as R2) are taken into account, and both are found to play significant roles in the dynamic behaviour of carbon particles. With the assumptions that these reactions are first order and are represented by surface reaction rates, ascribed to the instantaneous conditions at the surface of the particle, they write the rates of carbon loss as [70]:

$$\dot{\omega}_1 = \frac{K_1 p W_c}{W_{O_2}} Y_{O_2, w} \exp(-T_{a1}/T_p) \quad (2.106)$$

$$\dot{\omega}_2 = \frac{K_2 p W_c}{W_{CO_2}} Y_{CO_2, w} \exp(-T_{a2}/T_p) \quad (2.107)$$

where the reaction constants are defined as:  $K_1 = 8710 \text{ g}/(\text{cm}^2 \cdot \text{s} \cdot \text{atm})$ ,  $K_2 = 247 \text{ g}/(\text{cm}^2 \cdot \text{s} \cdot \text{atm})$ ,  $T_{a1} = 18000 \text{ K}$ ,  $T_{a2} = 21060 \text{ K}$ . Units are such as to yield  $\dot{\omega}_i$  values in units of mass flux of carbon ( $\text{g}/\text{cm}^2 \cdot \text{s}$ ).

In the nuclear field indeed, some publications on graphite combustion are reported. Nuclear graphite has been widely used as a moderating material, a structural material and a reflector material of nuclear reactors. The old graphite moderated reactors have been shut down

and thus the decommissioning of an old graphite reactor generates a huge amount of radioactive graphite waste. Also some contributions are related to graphite from fuel reprocessing of HTGR nuclear power plants. Xien and Xuejun [135] studied graphite combustion as a way to separate those carbon particles from the heavy metal core in the thorium-uranium fuel cycle. They discussed the effects of temperature and oxygen concentration on the specific combustion rate of the graphite and presented a combustion kinetics model.

According to their hypothesis, the combustion process would be limited by both the transport of oxygen in the external boundary layer and the oxidation reaction kinetics. On the approach they present, the oxygen mass transfer rate from the bulk gas flow to the graphite surface is:  $R_1 = h(C_{O_2} - C_{O_2}^s)$ , and the reaction rate at the graphite surface is:  $R_2 = kC_{O_2}^s$  (note that  $C_{O_2}$  and  $C_{O_2}^s$  are the oxygen concentrations in the bulk and at the surface, respectively). To calculate the mass transfer coefficient,  $h$ , they used the modified Ranz-Marshall correlation:

$$\frac{hr_t}{D} = 1 + 0.3S_c^{1/3}Re_0^{1/2} \left( \frac{r_t}{r_0} \right)^{1/2}, \quad (2.108)$$

where  $D$  is the oxygen diffusivity,  $S_c = \mu/(\rho D)$  and  $Re_0 = 2r_0u\rho/\mu$ , and  $u$  is the gas flow rate,  $r_0$  the initial radius of graphite particles,  $\mu$  is the initial viscosity, and  $\rho$  is the density.

The enthalpy of reaction is considered to be constant,  $\Delta H(18^\circ C) = 393.6$  kJ. A polynomial fitting, of a set of 14 experimental measurements on  $CO_2$  concentration, gives a relation for the combustion rate as a function of time.

$$\frac{dm}{dt} = 0.548 - 5.850 \cdot 10^{-4}t - 4.747 \cdot 10^{-7}t^2 + 4.86 \cdot 10^{-10}t^3 \quad (2.109)$$

The kinetic constant computed from the last relation is  $k = 3.082$  cm/s, for  $r_0 = 3$  cm (pretty big particles),  $T = 800$  °C,  $C_{O_2} = 4.45 \cdot 10^{-3}$  mol/l and  $u = 50$  cm/s, which we could affirm they are quite special. Also they state the activation energy for that sort of graphite particles is 250.9 kJ/mol.

As a conclusion of the study [135], in an effort to provide an expression as a function of temperature, which fits with an Arrhenius equation  $\dot{\omega} = k[O_2]_s$ , a kinetic constant  $k$  is presented ( in cm/s):

$$k = 4.382 \times 10^{12} \exp(-3.018 \times 10^4/T) \quad (2.110)$$

In the same field, Yang et al. [136] reported a study based on their research on the combustion kinetics of nuclear graphite waste, using a non-isothermal thermogravimetric analysis (TGA). They tackled the task of modelling the combustion kinetics of graphite by an Arrhenius equation which would take into account the oxygen partial pressure and temperature. The reaction rate was thus described as:

$$\dot{r} = k_0 (P_{O_2})^n \exp\left(-\frac{E}{RT}\right) f(\dot{r}), \quad (2.111)$$

where  $X$  is the conversion of graphite,  $P_{O_2}$  is the partial pressure of oxygen and  $k_0$  and  $n$  are model constants. The function  $f(\hat{r})$ , according to the authors, represents the influence of the conversion on the conversion rate [136]. The constants of the model and the function of graphite conversion were obtained from the analysis of experimental TGA data. The process was repeated for different  $O_2$  % conditions. The averaged activation energy was determined to be 166.6 kJ/mol. This value is a little smaller than the reported activation energies of IG-110 graphite, which are in the range of 187.9-218 kJ/mol. That difference could be explained by the fact that Yang et al. (2006) used graphite powders ranging in size from 47-106  $\mu\text{m}$ , while IG-110 graphite samples used by previous investigators, which were larger than 1 cm in diameter.

A manageable combustion model is that reported by O'Brien et al. [84], which is in fact recommended by ITER Project to safety analysis purposes [95]. This consists of two global equations for C oxidation by oxygen and water vapour, respectively: (i)  $C + O_2 \rightarrow CO_2 - 390$  kJ/mol, and (ii)  $C + H_2O \rightarrow CO + H_2 + 131$  kJ/mol.

The reaction for graphite oxidation in air assumes that the CO combustion in the boundary layer on the surface of the material is always possible and immediate [95]. Global kinetics for this reaction gives the following molar reaction rate for graphite oxidation,  $\hat{r}_{C,R8}$  ( $\frac{\text{mol}}{\text{m}^2 \cdot \text{s}}$ ):

$$\hat{r}_{C,i} = \begin{cases} -20.6 \exp\left(-\frac{5710}{T_p}\right) \left(\frac{P}{8.5 \cdot 10^4}\right), & \text{if } T_p < 1273\text{K} \\ -1.3 \exp\left(-\frac{2260}{T_p}\right) \left(\frac{P}{8.5 \cdot 10^4}\right), & \text{if } T_p \geq 1273\text{K} \end{cases} \quad (2.112)$$

As  $\hat{r}_{C,i}$  is given by unit surface, it might be converted into moles by unit volume, taking into account the total reaction surface. And, then, a mass reaction rate for graphite-dust per unit volume is obtained,  $\dot{\omega}_{C,R8}$  ( $\frac{\text{kg}_C}{\text{m}^3 \cdot \text{s}}$ ):

$$\dot{\omega}_{C,i} = \hat{r}_{C,i} M_C \frac{6\sigma}{d_p \rho_C} \quad (2.113)$$

where  $M_C$  denotes molar mass of C and  $\rho_C$  is graphite density. Regarding the carbon oxidation by water vapour, according to [84], the molar rate of  $H_2$  generated by unit surface can be obtained as:

$$\hat{r}_{H_2,ii} = \begin{cases} 1.6 \cdot 10^{11} \exp\left(-\frac{35760}{T_p}\right) \left(\frac{P}{8.5 \cdot 10^4}\right), & \text{if } T_p < 1460\text{K} \\ 9.7 \cdot 10^3 \exp\left(-\frac{11360}{T_p}\right) \left(\frac{P}{8.5 \cdot 10^4}\right), & \text{if } T_p \geq 1460\text{K} \end{cases} \quad (2.114)$$

in units ( $\frac{\text{mol}_{H_2}}{\text{m}^2 \cdot \text{s}}$ ). Then, from the value obtained for  $\hat{r}_{H_2,ii}$ , the mass rate of C oxidized per unit volume can be calculated as:

$$\dot{\omega}_{C,ii} = -\hat{r}_{H_2,ii} M_C \frac{6\sigma}{d_p \rho_p} \quad (2.115)$$

Table 1: Elementary surface reaction mechanism [3], where specific rate constants in the form of  $k_j = A_j T^{\alpha_j} \exp(-E_j/RT)$ 

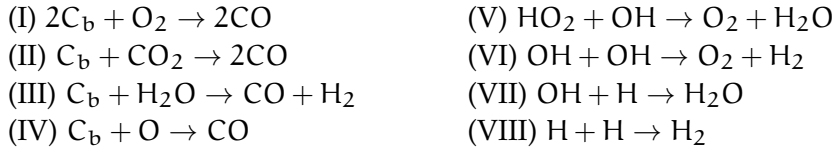
$j$	Reaction	$A_j$	$\alpha_j$	$E_j$
1	$2C_f + O_2 \rightarrow 2C'(O)$	$2.3 \times 10^{16}$	0	15000
2	$C_f + CO_2 \rightarrow C'(O) + CO$	$4.8 \times 10^9$	0	30000
3	$C_f + H_2O \rightarrow C'(O) + H_2$	$6.2 \times 10^8$	0	25000
4	$C'(O) \rightarrow C(O)$	$5.0 \times 10^{12}$	0	70000
5	$C(O) + C_b \rightarrow CO + C_f$	$2.0 \times 10^{11}$	0	60000
6	$C'(O) + C_b \rightarrow CO + C_f$	$2.0 \times 10^7$	0	40000
7	$2C'(O) + C_b \rightarrow CO_2 + 2C_f$	$4.0 \times 10^{13}$	0	35000
8	$C_f + O \rightarrow C'(O)$	$2.0 \times 10^9$	0	1000
9	$C_f + H \rightarrow C'(H)$	$2.0 \times 10^8$	0	1000
10	$C_f + OH \rightarrow C'(OH)$	$2.0 \times 10^8$	0	1000
11	$C_f + HO_2 \rightarrow C'(HO_2)$	$2.0 \times 10^8$	0	1000
12	$C'(H) + H \rightarrow H_2 + C_f$	$2.0 \times 10^9$	0	1000
13	$C'(H) + OH \rightarrow H_2O + C_f$	$2.0 \times 10^9$	0	1000
14	$C'(OH) + H \rightarrow H_2O + C_f$	$2.0 \times 10^9$	0	1000
15	$C'(OH) + OH \rightarrow H_2 + O_2 + C_f$	$2.0 \times 10^9$	0	1000
16	$C'(HO_2) + H \rightarrow H_2 + O_2 + C_f$	$2.0 \times 10^9$	0	1000
17	$C'(HO_2) + OH \rightarrow H_2O + O_2 + C_f$	$2.0 \times 10^9$	0	1000
18	$C'(OH) + C_f \rightarrow C'(O) + C'(H)$	$1.0 \times 10^{14}$	0	20000

Units: mole, cubic centimeters, seconds, Kelvin and calories per mole

Figure 2.14: Elementary reaction rates from [18].

in units  $\left(\frac{\text{kg}_C}{\text{m}^3 \cdot \text{s}}\right)$ .

Another research group in Virginia (USA) has introduced a number of specific contributions on graphite particles combustion, but they usually opt for more detailed chemical models. Chelliah and Miller [18] deal directly with graphite particles combustion in zero-gravity conditions. An elementary surface reaction model is reported (18 reactions) and also a reduced reaction model (8 steps) which is obtained from the elementary one by introducing the steady-state approximation for some species:



The molar rates of the semi-global reactions are computed from specific rate constants of the elementary model (Figure 2.14):

$$\begin{aligned}
 \omega_I &= \omega_1, & \omega_{VI} &= \omega_{15}, \\
 \omega_{II} &= \omega_2 - \omega_7, & \omega_{VII} &= \omega_9 + \omega_{10} - \omega_{15} - \\
 \omega_{III} &= \omega_3 + \omega_{18}, & \omega_{12} - \omega_{16} + \omega_{18}, \\
 \omega_{IV} &= \omega_8, & \\
 \omega_V &= \omega_{11}, & \omega_{VIII} &= \omega_{12} + \omega_{16} - \omega_{18}.
 \end{aligned}$$

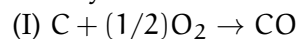
A special interest is shown to influence of particle's porosity into chemical kinetics. The model presented by Kassebaum and Chelliah [54] is basically focused on porous particles of carbon. The goal of that work is to decouple physical effect of porosity from chemical kinetics of the heterogeneous reaction. Their formulation assumes steady, spherically symmetric burning of an isolated porous carbon particle in a quiescent oxidising environment. The porosity is described as a function of the distance from the centre of the spheri-

cally symmetric particle, from which one can calculate the number of pores and the porous area. Regarding the reaction mechanisms, which might be more of interest for our study, the gas-phase reaction mechanism of CO oxidation is the detailed kinetics proposed by Yetter et al. [137]. Also semi-global rate constants by Makino et al. (see [17]) for porous carbon are used to obtain an initial solution. With that approximate solution for the gas phase, a semi-global surface reaction mechanism by Bradley et al. (see [17]) for non-porous carbon was used to describe the heterogeneous reaction rates. The way these reaction models are applied to solve combustion could be of interest, mainly when dealing the problem of porosity, but no values for kinetic constants are given on this paper. Some years before, Kasimov and Chelliah [53] claimed to have made a similar study for graphite particles combustion, but in that case no information about chemical mechanisms neither implementation is found.

The porous and non-porous reaction models by Makino and Bradley, respectively, are described in detail in [17]. Both mechanisms comprise a set of 5 reactions and 9 species. Intermediate, dissociated species are considered, as the carbon reaction with O-atoms has the highest reaction probability, an order of magnitude greater than that with O<sub>2</sub>. Porosity exerts a big influence: Two-orders of magnitude difference in C burning rates were found between non-porous and porous models. This two orders of difference was estimated to be comparable to the ratio of total surface area (external and internal) of porous graphite to that of nonporous graphite employed in the experiments. In addition, Chelliah [17] states that depending on the surface reaction scheme employed, the numerical integrations of the steady governing equations have identified a *critical* particle size, or diameter, below which strong burning conditions do not exist. This is significant for applications with small particles. As shown in Figure 2.15, under 380 μm the non-porous model allows no reaction for C burning, while reaction rate of the porous model increases for smaller diameters.

Another study by Delisle et al. [28], co-worker with Chelliah, focused on graphite combustion in oxygen enriched atmospheres, highlighting how tough is to obtain self-sustained oxidation under microgravity conditions, due to heat losses. The experimental results indicate that self-sustained oxidation is not possible with an oxygen mole fraction below 55%.

In an effort to find simple reaction schemes, Sami et al. [106], co-worker with Annamalai, within a study on co-firing of coal with biomass fuels, presented a skeletal model of char combustion. They assumed Oxygen transfer to carbon/char can occur via O<sub>2</sub>, CO<sub>2</sub> and/or H<sub>2</sub>O. The heterogeneous combustion of carbon/char occurs primarily via one or more of the following reactions:



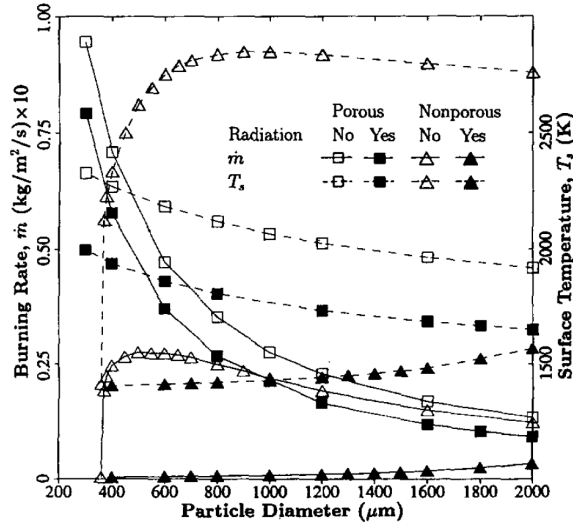


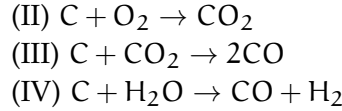
Figure 2.15: Variation of burning rates and surface temperatures with particle size (source [17]).

Step	Reaction	$i$	$A_i$	$n_i$	$E_i$	$\dot{s}_i$
NP1	$C_s + OH \rightarrow CO + H$	1	$3.61 \times 10^2$	-0.5	0.0	$\dot{s}_1 = k_1 P_{OH}$
NP2	$C_s + O \rightarrow CO$	2	$6.65 \times 10^2$	-0.5	0.0	$\dot{s}_2 = k_2 P_O$
NP3	$C_s + H_2O \rightarrow CO + H_2$	3	$4.8 \times 10^5$	0.0	68800	$\dot{s}_3 = k_3 P_{H_2O}^{0.5}$
NP4	$C_s + CO_2 \rightarrow 2CO$	4	$9.0 \times 10^3$	0.0	68100	$\dot{s}_4 = k_4 P_{CO_2}^{0.5}$
NP5	$C_s + 1/2 O_2 \rightarrow CO$	4	$2.4 \times 10^3$	0.0	30000	$\dot{s}_5 = \left[ \frac{k_5 P_{O_2} Y}{1 + k_6 P_{O_2}} \right]$
		6	$2.13 \times 10^1$	0.0	-4100	+ $k_7 P_{O_2} (1 - Y)$
		7	$5.35 \times 10^{-1}$	0.0	15200	where
		8	$1.81 \times 10^7$	0.0	97000	$Y = \left[ 1 + \frac{k_8}{k_7 P_{O_2}} \right]$

Table 2.2: Non-porous graphite reaction mechanism (Chelliah [17]), with the rate  $\dot{s}_i$  expressed in terms of  $k_i = A_i T^{n_i} \exp(-E_i/RT)$  and partial pressure  $P_i$ .

Step	Reaction	$B_i$	$\alpha_i$	$ED_i$
P1	$C_s + OH \rightarrow CO + H$	1.65	0.5	0
P2	$C_s + O \rightarrow CO$	3.41	0.5	0
P3	$C_s + H_2O \rightarrow CO + H_2$	$6.0 \times 10^7$	0.0	64300
P4	$C_s + CO_2 \rightarrow 2CO$	$6.0 \times 10^7$	0.0	64300
P5	$2C_s + O_2 \rightarrow 2CO$	$2.2 \times 10^6$	0.0	43000

Table 2.3: Porous graphite reaction mechanism [17], for rate constants  $\dot{s}_i = W_i B_i c_i T^{\alpha_i} \exp(-E_i/RT)$ . Units of  $\dot{s}_i$ ,  $BT^{\alpha_i}$ ,  $E_i$  and  $T$  are in  $kg/m^2/s$ ,  $m/s$ ,  $cal/mol$  and  $K$ , respectively.



Assuming first-order reaction for scheme (I), the oxygen consumption rate is given as,

$$\dot{\omega}_{\text{O}_2} \approx \pi d_p^2 B_{\text{O}_2} \exp\left(-\frac{E}{R_u T_p}\right) \rho_\infty Y_{\text{O}_2,w} \quad (2.116)$$

Similar expressions can be written using the other reactions. The dominant oxygen transfer mechanism at high temperatures is via reaction (I) with  $E/R_u \approx 26200$  K and  $B_{\text{O}_2} = 2.3 \times 10^7$  m/s. Reaction (II) has an activation energy of  $E/R_u = 20000$  K and  $B_{\text{O}_2} = 1.6 \times 10^5$  m/s. Reaction (III), the Boudouard reduction reaction, proceeds with an  $E/R_u$  of about 40000 K. In general, char reaction with steam has been found to be 50 times faster than char reaction with  $\text{CO}_2$  for temperatures up to 2073 K (Montana Rosebud char, 75-100 mm, 1 atm) [106]. While, at lower temperatures (1150 K), reactions (III) and (IV) proceed at approximately the same rate and that the reaction (I) proceeds 104-105 times faster than reaction (III) between 1100 and 1200 K. Reaction (II) is significant at low temperatures (e.g. ignition conditions) while reaction (I) is dominant under typical combustion conditions.

According to thermal explosion theory, ignition occurs if the rate of heat release due to chemical reaction is higher than the rate of heat loss due to convection, radiation, etc., and if the process results in runaway conditions. For temperatures below the heterogeneous ignition temperature  $T_{p,I}$ , ignition of the coal particle will not occur. An implicit correlation for  $T_{p,I}$  is given in [106]:

$$T_{p,I} = \frac{(E/R_u)}{\ln \left[ \frac{B_{\text{O}_2} d_p Y_{\text{O}_2,\infty} h_c E}{Sh D_w \nu_{\text{O}_2} R_u T_{p,I}^2 C_p} \right]} \quad (2.117)$$

#### 2.4.7 Tungsten combustion laws

Tungsten (W) is a very heavy metal, having a density of about 20,000 kg/m<sup>3</sup> at ambient temperatures. As previously stated, the computational analysis of problems involving the mobilisation or combustion of tungsten particles has proven to be a complex issue.

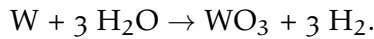
In this section we will pay attention to the oxidation reactions of tungsten with  $\text{O}_2$ , which yields  $\text{WO}_3$  as product, and with steam ( $\text{H}_2\text{O}$ ), which gives  $\text{H}_2$  as product as well.

So, the reactions we will consider are those referred above, in particular:

- Air [reaction (W-1)]:  

$$\text{W} + 3/2 \text{O}_2 \rightarrow \text{WO}_3,$$

- Water vapour [reaction (W-2)]:



As mentioned, W-steam reactions pose some potential for producing  $H_2$ , but typically, production of  $H_2$  from W-steam reactions is less important than Be-steam or C-steam because the hydrogen production per kilogram reacted is 5-7 times lower and the buildup of tungsten in ITER vacuum chamber dust is limited by confinement concerns [120].

We should note that, by considering the previous reactions, we are neglecting the presence of other tungsten oxides different from  $WO_3$ . At the surface of the particle this is the most likely to occur. In the case of reaction (W-1), other oxides could be  $WO$  and  $WO_2$ . The oxidation begins approximately at temperatures greater than  $400^\circ\text{C}$  and, in general, there is a sublimation of oxides above  $900^\circ\text{C}$ . In reaction (W-2), other likely products are  $WO_2$  and  $WO_2(OH)_2$ , and the oxidation begins approximately at temperatures over  $600^\circ\text{C}$  [105]. According to this reference, at “nano-scale”, with diameters lower than 150 nm, oxidation with  $O_2$  can be seen at temperatures as low as  $300^\circ\text{C}$ , however it is pointed out that the most rapid oxidation is found at temperatures between  $450$  and  $600^\circ\text{C}$  and may be found to be a function of the particle diameter below certain value. In our study we will assume that the trioxide remains solid after the reaction.

This approach is somewhat conservative taking into account that at above of  $1250^\circ\text{C}$  no solid oxides are formed and the addition of water accelerates the vaporisation process.

Tungsten combustion was experimentally studied by several researchers few decades ago. Among these works we can stand [74, 49], where they studied cylindrical rods of tungsten of 4 and 8 mm and burned them in an argon and oxygen stream. In general, they pointed out that at “the temperatures at which they made their studies” the specimen surfaces covered by a oxide crystal which complicates the diffusion of oxygen and melt when the melting point of tungsten trioxide is reached ( $T_{\text{melting}} = 1740 \text{ K}$ ). This facilitates the combustion. Unlike other metals, tungsten burns in the solid state as its melting temperature is  $T_{\text{melting}} = 3650 \text{ K}$ .

In Figure 2.16, we can check that there is an increase of the ignition temperature with the rod diameter, this is due to the lower oxygen diffusion in the oxide coating for small-diameter rods. The authors stated that with reduced rods they would expect that the specimen did not burn even in pure oxygen [74].

In their work, they considered tungsten kinematic viscosity constant and equal to  $1.5 \text{ cm}^2/\text{s}$ . They provided an expression for the burned mass of metal as a function of Reynolds number which is difficult to implement in our code. Important works in this field are

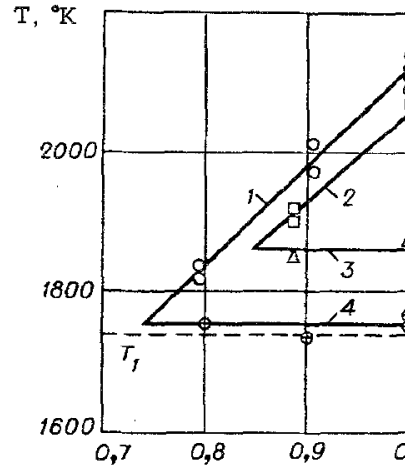


Figure 2.16: Combustion (1, 2) and ignition (3, 4) temperatures of tungsten as a function of the oxygen concentration in the flow.  $T_f$ : melting point of  $WO_3$ ; (1, 4):  $d_{rod} = 6$  mm; (2, 3):  $d_{rod} = 3$  mm. Source: [74].

those by Ong [50] or Bartlett at high temperatures [6] in the case of the oxidation with oxygen. Among the works that study the interaction of water steam with tungsten, we can mention [34, 3, 57]. Conversely, in the field of pyrotechnics the work by [49] stands out.

In the 90's, this subject received new interest due to use of tungsten as a structural material in nuclear fusion reactors [113, 114] and in proton accelerator components [124]. [113] made a review of the worked carried out in this field up to date. Some of the references studied in this paper have already been mentioned above. They experimentally studied the oxidation rate of a tungsten alloy in air for temperatures between  $700^\circ\text{C}$  and  $1300^\circ\text{C}$ , and oxygen partial pressures between 0.0013 and 20.8 atm. He only gave the so-called recession rate

$$\frac{dx}{dt} (\text{mm/s}) = 0.847e^{-12170/T} p_{O_2}^{1/2}, \quad (2.118)$$

where oxygen partial pressure is in atmospheres and  $T$  is in Kelvin. He also performed some experiments to study the reaction of  $W$  with steam. This correlated his data to obtain the rate of  $H_2$  produced during the reaction, so that,

$$\dot{v} = 49000e^{-15600/T} \quad (l \text{ H}_2/\text{m}^2 \cdot \text{s}). \quad (2.119)$$

to convert it into  $\text{kg H}_2/(\text{m}^2 \cdot \text{s})$  we should multiply by the density of  $H_2$  in the gas mixture,  $\rho_{H_2}$ . If  $p_{H_2}$  is the partial pressure of  $H_2$  in it,  $T_g$  is the temperature of the gas mixture, and  $R_{H_2}$  the  $H_2$  constant, we have

$$\dot{\omega} = \dot{v} \frac{p_{H_2}}{R_{H_2} T_g} \quad (2.120)$$

This was obtained for temperatures between 600 and 1200 °C, for a mixture of steam and argon with 50% and for a steam pressure of 0.42 atm (we understand this pressure as partial pressure).

This work was improved by the authors in [114]. In that occasion, they performed experiments to analyse the effect of temperature, pressure, and flow velocity in the combustion of tungsten. This resulted in the following more realistic expression for rate of hydrogen production

$$\dot{v}_{\text{H}_2,7} = 1.02 \times 10^5 p^{0.78} V^{0.56} e^{\left(-\frac{16720}{T}\right)} \quad (\text{l H}_2(\text{STP})/\text{m}^2 \cdot \text{s}) \quad (2.121)$$

where  $p$  is pressure in Pa, and  $V$  is the gas velocity (m/s). Standard conditions are at 1 atm (101325 Pa) and 293 K. This expression was obtained for temperatures between 500 and 1200 °C. In the experiments, a solid block of tungsten was oxidised inside a furnace by an air flow with certain speed  $V$  at pressure  $p$  and temperature  $T$ . For the application of this expression in our models,  $V$  must be taken as the relative velocity between gas and solid phase.

After calculating the rate of hydrogen, we should convert the volume at standard conditions into our conditions taking into account ideal gas law

$$\frac{pv}{T} = \frac{p' \cdot v'}{T'} \quad \rightarrow \quad v = \frac{T}{T'} \frac{p'}{p} v'. \quad (2.122)$$

Finally, to obtain the mass reaction rate for W-dust, oxidised according to reaction (W-2) is then  $\omega_{\dot{W},7} \left( \frac{\text{kgW}}{\text{m}^3 \text{s}} \right)$

$$\omega_{\dot{W},7} = -\frac{\dot{v}_{\text{H}_2,7}}{10^3} \frac{M_W P_6 \sigma}{R_u T d_p \rho_W} \quad (2.123)$$

where  $M_W$  and  $\rho_W$  are, respectively, the molar mass and density of tungsten.

Recently, Sabourin studied the reaction kinetics and mechanisms of tungsten oxidation [105]. We can find in his work a review of the existing literature on tungsten up to 2010. The motivation of this work is the implication of tungsten oxidation in the erosion of nozzle rockets.

In addition to the previous works, and in the context of ITER, we have also evaluated the expressions included in MELCOR for the calculation of the different production rates mentioned above. MELCOR is a software developed by the US Sandia National Laboratory which was adapted to analyse the sort of problem encountered in ITER safety analyses [80].

Thus, the expressions recommended in the report of the updates of the MELCOR code up to 2007, [79]) for the oxidation rate of tungsten in air is:

$$\dot{\omega}_{W-O_2} \left( \frac{\text{kg}}{\text{m}^2\text{s}} \right) = \begin{cases} p_M (1.62 \times 10^6 e^{-24000/T}) & \text{if } T < 973\text{K} \\ p_M (7.448e^{-12170/T}) & \text{if } T \geq 973\text{K} \end{cases} \quad (2.124)$$

where  $p_M$  is a scaling factor for oxygen pressure defined as

$$p_M = (p_{O_2}/p_o)^{0.78} \quad (2.125)$$

and where  $p_o = 0.181 \times 10^5$  Pa.

The expression for the oxidation rate of tungsten in steam is

$$\dot{\omega}_{W-H_2O} \left( \frac{\text{kg}}{\text{m}^2\text{s}} \right) = p_M \left( 41238e^{-33106/RT} \right) \quad T < 1470\text{K} \quad (2.126)$$

where  $p_M$  is a scaling factor for steam pressure defined as

$$p_M = (p_{H_2O}/p_o)^{0.78} \quad (2.127)$$

and where  $p_o = 0.84 \times 10^5$  Pa. The author points out that these equations were taken from a previous ITER safety report: "Safety Analysis Data List," (G81-RI10-03-08-08W0.1, Version: 4.0.3 SADL), September 26, (2003).

Later in 2008, Topilski [120] suggested other expressions for the estimation of the tungsten reaction rates, in the frame of a Safety Report of ITER project. Those expressions, discussed below, are slightly different from those previously introduced.

For W oxidation in air (W-1), the following rate for the production of  $WO_3$   $\dot{r}_{WO_3,6}$   $\left( \frac{\text{mol}_{WO_3}}{\text{m}^2\text{s}} \right)$  is suggested:

$$\dot{r}_{WO_3,6} = \begin{cases} p_M \left( 8.85 \times 10^6 e^{-\frac{24000}{T}} \right), & \text{if } T < 973, \\ p_M \left( 40.7e^{-\frac{12170}{T}} \right), & \text{if } T \geq 973, \end{cases} \quad (2.128)$$

where  $p_M$  is again a scaling factor for steam pressure defined as

$$p_M = (p_{O_2}/p_o)^{0.5}. \quad (2.129)$$

The value of  $p_o$  is not provided in [120]. We assume this is the same as in [79],  $p_o = 0.181 \times 10^5$  Pa. Indeed, the exponent is given, although it is different from that in Equation 2.124. The authors state the actual value of the exponent is 0.5.

Meanwhile, the reaction rate for W-dust per unit volume  $\dot{\omega}_{W,6}$ , in units  $\left( \frac{\text{kg}_W}{\text{m}^3\text{s}} \right)$ , can be calculated as follows:

$$\dot{\omega}_{W,6} = -\dot{r}_{WO_3,6} M_W \frac{6\sigma}{d_p \rho_W} \quad (2.130)$$

where  $M_W$  and  $\rho_W$  are, respectively, the molar mass and density of tungsten;  $\sigma$  is the particle concentration, and  $d_p$  the average particles diameter.

For the W reaction with steam, the expression proposed for the hydrogen generation,  $\dot{v}_{H_2}$  in units  $(\frac{1}{m^2s})$ , is calculates as:

$$\dot{v}_{H_2} = p_M \left( 41238 \times 10^{-33106/RT} \right) \quad T < 1470K \quad (2.131)$$

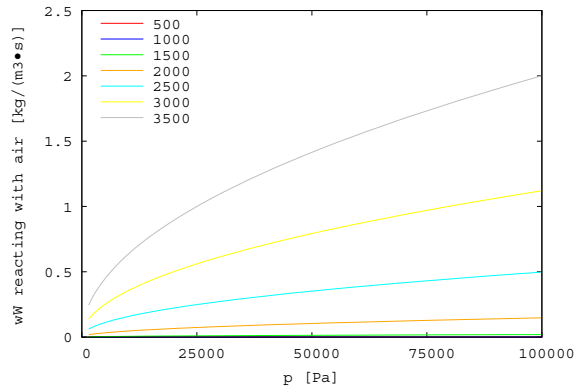
where  $p_M$  is a scaling factor for steam pressure defined as

$$p_M = (p_{H_2O}/p_o)^{0.78}. \quad (2.132)$$

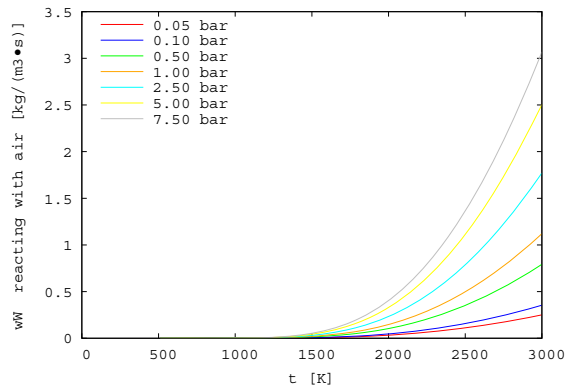
$p_o$ , it is not defined explicitly, considering the data in the reference we will assume  $p_o = 0.85 \times 10^5$  Pa. No interval of validity or application is given.

The heats of reaction have been taken from [120] as well. In particular, for the tungsten-air reaction (W-1), we have assumed that heat of reaction is -841 kJ/mol, and for the tungsten steam reaction (W-2) the heat of reaction has a value of -156 kJ/mol.

The reaction rates in Equations 2.128 and 2.131 have been studied at different pressures, varying temperature, and also at different fixed temperatures, varying pressure. The objective is to assess the influence of these variables on the global reaction rates and, in addition, to check if any of the reactions is dominant. In Figures 2.17 and 2.18, this influence can be observed. First, in Figure 2.17, we focus on reaction W-1: different values of temperature are fixes from 500 to 3500 K to evaluate the influence of pressure in the reaction rate; then, different pressures are fixed (from 0.05 to 7.5 bar) in order to see the influence of temperature. Later, in Figure 2.18, the same parametric study is addressed with reaction W-2.

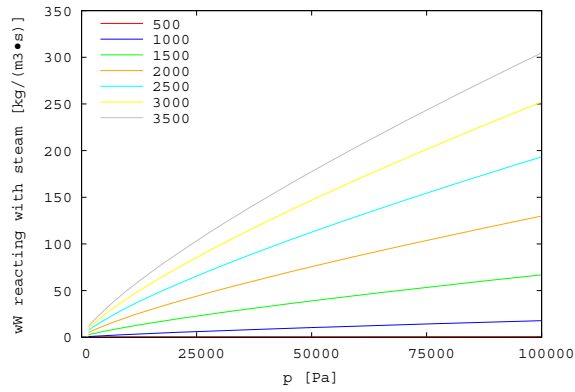


(a) Influence of pressure on the reaction rate.

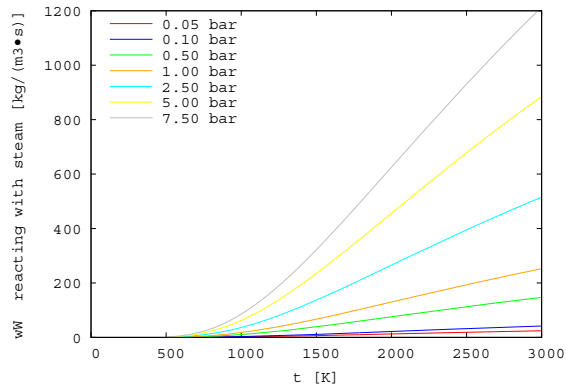


(b) Influence of temperature on the reaction rate.

Figure 2.17: Reaction rate of reaction W-1 as a function of pressure (a), and as a function of temperature (b): W oxidation with air.



(a) Influence of pressure on the reaction rate.



(b) Influence of temperature on the reaction rate.

Figure 2.18: Reaction rate of reaction W-2 as a function of pressure (a), and as a function of temperature (b): W oxidation with steam.



## PHYSICAL MODELS FOR REACTIVE TWO-PHASE MIXTURES

---

This work is devoted to the study of reactive high dilute mixtures of gases and particles. Thus, the model of reactive Euler equations for two-phase flows is considered and discussed. Notwithstanding, several concepts about this kind of models might be previously discussed, such as the hyperbolicity, because of its importance in numerical methods that will be explained in [Chapter 4](#). Also the Riemann problem is briefly introduced in [Section 3.1.1](#), as well as the structure of its solution, as this would be repeatedly referenced throughout the text.

Later, in [Section 3.4](#), physical models for different phenomena observed in the problem are exposed in detail (namely, chemical reaction, particle drag, heat exchange and gravity). Those are included in the model by means of source terms.

### 3.1 HYPERBOLIC SYSTEMS OF CONSERVATION EQUATIONS

Let us consider a system of conservation laws and its associated Cauchy problem, expressed in conservative form:

$$\begin{cases} \frac{\partial \mathbf{U}}{\partial t} + \frac{\partial \mathbf{F}(\mathbf{U})}{\partial x} = 0 \\ \mathbf{U}(x, t = 0) = \mathbf{U}_0(x) \end{cases} \quad (3.1)$$

with

$$\begin{aligned} \mathbf{U} : \mathfrak{X} \times \mathfrak{X}^+ &\rightarrow \Omega \in \mathfrak{R}^p \\ (x, t) &\mapsto \mathbf{U}(x, t) \end{aligned}$$

where  $\Omega$  is an open subset of  $\mathfrak{R}^p$  and  $\mathbf{F}$  is a smooth flux function so that:

$$\begin{aligned} \mathbf{F} : \Omega &\rightarrow \mathfrak{R}^p \\ \mathbf{U} &\mapsto \mathbf{F}(\mathbf{U}) \end{aligned}$$

If  $\mathbf{U}$  is a function  $C^1$ , the problem ([Equation 3.1](#)) can be written in *quasi-linear* form:

$$\begin{cases} \frac{\partial \mathbf{U}}{\partial t} + \mathbf{A}(\mathbf{U}) \frac{\partial \mathbf{U}}{\partial x} = 0 & (x, t) \in \mathfrak{X} \times \mathfrak{X}^+ \\ \mathbf{U}(x, t = 0) = \mathbf{U}_0(x) \end{cases} \quad (3.2)$$

with  $\mathbf{A}$  the Jacobian matrix:

$$\mathbf{A}(\mathbf{U}) = d\mathbf{F}(\mathbf{U}) = \frac{\partial \mathbf{F}(\mathbf{U})}{\partial \mathbf{U}} \quad (3.3)$$

The system is said to be **hyperbolic** if all eigenvalues  $\lambda^{(k)}$ ,  $k = 1, \dots, p$ , of the Jacobian matrix  $\mathbf{A}$  are real and  $\mathbf{A}$  is diagonalisable [122, 69]. Also, the system is **strictly hyperbolic** if all eigenvalues are different one from another, so they can be arranged as

$$\lambda^{(1)} < \lambda^{(2)} < \dots < \lambda^{(p-1)} < \lambda^{(p)}$$

In such case the Jacobian matrix is diagonalisable and

$$\mathbf{A}\mathbf{R} = \mathbf{R}\Lambda, \quad \mathbf{L}\mathbf{A} = \Lambda\mathbf{L} \quad (3.4)$$

where  $\Lambda$  is the diagonal matrix of the eigenvalues of  $\mathbf{A}$ :

$$\Lambda = \text{diag}(\lambda^{(1)}, \dots, \lambda^{(p)}) \quad (3.5)$$

$\mathbf{R}$  is the column matrix of the right eigenvectors of  $\mathbf{A}$ :

$$\mathbf{R} = [\mathbf{r}^{(1)}, \dots, \mathbf{r}^{(p)}] \quad (3.6)$$

Also, applying the properties of the diagonalisable matrix we can check that

$$|\mathbf{A}| = \mathbf{R}|\Lambda|\mathbf{L} \quad (3.7)$$

where

$$|\Lambda| = \text{diag}(|\lambda^{(1)}|, \dots, |\lambda^{(p)}|) \quad (3.8)$$

The matrix whose rows are the left eigenvectors of  $\mathbf{A}$ , can be defined as:

$$\mathbf{L} = \mathbf{R}^{-1} = [\mathbf{l}^{(1)}, \dots, \mathbf{l}^{(p)}]^T \quad (3.9)$$

If the system in Equation 3.1 is linear, i.e, if the matrix  $\mathbf{A}$  is constant, we can decompose the system in  $p$  independent equations by defining a vector of *characteristic variables* as:

$$\mathbf{G} = \mathbf{L}\mathbf{U} \quad (3.10)$$

When the problem is non-linear, we can decompose the system in  $p$  independent equations, if the solution is smooth, and is exact the differential form:

$$\delta\mathbf{G} = \mathbf{L} \cdot \delta\mathbf{U} \quad (3.11)$$

It is worth noting that, if the system of hyperbolic equations is non-linear, the eigenvalues and eigenvector depend on  $\mathbf{U}$  itself [122].

In any case, we can write the system in [Equation 3.1](#) in the *characteristic form*:

$$\begin{cases} \frac{\partial \mathbf{G}}{\partial t} + \Lambda(\mathbf{G}) \frac{\partial \mathbf{G}}{\partial x} = 0 \\ \mathbf{G}(x, t = 0) = \mathbf{G}_0(x) \end{cases} \quad (3.12)$$

Let us now write the system of the problem [3.1](#) in integral form. There are two reasons for considering the integral form of the conservation laws: (i) the derivation of the governing equations is based on physical conservation principles expressed as integral relations on control volumes, (ii) the integral formulation requires less smoothness of the solution, which paves the way to extending the class of admissible solutions, to include discontinuous solutions. By using the Green's theorem into [Equation 3.1](#), the integration of the conservation equations in a control volume  $V$  yields:

$$\oint [\mathbf{U} dx - \mathbf{F}(\mathbf{U}) dt] = 0 \quad (3.13)$$

with  $V$  compact in  $\mathfrak{R}^m \times \mathfrak{R}^+$ . We can particularise for the case of a 1D space control volume  $V = [x_L, x_R] \times [t_1, t_2]$  on the  $x - t$  plane. The integral form in one space dimension is:

$$\frac{d}{dt} \int_{x_L}^{x_R} \mathbf{U}(x, t) dx = \mathbf{F}(\mathbf{U}(x_L, t)) - \mathbf{F}(\mathbf{U}(x_R, t)) \quad (3.14)$$

Again, by integrating in time between  $t_1$  and  $t_2$ ,  $t_1 < t_2$ , we have:

$$\int_{x_L}^{x_R} \mathbf{U}(x, t_2) dx = \int_{x_L}^{x_R} \mathbf{U}(x, t_1) dx + \int_{t_1}^{t_2} \mathbf{F}(\mathbf{U}(x_L, t)) dx - \int_{t_1}^{t_2} \mathbf{F}(\mathbf{U}(x_R, t)) dx \quad (3.15)$$

Adopting a more mathematical approach, we can express the problem [\(3.1\)](#) in *weak form* [\[69\]](#):

$$\int_0^{+\infty} \int_{-\infty}^{+\infty} \left\{ \frac{\partial \phi}{\partial t} \mathbf{U} + \frac{\partial \phi}{\partial x} \mathbf{F}(\mathbf{U}) \right\} dx dt = - \int_{-\infty}^{+\infty} \phi(x, 0) \mathbf{U}_0(x) dx \quad (3.16)$$

The function  $\mathbf{U}(x, t)$  is said to be a *weak solution* or general solution [\[122\]](#) of the problem in [Equation 3.1](#) if,  $\forall \phi \in C_0^\infty(V)$  with  $V$  compact in  $\mathfrak{R} \times \mathfrak{R}^+$  [\[8\]](#). That means,  $\phi$  is a *test function* that is differentiable in  $V$  and it vanishes outside the bounded set. The integral expression in [Equation 3.14](#), [3.15](#) and [3.16](#) are valid for any system in conservative form, not only for Euler equations.

A weak solution is also a *classical solution* whenever it is differentiable. In general, weak solutions are piecewise  $C^1$  functions, which contain some discontinuities. However, not every discontinuity is admissible: the *Rankine-Hugoniot condition* must be satisfied. That is,

for a system of hyperbolic conservation laws (Equation 3.1) and a discontinuous solution with wave speed  $S_i$ , the jump must fulfil the condition:

$$\Delta \mathbf{F} = S_i \Delta \mathbf{U} \quad (3.17)$$

with  $\Delta \mathbf{U} \equiv \mathbf{U}_R - \mathbf{U}_L$ ,  $\Delta \mathbf{F} \equiv \mathbf{F}_R - \mathbf{F}_L$ ,  $\mathbf{F}_R = \mathbf{F}(\mathbf{U}_R)$ ,  $\mathbf{F}_L = \mathbf{F}(\mathbf{U}_L)$ . Variables  $\mathbf{U}_R$  and  $\mathbf{U}_L$  represent the respective states immediately to the left and right of the discontinuity.

### 3.1.1 Exact solution of the Riemann problem for a linear hyperbolic system

The Riemann problem is a Cauchy problem (Equation 3.1) where initial conditions are presented in a particular form:

$$\mathbf{U}_0(x) = \begin{cases} \mathbf{U}_L & \text{if } x < 0, \\ \mathbf{U}_R & \text{if } x \geq 0 \end{cases} \quad (3.18)$$

Let us now consider the Riemann problem for the hyperbolic, constant coefficient system in Equation 3.2. The system is considered linear as every coefficient in  $\mathbf{A}$  is constant, as well as its eigenvalues.

The system is also considered as strictly hyperbolic, as all the eigenvalues could be ordered in the following way:

$$\lambda^{(1)} < \lambda^{(2)} < \dots < \lambda^{(p-1)} < \lambda^{(p)}$$

The structure of the solution of the Riemann problem (3.18) in the  $x - t$  plane is depicted in Figure 3.1. It consists of  $p$  waves emanating from the origin, one for each  $\lambda^{(i)}$ . Each wave  $i$  carries a jump discontinuity in  $\mathbf{U}$  propagating with speed  $\lambda^{(i)}$ . Naturally, the solution to the left of the  $\lambda^{(1)}$ -wave is simply the initial data  $\mathbf{U}_L$  and to the right of the  $\lambda^{(p)}$ -wave is  $\mathbf{U}_R$ . The task at hand is to find the solution in the wedge between the  $\lambda^{(1)}$  and  $\lambda^{(p)}$  waves.

As the eigenvectors  $\mathbf{r}^{(1)}, \dots, \mathbf{r}^{(p)}$  are linearly independent, we can expand the data  $\mathbf{U}_L$ , constant left state, and  $\mathbf{U}_R$ , constant right state, as linear combinations of the set  $\mathbf{r}^{(1)}, \dots, \mathbf{r}^{(p)}$  [122], that is,

$$\mathbf{U}_L = \sum_{i=1}^p \alpha_i \mathbf{r}^{(i)}, \quad \mathbf{U}_R = \sum_{i=1}^p \beta_i \mathbf{r}^{(i)} \quad (3.19)$$

with constant coefficients  $\alpha_i$  and  $\beta_i$  for  $i = 1, \dots, p$ . In terms of the characteristic variables, we would get  $p$  scalar Riemann problems for the following partial derivative equations:

$$\frac{\partial G_i}{\partial t} + \lambda^{(i)} \frac{\partial G_i}{\partial x} = 0, \quad (3.20)$$

with initial data:

$$G_i^{(0)}(x) = \begin{cases} \alpha_i & \text{if } x < 0, \\ \beta_i & \text{if } x > 0, \end{cases} \quad (3.21)$$

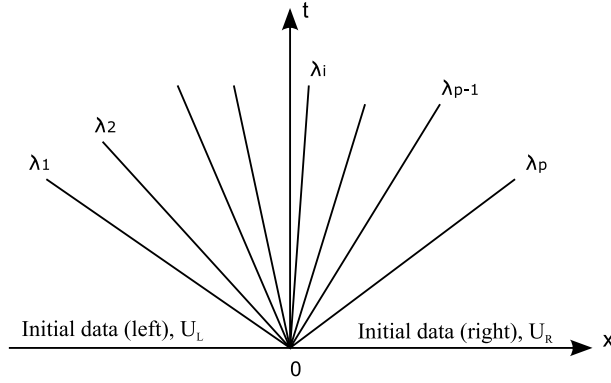


Figure 3.1: Structure of the solution of a Riemann problem for a general, linear, hyperbolic system with  $p$  equations and constant coefficients.

for  $i = 1, \dots, p$ .

From the resolution of the scalar Riemann problem (see [69, 122]), we know that each scalar solution is given by:

$$G_i(x, t) = G_i^{(0)}(x - \lambda^{(i)}t) = \begin{cases} \alpha_i & \text{if } x - \lambda^{(i)}t < 0, \\ \beta_i & \text{if } x - \lambda^{(i)}t > 0. \end{cases} \quad (3.22)$$

We can thus write the final solution in terms of the original variables as:

$$\mathbf{U}(x, t) = \sum_{i=I+1}^p \alpha_i \mathbf{r}^{(i)} + \sum_{i=1}^I \beta_i \mathbf{r}^{(i)}, \quad (3.23)$$

where the integer  $I = I(x, t)$  is the maximum value of the sub-index  $i$  for which  $x - \lambda^{(i)}t > 0$ .

### 3.1.2 Non-linearities and shock formation

In the previous case, when all coefficients in the Jacobian matrix  $\mathbf{A}$  are constant, every characteristic speed ( $\lambda^{(i)}$ ) is also constant and hence, *characteristic curves* are defined as straight lines in the plane  $(x, t)$ . In general, for a system of  $p$  equations, we have  $p$  different fields with characteristic speeds  $\lambda^{(1)}, \dots, \lambda^{(p)}$ . Then, the solution consists of the initial data  $\mathbf{U}_0(x)$  translated in the plane  $(x, t)$  without distortion (see Figure 3.2(a) where a draft is depicted on how characteristic curves might appear for a linear system). By contrast, in the non-linear case, the Jacobian matrix  $\mathbf{A}(\mathbf{U}) = \partial \mathbf{F}(\mathbf{U}) / \partial \mathbf{U}$  is a function of the solution itself, and so are the characteristic speeds. Distortions are therefore produced as a differentiating feature of non-linear problems (Figure 3.2(b)), provoked by characteristics travelling with different speeds. That leads to different compressive and expansive regions in the solution, according to the orientation of the respective

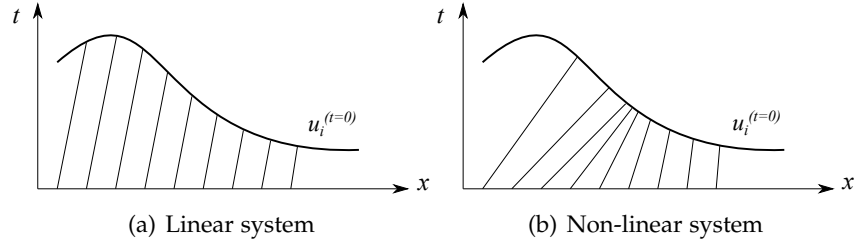


Figure 3.2: Characteristic curves for equation  $i$  of a linear (left) and non-linear system (right) of hyperbolic equations at the initial time.

characteristic curves. Expansive regions tend to make flatter profiles in the solution, whilst compressive regions will tend to get steeper and narrower as time evolves. The wave steepening mechanism will eventually produce folding over of the solution profile, with corresponding crossing of characteristics [122].

Let us give the following definitions:

- We call  $k$ -field of a hyperbolic system the part of the solution relative to the  $k$ -th eigenvalue.
- A  $k$ -field is *Genuinely non-linear* (GNL) if

$$\mathbf{r}^{(k)}(\mathbf{U}) \cdot \frac{d\lambda^{(k)}(\mathbf{U})}{d\mathbf{U}} \neq 0 \quad (3.24)$$

- A  $k$ -field is *Linearly degenerate* (LD) if

$$\mathbf{r}^{(k)}(\mathbf{U}) \cdot \frac{d\lambda^{(k)}(\mathbf{U})}{d\mathbf{U}} = 0 \quad (3.25)$$

Hereinafter, we limit our interest to the case where  $\mathbf{F}$  is a convex function of  $\mathbf{U}$ , i.e.

$$\frac{d\mathbf{F}(\mathbf{U})}{d\mathbf{U}} > 0 \quad (3.26)$$

Then, for a determined field  $i$  of the solution, the characteristic speeds  $\lambda^{(i)}(\mathbf{U})$  are a monotone function of  $\mathbf{U}$ . In that case, the hyperbolic system is said *convex*. More generally, we say that a hyperbolic problem is convex if each field can be either GNL or LD [69, 8]. Moreover, if the  $i$ -field is GNL, we can distinguish between two cases:

- if  $\lambda^{(i)}(\mathbf{U}_L) < \lambda^{(i)}(\mathbf{U}_R)$ , we have the right state travelling faster than the left one, and so we have a smooth solution, a so called **rarefaction wave** or simple wave. In the  $(x, t)$ -plane, this is a one-parameter curve corresponding to a self-similar solution of the system of conservation laws, each point of which propagates along  $x$  direction with constant velocity  $\lambda^{(i)}(\mathbf{U}_R)$ . A rarefaction wave is bound to an expansion region. The solution to

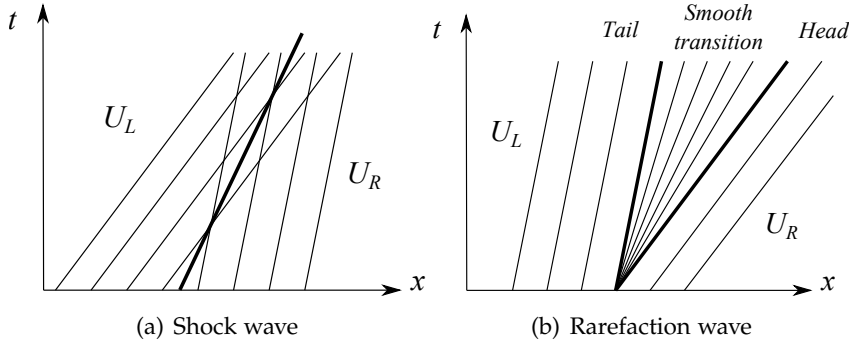


Figure 3.3: Characteristic curves for compressive (left) and expansive (right) discontinuous initial data leading, respectively, to a shock wave and a rarefaction wave.

this problem is found by following characteristics, as discussed previously, and consists of two constant states,  $\mathbf{U}_L$  and  $\mathbf{U}_R$ , separated by a region of smooth transition between both data values. A centred rarefaction wave is illustrated in [Figure 3.2\(a\)](#).

- if  $\lambda^{(i)}(\mathbf{U}_L) > \lambda^{(i)}(\mathbf{U}_R)$ , we have a **shock** propagating in the field  $i$  with a speed that is determined by the Rankine-Hugoniot condition ([Equation 3.17](#)). It is a one-parameter curve, as in the previous case. Shock waves ([Figure 3.2\(b\)](#)) are small transition layers of very rapid changes of physical quantities such as pressure, density and temperature. The transition layer for a strong shock is of the same order of magnitude as the mean free path of the molecules, i.e. about  $10^{-7}$  m. Therefore, replacing these waves as mathematical discontinuities is a reasonable approximation. Very weak shock waves, such as sonic booms, are an exception [[122](#)].

For the physical existence of a  $i$ -shock travelling with speed  $S_i$ , the *Lax entropy condition* states that

$$\lambda^{(i)}(\mathbf{U}_L) > S_i > \lambda^{(i)}(\mathbf{U}_R) \quad (3.27)$$

$$\lambda^{(i-1)}(\mathbf{U}_L) > S_i > \lambda^{(i-1)}(\mathbf{U}_R) \quad (3.28)$$

For sufficiently weak shock waves, the Lax entropy condition is equivalent to the requirement that the shock is an entropy-respecting solution. In the general case, it is not clear whether these entropy conditions are equivalent, except in some particular cases [[69](#)].

In general, the solution of a Riemann problem is self-similar [[8](#)]. Moreover, it consists of a combination of the  $p$  different  $i$ -fields. Thus it can be solved by using the so called *field-by-field* decomposition: we have to determine the intermediated states  $\mathbf{U}_{(1)}, \dots, \mathbf{U}_{(p-1)}$  such that

$\mathbf{U}_{(1)}$  is connected to the left state  $\mathbf{U}_L$  by the 1-field,  $\mathbf{U}_{(2)}$  is connected to its left state  $\mathbf{U}_{(1)}$  by the 2-field..., that is:

$$\mathbf{U}_L \xrightarrow{\lambda^{(1)}} \mathbf{U}_{(1)} \xrightarrow{\lambda^{(2)}} \dots \xrightarrow{\lambda^{(p-1)}} \mathbf{U}_{(p-1)} \xrightarrow{\lambda^{(p)}} \mathbf{U}_R$$

For each eigenvalue  $\lambda^{(i)}$  (and so for each  $i$ -field) there is a wave family (Figure 3.1). For linear systems with constant coefficients each wave is a discontinuity of speed  $S_i = \lambda^{(i)}$  and defines a LD field. For non-linear systems, the waves may be discontinuities such as shock waves and contact waves, or smooth transition waves such as rarefactions.

This is valid for hyperbolic convex systems of conservation laws which are strictly hyperbolic but also non-strictly hyperbolic, with a complete set of eigenvectors and eigenvalues with constant multiplicity [69]. The possible types of waves present in the solution of the Riemann problem depends decisively on closure conditions. For the Euler equations we shall only consider Equations of State such that the only waves present are shocks, contacts and rarefactions.

### 3.2 EULER EQUATIONS FOR A MIXTURE OF GASES

In this Section the Euler model of equations for mixtures of gases is introduced. We hold the hypothesis of ideal gas and the equations of state for an equilibrium mixture of gases with temperature-dependent specific heats, as pointed in Section 2.4.4.1. In particular, we show that these equations constitute a hyperbolic set of conservation laws (see Section 3.1), and also that the system is convex, as sound speed is a non-decreasing function with temperature.

As a matter of fact, the use of the ideal gas model allows us to ensure the convexity of the model. Just as in the polytropic ideal case, intermolecular forces between particles are neglected. Instead, the vibrational degrees of freedom of polyatomic molecules are taken into account via the dependence of specific heat capacities with respect to the temperature. Thus, this gas model is more complex than the polytropic ideal one, where the specific heat capacities of the single species are constant, but less complex than other gas models, for which the 1D Euler equations result to be a non-convex hyperbolic system of conservation laws (e.g. the van der Waals gas model).

The Euler equations express the conservation of mass, momentum and total energy for a fluid when heat conduction and viscous phenomena are neglected ([122] for their derivation from the Navier-Stokes equations). We consider a fixed cartesian coordinate system for the formulation of the equations.

For a mixture of  $n$  gases, the 1D Euler equations became a system that can be written in conservative differential form as:

$$\frac{\partial \mathbf{U}}{\partial t} + \frac{\partial \mathbf{F}(\mathbf{U})}{\partial x} = \mathbf{0} \quad (3.29)$$

where  $\mathbf{U}$  is the vector of conservative variables and  $\mathbf{F}$  is the vector flux:

$$\mathbf{U} = \begin{bmatrix} \rho \\ \rho u \\ \rho e_t \\ \rho Y_1 \\ \dots \\ \rho Y_{n-1} \end{bmatrix}, \quad \mathbf{F} = \begin{bmatrix} \rho u \\ \rho u^2 + p \\ \rho u h_t \\ \rho u Y_1 \\ \dots \\ \rho u Y_{n-1} \end{bmatrix} \quad (3.30)$$

In Equation 3.30,  $u$  is the flow velocity, as all gas species are assumed to be moving at equal speed (it is a scalar, since we are dealing with a one-dimensional problem). The total specific energy and total enthalpy are defined, respectively, as:

$$e_t = e + \frac{1}{2}u^2, \quad h_t = h + \frac{1}{2}u^2 \quad (3.31)$$

The mass fraction of species  $i$  is defined as:

$$Y_i = \frac{m_i}{\sum_{j=1}^n m_j} \quad (3.32)$$

Note that, if  $n$  represents the total number of gas species in the system, the  $n$ -th mass fraction can be recovered from the fact that:

$$\sum_{i=1}^n Y_i = 1 \quad (3.33)$$

Moreover, we need to add to Equation 3.30 an equation expressing  $p$  as a function of the independent variables. We suppose that the mixture of gases is only subjected to quasi static transformations and can be considered at each time in local equilibrium. Then we can introduce an equation of the state for the system in the form:

$$p = p(\rho, e, \mathbf{Y}) \quad (3.34)$$

with  $\mathbf{Y} = (Y_1, \dots, Y_n)^\top$ .

After some transformations [122], the Euler model (system of equations 3.29) can be expressed in quasi-linear form, as a function of the primitives variables  $\mathbf{V} = (\rho, u, p, Y_1, \dots, Y_{n-1})^\top$ , more easily affordable for an analytical analysis than that with conservative variables. The quasi-linear form of the system is:

$$\frac{\partial \mathbf{V}}{\partial t} + \mathbf{B}(\mathbf{V}) \frac{\partial \mathbf{V}}{\partial x} = \mathbf{0} \quad (3.35)$$

where the Jacobian matrix of the system is given by:

$$\mathbf{B}(\mathbf{V}) = \begin{pmatrix} u & \rho & 0 & 0 & \dots & 0 \\ 0 & u & 1/\rho & 0 & \dots & 0 \\ 0 & \rho a^2 & u & 0 & \dots & 0 \\ 0 & 0 & 0 & u & \dots & 0 \\ \vdots & \vdots & \vdots & \vdots & \ddots & \vdots \\ 0 & 0 & 0 & 0 & \dots & u \end{pmatrix} \quad (3.36)$$

It is interesting to note that another interesting way of writing the Euler equation in quasi-linear form is that based in the following set of primitive variables:  $(\rho, u, s, Y_1, \dots, Y_{n-1})$ , being  $s$  the entropy (see [122]).

Regarding the  $\mathbf{B}(\mathbf{V})$  matrix eigenstructure, it can be easily shown that the Jacobian has three different eigenvalues:  $\lambda^{(\pm)} = u \pm a_s$ , with multiplicity one, and  $\lambda^{(0)} = u$  with multiplicity  $n$ . The Jacobian matrix is diagonalisable, as it presents  $n + 2$  linearly independent left (or right) eigenvectors. If  $\mathbf{R}$  is the column matrix of right eigenvectors, as defined in Equation 3.6, there are  $p = 3 + n - 1$  right eigenvectors:

$$\mathbf{r}^{(+)} = (\rho, a_s, \rho a_s^2, 0, \dots, 0)^T$$

$$\mathbf{r}^{(-)} = (\rho, -a_s, \rho a_s^2, 0, \dots, 0)^T$$

$$\mathbf{r}^{(1)} = (1, 0, 0, 0, \dots, 0)^T$$

$$\mathbf{r}^{(2)} = (0, 0, 0, 1, \dots, 0)^T$$

...

$$\mathbf{r}^{(n)} = (0, 0, 0, 0, \dots, 1)^T$$

And also  $p$  left eigenvectors, calculated with Equation 3.9:

$$\mathbf{l}^{(+)} = \frac{1}{2\rho c_s^2} (0, \rho a_s, 1, 0, \dots, 0)^T$$

$$\mathbf{l}^{(-)} = \frac{1}{2\rho c_s^2} (0, -\rho a_s, 1, 0, \dots, 0)^T$$

$$\mathbf{l}^{(1)} = \frac{1}{c_s^2} (c_s^2, 0, -1, 0, \dots, 0)^T$$

$$\mathbf{l}^{(2)} = (0, 0, 0, 1, \dots, 0)^T$$

...

$$\mathbf{l}^{(n)} = (0, 0, 0, 0, \dots, 1)^T$$

## 3.3 GOVERNING EQUATIONS FOR UNSTEADY, THREE-DIMENSIONAL, TWO-PHASE FLOW

The conservation equations that make up the governing balances for both the gas and the particle phase are, for the most part, similar to those found in Korobeinikov et al. [65] and Chen and Fan [19]. Those can be derived from the model of Baer and Nunziato [4] under the hypothesis of highly diluted mixture. As mentioned earlier, the approach taken in developing the conservation equations assumes that there are two distinct continua, one for solids and one for the gas, each moving through its own control volume. Owing to this approach the sum of these two volumes must represent an average mixture volume, while at the same time the equations which describe the two continua must account for the effect that one flow has on the other. To obtain this, the system of equations consists of two sets of conservation equations for each phase (gas and solid), formed by the equations of mass, momentum, total energy and those corresponding to the concentration of the species of each mixture. The void fraction is assumed to be practically equal to one ( $\alpha \approx 1$ ), since the mixture of gases and particles is considered as highly diluted, and pressure effect on the solid phase is negligible. So, the dynamic behaviour of the mixture is characterised by the systems of conservation equations for each phase, which are only coupled by the source terms (Equation 3.37):

$$\frac{\partial \rho_g}{\partial t} + \vec{\nabla} \cdot (\rho_g \vec{u}_g) = \Gamma \quad (3.37)$$

$$\frac{\partial}{\partial t} (\rho_g \vec{u}_g) + \vec{\nabla} \cdot (\rho_g \vec{u}_g \otimes \vec{u}_g + p \vec{I}) = \rho_g \vec{g} - \vec{F}_d + \Gamma \vec{u}_p \quad (3.38)$$

$$\frac{\partial}{\partial t} (\rho_g E_g) + \vec{\nabla} \cdot (\rho_g \vec{u}_g H_g) = \rho_g \vec{u}_g \cdot \vec{g} - \vec{F}_d \cdot \vec{u}_p - Q_g + \Gamma E_p + Q_{c,g} \quad (3.39)$$

$$\frac{\partial}{\partial t} (\rho_g Y_{g,k}) + \vec{\nabla} \cdot (\rho_g Y_{g,k} \vec{u}_g) = \dot{\omega}_{g,k} \quad k = 1, \dots, \text{NGSP} - 1 \quad (3.40)$$

$$\frac{\partial \sigma}{\partial t} + \vec{\nabla} \cdot (\sigma \vec{u}_p) = -\Gamma \quad (3.41)$$

$$\frac{\partial}{\partial t} (\sigma \vec{u}_p) + \vec{\nabla} \cdot (\sigma \vec{u}_p \otimes \vec{u}_p) = \sigma \vec{g} + \vec{F}_d - \Gamma \vec{u}_p \quad (3.42)$$

$$\frac{\partial}{\partial t} (\sigma E_p) + \vec{\nabla} \cdot (\sigma \vec{u}_p E_p) = \sigma \vec{u}_p \cdot \vec{g} + \vec{F}_d \cdot \vec{u}_p + Q_g - \Gamma E_p + Q_{c,p} \quad (3.43)$$

$$\frac{\partial}{\partial t} (\sigma Y_{p,k}) + \vec{\nabla} \cdot (\sigma Y_{p,k} \vec{u}_p) = -\dot{\omega}_{p,k} \quad k = 1, \dots, \text{NPSP} - 1 \quad (3.44)$$

where  $\rho_g$  is the density of the gas mixture,  $\sigma$  the concentration of solids,  $\vec{u}_m$  is the velocity of phase  $m$  ( $g$ : gas or  $p$ : solid, depending

on the case),  $Y_{m,k}$  is the mass fraction of species  $k$  in phase  $m$ . The gas mixture is formed by NGSP gaseous species and the solid mixture is formed by NPSP solid species.

In the system of partial differential equations (Equation 3.37),  $E$  represents the total internal energy and  $H$  is the total enthalpy,  $\bar{F}_d$  is the gas-particle drag force,  $Q_g$  is the interfacial heat transferred between the phases,  $\Gamma$  stands for the total mass exchange between phases and  $Q_{c,k}$  represents the heat released in the reactions by the gaseous ( $k = g$ ) or solid ( $k = p$ ) components (see Section 3.4.2). Note that, the term  $\Gamma \cdot \vec{u}_p$ , accounts for the quantity of momentum exchanged between phases as a result of chemical processes. According to literature, several approaches can be found to choose the velocity at which the interface is moving. In highly diluted mixtures, the velocity of the carried phase,  $u_p$ , is usually adopted [65].

The gas phase is assumed to behave as an ideal gas. The following equation is held:

$$p = [\gamma_g(T_g) - 1] \rho_g c_v(T_g) T_g \quad (3.45)$$

as well as the expressions stated in Section 2.4.4.1. The solid phase is considered incompressible. The heat capacities, and thus the adiabatic constant, are assumed to be a function of temperature. Polynomial correlations are used to find the  $c_v(T_g)$  for each species as a function of temperature.

The problem is being modelled on the basis of Euler equations, as the Reynolds number is very high in the problems under study. Thus, viscous effects in gaseous phase are limited to a narrow zone near the walls that is not resolved under this model. However, viscous effects related to interfacial drag transport, which have by contrast a great relevance, are taken into account by the source term  $\bar{F}_d$ . The same happens with transport terms between phases in energy equation; since  $Re \cdot Pr \gg 1$ , heat conduction in gaseous phase is neglected, but interfacial energy transport is indeed considered under the source term  $Q_g$ .

### 3.3.1 Hyperbolicity of the system

The model equations corresponding to each phase may be considered separately as two different sub-systems, due to the decoupling existing between them except for the source terms. Then, the homogeneous part of the gas system of equations matches with the Euler system of equations for a mixture of non-viscous gases. This sub-system is hyperbolic as the Jacobian matrix associated to the physical flux has real eigenvalues given by  $\lambda^{(1)} = u_g - c_g$ ,  $\lambda^{(2)} = u_g$  and  $\lambda^{(3)} = u_g + c_g$ , where the speed of sound of the gas phase is:

$$c_g^2 = (\gamma_g - 1) c_{p,g} T_g \quad (3.46)$$

On the other hand, the Jacobian matrix of the physical flux of the solid sub-system of equations has only one eigenvalue,  $u_p$ , with multiplicity  $3 + (\text{NPSP} - 1)$ . This yields a degenerate system for this phase.

### 3.4 DEFINITION OF THE SOURCE TERMS IN THE MODEL

Source terms in the system of EDPs (Equation 3.37) account for different effects modelled in the problem, such as homogeneous and heterogeneous chemical reaction, gravity and coupling between phases, modelled as an exchange of mass, momentum and energy.

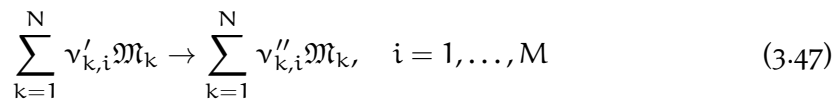
#### 3.4.1 Drag force on particles and interfacial heat transfer

Coupling effects between gas and particles are accounted by means of particle-interface interactions: the drag force acting on particles and the heat transferred through the particle's surface. For the definition of the drag force, the expressions in Section 2.4.2 are applied. In particular, the force acting on a single particle is given by Equation 2.47 whilst in a control volume, where concentration of particles is  $\sigma$ , the volume-averaged drag force ( $\bar{F}_d$  in the model of equations 3.37) can be calculated by following Equation 2.48. The expression adopted hereinafter for the drag coefficient,  $C_d$ , is the one proposed by Otterman and Levine [89], used by Miura and Glass [81] (see Equation 2.49).

Meanwhile, the modelling of the particle-interface heat transfer is discussed in Section 2.4.3.  $Q_g$ , the heat transferred from the gas to a number of particles through its surface in a control volume, can be defined by Equation 2.66. The formula proposed by Knudsen and Katz [64] is assumed for the definition of Nusselt number.

#### 3.4.2 Modelling of combustion

We focus now on the task of choosing expressions to model the source terms related to combustion. Let us generalise for  $N$  reacting species and  $M$  simultaneous reactions. This complex situation is found in the kind of problems we discuss later, when multiple reactions affect a single species (e.g., Oxygen is usually involved in several oxidation processes with various reducing agents simultaneously). An arbitrary number of  $M$  simultaneous reactions may be represented by the equation:



where  $v'_{k,i}$  and  $v''_{k,i}$  are the stoichiometric coefficients for species  $k$  appearing as reactant and product, respectively in reaction  $i$ , and  $\mathfrak{M}_k$

is the chemical symbol for species  $k$ . If the rate of production of species  $k$  in reaction  $i$  is defined as  $\dot{\omega}_{k,i}$  (moles per unit volume per second), then the net rate of production of species  $k$  in all chemical reactions will be given by the following equation (Williams [134]):

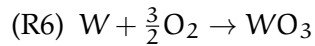
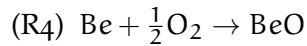
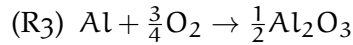
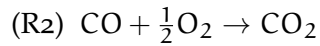
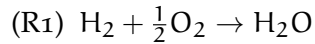
$$\dot{\omega}_k = \sum_{i=1}^M \dot{\omega}_{k,i}, \quad k = 1, \dots, N \quad (3.48)$$

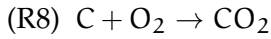
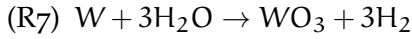
The mass transfer rate, term  $\Gamma$  in Equation 3.37, is formed by the reaction rates for all the reactive gas species, or for the particle species, on other hand:

$$\Gamma = \sum_{k=1}^{\text{NPSP}} \dot{\omega}_{p,k} = - \sum_{k=1}^{\text{NGSP}} \dot{\omega}_{g,k} \quad (3.49)$$

Regarding the reaction rates, those are directly found from chemical kinetics. There are several approaches that can be adopted to estimate the rate of production/consumption of each species. As discussed in Section 2.4.5.1, detailed kinetic models usually include an excessive number of species and reactions (generally around 20). That makes its implementation non viable on detonation simulations. Given that the aim of the present study is to perform a transient simulation of a high-Reynolds fluid dynamics problem, robust and lightweight models are needed, so that the computational cost is affordable and reasonable. Therefore, all processes are assumed to be elementary one-step reactions, modelled as global reaction rates with Arrhenius coefficients from the literature.

All the gas and solid species modelled in the code developed during this thesis work are those assumed to exist in the LOVA and ICE scenarios, according to technical basis of ITER project [94]. That rise a total of 11, including: 6 species in gas phase ( $\text{O}_2$ ,  $\text{N}_2$ ,  $\text{H}_2$ ,  $\text{H}_2\text{O}$ ,  $\text{CO}$ ,  $\text{CO}_2$ ) and 5 species in condensed phase ( $\text{Be}$ ,  $\text{BeO}$ ,  $\text{W}$ ,  $\text{WO}_3$ ,  $\text{C}$ ). Also two more solid species are modelled ( $\text{Al}$ ,  $\text{Al}_2\text{O}_3$ ), since at a first stage of this research on metal particles combustion, aluminium was considered due to the vast literature available on that subject. Those species are considered to react simultaneously following a set of 9 reactions, namely:





For this nine-reaction chemical scheme, some species must be considered as both products and reagents of different reactions. Indeed, the mass fraction of a species could increase or decrease by the global effect of all chemical reactions, depending on temperatures, pressure or concentration of reactants. So, for the species  $k$ , the total mass reaction rate  $\omega_k$  is defined as the contribution of all reactions:  $\omega_k = \sum_{i=1}^{NR} \omega_{k,i} \cdot \delta_{k,i}$ ; with  $NR$  the number of reactions.  $\delta_{k,i} = 1$  if species  $k$  is involved in reaction  $i$  and  $\delta_{k,i} = 0$  if it is not.

All reactions could be classified into two types: gas phase or homogeneous reactions (R1 and R2), and two-phase or heterogeneous reactions (all the rest from R3 to R9). This distinction will be noted in the way that the equations of each phase are affected by reaction source terms. Let us recall the reaction source terms introduce the effects of chemical reactions in the conservation equations of the model: mass transfer and heat of reaction. In particular,

- In case of gas phase reactions, the heat of reaction source term is only applied to the gas phase energy equation; and since no mass exchange is seen between phases, the reaction rate is only included in the conservation equations of the species involved in the reaction.
- By contrast, in the case of two-phase reactions, a mass exchange between phases will occur. That implies the reaction rate will influence the mass conservation equation of the solid phase and also the conservation equations of the species involved in the reaction. Furthermore, a certain quantity of material moves from one phase to another, that means an enthalpy exchange. Finally, the heat of reaction in two-phase reactions, is added to each phase according to the void fraction,  $\alpha$ .

Finally, the heat released by chemical reactions is represented in the model of equations (3.37) by the terms  $Q_{c,g}$  and  $Q_{c,p}$ , which include the contributions of all the reactions. They are defined by:

$$Q_{c,g} = \sum_{i=1}^{NGSP} \dot{\omega}_{g,i} \Delta H_{g,i}^f, \quad Q_{c,p} = \sum_{i=1}^{NPSP} \dot{\omega}_{p,i} \Delta H_{p,i}^f; \quad (3.50)$$

where  $\Delta H_{k,i}^f$  is the heat of formation of species  $i$  (gaseous or solid depending on the phase considered). The interested reader is referred to [134] for a deeper analysis on combustion theory.

### 3.4.2.1 Reaction model for hydrogen detonation

The hydrogen-air detonation has extensively been studied and the kinetics is well understood. In the reaction process, triggered by a leading shock wave, we can distinguish between the induction stage and exothermic recombination stage. During the former we have only the production of free radicals, while the macroscopic variables remain almost constant. In the latter stage we have production of water, increase of the temperature and decrease of the pressure.

We consider, in our model, a one-step reaction mechanism (R1) proposed in some CEA codes, that is already implemented in Cast3M and validated for H<sub>2</sub> detonation in reactor safety assessment simulations [8], for which the reaction rate is given by a general Arrhenius law of the form:

$$\dot{R} = \mathcal{H}(T_g - T_s) A \rho^3 Y_{H_2}^2 Y_{O_2} T_g^{-b} \exp(-T_a/T_g) \quad (3.51)$$

in SI units ( $\text{mol} \cdot \text{m}^3 \text{s}^{-1}$ ).  $\mathcal{H}(y)$  is the Heavyside function,  $T_s$  the threshold temperature ( $T_s = 1200\text{K}$ ),  $A = 1.1725 \cdot 10^{14}$  (in units consistent with International System),  $T_a = 8310\text{K}$  y  $b = 0.91$ .

Then the reaction rates  $\dot{r}_{i,R1}$  ( $\frac{\text{mol}_i}{\text{m}^3 \text{s}}$ ) of each component is given by

$$\dot{r}_{H_2,R1} = -2M_{H_2} \dot{R}; \quad \dot{r}_{O_2,R1} = -M_{O_2} \dot{R}; \quad \dot{r}_{H_2O,R1} = 2M_{H_2O} \dot{R} \quad (3.52)$$

Note that our chemical model is a rough simplification of the hydrogen combustion: we consider only one reaction and a few species. Actually, the chemical reaction between hydrogen and oxygen involves many reactions and intermediate species (H, O, OH, HO<sub>2</sub>, H<sub>2</sub>O<sub>2</sub>, ...), and nitrogen itself undergoes thermal dissociation into NO at high temperatures [8].

A detailed study of a detonation wave would require mesh of the order of the reaction length which is about 1/100 – 1/10 the dimension of a detonation cell ( $\approx 1 - 100$  cm). In a 3D nuclear reactor it is practically impossible to correctly compute phenomena of similar lengths. Anyway, if we consider detonation phenomena in which the involved combustion is almost complete, this model gives a good estimation of the chemical released energy, i.e. a good estimation of the speed of propagation of the detonation wave.

### 3.4.2.2 Reaction mechanism for carbon monoxide oxidation

A comprehensive analysis of literature on CO oxidation has been carried out in [Section 2.4.5.1](#), in order to choose the most satisfactory one-step reaction mechanism for our conditions. Note that those global kinetics are pretty sensitive to the reference state for which they have been formulated.

Finally, the reaction mechanism selected for carbon monoxide oxidation is that proposed by Dryer and Glassman [30], with the reaction

parameters for the chemical kinetics suggested by Yetter et al. [137]. This gives a molar reaction rate for reaction (R2),  $\dot{R}_2$  ( $\frac{\text{mol}}{\text{m}^3\text{s}}$ ):

$$\dot{R}_2 = A \exp\left(-\frac{E_a}{R_u T_g}\right) c_{\text{CO}} c_{\text{O}_2}^{0.25} c_{\text{H}_2\text{O}}^0 \cdot 5 \quad (3.53)$$

where the pre-exponential factor  $A = 2.19313 \cdot 10^{12}$ , the activation energy  $E_a = 1.6736 \cdot 10^5$  and  $c_i$  are molar concentrations for species  $i$  in units ( $\frac{\text{mol}_i}{\text{m}^3}$ ).

### 3.4.2.3 Aluminium oxidation reaction rate

Ogle et al. [85] proposed to use a one-step reaction approach of a skeletal model developed by Markstein [75]. Other authors, such as Chen and Fan [19], have implemented the Ogle model on aluminium-dust explosion predictions.

The original model by Markstein is a reduced scheme where the aluminium particle oxidation process takes place through a number of six homogeneous and heterogeneous reactions. Although in the original study [75] metal is in powder form, the global equations by Ogle predict the oxidation of a liquid droplet (considering the flame temperature and melting point of aluminium).

The rate of the heterogeneous global reaction (R3) for aluminium oxidation,  $\dot{\omega}_{\text{Al},\text{R3}}$  ( $\frac{\text{kgAl}}{\text{m}^3\cdot\text{s}}$ ), can be computed by the expression:

$$\dot{\omega}_{\text{Al},\text{R3}} = -\alpha_{\text{Al}} S_v A \exp\left(\frac{-E_a}{R_u T_p}\right) \rho_m^{3/2} Y_{\text{Al}} Y_{\text{O}_2}^{1/2} \quad (3.54)$$

where  $E_a$  is the activation energy,  $A$  is the Arrhenius constant,  $S_v$  is defined as the surface to volume ratio of the aluminium droplet cloud, and  $\alpha_{\text{Al}}$  represents the volume fraction of aluminium in the control volume. Note that, similarly,  $Y_{\text{Al}}$  and  $Y_{\text{O}_2}$  are *not* the conserved variables  $Y_{p,\text{Al}}$  and  $Y_{g,\text{O}_2}$ , but two new variables defined in relation with the total mass (including both phases), that is:

$$Y_{\text{Al}} = \frac{m_{\text{Al}}}{m_p + m_g}, \quad Y_{\text{O}_2} = \frac{m_{\text{O}_2}}{m_p + m_g} \quad (3.55)$$

By using the mass conservation law for a reacting mixture with  $N$  species, ( $\sum_{i=1}^N \dot{\omega}_i = 0$ ), the rates of reaction for each species can be computed with  $s$  (the mass of oxidiser required to react with a unit mass of fuel):

$$\dot{\omega}_{\text{O}_2,\text{R3}} = s \cdot \dot{\omega}_{\text{Al},\text{R3}}$$

$$\dot{\omega}_{\text{Al}_2\text{O}_3,\text{R3}} = \dot{\omega}_{\text{Al},\text{R3}} - \dot{\omega}_{\text{O}_2,\text{R3}} = -(s + 1)\dot{\omega}_{\text{Al},\text{R3}}$$

By Hess's Law, the heat involved in reaction (absorbed or released) is the enthalpy change of reaction, which depends on the standard

enthalpies of formation of reagents and products. The six steps of the oxidation reaction [75] can be summarised in the following total heat of reaction:

$$\dot{Q}_{c,R3} = \dot{\omega}_{Al_2O_3} \frac{\Delta H_{Al_2O_3}^0}{M_{Al_2O_3}} - \dot{\omega}_{Al} \frac{\Delta H_{Al}^0}{M_{Al}} = \dot{\omega}_{Al_2O_3} \frac{\Delta H_{Al_2O_3}^0}{M_{Al_2O_3}} \left( \frac{J}{m^3 \cdot s} \right) \quad (3.56)$$

#### 3.4.2.4 Reaction mechanism for beryllium oxidation

There are two oxidation reactions to be taken into account in the model. These involve  $O_2$  and  $H_2O$  as oxidizer, respectively for reaction (R4) and reaction (R5), and Be as reducing agent.

Reaction rates [95] are based on the pure geometrical surface area. For dense Be, the molar reaction rates per unit surface, at reaction (R4),  $\dot{r}_{R4}$  ( $\frac{mol}{m^2 \cdot s}$ ):

$$\dot{r}_{R4} = \begin{cases} -5.37 \cdot 10^7 \exp\left(-\frac{26200}{T_p}\right) \left(\frac{P}{8.5 \cdot 10^4}\right), & \text{if } T_p \leq 1073K \\ -3.87 \cdot 10^3 \exp\left(-\frac{15900}{T_p}\right) \left(\frac{P}{8.5 \cdot 10^4}\right), & \text{if } T_p > 1073K \end{cases} \quad (3.57)$$

Dust reactions should be modelled in the following manner: dense particle properties should be applied for the metallic dust particles. The effective surface has to be calculated on the basis of the particle size distribution and the shape factor. As input for the model of equations, mass reaction rate per unit volume is needed,  $\dot{\omega}_{Be,R4}$  ( $\frac{kg}{m^3 \cdot s}$ ). It can be calculated from the molar rate as:

$$\dot{\omega}_{Be,R4} = S_p \frac{\sigma}{m_p} M_{Be} \dot{r}_{R4} = \frac{6\sigma}{d_p \rho_p} M_{Be} \dot{r}_{R4} \quad (3.58)$$

with  $S_p$  the particles surface and  $M_{Be}$  the molecular weight of Beryllium.

Also for 88 % porous Be oxidation in reaction (R5), only the volume rate of  $H_2$  released is reported,  $\dot{v}_{H_2,R5}$  ( $\frac{l}{m^2 \cdot s}$ ):

$$\dot{v}_{H_2,R5} = 1.23 \cdot 10^5 \exp\left(-\frac{12500}{T_p}\right) \left(\frac{P}{8.5 \cdot 10^4}\right)^{0.9} \quad (3.59)$$

Then, for reaction (R5), the Beryllium-dust mass reaction rate per unit volume,  $\dot{\omega}_{Be,R5}$  ( $\frac{kg_{Be}}{m^3 \cdot s}$ ), can be calculated as:

$$\dot{\omega}_{Be,R5} = - \left( \frac{\dot{v}_{H_2,R5}}{10^3} \right) \frac{P}{R_u T_g} M_{Be} \frac{6\sigma}{d_p \rho_{Be}} \quad (3.60)$$

Reactions (R4) and (R5) are exothermic with heats of reaction  $Q_{c,R4} = -610$  kJ/mol and  $Q_{c,R5} = -370$  kJ/mol, respectively, per mole of consumed Beryllium [95].

## 3.4.2.5 Reaction mechanism for oxidation of tungsten particles

Tungsten is oxidised by air, in reaction (R6), and by water vapour, reaction (R7). W/air and W/H<sub>2</sub>O reaction rates were reported by Smolik [113]. However, for W/H<sub>2</sub>O oxidation, more accurate relationships as a function of temperature, pressure and gas velocity are found in [114]. Therefore, for reaction (R6) the following rate is considered for WO<sub>3</sub> production:

$$\dot{r}_{\text{WO}_3, \text{R6}} = \begin{cases} 8.85 \cdot 10^6 \exp\left(-\frac{2400}{T_p}\right) \left(\frac{P}{8.5 \cdot 10^4}\right)^{0.5}, & \text{if } T_p < 973\text{K} \\ 40.7 \exp\left(-\frac{12170}{T_p}\right) \left(\frac{P}{8.5 \cdot 10^4}\right)^{0.5}, & \text{if } T_p \geq 973\text{K} \end{cases} \quad (3.61)$$

$T_p$  denotes the temperature at the surface of particles. Metal particles of such a small size are considered to have a low thermal inertia, so that particles need only a short instant to get equilibrium when temperature changes happen. In that case, one may consider as an assumption that the temperature at the whole particle is  $T_p$ .

The reaction rate for W-dust per unit volume,  $\dot{\omega}_{W, \text{R6}}$  ( $\frac{\text{kg}_W}{\text{m}^3\text{s}}$ ) is calculated as:

$$\dot{\omega}_{W, \text{R6}} = -\dot{r}_{\text{WO}_3, \text{R6}} M_W \frac{6\sigma}{d_p \rho_W} \quad (3.62)$$

where  $M_W$  and  $\rho_W$  are, respectively, the molar mass and density of tungsten;  $\sigma$  is the particle concentration and  $d_p$  the average particles diameter.

For reaction (R7), a burning velocity is obtained from [114], by combining results from three different experiments with constant pressure, constant temperature and constant gas velocity, respectively, giving the following expression:

$$\dot{v}_{\text{H}_2, \text{R7}} = 1.02 \cdot 10^5 [P]^{0.78} [u_g]^{0.56} \exp\left(-\frac{16720}{T_p}\right) \quad (3.63)$$

The mass reaction rate for W-dust oxidised according to reaction (R7),  $\dot{\omega}_{W, \text{R7}}$  ( $\frac{\text{kg}_W}{\text{m}^3\text{s}}$ ) is then:

$$\dot{\omega}_{W, \text{R7}} = -\left(\frac{\dot{v}_{\text{H}_2, \text{R7}}}{10^3}\right) \frac{M_W P}{R_u T_p} \frac{6\sigma}{d_p \rho_W} \quad (3.64)$$

where  $M_W$  and  $\rho_W$  are, respectively, the molar mass and density of tungsten.

Both reactions (R6) and (R7) are exothermic and their heats of reaction, released per mole of W oxidized are, respectively:  $Q_{c, \text{R6}} = -841$  kJ/mol and  $Q_{c, \text{R7}} = -156$  kJ/mol.

## 3.4.2.6 Graphite oxidation reaction rates

Reaction (R8) for graphite oxidation in air assumes that the CO combustion in the boundary layer on the surface of the material is always possible and immediate [95]. Global kinetics for this reaction gives the following molar reaction rate for graphite oxidation,  $\dot{r}_{C,R8}$  ( $\frac{\text{mol}}{\text{m}^2 \cdot \text{s}}$ ):

$$\dot{r}_{C,R8} = \begin{cases} -20.6 \exp\left(-\frac{5710}{T_p}\right) \left(\frac{P}{8.5 \cdot 10^4}\right), & \text{if } T_p < 1273\text{K} \\ -1.3 \exp\left(-\frac{2260}{T_p}\right) \left(\frac{P}{8.5 \cdot 10^4}\right), & \text{if } T_p \geq 1273\text{K} \end{cases} \quad (3.65)$$

And, as in previous cases, to obtain a mass reaction rate for graphite-dust per unit volume,  $\dot{\omega}_{C,R8}$  ( $\frac{\text{kg}_C}{\text{m}^3 \cdot \text{s}}$ ):

$$\dot{\omega}_{C,R8} = \dot{r}_{C,R8} M_C \frac{6\sigma}{d_p \rho_C} \quad (3.66)$$

where  $M_C$  denotes molar mass of C and  $\rho_C$  is graphite density.

Graphite is also assumed to react with the water vapour present in the two-phase system, following the reaction mechanism (R9). A molar reaction rate is selected [95], for which the molar rate of  $\text{H}_2$  generated by unit surface is:

$$\dot{r}_{\text{H}_2,R9} = \begin{cases} 1.6 \cdot 10^{11} \exp\left(-\frac{35760}{T_p}\right) \left(\frac{P}{8.5 \cdot 10^4}\right), & \text{if } T_p < 1460\text{K} \\ 9.7 \cdot 10^3 \exp\left(-\frac{11360}{T_p}\right) \left(\frac{P}{8.5 \cdot 10^4}\right), & \text{if } T_p \geq 1460\text{K} \end{cases} \quad (3.67)$$

in units ( $\frac{\text{mol}_{\text{H}_2}}{\text{m}^2 \cdot \text{s}}$ ). Then, from the value obtained for  $\dot{r}_{\text{H}_2,R9}$ , the mass rate of C oxidized per unit volume can be calculated as:

$$\dot{\omega}_{C,R9} = -\dot{r}_{\text{H}_2,R9} M_C \frac{6\sigma}{d_p \rho_p} \quad (3.68)$$

in units ( $\frac{\text{kg}_C}{\text{m}^3 \cdot \text{s}}$ ).

In respect to heats of reaction, according to literature [95], reaction (R8) is exothermic ( $Q_{C,R8} = -390$  kJ/mol), while (R9) is endothermic ( $Q_{C,R9} = 131$  kJ/mol).

In this chapter, numerical methods applied to solve the physical models detailed in [Chapter 3](#) are addressed.

Facing any problem in Fluid Dynamics, different methodologies shall be used in order to find some useful information about its solution: analytical theory, experimental methodology, Computational Fluid Dynamics (CFD) or hybrid methods. The first of them provides exact solutions for simple problems, or approximate solutions by simplifying the governing equations. However, quite few problems are suitable to be resolved with analytical methods. Other methodologies should be used for more complex problems. The second one, experimental is maybe the one more extended, although it presents certain drawbacks, mainly due to uncertainties in measurement processes or the needing to employ non-intrusive measurement equipments. Nowadays, the third one has burst due to the growing in computer capacities, also because of the great amount of information it is able to generate. Hybrid methods, on the other hand, arise from the union of concepts or results from the three previous methods (e.g. computational-experimental fluid mechanics), being this last probably the best way to front a complex problem in Fluid Mechanics.

This is the working line that has been followed in this thesis. The problems under consideration are resolved with a computational tool from the numerical point of view. Then the different models implemented in the code are checked, facing with experimental results from other authors in literature. Finally, the results from some complex experimental problems are compared with those generated by the code. Validation and verification are indispensable for every CFD study. In this chapter we focus in the description of the numerical procedures and methods employed in the code.

Computational Fluid Dynamics or CFD is the analysis of systems involving fluid flow, heat transfer and associated phenomena such as chemical reactions by means of computer-based simulation. The technique is very powerful and spans a wide range of industrial and non-industrial application areas.

Clearly the investment costs of a CFD capability are not small, but the total expense is not normally as great as that of a high quality experimental facility. Moreover, there are several unique advantages of CFD over experimental-based approaches to fluid systems design:

- substantial reduction of lead times and costs of new designs,
- ability to study where controlled experiments are difficult or impossible to perform (e.g. very large systems),

- ability to study systems under hazardous conditions at and beyond their normal performance limits (e.g. safety studies and accident scenarios),
- practically unlimited level of detail of results.

The variable cost of an experiment, in terms of facility hire and man-hour costs, is proportional to the number of data points and the number of configurations tested. In contrast, CFD codes can produce extremely large volumes of results at virtually no added expense and it is very simple to perform parametric studies, for instance to optimise equipment performance.

There are three distinct streams of numerical solution techniques: finite difference, finite element and spectral methods. In outline, the numerical methods that form the basis of the solver perform the following steps:

- A. Approximation of the unknown flow variables by means of simple functions.
- B. Discretisation by substitution of the approximations into the governing flow equations and subsequent mathematical manipulations.
- C. Solution of the algebraic equations.

The main differences between the three separate streams are associated with the way in which the flow variables are approximated and the discretisation processes.

Finite difference methods describe the unknowns of the flow problem by means of point samples at the node points of a grid of coordinate lines. Truncated Taylor series expansions are often used to generate finite difference approximations of derivatives in terms of point samples and its immediate neighbours. Smith (1985) gives a comprehensive account of all aspects of the finite difference method.

Finite Element Methods use simple piecewise functions (e.g. linear or quadratic) valid on elements to describe the local variations of unknown variables. The governing equation is precisely satisfied by the exact solution, but the piecewise approximations are not, and the residual is defined to measure the errors. This theory was initially developed for structural analysis. A standard work for fluids applications is Zienkiewicz and Taylor (1991).

Spectral methods approximate the unknowns by means of truncated Fourier series or series of Chebyshev polynomials. The approximations are not local but valid throughout the domain. The constraint that leads to the algebraic equations is provided by a weighted residual.

The Finite Volume Method was originally developed as a special finite difference formulation. This thesis is solely concerned with this

most well-established and thoroughly validated general purpose CFD technique. The numerical algorithm consists of the following steps:

- Formal integration of the governing equations of the fluid flow over all the finite control volumes of the solution domain.
- Discretisation involves the substitution of a variety of finite-difference-type approximations for the terms in the integrated equation representing flow processes such as convection, diffusion and sources. This converts the integral equations into a system of algebraic equations.
- Solution of the algebraic equations by an explicit or implicit (iterative) scheme.

The first step, the control volume integration, distinguishes the finite volume method from all other CFD techniques. The resulting statements express the (exact) conservation of relevant properties for each finite size cell. This clear relationship between the numerical algorithm and the underlying physical conservation principle forms one of the main attractions of the finite volume method [128].

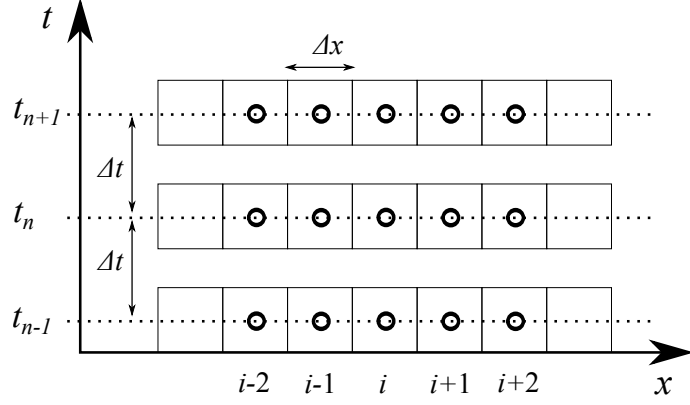
#### 4.1 CONSERVATIVE METHOD FOR HYPERBOLIC EQUATIONS

Despite of the versatility of numerical methods applied for CFD, some demanding problems require special features to numerical methods in order to make them provide reliable, physical solutions. Seeking accurate numerical schemes for capturing shock and contact discontinuities, with minimal numerical dissipation and oscillations, has been a lasting challenge to the computational fluid dynamicist as well as to the numerical analyst since the advent of computers [71].

Computing solutions containing discontinuities, such as shock waves, poses strict requirements on

- the mathematical formulation of the governing equations and
- the numerical schemes to solve the equations.

If we focus on hyperbolic systems of conservation equations, such as those exposed in Chapter 3, there are several ways to express the equations: differential or integral form. Also, there are various choices for the set of variables to be used. One obvious choice is the set of *conserved variables*  $\mathbf{U}$  in Equation 3.37. These hyperbolic systems are formulated on the basis of the conservation laws of the so called conserved variables. Moreover, formulations based on variables other than the conserved variables (non-conservative) fail at shock waves. Regarding the numerical schemes, while it is proven that non-conservative schemes do not converge to the correct solution if a shock wave is present in the solution [122], the Lax and

Figure 4.1: Discretisation of the 1D domain  $[0,L]$  into  $M$  finite volumes.

Wendroff theorem [68] states that conservative numerical methods, if convergent, do converge to the weak solution of the conservation law.

Let us consider the Cauchy problem for the conservative hyperbolic system in Equation 3.1. We will integrate the systems of EDPs over a determinate control volume. The integration process can be followed in [122] and [8] among many others. Given an uniform grid, with time step  $\Delta t$  and spatial mesh  $\Delta x$  (Figure 4.1), let us define:

$$x_i = i\Delta x, \quad x_{i\pm 1/2} = (i \pm 1/2)\Delta x, \quad t_n = n\Delta t \quad (4.1)$$

where  $x_i$  is the position of the  $i$ -th cell centre and  $x_{i\pm 1/2}$  are the positions of the  $i$ -th cell interfaces. Integrating the differential equation in the control volume  $(x_{i-1/2}, x_{i+1/2}) \times (t_n, t_{n+1})$ , we obtain:

$$\int_{x_{i-1/2}}^{x_{i+1/2}} \mathbf{U}(x, t_{n+1}) dx = \int_{x_{i-1/2}}^{x_{i+1/2}} \mathbf{U}(x, t_n) dx - \left( \int_{t_n}^{t_{n+1}} \mathbf{F}(\mathbf{U}(x_{i+1/2}, t)) dt - \int_{t_n}^{t_{n+1}} \mathbf{F}(\mathbf{U}(x_{i-1/2}, t)) dt \right) \quad (4.2)$$

By defining the cell averaged quantities,

$$\tilde{\mathbf{U}}_i^{(n)} = \frac{1}{\Delta x} \int_{x_{i-1/2}}^{x_{i+1/2}} \mathbf{U}(x, t_n) dx, \quad (4.3)$$

we can write Equation 4.2 in the form:

$$\tilde{\mathbf{U}}_i^{(n+1)} = \tilde{\mathbf{U}}_i^{(n)} - \frac{1}{\Delta x} \left( \int_{t_n}^{t_{n+1}} \mathbf{F}(\mathbf{U}(x_{i+1/2}, t)) dt - \int_{t_n}^{t_{n+1}} \mathbf{F}(\mathbf{U}(x_{i-1/2}, t)) dt \right) \quad (4.4)$$

Then we can easily compute  $\tilde{\mathbf{U}}_i^{(0)}$  from the initial condition and determine an approximation of  $\tilde{\mathbf{U}}_i^{(n)}$  once we have decided how to evaluate the time integrals of the interfacial fluxes. From now on, such approximation will be denoted as  $\mathbf{U}_i^{(n)}$ .

A numerical method is said to be *conservative* if it can be written as:

$$\mathbf{U}_i^{(n+1)} = \mathbf{U}_i^{(n)} - \frac{\Delta t}{\Delta x} \left( \mathbf{F}_{\text{num},i+1/2}^{(n)} - \mathbf{F}_{\text{num},i-1/2}^{(n)} \right) \quad (4.5)$$

where

$$\mathbf{F}_{\text{num},i+1/2}^{(n)} = \mathbf{F}(\mathbf{U}_{i-p}^{(n)}, \dots, \mathbf{U}_{i+q}^{(n)}) \quad (4.6)$$

is the so called *numerical flux*.

We usually consider a three point scheme, i.e.

$$\mathbf{F}_{\text{num},i+1/2}^n = \mathbf{F}(\mathbf{U}_i^n, \dots, \mathbf{U}_{i+1}^n) \quad (4.7)$$

For any particular choice of numerical flux  $\mathbf{F}_{\text{num},i+1/2}$ , a corresponding conservative scheme results [122] (see Section 4.3). This scheme is said to be *consistent* with the system of conservation laws if  $\mathbf{F}_{\text{num}}$  is a Lipschitz continuous function of each variable and  $\mathbf{F}_{\text{num}}(\mathbf{U}, \mathbf{U}) = \mathbf{F}(\mathbf{U})$ .

If we consider a Riemann problem for Equation 3.1 and we integrate it on the set  $(-M, M) \times (0, t_{n+1})$ , with  $M$  large enough, we obtain:

$$\int_{-M}^M [\mathbf{U}(x, t_{n+1}) - \mathbf{U}_0(x)] dx = t_{n+1} (\mathbf{F}(\mathbf{U}_L) - \mathbf{F}(\mathbf{U}_R)) \quad (4.8)$$

For the conservative numerical method it is:

$$\Delta x \left( \sum_i \mathbf{U}_i^{(n+1)} - \sum_i \mathbf{U}_i^{(0)} \right) = t_{n+1} (\mathbf{F}_{\text{num}}(\mathbf{U}_L, \mathbf{U}_L) - \mathbf{F}_{\text{num}}(\mathbf{U}_R, \mathbf{U}_R)) \quad (4.9)$$

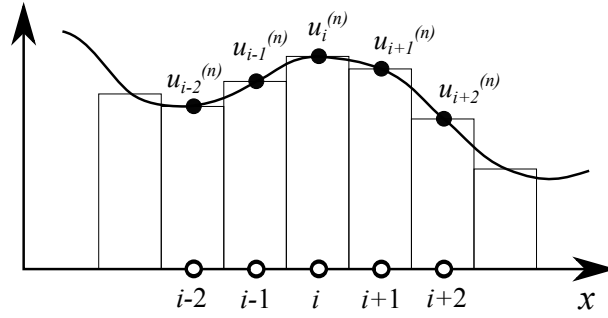
and, for a consistent numerical flux, combining Equation 4.8 and Equation 4.9, we have that

$$\int_{-M}^M [\mathbf{U}(x, t_{n+1}) - \mathbf{U}_0(x)] dx = \Delta x \left( \sum_i \mathbf{U}_i^{(n+1)} - \sum_i \mathbf{U}_i^{(0)} \right) \quad (4.10)$$

Finally, let us recall that, according to the Lax-Wendroff theorem, when a conservative consistent scheme converges to a function  $\mathbf{u}$  in the “integral” sense, then  $\mathbf{u}$  is a weak solution of Equation 3.1.

#### 4.1.1 Domain discretisation for the Conservative Scheme

As a first step for the Finite Volume Method, the domain must be divided into a set of control volumes. Each *finite volume*, computing cell (or simply cell), is represented by its faces and a node (center), where the average values of  $\mathbf{U}$  are computed.

Figure 4.2: Data piece-wise distribution, at time level  $n$ .

The conservative scheme (Equation 4.5) requires an appropriate definition of the discretisation of the domain. For the particular case of a 1D domain in the  $x-t$  plane,  $[0, L] \times [0, T]$ , it can be discretised as shown in Figure 4.1. The spatial domain of length  $L$  is subdivided into  $M$  finite volumes, given as:

$$x_{i-1/2} = (i-1)\Delta x \leq x \leq i\Delta x = x_{i+1/2} \quad (4.11)$$

The extreme values  $x_{i-1/2}$  and  $x_{i+1/2}$  of cell  $I_i$  define the position of the intercell boundaries at which the corresponding intercell numerical fluxes must be specified. The size of the cell is:

$$x_{i+1/2} - x_{i-1/2} = \Delta x = \frac{L}{M} \quad (4.12)$$

Obviously, one may discretise the domain into cells of irregular size. Let us concern now with the cell average defined over every finite volume. The average value of  $U$  is calculated according to Equation 4.3. Note that, although within cell  $i$  one may have spatial variations of  $U$  at time  $t = t_n$ , the integral average value is constant. We will assign that constant value at the centre of the cell, which gives rise to *cell-centred conservative methods*. Computationally, we shall deal with approximations to the cell averages which define a piece-wise constant distribution of the solution at time  $t_n$  (see Figure 4.2).

## 4.2 CONSERVATIVE UPWIND METHODS FOR THE TWO-PHASE REACTIVE SYSTEM

Let us write our non-linear system of equations (Equation 3.37) in vector form so that:

$$\mathbf{U}_t + \vec{\nabla} \cdot \mathcal{H}(\mathbf{U}) = \mathbf{S}(\mathbf{U}) \quad (4.13)$$

where  $\mathbf{U}$  is the vector of conserved variables,  $\mathcal{H} = [\mathbf{F} \ \mathbf{G} \ \mathbf{H}]$  the convective-flux tensor, and  $\mathbf{S}(\mathbf{U})$  the source-term vector:

$$\mathbf{U} = \begin{bmatrix} \rho_g \\ \rho_g u_{gx} \\ \rho_g u_{gy} \\ \rho_g u_{gz} \\ \rho_g E_g \\ \rho_g Y_{g,k} \\ \sigma \\ \sigma u_{px} \\ \sigma u_{py} \\ \sigma u_{pz} \\ \sigma E_p \\ \sigma Y_{p,k} \end{bmatrix}, \quad \mathbf{F} = \begin{bmatrix} \rho_g u_{gx} \\ \rho_g (u_{gx}^2 + p) \\ \rho_g u_{gy} u_{gx} \\ \rho_g u_{gz} u_{gx} \\ \rho_g H_g u_{gx} \\ \rho_g u_{gx} Y_{g,k} \\ \sigma u_{px} \\ \sigma u_{px}^2 \\ \sigma u_{py} u_{px} \\ \sigma u_{pz} u_{px} \\ \sigma u_{px} E_p \\ \sigma u_{px} Y_{g,k} \end{bmatrix}, \quad \mathbf{G} = \begin{bmatrix} \rho_g u_{gy} \\ \rho_g u_{gx} u_{gy} \\ \rho_g (u_{gy}^2 + p) \\ \rho_g u_{gz} u_{gy} \\ \rho_g H_g u_{gy} \\ \rho_g u_{gy} Y_{g,k} \\ \sigma u_{py} \\ \sigma u_{px} u_{py} \\ \sigma u_{py}^2 \\ \sigma u_{pz} u_{py} \\ \sigma u_{py} E_p \\ \sigma u_{py} Y_{g,k} \end{bmatrix}, \quad (4.14a)$$

$$\mathbf{H} = \begin{bmatrix} \rho_g u_{gz} \\ \rho_g u_{gx} u_{gz} \\ \rho_g u_{gy} u_{gz} \\ \rho_g (u_{gz}^2 + p) \\ \rho_g H_g u_{gz} \\ \rho_g u_{gz} Y_{g,k} \\ \sigma u_{pz} \\ \sigma u_{px} u_{pz} \\ \sigma u_{py} u_{pz} \\ \sigma u_{pz}^2 \\ \sigma u_{pz} E_p \\ \sigma u_{pz} Y_{g,k} \end{bmatrix}, \quad \mathbf{S} = \begin{bmatrix} \Gamma \\ \rho_g g_x - F_{dx} + \Gamma u_{px} \\ \rho_g g_y - F_{dy} + \Gamma u_{py} \\ \rho_g g_z - F_{dz} + \Gamma u_{pz} \\ \rho_g \vec{u}_g \cdot \vec{g} - \vec{F}_d \cdot \vec{u}_p - Q_g + \Gamma E_p + Q_{c,g} \\ \dot{\omega}_{g,k} \\ -\Gamma \\ \sigma g_x + F_{dx} - \Gamma u_{px} \\ \sigma g_y + F_{dy} - \Gamma u_{py} \\ \sigma g_z + F_{dz} - \Gamma u_{pz} \\ \sigma \vec{u}_p \cdot \vec{g} + \vec{F}_d \cdot \vec{u}_p + Q_g - \Gamma E_p + Q_{c,p} \\ -\dot{\omega}_{p,k} \end{bmatrix} \quad (4.14b)$$

The integration of the homogeneous part of this system in a control volume  $\Omega$  yields:

$$\frac{d}{dt} \iiint_{\Omega} \mathbf{U} d\Omega + \iint_{\Lambda} \mathcal{H} \hat{n} dA = 0, \quad (4.15)$$

where  $A$  is the boundary of  $\Omega$  and  $\hat{n}$  is the normal vector to surface  $A$ . Considering the first integral as a time-rate of change of the averaging of the conserved variables  $\mathbf{U}$  and the boundary  $A$  formed by  $N$  surfaces so that  $A = \sum_{n=1}^N A_s$ , Equation 4.15 can be written as

$$\frac{d\mathbf{U}}{dt} + \frac{1}{|\Omega|} \sum_{n=1}^N \iint \mathcal{H} \hat{n} dA = 0 \quad (4.16)$$

If the time derivative of the conserved variables is discretised as  $\frac{\mathbf{U}_i^{(n+1)} - \mathbf{U}_i^{(n)}}{\Delta t}$ , making use of the Rotational property  $\mathcal{H} \hat{n} = \Psi_s^{-1} \mathbf{F}(\Psi_s \mathbf{U})$  and the surface integral of the flux is approached by  $\iint_{A_s} \mathcal{H} \hat{n} dA \approx \Psi_s^{-1} \mathbf{F}(\Psi_s \mathbf{U}) A_s$  a finite volume scheme for multiple dimensions in unstructured grids is obtained, such that

$$\mathbf{U}_i^{(n+1)} = \mathbf{U}_i^{(n)} - \frac{\Delta t}{|\Omega|} \sum_{s=1}^N \Psi_s^{-1} \mathbf{F}(\Psi_s \mathbf{U}) A_s \quad (4.17)$$

where  $A_s$  is the area of the  $s^{\text{th}}$  surface which bounds the control volume  $\Omega$ ,  $\Psi_s$  is the rotation matrix, and  $\Psi_s^{-1}$  its inverse. Time step is computed by following a *Courant's* condition,  $\text{CFL} < 1$ , where:

$$\Delta t = \text{CFL} \frac{\Delta x}{|u_g + c_g|}. \quad (4.18)$$

For the numerical flux evaluation, we took advantage of the existing decoupling between the sets of balance laws of the gas and the particle phases. Both particle and gas conservative fluxes may be evaluated by using Approximate Riemann solvers, as detailed in Section 4.3.

Different orders of discretisation for the numerical method can be applied. The *finite-volume* scheme for multiple dimensions represented by Equation 4.17 is a first-order method [37] for the homogeneous part of the System 4.13. Computations with first and second-order space and time discretisation are reported in the present work. Second-order schemes were implemented in the code developed for this thesis and successfully tested [37]. A second order scheme for the convective part of the system can be obtained by using the MUSCL-variable extrapolation strategy. In the code developed, the following predictor-corrector algorithm is used:

- **Prediction step.** The primitive variables are calculated at a time step  $\Delta t/2$  by means of:

$$\tilde{V}_i^{(n+1/2)} = V_i^{(n)} + \hat{A}_i \frac{\partial V}{\partial x} + \hat{B}_i \frac{\partial V}{\partial y} + \hat{C}_i \frac{\partial V}{\partial z} \quad (4.19)$$

It is obtained by writing the homogeneous system 4.13 as

$$\frac{\partial \mathbf{U}}{\partial t} + \frac{\partial \mathbf{F}}{\partial x} + \frac{\partial \mathbf{G}}{\partial y} + \frac{\partial \mathbf{H}}{\partial z} = 0 \quad (4.20)$$

and transforming it, after some algebra, into

$$\frac{\partial \mathbf{V}}{\partial t} = \hat{\mathbf{A}} \frac{\partial \mathbf{V}}{\partial x} + \hat{\mathbf{B}} \frac{\partial \mathbf{V}}{\partial y} + \hat{\mathbf{C}} \frac{\partial \mathbf{V}}{\partial z} \quad (4.21)$$

Matrices  $\hat{\mathbf{A}}$ ,  $\hat{\mathbf{B}}$  and  $\hat{\mathbf{C}}$  stand respectively for  $(\frac{\partial \mathbf{U}}{\partial \mathbf{V}})^{-1} \frac{\partial \mathbf{F}}{\partial \mathbf{V}}$ ,  $(\frac{\partial \mathbf{U}}{\partial \mathbf{V}})^{-1} \frac{\partial \mathbf{G}}{\partial \mathbf{V}}$ , and  $(\frac{\partial \mathbf{U}}{\partial \mathbf{V}})^{-1} \frac{\partial \mathbf{H}}{\partial \mathbf{V}}$ .

- **Correction step.** The previously calculated primitive variables are space reconstructed by means of:

$$\tilde{\mathbf{V}}_i = \tilde{\mathbf{V}}_i + \vec{\nabla} \tilde{\mathbf{V}} \cdot (\vec{\mathbf{r}} - \vec{\mathbf{r}}_i) \quad (4.22)$$

where  $\vec{\mathbf{r}}$  is a vector characterising the position of the points considered in the reconstruction process. Then, the linearised conserved variables  $\tilde{\mathbf{U}}$  are obtained from  $\tilde{\mathbf{V}}$ .

- **Conserved variables update.** Finally, conserved variables are updated by means of:

$$\mathbf{U}_i^{(n+1)} = \mathbf{U}_i^{(n)} - \frac{\Delta t}{|\Omega|} \sum_{s=1}^N \Psi_s^{-1} \mathbf{F}(\Psi_s \tilde{\mathbf{U}}) A_s \quad (4.23)$$

where the numerical fluxes are evaluated by any of the numerical schemes discussed later in [Section 4.3](#) and using the already calculated linearised primitive variables  $\tilde{\mathbf{V}}$ . Gradients are approximated by means of the reconstruction method introduced by Beccantini [8]. Stability is a crucial issue in reactive flows computation, and spurious oscillations must be absolutely avoided because they can generate spurious combustion phenomena, changing completely the solution of the problem. Thus, in the gradient reconstruction, numerical gradients are limited by using a version of the Barth-Jespersen limiter.

Regarding the integration of the source-terms vector  $\mathbf{S}$ , a first option is a direct first-order solution of the inhomogeneous part of the system [4.13](#), to give the following explicit scheme:

$$\mathbf{U}_i^{(n+1)} = \mathbf{U}_i^{(n)} - \frac{\Delta t}{|\Omega|} \sum_{s=1}^N \Psi_s^{-1} \mathbf{F}(\Psi_s \mathbf{U}) A_s + \Delta t \mathbf{S}_i^{(n)}(\mathbf{U}) \quad (4.24)$$

The approach stated in [Equation 4.24](#) is what we call hereinafter a *conventional method*. It has been broadly implemented in previous works [35, 36, 37]. Another possibility to get approximate solutions to the system in [Equation 4.13](#) is the use of *splitting methods* [122, 115, 69], whereby at a first stage the advection problem is solved,

$$\mathbf{U}_t + \vec{\nabla} \cdot \mathcal{H}(\mathbf{U}) = 0 \quad (4.25)$$

and secondly, the ODE problem,

$$\mathbf{U}_t = \mathbf{S}(\mathbf{U}), \quad (4.26)$$

where we have sources for drag force, heat transfer, chemical reaction and gravity. On the solution of Equation 4.26, a new approach is proposed in the present work (Section 4.4), which could be named **Advanced Source-Term Treatment** (ASTT) as a relaxation method to deal with stiff source vectors. The new method is based on *splitting* source terms.

The use of splitting methods can be interpreted as follows: the update of the conserved variables in each cell is approached by a succession of integration operators [115]. Thus, the solution at the next time  $n + 1$  would be computed as:

$$\mathbf{U}^{n+1} = L_s^{\Delta t} L_h^{\Delta t} \mathbf{U}^n \quad (4.27)$$

where  $L_h^{\Delta t}$  is the solution operator for the advection problem (Equation 4.25) and  $L_s^{\Delta t}$  is the solution operator for the Ordinary Differential Equations (ODE) system. The main attraction of splitting schemes is in the fact that one can deploy the optimal, existing schemes for each sub-problem. In what follows, we will pay attention to this approach, since in the case we are studying it seems to improve our results, when stiff source terms are encountered.

It is worth noting that a first order scheme is obtained if the system of Equations 4.25 and 4.26 is solved as shown in Equation 4.27. In order to have a second order scheme, the hyperbolic operator  $L_h^{\Delta t}$ , and the integration operator for the source terms  $L_s$ , are applied as:

$$\mathbf{U}^{n+1} = L_s^{\Delta t/2} L_h^{\Delta t} L_s^{\Delta t/2} \mathbf{U}^n \quad (4.28)$$

### 4.3 CONVECTIVE FLUX EVALUATION

It is worthwhile to note that approximate Riemann solvers might be applied for the hyperbolic operator solving. We will not go deeply through this subject as convective flux evaluation is not the main topic of the present work. We should point to [122] for an extensive revision of approximate Riemann solvers, where many options are proposed for gas-phase Eulerian models.

AUSM+ (an upwind differencing scheme) [37] is a common choice often used in compressible CFD due to its simplicity and hence its low computational cost. It is known to be as accurate as flux difference splitting methods such as Roe's or Osher's approximate Riemann solvers [88, 99] without the cost of field-by-field wave decompositions. This makes AUSM methods quite appealing for its application on the resolution of any version of Euler model of equations. For the particle phase and due to the Eulerian mathematical character of the system of equations for particles, a Rusanov scheme might be

used, or an adapted AUSM scheme for a discrete solid phase, previously reported in [37]. Being the solid incompressible, its speed of sound is constant and does not play any role, so AUSM fluxes are formulated on velocity instead of on the Mach number functions usually employed [37].

In what follows, a brief review about Riemann solvers is performed, with some emphasis on the difference between exact and approximate solvers for the flux evaluation. In particular, Godunov's first-order method is introduced in Section 4.3.1 and some approximate solver used in the present work are described in Section 4.3.2, including newly developed versions for AUSM+ and Rusanov schemes for particle phases.

#### 4.3.1 First-order Upwind Method by Godunov

The first successful conservative extension of the first-order upwind method by Courant, Isaacson and Rees (1952), to non-linear systems of conservation laws was developed by Godunov [39]. The term *upwind*, or upstream, refers to the fact that spatial differencing is performed using the mesh points on the side from which information (wind) flows.

Godunov's first-order upwind method is a conservative method of the form of Equation 4.5, where the intercell numerical fluxes  $F_{\text{num},i+\frac{1}{2}}$  are computed by using solutions of local Riemann problems. A basic assumption of the method is that at a given time level  $n$  the data has a piece-wise constant distribution as depicted in Figure 4.2. The data at time level  $n$  may be seen as pairs of constant states  $(\mathbf{U}_i^n, \mathbf{U}_{i+1}^n)$  separated by a discontinuity at the intercell boundary  $x_{i+1/2}$  [122]. Then, locally, one can define a Riemann problem:

$$u_t + f(u)_x = 0 \quad (4.29)$$

$$u(x, 0) = u_0(x) = \begin{cases} u_i^n & \text{if } x < 0, \\ u_{i+1}^n & \text{if } x \geq 0. \end{cases} \quad (4.30)$$

This *local* Riemann problem may be solved analytically, if desired. Thus, at a given time level  $n$ , at each intercell boundary we have the local Riemann problem:  $\text{RP}(\mathbf{U}_i^n, \mathbf{U}_{i+1}^n)$ .

To find the solution of the *global* problem at a later time level  $n+1$ , Godunov proposed a scheme by the following steps:

- (i) Solving the two Riemann problems  $\text{RP}(\mathbf{U}_{i-1}^n, \mathbf{U}_i^n)$  and  $\text{RP}(\mathbf{U}_i^n, \mathbf{U}_{i+1}^n)$  for the system of conservation equations,
- (ii) Taking an integral average in cell  $i$  of the combined solutions of these two local problems and

(iii) Assigning the value to  $U_i^{n+1}$ .

For example, for the simple case of an scalar conservation equation, with  $f(u) = au$ ,  $a > 0$ , the exact solution of  $RP(u_{i-1}^n, u_i^n)$  is

$$u_{i-\frac{1}{2}}(x/t) = \begin{cases} u_{i-1}^n & \text{if } x/t < a, \\ u_i^n & \text{if } x/t > a \end{cases} \quad (4.31)$$

where the local origin of the Riemann problem is  $(0, 0)$ . Likewise, the solution of  $RP(u_i^n, u_{i+1}^n)$  is given by

$$u_{i+\frac{1}{2}}(x/t) = \begin{cases} u_i^n & \text{if } x/t < a, \\ u_{i+1}^n & \text{if } x/t > a \end{cases} \quad (4.32)$$

The Godunov scheme defines the updated solution as:

$$u_i^{n+1} = \frac{1}{\Delta x} \left[ \int_0^{\Delta x/2} u_{i-1/2}(x/\Delta t) dx + \int_{-\Delta x/2}^0 u_{i+1/2}(x/\Delta t) dx \right]. \quad (4.33)$$

This integral is evaluated at time  $\Delta t$ . The method imposes a restriction in this time step in order to preserve stability, i.e. the *Courant-Friedrichs-Lewy* condition:

$$\text{CFL} = \frac{a\Delta t}{\Delta x} \leq \frac{1}{2} \quad (4.34)$$

For a non-linear problem, at each time, there are multiple velocities of wave propagation  $a$  and, thus, multiple associated CFL numbers. If we denote by  $S_{\max}^n$  the maximum wave speed travelling through the domain at time  $n$ , we define the maximum CFL as:

$$\text{CFL}_{\max} = \frac{\Delta t S_{\max}^n}{\Delta x} \quad (4.35)$$

For an explicit scheme in form of [Equation 4.5](#), the value of CFL should range from 0 to 1. The time step value is then enclosed to

$$\Delta t = \frac{\text{CFL}_{\max} \Delta x}{S_{\max}^n} \quad (4.36)$$

### 4.3.2 Approximate Riemann Solvers

Godunov's method and its high-order variants require the solution of the Riemann problems for each pair of cells every time step. In practice, it might be computationally solved billions of times, making the solution of the global Riemann problem a costly numerical process. In order to find the exact solution, this iterative process is needed and probably such a computational effort is not worthwhile. This effort can dramatically be increased by complex algebraic

equations of state or the complexity of the system of equations to be solved.

Fortunately, approximate non-iterative solutions have the potential to provide the information that is needed for the numerical objectives we face. That is why in the present work we focus on *approximate Riemann solvers*.

One can find, essentially, two ways to extract approximate information from the solution of a Riemann problem to be used in conservative methods: (i) one of them is to find an approximation to the numerical flux employed directly in the method (as in schemes HLL, Roe or Osher), (ii) the second consists of finding an approximation to the *state* and then evaluating the physical flux functions in that state.

Next we will briefly describe Roe's scheme and the two numerical schemes we have extended in the framework of this thesis to solve the system of equations for reactive, multicomponent, two-phase flow.

#### 4.3.2.1 Roe's Splitting Scheme

One of the most well-known of all approximate Riemann solvers is the numerical scheme due to Roe [99]. The Roe scheme can be applied to the resolution of the convective part of the system in Equation 4.13, via a phase-splitting procedure, that is, by solving separately the gas-phase part of system (4.13) and the solid-phase part. The resolution is done by means of a explicit conservative method (Equation 4.17) which in 1D approach turns into Equation 4.5.

For a system of conservation equations (Equation 3.1), Roe solved the Riemann problem (Equation 3.18) approximately, by replacing the Jacobian matrix,  $\mathbf{A}(\mathbf{U})$  in Equation 3.2, by a constant matrix  $\tilde{\mathbf{A}} = \tilde{\mathbf{A}}(\mathbf{U}_L, \mathbf{U}_R)$ . That creates a new system of linear conservation equations and, thus, an approximate Riemann problem which is solved exactly:

$$\begin{cases} \frac{\partial \mathbf{U}}{\partial t} + \tilde{\mathbf{A}} \frac{\partial \mathbf{U}}{\partial x} = 0 \\ \mathbf{U}(x, 0) = \begin{cases} \mathbf{U}_L, & x < 0 \\ \mathbf{U}_R, & x \geq 0 \end{cases} \end{cases} \quad (4.37)$$

The approximated Jacobian matrix should preserve the hyperbolicity of the system of equations, i.e.,  $\tilde{\mathbf{A}}$  is required to have real eigenvalues and a complete set of linearly independent right eigenvectors. It must be also consistent with the exact Jacobian,  $\tilde{\mathbf{A}}(\mathbf{U}, \mathbf{U}) = \mathbf{A}(\mathbf{U})$  and allow conservation across discontinuities  $\mathbf{F}(\mathbf{U}_R) - \mathbf{F}(\mathbf{U}_L) = \tilde{\mathbf{A}}(\mathbf{U}_R - \mathbf{U}_L)$ .

Once the matrix  $\tilde{\mathbf{A}}$ , its eigenvalues  $\tilde{\lambda}_i$  and right eigenvalue vectors  $\tilde{\mathbf{r}}^{(i)}(\mathbf{U}_L, \mathbf{U}_R)$  are available, the Riemann problem 4.37 is solved by direct application of the method discussed in Section 3.1.1.

After some algebra [122], the approximate numerical fluxes can be obtained as:

$$\mathbf{F}_{i+1/2} = \mathbf{F}_L + \sum_{\tilde{\lambda}_i \leq 0} \tilde{\alpha}_i \tilde{\lambda}_i \tilde{\mathbf{r}}^{(i)} \quad (4.38)$$

or

$$\mathbf{F}_{i+1/2} = \mathbf{F}_R - \sum_{\tilde{\lambda}_i \geq 0} \tilde{\alpha}_i \tilde{\lambda}_i \tilde{\mathbf{r}}^{(i)} \quad (4.39)$$

where  $\tilde{\alpha}_i$  are the *wave strengths* such that  $\Delta \mathbf{U} = \mathbf{U}_R - \mathbf{U}_L = \sum_{i=1}^p \tilde{\alpha}_i \tilde{\mathbf{r}}^{(i)}$ . So, first a choice has to be done to find the approximate Jacobian  $\tilde{\mathbf{A}}$  and later, a linear system of  $p$  equations has to be resolved [122] to find the wave strengths.

A refinement to the Roe's approach was introduced by Roe and Pike [98], whereby the computation does not require the Roe averaged Jacobian matrix and, thus, it is a more simple approach, useful in solving the Riemann problem for new, complicated sets of hyperbolic conservation laws.

The Roe-Pike approach assumes that the original system of equations is actually hyperbolic and the set of linearly independent right eigenvectors are available. Two steps must be followed in the implementation of this numerical scheme:

- i First, to find analytical expressions to the wave strengths  $\alpha_i$ , the method assumes a linearised form of the governing equations based on the assumption that the data states  $\mathbf{U}_L$  and  $\mathbf{U}_R$  are close to a reference state  $\hat{\mathbf{U}}$ , to order  $\mathcal{O}(\Delta^2)$ . Linearisation of the conservation laws about this state gives:

$$\mathbf{U}_t + \mathbf{F}(\mathbf{U})_x \equiv \mathbf{U}_t + \left( \frac{\partial \mathbf{F}}{\partial \mathbf{U}} \right) \mathbf{U}_x \approx \mathbf{U}_t + \hat{\mathbf{A}} \mathbf{U}_x = 0 \quad (4.40)$$

where  $\hat{\mathbf{A}}$  is the exact Jacobian matrix, which is assumed to be variable, computed at the reference state  $\hat{\mathbf{U}}$ . The analytical wave strengths at the reference state,  $\hat{\alpha}_i$ , we solve the jump equation  $\Delta \mathbf{U} = \mathbf{U}_R - \mathbf{U}_L = \sum_{k=1}^p \hat{\alpha}_k \hat{\mathbf{r}}^{(k)}$ . Note that this linearisation is not the Roe linearisation resulting from the Roe matrix  $\tilde{\mathbf{A}}$ .

- ii Then, from the analytical expressions found in the first step, an average vector  $\tilde{\mathbf{W}}$ , normally based on the primitive variables, is to be found by setting:

$$\tilde{\alpha}_i = \hat{\alpha}_i(\tilde{\mathbf{W}}), \quad \tilde{\lambda}_i = \lambda_i(\tilde{\mathbf{W}}), \quad \tilde{\mathbf{r}}^{(i)} = \mathbf{r}^{(i)}(\tilde{\mathbf{W}}); \quad (4.41)$$

the analytical expressions for  $\lambda_i$ ,  $\mathbf{r}^{(i)}$  and  $\tilde{\alpha}_i$  are evaluated at the unknown average state  $\tilde{\mathbf{W}}$ . Then,  $\tilde{\mathbf{W}}$  is found by solving the algebraic problem posed by the following two sets of equations:

$$\Delta \mathbf{U} = \mathbf{U}_R - \mathbf{U}_L = \sum_{k=1}^p \tilde{\alpha}_k \tilde{\mathbf{r}}^{(k)} \quad (4.42)$$

$$\Delta \mathbf{F} = \mathbf{F}_R - \mathbf{F}_L = \sum_{k=1}^p \tilde{\alpha}_k \tilde{\lambda}_k \tilde{\mathbf{f}}^{(k)} \quad (4.43)$$

#### 4.3.2.2 Rusanov's Scheme

The scheme by Rusanov [103] (also called TVD Lax-Friedrich or TVDLF) has been prized for its robustness and ease of implementation. The numerical flux is computed by means of a single expression, as a function of the left and right states of the cell interface,  $\mathbf{U}_L$  and  $\mathbf{U}_R$ , respectively. The numerical flux in the interface  $i + 1/2$  is computed as:

$$\mathbf{F}_{i+1/2} = \frac{1}{2} [\mathbf{F}_L + \mathbf{F}_R - S^+ (\mathbf{U}_R - \mathbf{U}_L)] \quad (4.44)$$

where  $\mathbf{F}_L = \mathbf{F}(\mathbf{U}_L)$ ,  $\mathbf{F}_R = \mathbf{F}(\mathbf{U}_R)$ , and the wave speed  $S^+$  has been chosen such that

$$S^+ = \max\{|\mathbf{u}_{kL}|, |\mathbf{u}_{kR}|\}.$$

Another option for the speed  $S^+$ , proposed by Davis (see [122]), includes the speed of sound:

$$S^+ = \max\{|\mathbf{u}_L - \mathbf{a}_L|, |\mathbf{u}_R - \mathbf{a}_R|, |\mathbf{u}_L + \mathbf{a}_L|, |\mathbf{u}_R + \mathbf{a}_R|\} \quad (4.45)$$

The Rusanov flux function is very efficient in shock resolution, but more diffusive than the Roe flux. Especially contact discontinuities diffuse fast for the Rusanov flux function. This scheme can be successfully implemented in either the gas or solid phase due to its simplicity. The combination of this scheme in solid phase with other more complex methods for gas phase (such as AUSM) provides, in tests studied, very satisfactory results, as shown later in [Chapter 5](#).

#### 4.3.2.3 Rusanov's Scheme for the solid phase

Rusanov's scheme can be adapted to a sub-system of equations of a solid phase consisting in multiple particles. As an Eulerian-Eulerian model is being considered for the two-phase system, also the solid particulate phase is modelled as a continuum which is discretised in space and, thus, the concept of Rusanov's scheme can be applied.

Nevertheless, the inherent physical nature of the solid phase makes the speed of sound of the solid material having no sense as a phase speed of sound. That could be a problem to find a proper value for the wave speed  $S_p^+$ . However, that problem vanishes if we follow the proposal by Davis [26] and we use the maximum eigenvalue for the left and right non-linear waves. As remarked in [Section 3.3.1](#), the only eigenvalue of the sub-system of equations for particles is  $u_p$  with multiplicity  $\text{NPSP} + 2$ , thus the wave speed can be chosen as:

$$S_p^+ = \max\{|\mathbf{u}_{p,L}|, |\mathbf{u}_{p,R}|\}. \quad (4.46)$$

and so the numerical flux at the intercell  $i + 1/2$  is:

$$\mathbf{F}_{i+1/2} = \frac{1}{2} [\mathbf{F}_L + \mathbf{F}_R - S_p^+ (\mathbf{U}_R - \mathbf{U}_L)]. \quad (4.47)$$

#### 4.3.2.4 Flux Vector Splitting schemes

The Godunov approach, with the approximate Riemann solvers cited above, usually referred to as *Flux Difference Splitting* (FDS) methods, need some information about the direction of propagation of the information in the problem, that must be incorporated from the physical phenomena. Oppositely to the Godunov methods, *Flux Vector Splitting* (FVS) methods encompasses a family of schemes for which the upwinding direction is achieved with less effort, leading to simple and somewhat more efficient schemes. That made them very attractive for a wide range of computational problems on Aerodynamics. The reduced sophistication of FVS schemes however, as compared with Godunov-type schemes, results in poorer resolution of discontinuities [122]. Nevertheless, the increased accuracy of FDS methods is accompanied with an increased operation count and complexity in arriving at the complete linearisation of flux formulae while, by contrast, the simplicity of FVS is still motivating the development of new schemes [73].

Generally speaking, FVS methods entail a splitting of the flux vector  $\mathbf{F}$  into two components  $\mathbf{F}^+(\mathbf{U})$  and  $\mathbf{F}^-(\mathbf{U})$  such that,

$$\mathbf{F} = \mathbf{F}^+(\mathbf{U}) + \mathbf{F}^-(\mathbf{U}). \quad (4.48)$$

The functions  $\mathbf{F}^\pm(\mathbf{U})$  must satisfy some properties: consistency, the continuity of their Jacobians, invariance with respect to the orientation of the  $x$ -axis, upwinding [8]. Moreover, the Jacobians must respectively have non-negative and non-positive eigenvalues. That is, if we consider a general system of non-linear hyperbolic conservation laws with a Jacobian matrix  $\mathbf{A} = \mathbf{A}(\mathbf{U})$ , the splitting is required to satisfy the condition:

$$\hat{\lambda}^+ \geq 0; \quad \hat{\lambda}^- \leq 0, \quad (4.49)$$

where the eigenvalues  $\hat{\lambda}^+$  and  $\hat{\lambda}^-$  come from the definition of the Jacobian matrices:

$$\hat{\mathbf{A}}^+ = \frac{\partial \mathbf{F}^+}{\partial \mathbf{U}}, \quad \hat{\mathbf{A}}^- = \frac{\partial \mathbf{F}^-}{\partial \mathbf{U}} \quad (4.50)$$

The splitting is also required to reproduce regular upwinding when all eigenvalues  $\lambda_i$  of the coefficient matrix  $\mathbf{A}$  are all positive or zero, or all negative or zero. That is,

$$\mathbf{F}^+ = \mathbf{F}; \mathbf{F}^- = 0 \quad \text{if } \lambda_i \geq 0, \quad (4.51)$$

$$\mathbf{F}^+ = 0; \mathbf{F}^- = \mathbf{F} \quad \text{if } \lambda_i \leq 0, \quad (4.52)$$

for  $i = 1, \dots, m$  [122].

Regarding specific schemes for the vector splitting and the definition for  $\mathbf{F}^+$  and  $\mathbf{F}^-$ , various FVS popular options have been widely tested in literature. Some of them are the van Leer splitting method [125] and the van Leer-Hännel scheme. They are robust in dealing with strong shock and rarefaction waves, but more dissipative than the FDS methods. In particular they strongly diffuse stationary contact discontinuities and slow moving contact discontinuities. If the numerical diffusion linked to the convective solver is significant compared to the physical one, the results obtained are completely inaccurate [8]. In our case, this lack of accuracy is crucial from a practical point of view, as we aim to predict both strong detonation and weak deflagration [134].

The van Leer-Hännel scheme was implemented and tested in the code developed for this thesis, although it was finally rejected for stability problems in the solution. Here we underline the AUSM family of hybrid schemes, valued for their stability and accuracy in shock capturing.

#### 4.3.2.5 Van Leer-Hännel Scheme

In this section we briefly describe the FVS of van Leer-Hännel, which can be readily used to compute ideal gases with temperature dependent specific heat capacities. We emphasize that it differs from original van Leer scheme [125] only on the splitting of the energy [8]. Let us present the scheme with the same notation as Liou [71], by using the Mach and pressure functions:

$$\mathcal{M}^\pm = \begin{cases} \pm \frac{1}{4}(M \pm 1)^2 & \text{if } |M| \leq 1, \\ \frac{1}{2}(M \pm |M|) & \text{otherwise;} \end{cases} \quad (4.53)$$

$$\mathcal{P}^\pm = \begin{cases} \pm \frac{1}{4}(M \pm 1)^2 [3 - (1 \pm M)] & \text{if } |M| \leq 1, \\ \frac{1}{2}(1 \pm \text{sign}(M)) & \text{otherwise.} \end{cases} \quad (4.54)$$

In that case, the numerical flux,

$$\mathbf{F}^\pm(\mathbf{U}) = \begin{pmatrix} \mathcal{M}^\pm(M) \rho c_s \\ \mathcal{M}^\pm(M) \rho c_s \mathbf{u} + \mathcal{P}^\pm(M) + p \\ \mathcal{M}^\pm(M) \rho c_s H_t \\ \mathcal{M}^\pm(M) \rho c_s \mathbf{Y} \end{pmatrix}, \quad (4.55)$$

where  $H_t$  represents the total enthalpy and  $\mathbf{Y}$  is the vector of mass fractions.

#### 4.3.2.6 The AUSM family of schemes

Hybrid schemes try to couple the robustness of the FVS methods with the capability of the FDS methods in capturing the stationary

contact discontinuities. A relatively recent scheme, the *Advection Upwind Splitting Method* (AUSM), first reported by Liou and Steffen [73], has been formulated in basis of Euler equations and consists of splitting the numerical flux vector into a *convective* component,  $\mathbf{F}_{\text{num}}^{(c)}$  and a *pressure* component,  $\mathbf{F}_{\text{num}}^{(p)}$ . The scheme is a mixture, but it has the advantages of both FDS and FVS methods [73]. AUSM is as accurate as Roe scheme and much simpler to construct, and thus more efficient. The scheme does not involve differentiation of fluxes, unlike Roe's splitting, and pressure derivatives do not explicitly appear in the flux formulae.

Later, a second version of the scheme, termed AUSM+, was derived by Liou [71] aiming to have the following features: (1) exact resolution of a stationary normal shock or contact discontinuity, (2) positivity-preserving property, and (3) improvement in accuracy over its predecessor AUSM and other popular schemes, (4) simplicity and easy generalization to other conservation laws [71].

In the general case, for three-dimensional flow, we have

$$\mathbf{F}(\mathbf{U}) = \begin{bmatrix} \rho u \\ \rho u^2 \\ \rho uv \\ \rho uw \\ u(E + p) \end{bmatrix} = \begin{bmatrix} \rho u \\ \rho u^2 \\ \rho uv \\ \rho uw \\ \rho uH \end{bmatrix} + \begin{bmatrix} 0 \\ p \\ 0 \\ 0 \\ 0 \end{bmatrix} \equiv \mathbf{F}^{(c)} + \mathbf{F}^{(p)}, \quad (4.56)$$

with the obvious definition of the convective,  $\mathbf{F}^{(c)}$ , and the pressure component,  $\mathbf{F}^{(p)}$ . Introducing the Mach number and the enthalpy,

$$M = \frac{u}{a}, \quad H = \frac{E + p}{\rho} \quad (4.57)$$

we can write the convective part as follows:

$$\mathbf{F}^{(c)} = M \begin{bmatrix} \rho a \\ \rho a u \\ \rho a v \\ \rho a w \\ \rho a H \end{bmatrix} \equiv M \hat{\mathbf{F}}^{(c)}, \quad (4.58)$$

In order to define the numerical flux at intercells,  $\mathbf{F}_{i+1/2}$ , Liou and Steffen take

$$\mathbf{F}_{i+1/2} = \mathbf{F}_{i+1/2}^{(c)} + \mathbf{F}_{i+1/2}^{(p)}, \quad (4.59)$$

where the convective part of the flux is given by

$$\mathbf{F}_{i+1/2}^{(c)} = M_{i+1/2} \left[ \hat{\mathbf{F}}^{(c)} \right]_{i,i+1} \quad (4.60)$$

Note that in Equation 4.60 we defined:

$$[\hat{\mathbf{F}}^{(c)}]_{i,i+1} = \begin{cases} [\hat{\mathbf{F}}^{(c)}]_i & \text{if } M_{i+1/2} \geq 0, \\ [\hat{\mathbf{F}}^{(c)}]_{i+1} & \text{if } M_{i+1/2} < 0. \end{cases} \quad (4.61)$$

It is also worth noting that the flux vector in Equation 4.60 is up-winded, according with the sign of the advection velocity involved in the inter-cell Mach number,  $M_{i+1/2}$ , which is defined as:

$$M_{i+1/2} = M_i^+ + M_{i+1}^- \quad (4.62)$$

For the Mach number splitting, similar to van Leer (in MUSCL), Liou and Steffen denote:

$$M^\pm = \begin{cases} \pm \frac{1}{4}(M \pm 1)^2 & \text{if } |M| \leq 1, \\ \frac{1}{2}(M \pm |M|) & \text{if } |M| > 1. \end{cases} \quad (4.63)$$

The pressure part of the numerical flux is also split:

$$p_{i+1/2} = p_i^+ + p_{i+1}^- \quad (4.64)$$

where two options arise for the calculation of  $p_i^\pm$ , namely:

$$p^\pm = \begin{cases} \frac{1}{2}p(M \pm 1) & \text{if } |M| \leq 1, \\ \frac{1}{2}p \frac{(M \pm |M|)}{M} & \text{if } |M| > 1. \end{cases} \quad (4.65)$$

and

$$p^\pm = \begin{cases} \frac{1}{4}p(M \pm 1)^2(2 \mp M) & \text{if } |M| \leq 1, \\ \frac{1}{2}p \frac{(M \pm |M|)}{M} & \text{if } |M| > 1. \end{cases} \quad (4.66)$$

The original method proposed by Liou and Steffen [73] for standard compressible aerodynamic flows, was later substantially improved with the AUSM+ method [71] so it gained more accuracy and robustness. To extend its capacities to all speed regimes and multiphase flow, the method was further improved in [72] (AUSM+-up), [32] and [14].

The main features of AUSM+ method, which made us opt for it to resolve our particular problem, are detailed below:

- It captures in a precise way shock waves and other discontinuities,
- The solution satisfies the entropy condition,
- The algorithm is quite simple (it does not need to explicitly know the Jacobian eigenvalues or eigenvectors),
- The scheme is free of the “carbuncle” phenomenon and
- Convergency and accuracy are uniform for any Mach number.

Since the method does not require to know the eigenvectors and eigenvalues, it is specially appealing for systems whose eigenstructure is unknown, as in the model of conservation equations for two phases (gas and particles) with multiple source terms in Equation 3.37.

#### 4.3.2.7 AUSM+ for Euler equations with multiple species

As mentioned before, the convective part of the system (i.e. [Equation 4.25](#)) is solved separately for each phase. A different version of the AUSM+ scheme is implemented for each one, due to the distinctive features of gas and solid phases. Let us now present a particular version of the AUSM+ scheme for model of equations of gas phase with multiple species. Indeed, the resolution of a homogeneous system of Euler equations is addressed, and equations for mass fractions  $Y_{g,i}$  are accounted.

Thus, we can proceed to the implementation of the scheme, by defining both components (convection and pressure parts) of the approximate numerical flux (the one-dimensional version of the method is shown for simplicity):

$$f_{i+\frac{1}{2}}^{(c)} = \dot{m}_{g1/2} \begin{cases} \Psi_L & \text{if } \dot{m}_{g1/2} > 0, \\ \Psi_R & \text{otherwise,} \end{cases}, \quad \Psi = \begin{bmatrix} 1 \\ u_g \\ (E_g + p)/\rho_g \\ Y_{g,i} \end{bmatrix}, \quad (4.67)$$

$$f_{i+\frac{1}{2}}^{(p)} = \begin{bmatrix} 0 \\ p_{1/2} \\ 0 \\ 0 \end{bmatrix}. \quad (4.68)$$

#### 4.3.2.8 AUSM+ for the particle phase

Let us recall the highly-diluted model we chose for the description of the two-phase flow incorporate the assumption that pressure does not affect the solid phase (see [Chapter 3](#)). Then, as the pressure term is not present in the physical fluxes of particle phase, the numerical flux is purely convective.

As the solid is considered as incompressible and sound speed in solid is constant, the numerical fluxes might be redefined in terms of numeric velocity of particles at the intercells:

$$f_{i+\frac{1}{2}} = \dot{m}_{g1/2} \begin{cases} \Psi_L & \text{if } \dot{m}_{g1/2} > 0, \\ \Psi_R & \text{otherwise,} \end{cases}, \quad \Psi = \begin{bmatrix} 1 \\ u_p \\ (c_p T_p + \frac{1}{2} u_p^2) \\ Y_p \end{bmatrix}. \quad (4.69)$$

The numerical mass flow rate can be calculated as a function of left (L) and right (R) states as follows:

$$\dot{m}_{g1/2} = \rho_p \left( u_{pL}^+ (1 - \alpha_L) + u_{pR}^+ (1 - \alpha_R) \right), \quad (4.70)$$

where the *void fraction*  $\alpha = 1 - \sigma/\rho_p$  and the numeric velocity of particles are defined as:

$$u_p^\pm = \frac{1}{2} (u_p \pm |u_p|). \quad (4.71)$$

#### 4.4 SOURCE TERMS SOLUTION

Let us introduce now the new Advanced Source-Term Treatment (ASTT) approach. In order to solve the ODE (Equation 4.26), it is done in four fractional steps. Firstly, we will solve for the interfacial friction (represented by the operator  $L_f^{\Delta t}$ ), then for the interfacial heat transfer ( $L_{ht}^{\Delta t}$ ), afterwards the combustion terms ( $L_c^{\Delta t}$ ), and finally we address the resolution of the rest of source terms,  $L_g^{\Delta t}$  (gravity in this particular case).

Thus, the solution operator for the ODE system,  $L_s^{\Delta t}$  in Equation 4.27, can be expressed as:

$$L_s^{\Delta t} = L_g^{\Delta t} L_c^{\Delta t} L_{ht}^{\Delta t} L_f^{\Delta t} \quad (4.72)$$

The proposed splitting strategy plays a key role in the successful computation of reactive gas-solid mixtures (under adverse conditions, such as low pressure, small particle diameters or high density of particles). For the type of problems we are dealing with (see Section 5.3), we can state a combination of parameters constituting a threshold beyond which the ASTT method is needed: given a pressure of 4200 Pa, a particle diameter of 4 microns and temperature of 300 K (as in ITER test specifications), the conventional method will fail, if concentration is greater than 7.36 kg/m<sup>3</sup>. If concentration is fixed to the nominal value of 119.86 kg/m<sup>3</sup> of the test, the diameters could not be smaller than 6.9 microns, otherwise the advanced treatment should be used. Numerical examples are given later in Chapter 5 to illustrate the performance of the ASTT method even in those situations when the conventional method yields no solution.

## 4.4.1 First step: friction terms

If only source terms that account for friction were considered as a first step, the system of ODEs to solve would be:

$$\frac{\partial \rho_g}{\partial t} = 0 \quad (4.73)$$

$$\frac{\partial \rho_g \vec{u}_g}{\partial t} = -\vec{F}_d \quad (4.74)$$

$$\frac{\partial \rho_g E_g}{\partial t} = -\vec{F}_d \vec{u}_p \quad (4.75)$$

$$\frac{\partial \sigma}{\partial t} = 0 \quad (4.76)$$

$$\frac{\partial \sigma \vec{u}_p}{\partial t} = \vec{F}_d \quad (4.77)$$

$$\frac{\partial \sigma E_p}{\partial t} = \vec{F}_d \vec{u}_p \quad (4.78)$$

We follow a similar procedure to that introduced by Saurel and Abgrall [107], with some differences. Friction terms considered are a function of the relative velocity  $|\vec{u}_g - \vec{u}_p|$ . In fact, the typical form of the drag force includes the product  $|\vec{u}_g - \vec{u}_p| (\vec{u}_g - \vec{u}_p)$  that makes the evaluation more complex. Let us denote by the superscript “0” the initial state and with no index the new state we have after the different integrations. Let us integrate now the mass conservation equations (Eqs. 4.73 and 4.76):

$$\rho = \rho^0 \text{ and } \sigma = \sigma^0. \quad (4.79)$$

If we sum the momentum equations (Eqs. 4.74 and 4.77), we have

$$\frac{\partial \rho_g \vec{u}_g}{\partial t} + \frac{\partial \sigma \vec{u}_p}{\partial t} = 0 \quad (4.80)$$

Let us integrate Equation 4.80. If we bear in mind the mass conservation equations (Eqs. 4.73 and 4.76), it is possible to obtain the following:

$$\rho_g (\vec{u}_g - \vec{u}_g^0) + \sigma (\vec{u}_p - \vec{u}_p^0) = 0 \quad (4.81)$$

which allows us to express the update of the particle velocity as

$$\vec{u}_p = \vec{u}_p^0 - \frac{\rho_g}{\sigma} (\vec{u}_g - \vec{u}_g^0) \quad (4.82)$$

We can also transform the momentum equations into

$$\frac{\partial \vec{u}_g}{\partial t} = -\frac{1}{\rho_g} \vec{F}_d \quad (4.83)$$

and

$$\frac{\partial \vec{u}_p}{\partial t} = \frac{1}{\sigma} \vec{F}_d \quad (4.84)$$

and write down the time derivative of the relative velocity as:

$$\frac{\partial(\vec{u}_g - \vec{u}_p)}{\partial t} = -\left(\frac{1}{\rho_g} + \frac{1}{\sigma}\right)\vec{F}_d = \frac{\pi}{8}d_p^2\rho_g C_d |\vec{u}_g - \vec{u}_g^0| (\vec{u}_g - \vec{u}_g^0) \quad (4.85)$$

If we define, for simplicity,  $\xi_x = u_{g,x} - u_{p,x}$ ;  $\xi_y = u_{g,y} - u_{p,y}$ ;  $\xi_z = u_{g,z} - u_{p,z}$ ;  $A = -(\rho_g - \sigma)\frac{\pi}{8}\frac{d_p^2}{m_p}$  and  $B = 28\left(\frac{\rho_g d_p}{\mu_g}\right)^{-0.85}$ ; then Equation 4.85 turns into:

$$\frac{\partial \xi_x}{\partial t} = A\xi_x(\xi_x^2 + \xi_y^2 + \xi_z^2)^{\frac{1}{2}} \left(0.28 + B(\xi_x^2 + \xi_y^2 + \xi_z^2)^{\frac{-0.85}{2}}\right) \quad (4.86)$$

$$\frac{\partial \xi_y}{\partial t} = A\xi_y(\xi_x^2 + \xi_y^2 + \xi_z^2)^{\frac{1}{2}} \left(0.28 + B(\xi_x^2 + \xi_y^2 + \xi_z^2)^{\frac{-0.85}{2}}\right) \quad (4.87)$$

$$\frac{\partial \xi_z}{\partial t} = A\xi_z(\xi_x^2 + \xi_y^2 + \xi_z^2)^{\frac{1}{2}} \left(0.28 + B(\xi_x^2 + \xi_y^2 + \xi_z^2)^{\frac{-0.85}{2}}\right) \quad (4.88)$$

Let us call  $\Xi = (\xi_x, \xi_y, \xi_z)^t$ . Then, we can write the system of equations above in vector form as:

$$\frac{\partial \Xi}{\partial t} = S. \quad (4.89)$$

Integrating, we have:

$$\frac{\Xi - \Xi^0}{\Delta t} = S \quad (4.90)$$

Linearising  $S$  around  $\Xi^0$  gives:

$$\frac{\Xi - \Xi^0}{\Delta t} = S^0 - \left(\frac{\partial S}{\partial \Xi}\right)^0 (\Xi - \Xi^0) \quad (4.91)$$

Once we have got  $\Xi$ , we can determine  $\vec{u}_g$  and  $\vec{u}_p$  from the value of  $\xi_x$ ,  $\xi_y$ , and  $\xi_z$ , by considering Equation 4.81. Let us proceed to integrate now the energy equations. Here we follow recommendation from Saurel and Abgrall [107]. Considering mass conservation equations (Eqs. 4.73 and 4.76) we can re-write energy equations (Eqs. 4.75 and 4.78) as

$$\rho_g \frac{\partial E_g}{\partial t} = \rho_g \frac{\partial e_g}{\partial t} + \rho_g \frac{\partial |\vec{u}_g|^2 / 2}{\partial t} = \rho_g \frac{\partial e_g}{\partial t} + \rho_g \vec{u}_g \frac{\partial \vec{u}_g}{\partial t} = -\vec{F}_d \vec{u}_p \quad (4.92)$$

$$\sigma \frac{\partial E_p}{\partial t} = \rho_g \frac{\partial e_p}{\partial t} + \sigma \frac{\partial |\vec{u}_p|^2 / 2}{\partial t} = \sigma \frac{\partial e_p}{\partial t} + \sigma \vec{u}_p \frac{\partial \vec{u}_p}{\partial t} = \vec{F}_d \vec{u}_p \quad (4.93)$$

which turns into

$$\rho_g \frac{\partial e_g}{\partial t} - \vec{F}_d \vec{u}_g = -\vec{F}_d \vec{u}_p \quad (4.94)$$

$$\sigma \frac{\partial e_p}{\partial t} + \vec{F}_d \vec{u}_p = \vec{F}_d \vec{u}_g \quad (4.95)$$

The integration of Eqs. 4.92 and 4.93 yields

$$e_g = e_g^0 + \frac{1}{\rho_g} \vec{F}_d(\vec{u}_g - \vec{u}_p) \Delta t, \quad (4.96)$$

and  $e_p = e_p^0$ , or in terms of temperatures,

$$T_g = T_g^0 + \frac{\gamma_g}{c_{pg} \rho_g} \vec{F}_d(\vec{u}_g - \vec{u}_p) \Delta t \quad (4.97)$$

and  $T_p = T_p^0$ .

#### 4.4.2 Second step: heat transfer terms

In this case, the system of ODEs to solve only accounts for source terms for inter-phase heat transfer:

$$\frac{\partial \rho_g}{\partial t} = 0 \quad (4.98)$$

$$\frac{\partial \rho_g \vec{u}_g}{\partial t} = \vec{0} \quad (4.99)$$

$$\frac{\partial \rho_g E_g}{\partial t} = -Q_g \quad (4.100)$$

$$\frac{\partial \sigma}{\partial t} = 0 \quad (4.101)$$

$$\frac{\partial \sigma \vec{u}_p}{\partial t} = \vec{0} \quad (4.102)$$

$$\frac{\partial \sigma E_p}{\partial t} = Q_g. \quad (4.103)$$

From the integration of Eqs. 4.98, 4.99, 4.101, and 4.102, we obtain  $\sigma = \sigma^0$ ,  $\rho = \rho^0$ ,  $\vec{u}_g = \vec{u}_g^0$ , and  $\vec{u}_p = \vec{u}_p^0$ . Following a procedure similar to that applied above, Eqs. 4.100 and 4.103 can be transformed into

$$\rho_g \frac{\partial E_g}{\partial t} = \rho_g \frac{\partial}{\partial t} \left( \frac{c_{pg}}{\gamma_g} T_g + \frac{|\vec{u}_g|^2}{2} \right) = -Q_g \quad (4.104)$$

$$\sigma \frac{\partial E_p}{\partial t} = \sigma \frac{\partial}{\partial t} \left( c_{pp} T_p + \frac{|\vec{u}_p|^2}{2} \right) = Q_g \quad (4.105)$$

which finally are reduced to

$$\rho_g c_{pg} \frac{\partial}{\partial t} T_g = -Q_g \quad (4.106)$$

$$\sigma c_{pp} \frac{\partial}{\partial t} T_p = Q_g \quad (4.107)$$

Subtracting Eqs. 4.106 and 4.107, we have

$$\frac{\partial}{\partial t} (T_g - T_p) = - \left( \frac{\gamma_g}{c_{pg} \rho_g} + \frac{1}{\sigma c_{pp}} \right) Q_g \quad (4.108)$$

which turns into

$$\frac{\partial}{\partial t}(\Gamma_g - \Gamma_p) = - \left( \frac{\gamma_g}{c_{pg}\rho_g} + \frac{1}{\sigma c_{pp}} \right) C(\Gamma_g - \Gamma_p) \quad (4.109)$$

where  $C = \frac{\sigma}{m_p} \pi d_p \mu_g c_{pg} \text{Pr}^{-1} \text{Nu}$ . Solving Equation 4.109 for  $(\Gamma_g - \Gamma_p)$  we have

$$(\Gamma_g - \Gamma_p) = (\Gamma_g^0 - \Gamma_p^0) \exp \left[ - \left( \frac{\gamma_g}{c_{pg}\rho_g} + \frac{1}{\sigma c_{pp}} \right) C \Delta t \right] \quad (4.110)$$

In Equation 4.110 it is assumed that:  $\text{Re} \approx \text{Re}^0$ ,  $\text{Pr}_g \approx \text{Pr}_g^0$ , and  $\mu_g \approx \mu_g^0$ ,

On the other hand, the sum of Eqs. 4.106 and 4.107 gives us:

$$\rho_g \frac{c_{pg}}{\gamma_g} \frac{\partial}{\partial t} \Gamma_p = 0, \quad (4.111)$$

which can be integrated to have:

$$\Gamma_p = \Gamma_p^0 - \frac{\rho_g c_{pg}}{\sigma c_{pp} \gamma_g} (\Gamma_g - \Gamma_g^0). \quad (4.112)$$

Finally,  $\Gamma_g$  and  $\Gamma_p$  are obtained from both Eqs. 4.111 and 4.112.

#### 4.4.3 Third step: integration of the reactive source terms

This step in the resolution of the source terms addresses those relating to chemical reaction. For the integration of those terms, an implicit backward Euler method proposed by Beccantini [8] is chosen. This is a robust time integration scheme reported for the combustion of multicomponent gas mixtures. Let us consider the ODEs for gas phase, with chemical source terms:

$$\frac{\partial \rho_g}{\partial t} = \Gamma \quad (4.113)$$

$$\frac{\partial \rho_g \vec{u}_g}{\partial t} = \Gamma \vec{u}_p \quad (4.114)$$

$$\frac{\partial E_g}{\partial t} = \Gamma E_p + \alpha Q_c \quad (4.115)$$

$$\frac{\partial \rho_g Y_{g,i}}{\partial t} = \dot{\omega}_{g,i} \quad (4.116)$$

Eqs. 4.113, 4.114, and 4.115 are directly discretised and integrated, once we know the value of  $\Gamma$ , for what we need first to solve Equation 4.116. Note that there are so many equations as species in gas phase. For a species  $i$ , we re-write the consumption equation Equation 4.116 as:

$$\frac{\partial(\rho_g Y_{g,i})}{\partial t} = K(\rho_g Y_{g,i}) \quad (4.117)$$

with  $K = -\frac{\omega_{g,i}}{\rho_g Y_{g,i}}$  and  $\omega_{g,i}$  the reaction rate of species  $i$ . A first-order integration gives:

$$\frac{(\rho_g Y_{g,i})^{n+1} - (\rho_g Y_{g,i})^n}{\Delta t} = K^n (\rho_g Y_{g,i})^{n+1} \quad (4.118)$$

Then

$$(\rho_g Y_{g,i})^{n+1} = \frac{(\rho_g Y_{g,i})^n}{1 + K^n \Delta t} \quad (4.119)$$

For the solid phase the procedure would be similar.

#### 4.4.4 Fourth step: rest of source terms (gravity)

The integration of the rest of the source terms, including those for gravity acceleration, is done directly by means of the first order approximation:  $U^{n+1} = U^n + \Delta t S^n$ .

#### 4.4.5 Time step modelling for the case of combustion of multiple species

A dynamic time-stepping strategy is implemented in the code which is used for all the applications in this doctoral thesis. In the general case, the most common and simple way to address the time step calculation is by means of a stability constraint, i.e., the Courant's condition, as described in [Section 4.2](#). That stability constraint forces the time step to be lower than a certain value given by [Equation 4.18](#). Notwithstanding, different points of view can and must be taken when dealing with combustion phenomena.

Let us note that no information at all has been found in the literature up to date, about how to compute time step for specific combustion problems, in order to ensure stability. Transient combustion calculations, moreover those involving detonation, tend to be quite demanding for numerical methods and usually pretty small values for CFL are needed. That makes the calculation slower and more computational resources are then required. Let us take a glance at numerical methods. As specified in [Section 4.2](#), a splitting technique is proposed so that the convection-advection problem is first solved and, later, an ODE problem is solved including the source terms. It is easy to understand that two time stepping arise from this dual resolution process. One first determines the time step  $\Delta t_a$  for the advection problem. If this problem is solved by a explicit method, then  $\Delta t_a$  is found from Courant's (CFL) condition as mentioned. The solution of the advection problem is computed at every mesh point  $j$  and the selected stepping time is the minimum among all cells, so the whole domain remains stable. Then, if the ODEs are solved by some implicit method, then there will be no stability restriction on the time step, and therefore one can advance the solution via the ODE solver

by a time  $\Delta t_s = \Delta t_a$  in one go [122]. However, if an explicit method is used to solve the ODEs, then a stable time step  $\Delta t_s$  must first be found. If  $\Delta t_s \geq \Delta t_a$ , then one may again advance the solution via the ODEs by a time  $\Delta t_a$ . But if  $\Delta t_s < \Delta t_a$ , then one possibility is to update via the ODEs in  $n$  steps of size  $\Delta t_s = \Delta t_a/n$ , where  $n$  is a positive integer.

For a specific  $\Delta t$ , besides the stability issue, when reactions are taking place a tricky question is to ensure that not more of a given species is burnt than what there is actually present in a determined cell. This is a physical condition: to make sure that the minimum value of a given mass fraction is not lesser than zero after combustion has ended, i.e.,  $(\rho Y_k) \geq 0$ , for species  $k$ . To ensure the stability constraints are satisfied, as well as mass conservation, two approaches with different complexity are developed for this thesis:

- A first approach can be useful providing few species are present, few chemical reactions are implemented or, at least, species cannot be both reagents and products in the chemical scheme. Thus, let us assume we have  $k = 1, \dots, NRS$  different species that are being consumed due to chemical reactions, and non of them are simultaneously a product of other reactions. Then, the reaction rates  $\dot{\omega}_k$  of these species are all negative, as determined according to the sign of  $\Gamma$  in Equation 3.49, and we can estimate the time required for each species to vanish as:

$$\Delta t_k = \frac{(\rho Y_k)}{|\dot{\omega}_k|} \quad (4.120)$$

We can arrange the burning times for each species from the lowest to highest and, hence, the first species to vanish can be selected. So we define the *combustion* time as  $\Delta t_c = \min_k \{\Delta t_k\}$ . Logically, if a time step  $\Delta t_s$  is set for the ODE resolution, such that  $\Delta t_s > \Delta t_c$ , then the use of  $\Delta t_s$  would lead to negative mass fractions. Instead, the lower time  $\Delta t_c$  should be used for the ODE problem.

Now, with this first approach, the time step finally used one in go for both the advection and ODE problems is  $\Delta t_a = \Delta t_c$ , and this is consistent with stability as long as  $\Delta t_c$  fulfils the Courant's condition.

However, there is a important drawback on the use of this time stepping method. As a detonation wave travels along the domain, there will always be at least one cell where reagents are about to vanish and, then, at any time there will be an infinitesimally small  $\Delta t_c$ . This makes simulations to progress very slowly and, although the final outcome is correct, for large domains this method becomes impractical.

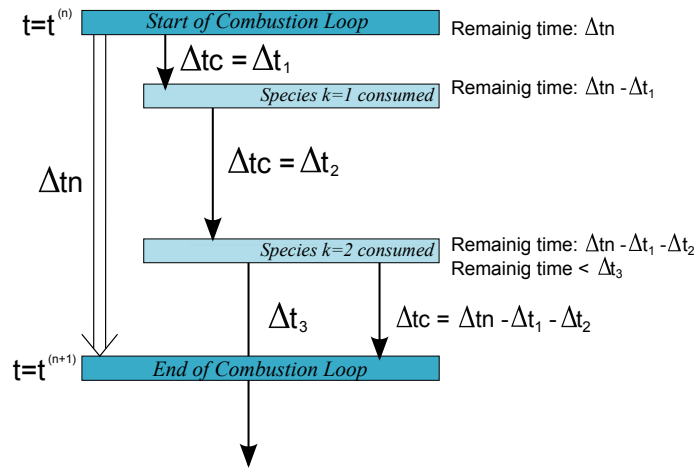


Figure 4.3: Outline of the time stepping strategy for the case of multiple species in multiple reactions. Time period between  $t^{(n)}$  and  $t^{(n+1)} = t^{(n)} + \Delta t_n$ .

- A more general approach has been developed for this thesis allowing to account for multiple reactions where species can be both reagents and products of different reactions. Moreover, it requires less computational resources than the previous one. In this case, the time stepping of the split numerical method, both advection and source terms, is done exclusively under stability criteria. We call this numerical time step,  $\Delta t_n$ . The second constraint, on mass positiveness after combustion, is accounted by means of a *combustion loop* that holds inside each  $\Delta t_n$ .

At this point, the rate of production of species  $k$  in reaction  $i$  can be either positive or negative and Equation 3.48 will determine whether species  $k$  is being generated or consumed in the overall system. Then, for those species such that  $\dot{\omega}_k < 0$ , the burning times are computed according to Equation 4.120, and arranged from lowest to highest. Inside the combustion loop, the different  $\Delta t_k$  are applied sequentially in order to solve the ODE problem only for combustion source terms, starting by the lowest, and without exceeding the numerical time step,  $\Delta t_n$ . A depiction of this time step loop is represented in Figure 4.3 to illustrate the idea.

The loop stops when the total combustion time (the sum of all  $\Delta t_k$  applied so far in the loop) equals  $\Delta t_n$ . Hence, at every turn of the loop, the remaining time must be higher than the following  $\Delta t_k$  to be applied. If this condition is not satisfied at any given time, that would be the last turn of the loop, and finally the remaining time would be set as the last combustion time step. This process is represented in the flowchart of Figure 4.4.

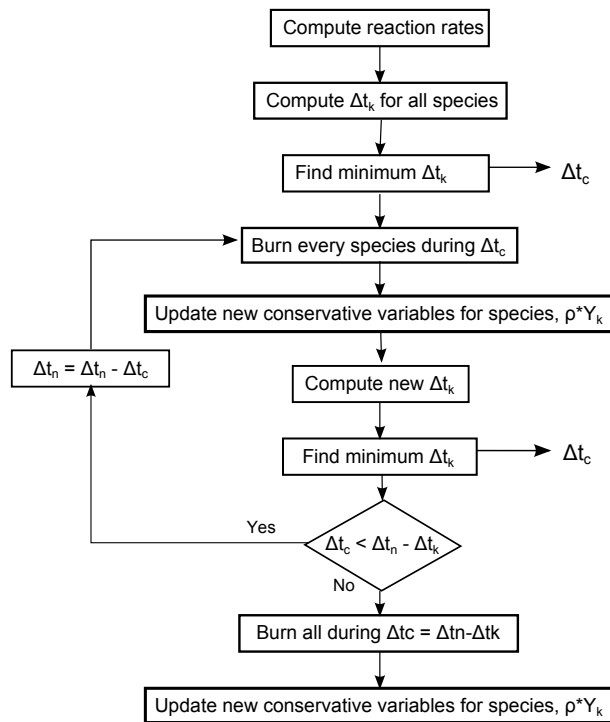


Figure 4.4: Flowchart of the computational loop on combustion time stepping.

#### 4.5 BOUNDARY CONDITIONS

All problems on Computational Fluid Dynamics are defined in terms of initial and boundary conditions. In transient problems, in addition, the initial values of all flow variables need to be specified at all solution points in the flow domain. Since this involves no special measures other than initialising the appropriate data arrays in the CFD code this topic does not need to be further discussed (see [128]).

In order to impose at the domain's boundaries the correct values related to boundary conditions, when constructing a staggered grid arrangement, we set up additional nodes surrounding the physical boundary. The calculations are performed at the internal nodes only. In this way, the physical boundaries coincide with the scalar control volume boundaries and the nodes just outside the physical domain are available only to store the values related to boundary conditions. Those values are chosen to fix the flux to the adjacent cells or in order to set a variable at a cell face, depending on the type of boundary condition to be imposed (inlet, outlet, wall, prescribed pressure, symmetry, periodicity...). In the present work wall and inlet boundary conditions are applied on the numerical tests of [Chapter 5](#) and [Chapter 6](#).

Boundary conditions are directly applied to primitive variables ( $r_g$ ,  $u_g$ ,  $p$ ,  $T_g$ ,  $Y_g$ ,  $\sigma$ ,  $u_p$ ,  $T_p$ ,  $Y_p$ ). In our code, the introduction of the

boundary conditions take place after the conservative variables have been updated for time level  $n$ .

For a one-dimensional domain of length  $L$ , divided in  $M$  uniform cells, the boundaries of the domain are found in the extremes of the domain, i.e. cells 1 and  $M$  (Figure 4.5).

The conservative numerical method (Equation 4.5) can be directly applied to every cell  $i$ , from  $i = 2$  to  $i = M - 1$ . Therefore, for every of those cells, fluxes at the intercell boundaries at  $x_{i-1/2}$  and  $x_{i+1/2}$  are defined in terms of the corresponding Riemann problem. Whilst, for the two extrem cells of the domain, i.e.  $i = 1$  and  $i = M$ , adjacent respectively to the left and the right ends, we only have a numerical flux and, therefore, we must compute the other with any special procedure.

Let us focus on the domain's left boundary. First, one possibility is to assume boundary function  $u_1(t)$  fixed on that point. Then, we could define the flux as  $F_{1/2} = F(u_1(t))$ .

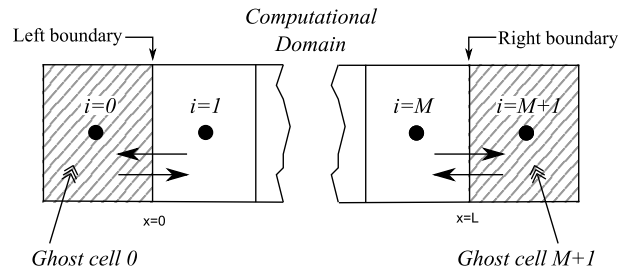


Figure 4.5: Boundary conditions in a 1D domain. Ghost cells outside the computational domain.

Another usual choice is to specify a fictitious cell or *ghost cell* ( $i = 0$ ) at the left boundary ( $x = 0$ ) plus an average value for that cell ( $u_0^n$ ), at each time level  $n$  (Figure 4.5). That way, the cell associated Riemann problem  $RP(u_0^n, u_1^n)$  can be posed and solved to find the missing flow. On the other hand, for the right boundary, a ghost cell can be similarly imposed ( $M + 1$ ) with its average value  $u_{M+1}^n$  in order to find the flux  $F_{M+1/2}$ . The fictitious states that are fixed are totally dependent on the physics in the problem. For the particular case of combustion in a closed vessel, we can choose what is known as *reflective* boundary condition: it physically consists of a fixed, reflective impermeable wall. The fictitious states at both ends,  $i = 0$  and  $i = M + 1$ , are defined from the known states inside the computational domain (at  $i = 1$  and  $i = M$ , respectively), so that the intercell fluxes are  $F_{1/2} = F_{M+1/2} = 0$ . E.g., for the left end:

$$\rho_{g,0}^n = \rho_{g,1}^n; \quad u_{g,0}^n = -u_{g,1}^n; \quad p_0^n = p_1^n; \quad Y_{g,0}^n = Y_{g,1}^n; \quad (4.121)$$

and

$$\sigma_0^n = \sigma_1^n; \quad u_{p,0}^n = -u_{p,1}^n; \quad T_{p,0}^n = T_{p,1}^n; \quad Y_{p,0}^n = Y_{p,1}^n. \quad (4.122)$$

In two-dimensional and three-dimensional models, as is well known, the presence of walls have a fundamental effect on the flow. The adherence condition (or no-slip condition) forces the relative flow speed to be zero just near the walls. All wall-type boundary conditions in this work are assumed to be non-porous, stationary walls.

Regarding the wall friction, many different approaches can be considered, depending on the wall roughness height, the sort of material or the near-wall flux theory used. These phenomena might be taken into account in the model by using the friction coefficient  $\lambda_w$ . Among many others, the following expression proposed by Veyssi ere and Khasainov [131] can be used:

$$\lambda_w = \frac{1}{[1.74 - 2 \ln(2h/d_w)]^2}, \quad (4.123)$$

which is dependent upon the parameter of roughness  $h$ . In fact, it is known that the computed detonation structure is very sensitive to momentum and heat losses to the tube walls. Hence, it is critical that the value chosen for  $h$  is as realistic as possible, as being characteristic of a “technical” roughness of wall surfaces.



Part II

NUMERICAL STUDY



## RESULTS FOR MOBILISATION TESTS

Numerical tests are performed without paying a particular attention to the accuracy of the physical models because the focus is rather on demonstrating the proposed numerical approach allows to tackle difficult test problems; numerically adverse source term conditions, making the system increasingly stiff, will be progressively introduced in 1D test-cases; a complex 3D problem of industrial interest (in the context of the safety analysis of the ITER fusion reactor) will be eventually addressed making use of the methodology proposed in this contribution.

## 5.1 MOBILISATION OF DUST INDUCED BY A 1D SHOCK WAVE

In this section, the influence of the thermodynamic variables in the numerical resolution of a shock tube problem is addressed. The classic Miura and Glass shock tube problem [81] is considered, although the initial pressure values are varied so we can study the propagation of the shock along the tube with different sets of conditions. Then, a sensitivity analysis is made by varying particle diameters and concentrations. Finally, as a second test, the initial values of the Riemann problem are modified, to meet all the adverse conditions where the source terms become stiffer: very low initial pressure, high particle concentration and high density of solid particles.

## 5.1.1 Description of the test

The original shock tube problem posed in [81] consists of a straight tube (1.15 m long in this analysis) in which there are two distinct zones (left and right) separated by a membrane (Figure 5.1) where the initial conditions of Table 5.1 are set.

For the sake of simplicity, this test considers only a mixture of mono-component phases. The gas phase is considered perfect, viscous friction and conduction heat transfer effects are neglected and particles are assumed as spherical with uniform size.

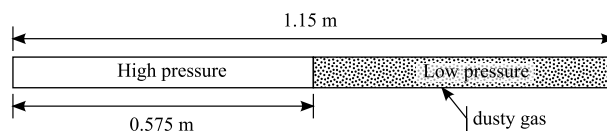


Figure 5.1: Shock tube problem geometry.

	LEFT	RIGHT
$P$ (Pa)	$10p_{\text{ref}}$	$p_{\text{ref}}$
$u_g = u_p$ (m/s)	0	0
$T_g = T_p$ (K)	300	300
$\sigma$ (kg/m <sup>3</sup> )	0	$\rho_g$ ( $10^5$ Pa, 300 K)

Table 5.1: Shock tube problem initial conditions.

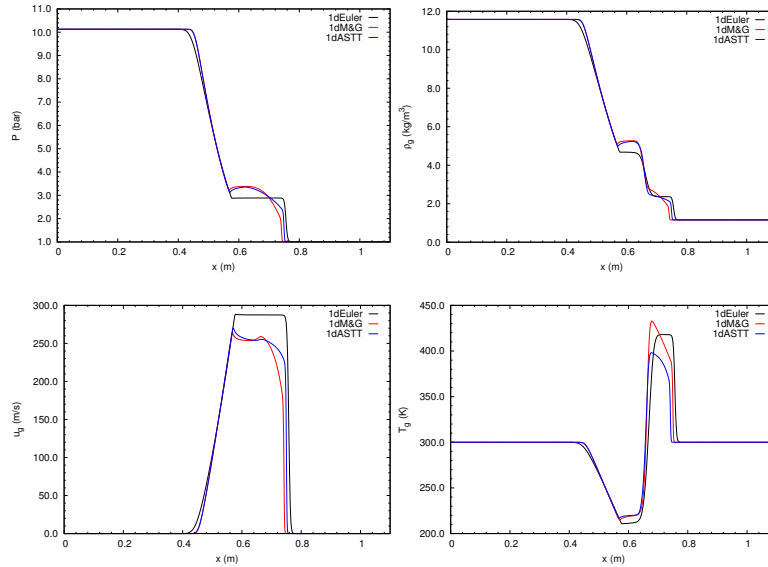


Figure 5.2: Laws for CD from literature, as a function of Re number.

### 5.1.2 Sensitivity Study Numerical results: influence of the thermodynamic variables on the wave structure

First we start with a comparative study of the solution Miura and Glass test which is solved with both the conventional and Advanced Source-Term Treatment. The results (Figure 5.2) are obtained for a case with standard conditions (300 K and 101300 Pa), as in [81]. 4  $\mu\text{m}$  tungsten particles are added in the right half of the tube. Both methods perform quite well under those settings, but the results with the ASTT method are qualitatively better as the dispersion in the shock is reduced.

However, as mentioned before, some difficulties to obtain a numerical solution were found when dealing with the adverse conditions inside the reactor in ITER tests, namely: a fairly low pressure  $p_{\text{ref}} = 0.042$  bar, small particles  $d_p = 4 \times 10^{-5}$  m of W, with a very high density  $\rho_W = 19,386.753$  kg/m<sup>3</sup>, a low  $c_{p,W} = 129.126$  J/(kg·K) and high dust concentration 119.86 kg/m<sup>3</sup>. The first analysis performed consists of a sensitivity study to characterise the influence of the ther-

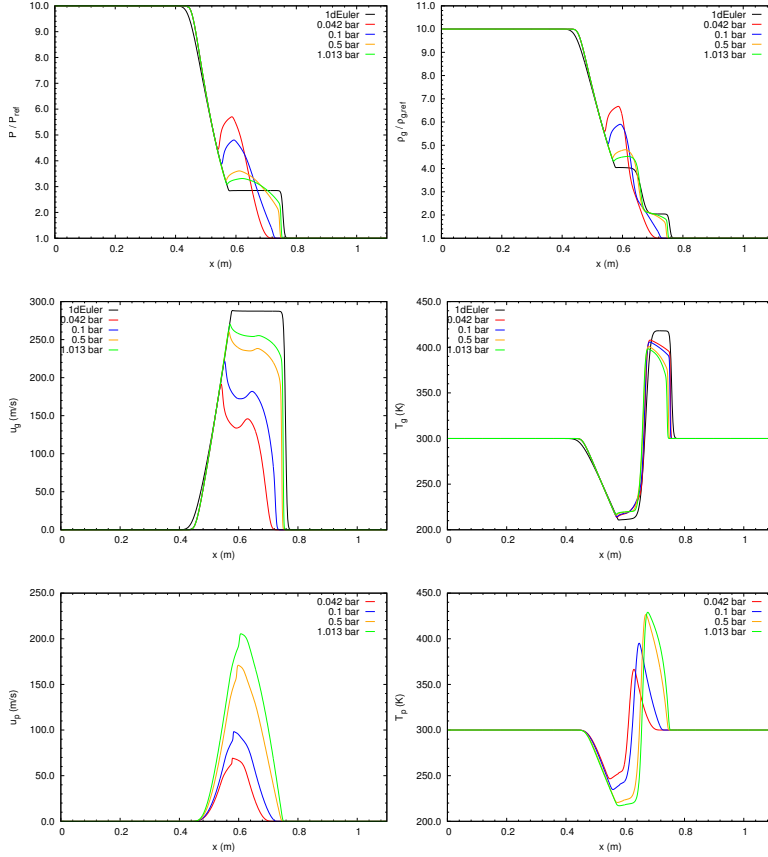


Figure 5.3: Comparison of 1D shock tube problem in the cases of single phase (1dEuler) and two-phase flow at four different reference pressures ( $d_p = 10^{-5}$  m in all cases).

modynamic variables on the wave structure, ranging from what we could state as *standard* conditions, to those just mentioned.

Firstly, the influence of the pressure value on the wave structure is examined. In Figure 5.3 we gather the results corresponding to four different reference pressures  $p_{ref}$ , varying from atmospheric pressure (as in Miura and Glass [81]) to ITER's low pressure. Thus, different  $p_{ref}$  are studied, which are increasingly demanding with numerical methods: 1.013, 0.5, 0.1, 0.042 bar. The reference pressure corresponds to the right state of the shock tube, the left state being characterised by a pressure of  $10 \times p_{ref}$ . In all cases,  $d_p = 10^{-5}$  m, particle density is  $\rho_p = 2500$  kg/m<sup>3</sup> and  $\sigma \approx 1.15$  kg/m<sup>3</sup>. Regarding the numerical scheme, fluxes were evaluated with AUSM schemes in all cases, CFL = 0.5 and the mesh has 500 cells uniformly distributed. The different figures correspond to the distribution of gas density, gas velocity, pressure and gas temperature at time  $t = 1.67 \times 10^{-2}$  s. The two last graphs in Figure 5.3 illustrate the influence of the pressure level on the particles velocity and temperature.

From the inspection of Figure 5.3, we see, when comparing with the only-gas shock tube (labelled as 1dEuler in the figures), that the

gas-particle shock wave by Miura and Glass test (labelled as *1dM&G*) weakens when the reference pressure decreases. Gas velocity and gas temperature maximum values decrease as well. As a consequence, particle velocity and temperature decrease as well and, therefore, particle mobilisation is less “effective” as compression is weaker. Drag force is eventually affected by density (recall Equation 2.48) and then its value will decrease as gas density linearly decreases with pressure.

Let us move on to study the influence of the particle diameter on the different variables. An effect we expected, regarding the movement of the particles, is shown in Figure 5.4: larger particles are more difficult to be moved by the gas phase (carrier phase). So the number of particles mobilised will be higher in the case of the lowest in diameter. This will have an effect on the particle velocity which will decrease with the increase in diameter of the particles. Unlike this, gas velocity increases due to the decrease of the number of particles with the increase of the diameter.

Other effects may be also noticed: The heat transferred to the solid phase is lower for larger particles and therefore the increase of temperature is lower as well. This is because the heat exchange surface decreases with increasing diameters. The effects on gas density and pressure are less important, nevertheless we notice a weakening of the compression wave when the diameter decreases. Thus, at constant particle concentration, the larger the diameter, the lower the influence of particles on the gas phase.

One might wonder what would happen in the opposite case, when increasing the concentration with a constant particle diameter. That would mean to increase the number of particles. The authors propose another study to be tackled in order to assess this effect. Several concentrations  $\sigma = 1, 5, 25, 50, 75,$  and  $119.86 \text{ kg/m}^3$  have been tested. The rest of the variables are set to the original values from Miura and Glass’ test [81]. As shown in Figure 5.5, the effect on the shock is quite interesting; a top value of the particle concentration is found for which the high number of particles avoids the shock wave propagation and particles move with difficulty.

### 5.1.3 Results for Shock Tube Problem under numerically adverse source-term conditions

The shock tube problem is now modified to meet adverse conditions where the source terms become stiffer. The objective of this case corresponds to the specifications of ITER test’s initial conditions (simplified operation conditions), where all the adverse effects mentioned above are set together:  $p_{ref} = 0.042 \text{ bar}$ ,  $d_p = 4 \times 10^{-6} \text{ m}$ ,  $\rho_W = 19386.753 \text{ kg/m}^3$ ,  $c_{p,W} = 129.126 \text{ J/(kg}\cdot\text{K)}$  and  $119.86 \text{ kg/m}^3$ . The initial temperatures are  $T_g = T_p = 300 \text{ K}$  and the stagnation

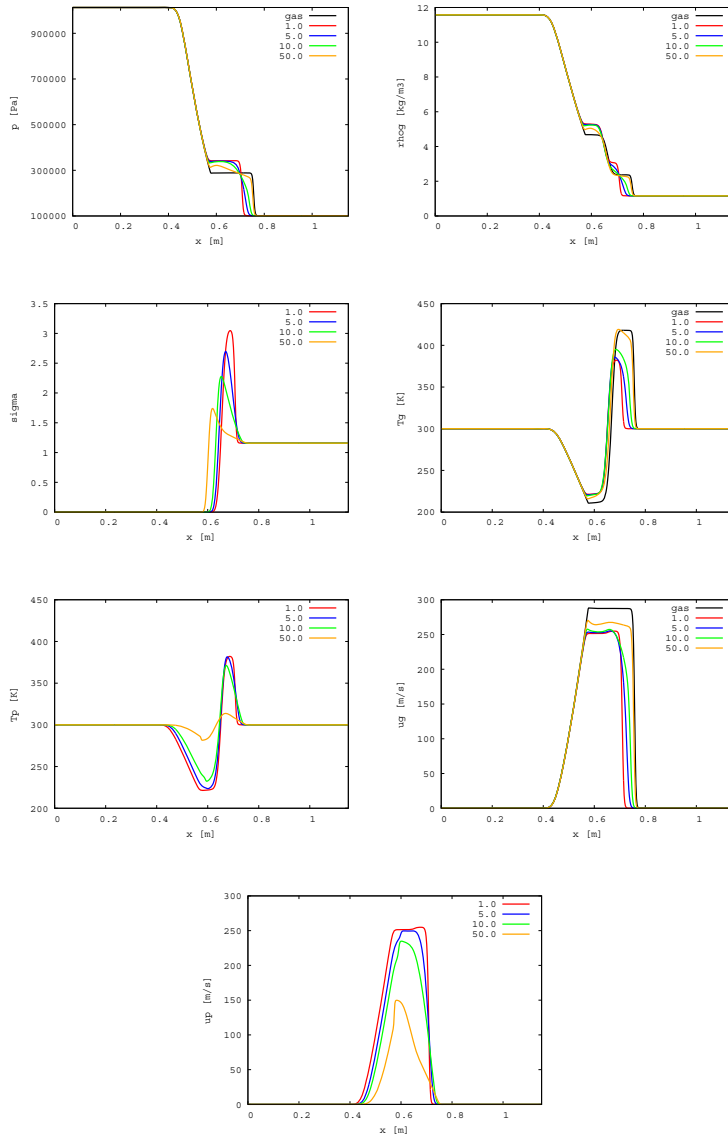


Figure 5.4: Influence of particle diameter ( $\mu\text{m}$ ) on gas and particle variables.

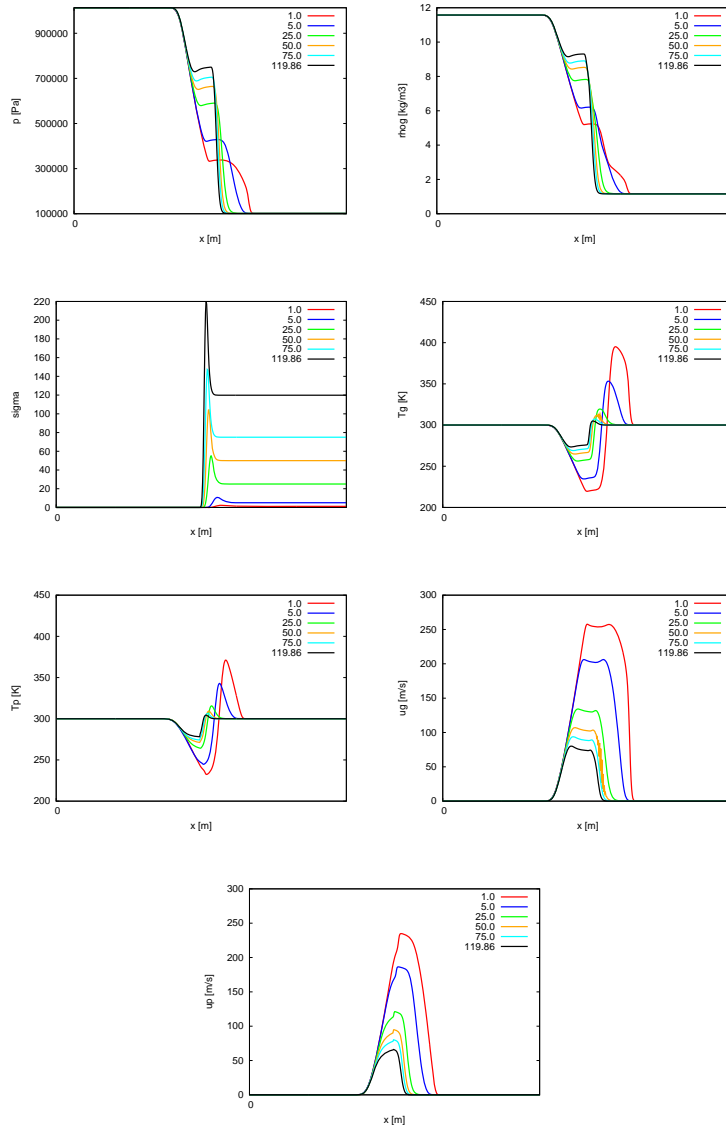


Figure 5.5: Influence of particle concentration on gas and particle variables.

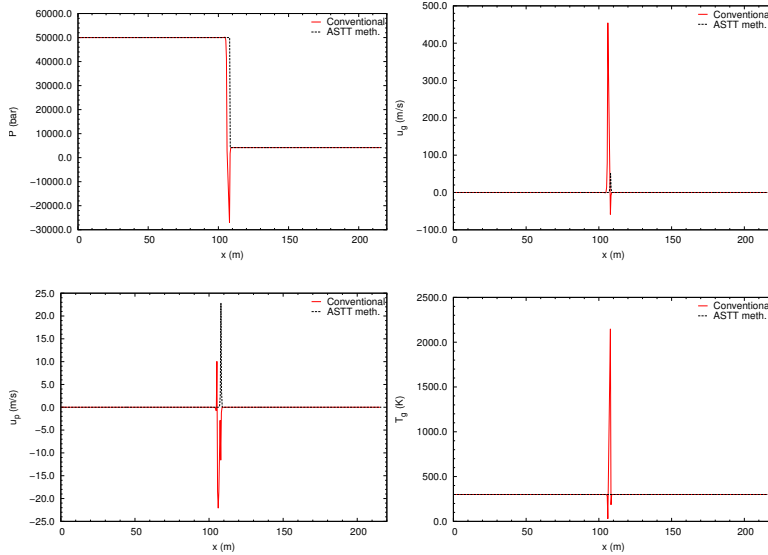


Figure 5.6: Results obtained with both the conventional and the ASTT methods for the ITER adverse initial conditions.  $t = 0.23$  ms, just before the conventional method failure.

conditions:  $p_0 = 10^{-5}$  Pa,  $T_0 = 300$  K. Both phases are initially at rest.

Let us start by analysing the performance of the conventional method under these conditions. The code is not able to run more than a few time steps without the ASTT. With a reduced CFL = 0.008 we are able to achieve a solution for the first 0.23 ms. Those results show a strong oscillation (as represented in Figure 5.6) that leads even to negative values of pressure and temperature near 0 K. The reason for this collapse lies in the instability of the energy equation, caused by the unstable behaviour of the source terms for interfacial heat transport ( $Q_g$ ) and drag ( $\vec{F}_d \cdot \vec{u}_p$ ).

On the contrary, the solution provided with the ASTT (Figure 5.6) shows no alteration. The new integration method is able to compute the simulation, and the results obtained for a shock tube problem posed with these initial values are shown in Figure 5.7 and 5.8. The W problem (labeled as *1dMiuraW*) is evaluated in Figure 5.7, using as a benchmark the only-gas shock tube problem with the same conditions, and the profile of the primitive variables at three different instants ( $t = 1.67 \times 10^{-2}$  s,  $2t$  and  $3t$ ) are compared in Figure 5.8. We see again, as in previous analyses, that high concentrations avoids the progression of the shock wave through the dense mixture. This results in a small effect on the other variables of the right zone of the shock tube problem.

In these cases, in which we have the adverse conditions we mentioned before, the conventional solver we have tested is not able to approximate solutions at all. By contrast, we succeeded by using split-

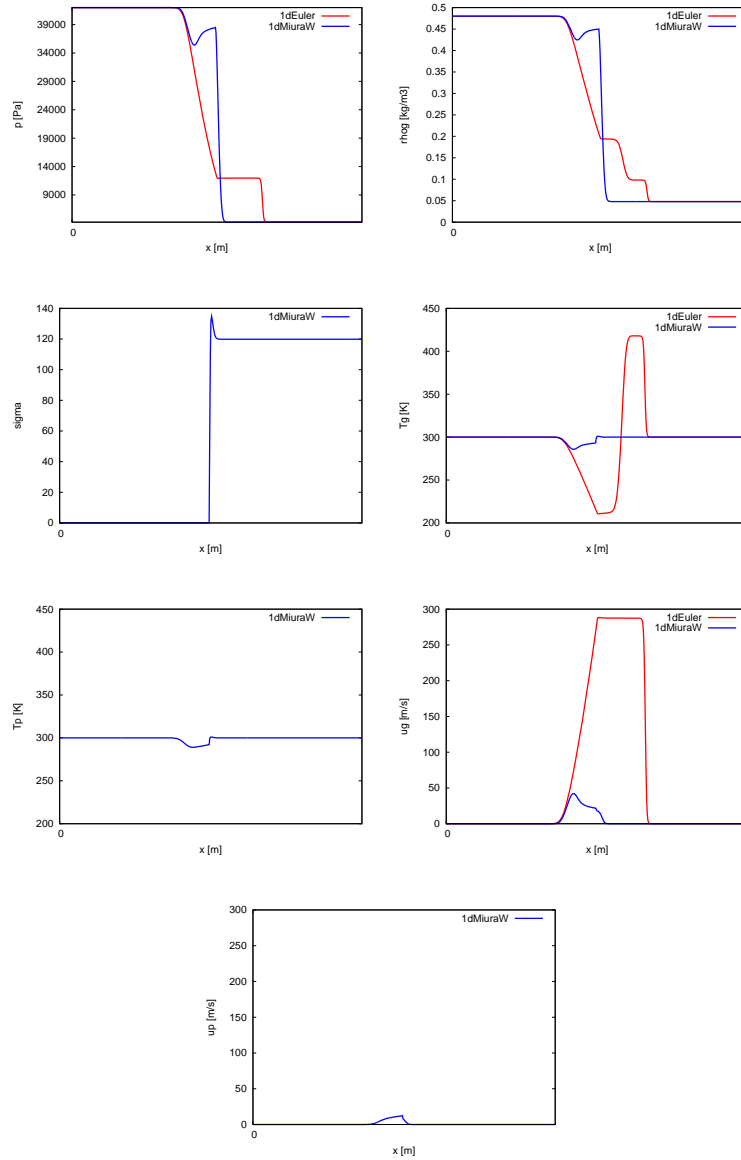


Figure 5.7: Results obtained for the modified problem with W.

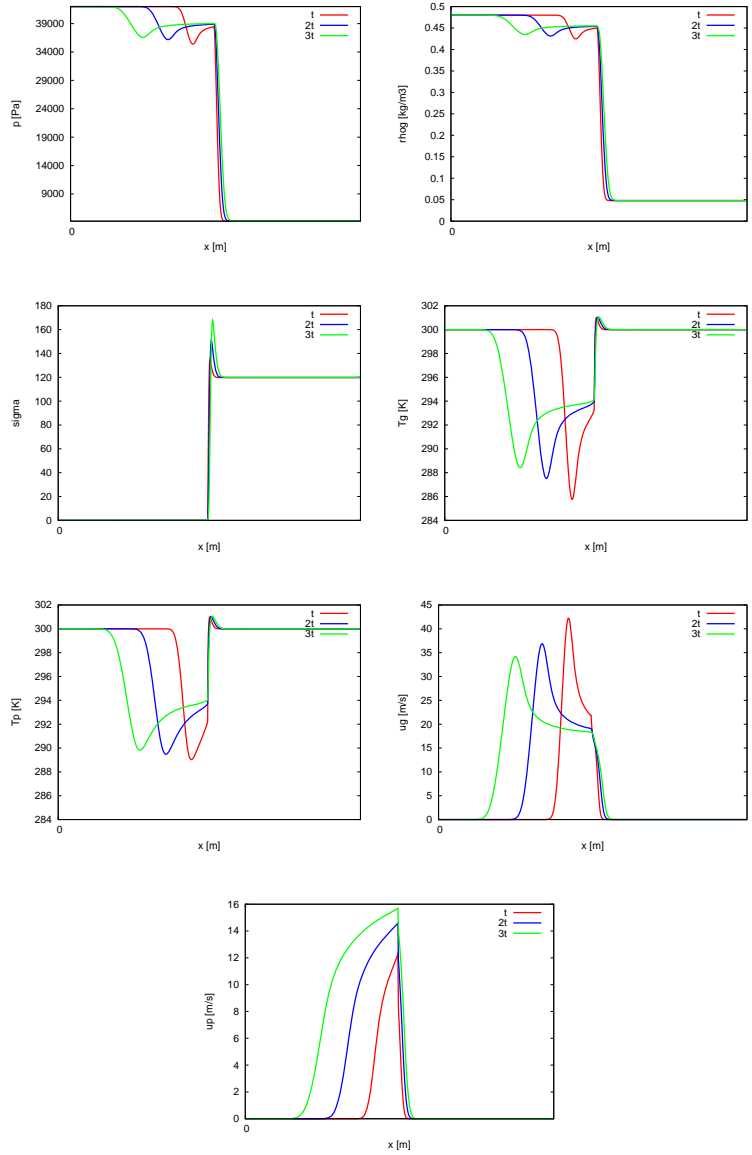


Figure 5.8: Results obtained for the modified problem with W after three different computational times.

ting schemes with the ASTT method. This last, introduced in this study has proved to be more suitable from the viewpoint of the computational time and the CFL required. If we compare the ASTT with other integration schemes for the integration of the ODE of Equation 4.26, such as multi-step Euler method or Runge-Kutta, the new scheme is more effective. We found that only with a tenth order Euler method (or superior) a solution is achieved (with a very low CFL = 0.001). On the other hand 2<sup>nd</sup> order Runge-Kutta cannot deal with this problem. We have checked that ASTT method needs 2.1 seconds (CFL = 0.25) to compute the Miura & Glass test with stiff source terms (Figure 5.7) while 10<sup>th</sup>-order Euler takes 102.8 s (Intel C. i7 Q720 at 1.60GHz, 8GB RAM). This shows the effectiveness of the source term treatment proposed in this study.

#### 5.1.4 Grid convergence study for the one-dimensional shock-wave simulations

In order to demonstrate the grid convergence of the 1D result, a study is presented based on the Miura and Glass test under ITER conditions. Five different one-dimensional grids have been considered, with 100, 240, 500, 1000 and 2000 elements, respectively. This will show the influence of the element size on the results. Let us have in mind that the time step is computed for stability according to Courant's condition (see Section 3), and then  $\Delta t$  is a function on the grid resolution.

All the parameters used for the analysis are taken from last test in Section 5.1.3. The reference pressure is 4200 Pa and the solid phase is assumed to be a fine dust of tungsten particles ( $d_p = 4\mu\text{m}$ ) with  $\sigma = 119.86 \text{ kg/m}^3$ . The final time of the simulation is computed as  $t_{\text{final}} = 4.175 \times 10^{-4} \text{ s}$ . From the different curves depicted in Figure 5.9, it is apparent that grid convergence is actually reached and uncertainties related to the mesh are considerably reduced (results with 1000 and 2000 cells are pretty similar). On the other hand, the intermediate mesh of 500 elements seems to be a compromise choice, as it provides suitable results with a significantly lower computational time.

## 5.2 2D AND 3D DUST MOBILISATION DUE TO RAREFACTION WAVES

In this section we study the behaviour of the proposed numerical treatment for the source terms in the 2D and 3D solution of a rarefaction wave problem when the thermodynamic conditions are adverse. The main goal of this section is to verify the solution of the model of equations in 2D and 3D, with the mathematical complexity they entail, so that it can reproduce the solution of an essentially 1D test, which has been validated in the literature. For this purpose, we will

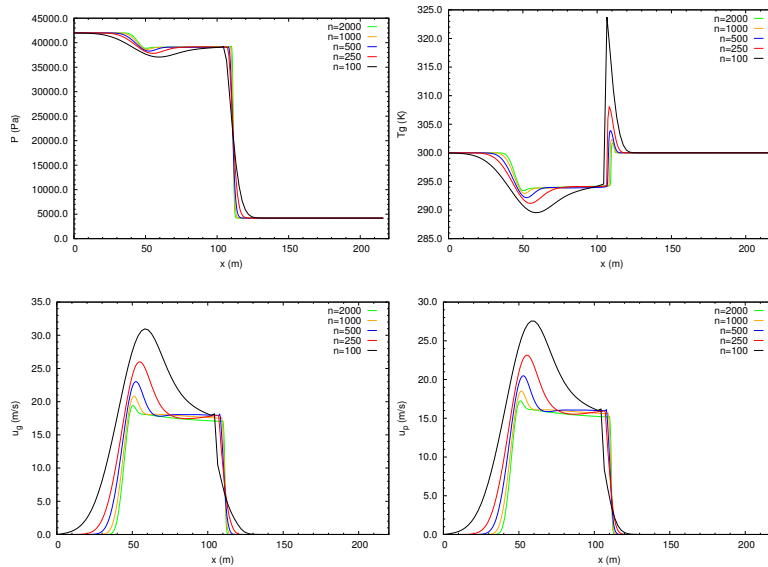


Figure 5.9: Grid convergence analysis for the 1D mesh with Miura & Glass test.

consider the experimental test carried out by Medvedev et al. [78] which analyses the dispersion of a dust layer due to the action of a rarefaction wave. The descriptions of the facility and the experimental results presented by the authors are poor. Despite this, it was studied numerically with some modifications by Klemens and Kosinski [61, 62]. García-Cascales et al. [37] also studied this test for the analysis of highly diluted and dense gas-particles mixture models as well as for the extension of several numerical schemes such as AUSM and Rusanov to gas-particle mixtures.

At first, the proposed test is analysed in order to study the propagation of the problem variables ( $p$  and  $\sigma$ ) with time. First order and second order approximations are used. Then, the problem is modified to meet the adverse conditions for which the source terms become stiffer: very low initial pressure, high particle concentration and high density of solid particles. As in the previous case, first order and second order discretisation schemes are used, but also the ASTT method is needed for the numerical treatment of this problem.

### 5.2.1 Description of the Test

The original problem posed in [78] consists of a long vertical tube which has a 50 mm deposit of particles under high pressure (Figure 5.10) situated at the bottom of the vertical tube. The goal of this test is to prove that the implementation of 2D and 3D system of equations is correct. Indeed, this test can be considered as one-dimensional, but it is modelled with multi-dimensional equations

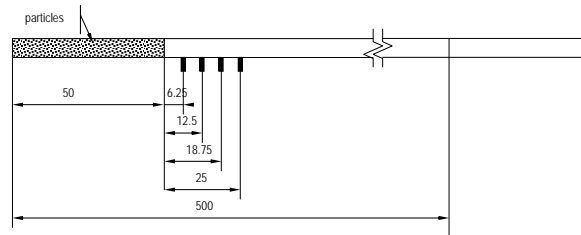


Fig. 11: Dust mobilisation problem geometry.

Figure 5.10: Dust mobilisation problem geometry.



Figure 5.11: 2D mesh for the analysis of dust mobilisation problem provoked by rarefaction waves (the evolution line is depicted in black).

and solved in a lengthened mesh, so that the solution it yields can be matched with that in previous works [37].

On the right side of the figure (i.e. the upper side of the tube), there is a low-pressure region, with an arbitrary length which is separated from the left side (i.e. the bottom side of the tube) by a membrane situated at 500 mm from the left end. When the membrane is removed, a rarefaction wave mobilises the dust layer situated at the bottom of the vertical tube. On the left hand side, four probes are set at 56.25, 62.5, 68.75 and 75 mm, where dust concentration is measured as a function of time (Figure 5.10). In the papers published by Klemens and Kosinski [61, 62], they do not take into account gravity and, in addition, there seem to be differences in the membrane position with respect to [78].

Thus, taking into account these considerations, initial conditions are ambient temperature in both parts ( $T_g = 298$  K), a 2 bar pressure inside the left part and 1 bar in the right part. The phases are supposed initially at rest. Other important initial parameters used to complete the problem definition are the particle concentration, its density and its diameter which are:  $\sigma = 500$  kg/m<sup>3</sup>,  $\rho_p = 2000$  kg/m<sup>3</sup>,  $d_p = 10^{-5}$  m. Regarding the closure laws used, air has been considered as a perfect gas with a specific heat ratio,  $\gamma_g = 1.4$  and  $c_{pg} = 1008$  J/(kg·K). The solid phase is supposed incompressible. Drag force and heat transfer have been considered, the expressions used by Klemens and Kosinski [61, 62] are those proposed by Crowe et al. [24].

As for the computational grid, Figure 5.11 shows a view of the 2D mesh generated with CAST3M in order to solve this problem (a straight line is depicted in black where the evolution of the variables will be represented). Figure 5.12 shows a detailed view of the 3D mesh used for this test.

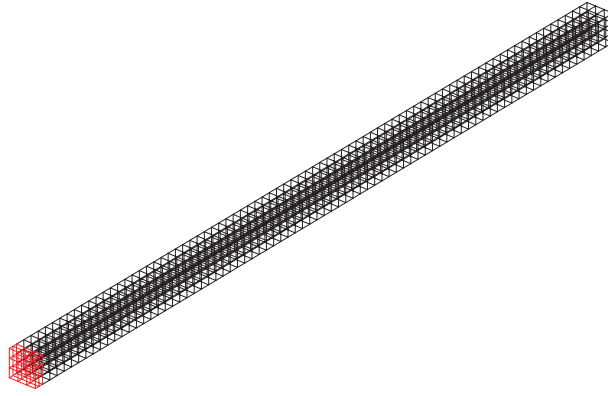


Figure 5.12: 3D mesh for the analysis of dust mobilisation problem provoked by rarefaction waves.

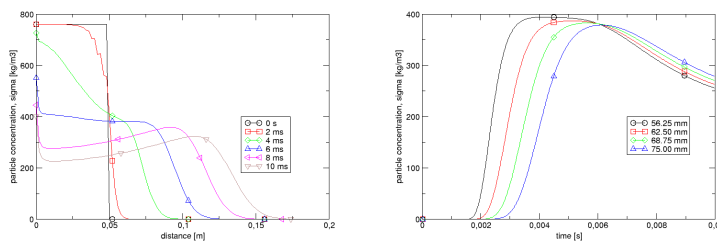


Figure 5.13: Klemens Test. Particle concentration distribution in the tube at different times (left) and evolution of particle concentration at different positions (right). 1<sup>st</sup> order approximation.

### 5.2.2 Numerical results on validation of the numerical source term treatment proposed

A 2D mesh of  $3 \times 2000$  points has been used for all the cases studied and a  $CFL = 0.5$  has been assumed. The results obtained for the particle concentration are shown in Figure 5.13 and 15. Both of them show the distribution of particle concentration at different times  $t = 0, 2, 4, 6, 8$  and  $10$  ms, and the evolution of the dust concentration at several points of the tube. Figure 5.13 is the first order approximation and Figure 5.14 the second order one. As shown, some oscillations appear in the result. They are mostly due to the coarse mesh we have initially considered. If the mesh is refined, the oscillations decrease as is shown in Figure 5.15 for a mesh of  $3 \times 4000$  points. The results provided by Klemens and Kosinski in [61, 62] show the distribution of the particle concentration along the tube for different instants,  $t = 0, 2.5, 5, 7.5,$  and  $10$  ms and the value of dust concentration as a function of time at several positions along the tube. The interested reader may check that the numerical results presented by the authors match quite well with those reported by Klemens and Kosinski [61, 62].

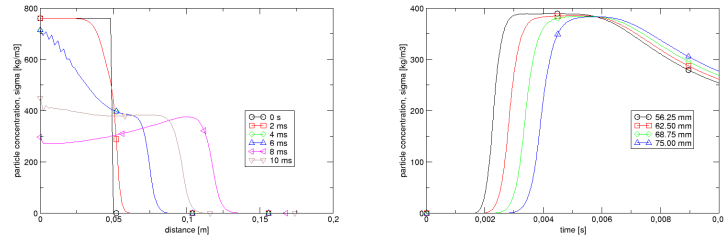


Figure 5.14: Klemens Test. Particle concentration distribution in the tube at different times (left) and evolution of particle concentration at different positions (right).  $2^{\text{nd}}$  order approximation.

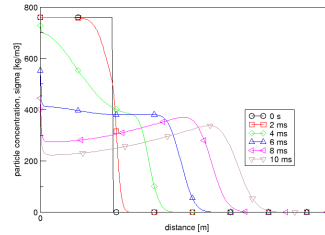


Figure 5.15: Particle concentration distribution in the tube at different times with a finer mesh ( $3 \times 4000$  cells).  $2^{\text{nd}}$  order approximation.

### 5.2.3 Results for the rarefaction wave problem under numerically adverse source term conditions

As in the previous section, we now modify the initial physical conditions of the test towards low initial pressure, high particle density and high particle concentration conditions, where the source terms become stiffer. The new imposed conditions are: Tungsten particles with a  $d_p = 4 \times 10^{-6}$  m of a density of  $\rho_W = 19386.753 \text{ kg/m}^3$  and a specific heat at constant pressure of  $c_{p,W} = 129.126 \text{ J/(kg}\cdot\text{K)}$ . Particle concentration is  $\sigma = 760 \text{ kg/m}^3$ .

Under these conditions, we have checked that the difficulties in the case of dust mobilisation due to a rarefaction wave appear when the diameter of the particles decreases as the interfacial friction term increases considerably, and the terms become so stiff that the numerical scheme cannot deal with these discontinuities. In [Figure 5.16](#) the results corresponding to these adverse initial conditions are shown. The upper plot ([Figure 5.16 up](#)) shows the spatial distribution of concentration for different times  $t = 0, 2, 4, 6, 8, 10$  ms, which only can be given by ASTT method. The central plot ([Figure 5.16 centre](#)) shows the time evolution of the concentration, taken at four different positions. The influence of the rarefaction wave is clearly seen in the plots as it mobilises the particles as soon as it reaches the dust layer.

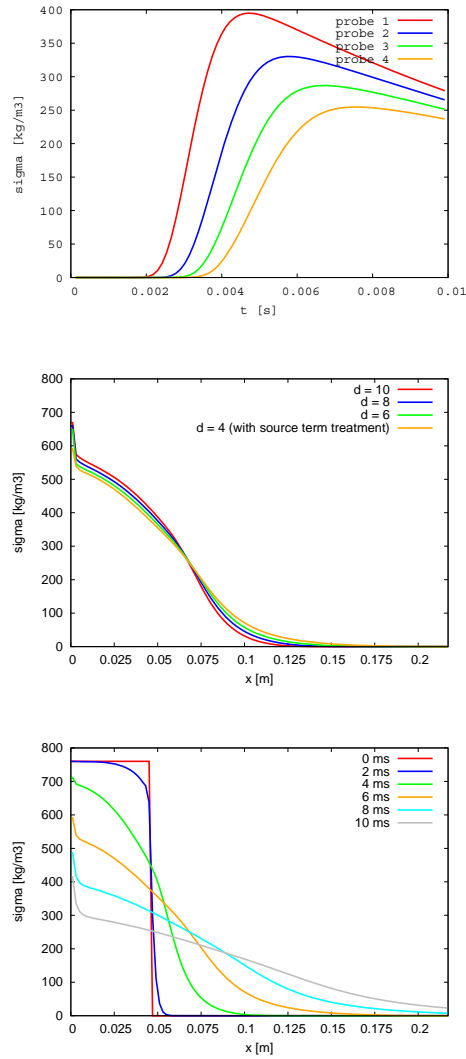


Figure 5.16: Particle concentration distribution evolution at different times (up), particle concentration history at different positions in the tube (centre) and for different particle diameters (down).

Finally, different particle diameters are tested, whilst the rest of parameters are fixed. The last plot (Figure 5.16 down) shows the distribution of the particle concentration along the tube at  $t = 6$  ms for different diameters, 10, 8, 6 and 4  $\mu\text{m}$ . As the diameter decreases, the total surface in contact with air increases (if  $\sigma$  does not vary), and so, the interfacial friction becomes higher. The last two cases (with 6 and 4  $\mu\text{m}$  particles) cannot be evaluated without the ASTT proposed in this paper. By contrast, for higher diameters, and at more relaxed conditions, both methods provide equal results. This shows the effectiveness of the new approach, when facing this kind of numerically adverse physical conditions.

### 5.3 ANALYSIS OF 3D DUST MOBILISATION PROBLEMS INSIDE OF ITER

As mentioned in Section 1.2.1.1, one of the hypothetical events currently considered beyond the design basis in the ITER safety analysis is a LOVA consisting of air ingress into the vacuum vessel causing a pressurisation and a shock wave, followed by a hydrogen deflagration or detonation, plus a possible dust explosion [95]. This event is an aggravation of Reference Event V<sub>3</sub> [121] and could occur in a case where intended hydrogen mitigation measures failed. Understanding of the different transport and combustion phenomena present in those events in the case of severe accident conditions is crucial to ensuring safety. The operation scenario selected for the mobilisation simulation, assumes conditions corresponding to the installation shutdown, with low wall temperature. The initial conditions of the tests considered are:  $p_i = 4200$  Pa,  $T_i = 300$  K,  $d_p = 4 \times 10^{-6}$  m, stagnation condition  $p_0 = 10^{-5}$  Pa,  $T_0 = 300$  K. Particles are of W whose density is assumed constant and equal to  $19386.753$  kg/m<sup>3</sup> and with a specific heat of  $129.126$  J/(kg·K). A concentration at the bottom of the VV of  $119.86$  kg/m<sup>3</sup> is also considered. In other words, 1000 kg of W are considered to be distributed upon the divertor (depicted in red in Figure 5.17).

The mesh has been created taking advantage of the existing symmetry. Figure 5.17 shows an example of the mesh constructed with DUST. The mesh used in the reported calculations presents 48345 elements (its volume ranging from  $1.01 \times 10^{-4}$  m<sup>3</sup> and  $4.43 \times 10^{-2}$  m<sup>3</sup>). The region inside the divertor where dust is concentrated is depicted in red. A breach of 20 cm<sup>2</sup> has been considered (depicted in blue in Figure 5.17). The problem considers a breach situated just beside the divertor through one lower port. Boundary conditions at the inlet are sonic conditions, so the expansion from stagnation to the throat conditions is assumed isentropic.

Several strategies were previously tried to afford numerically this sequence without success due to the numerically adverse physical

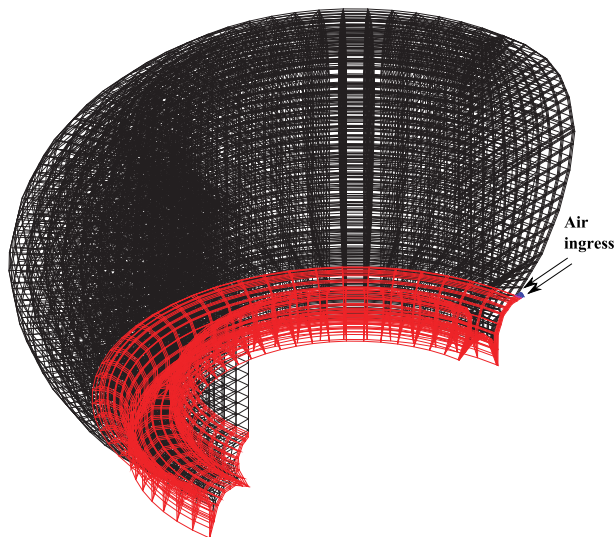


Figure 5.17: ITER VV mesh for the study of the mobilisation problem.

conditions, i.e. a very low initial pressure, small particle size, high particle concentration and very high particle density. As in previous tests, these conditions make the problem become very stiff. The relaxation of this stiffness is obtained with the source term treatment presented in this paper. Again, this shows the effectiveness of this new approach when facing this kind of numerically adverse physical conditions.

In this paper we present the initial 8 seconds of the transient problem. Simulations were performed in a system with two processors *Intel Xeon Quad-Core E5462* running at 2.80 GHz, and using a 1600 MHz FSB. 16 GB of RAM are available. The processor has a theoretical performance of 11.2 GFLOPS. The code is not parallelised yet, although this task is scheduled for the near future. Thus, only one of eight available cores is used for this test. As a result, a CPU time of 132 h approximately is spent to compute the transient until  $t = 8$  seconds (time step is computed by a  $CFL = 0.25$ ).

Figure 5.18 shows the results for the evolution of concentration at several calculation times: from 1 to 8 seconds at intervals of 1 second. Coloured cells are those which are filled with a certain amount of dust, whose concentration is that noted in the contour legend. As shown, the breach generates a shock wave due to the pressure difference and an air jet which sweeps the dust in the bottom of the divertor, promoting the expansion of a dust cloud that covers nearly completely the VV except for the upper side of the ring over the breach.

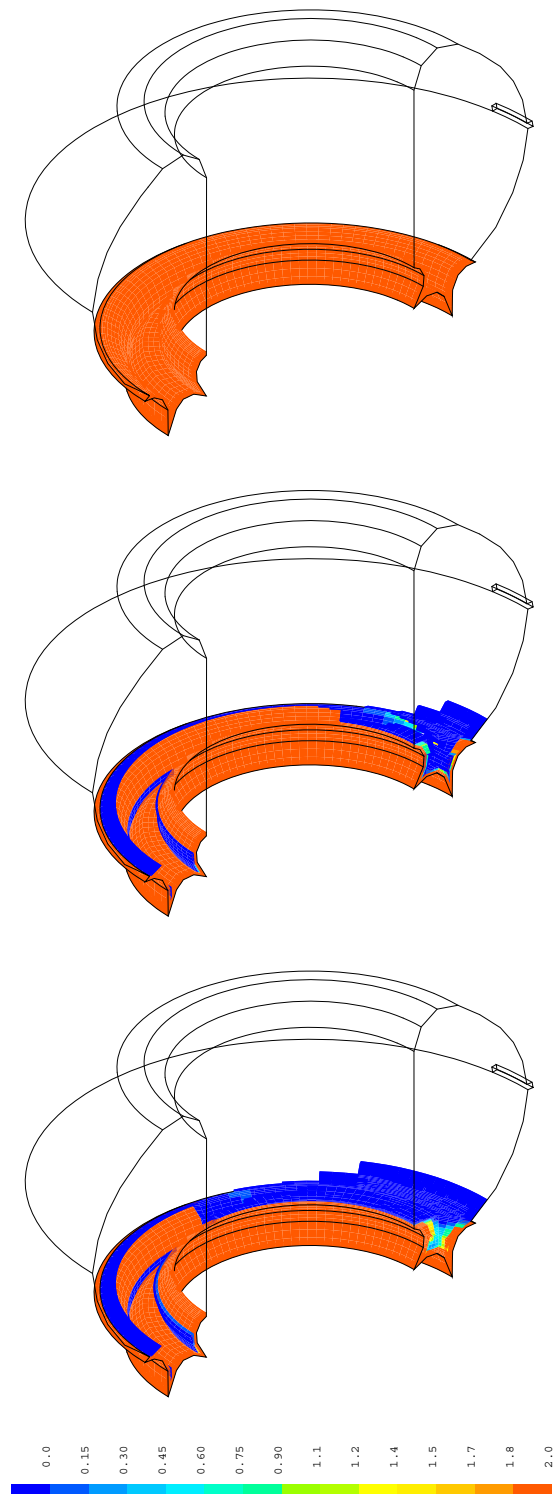
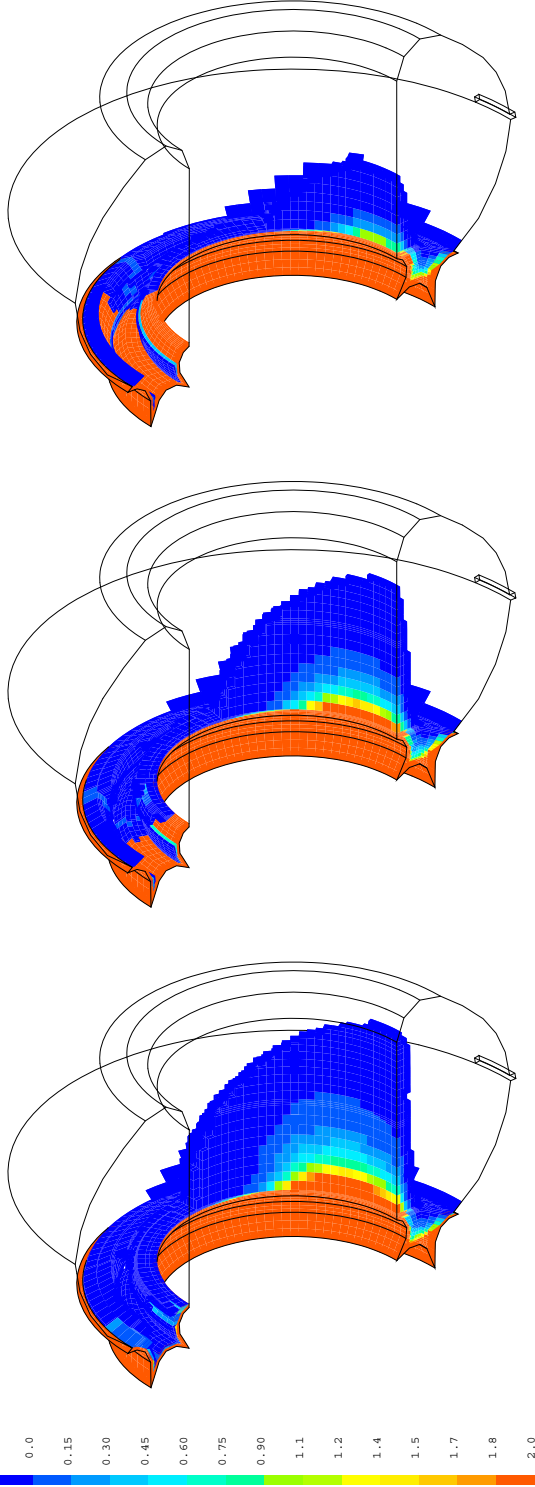
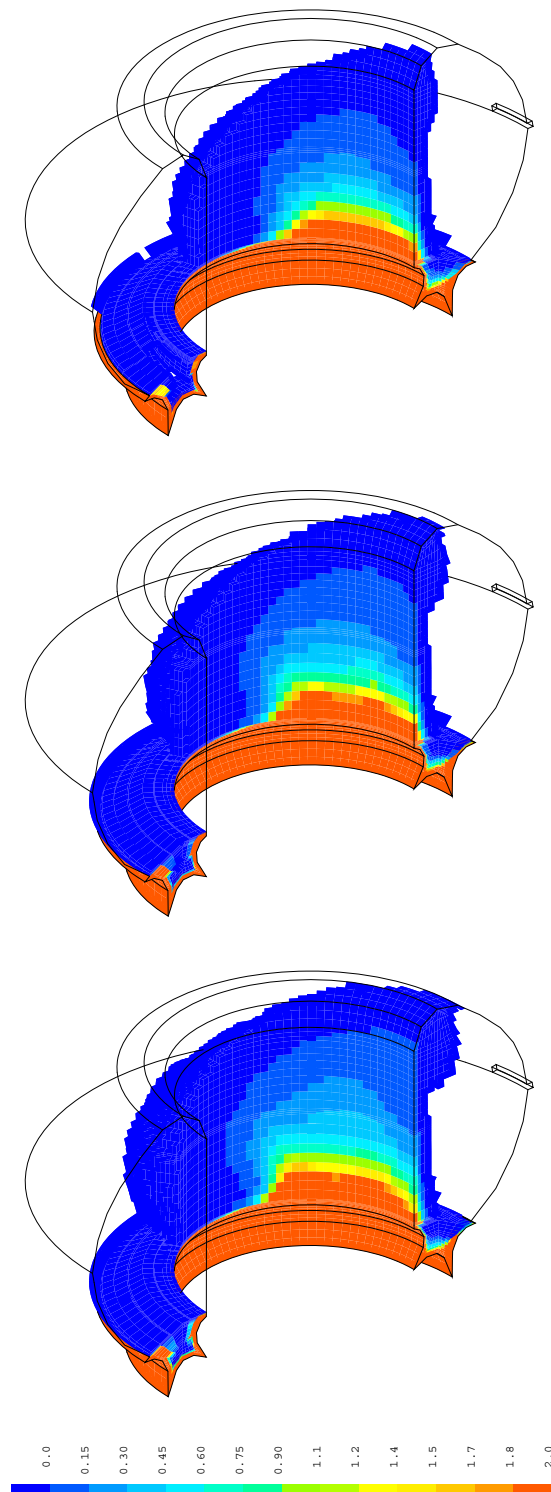


Figure 5.18: Evolution of dust concentration ( $\text{kg}/\text{m}^3$ ) during the mobilisation of particles inside ITER (from  $t = 0$  to  $t = 45.0$  ms).



Evolution of dust concentration ( $\text{kg/m}^3$ ) during the mobilisation of particles inside ITER (from  $t = 67.5$  to  $t = 112.5$  ms).



Evolution of dust concentration ( $\text{kg}/\text{m}^3$ ) during the mobilisation of particles inside ITER (from  $t = 135.0$  to  $t = 180.0$  ms).

## RESULTS FOR COMBUSTION TESTS

---

### 6.1 SHOCK WAVE INDUCED BY COMBUSTION OF PARTICLES IN SUSPENSION: CHEN TEST

After the resolution of the mobilisation problems addressed in [Chapter 5](#), let us move forward into the study of two-phase combustion problems. The first test on two-phase combustion deals with the explosive oxidation of Aluminium dust with atmospheric air in a closed domain.

To this end, experimental results on two-phase combustion reported by Chen et al. [20], [19] are used here to validate the performance of the model of equations previously defined in [Section 3.3](#). The experiments by Chen comprised the study of Aluminium dust explosion within a dry air atmosphere, inside a straight detonation tube, as described briefly in [Section 2.2.1](#). At the first moment, the Al dust suspension is uniformly distributed and fills the available space with a diluted but homogeneous cloud. Since the gas phase is not reactive by itself, the energy to maintain the shock is delivered solely by dust oxidation.

A one-dimensional version of the model of equations was implemented in the code in order to check how reliable the closure laws are, when predicting phenomena related to metal combustion. Later, 2D and full 3D versions of the model of equations were also implemented and applied on the resolution of this test. Again, we deal with a computational test which is essentially one-dimensional, since the extremely elongated geometry of the tube prevents the flame spreads in any direction other than  $x$ , the longitudinal direction of the tube. The solution of the problem in one or more dimensions should produce similar results if multi-dimensional sets of equations have been correctly implemented. The comparison of these results with the benchmark of Chen et al. [20] and [19] allows the validation of the code, as a previous step to other tests featuring more complex geometries.

#### 6.1.1 *Initial conditions and test configuration*

Chen's installation geometry is modelled as a 12 m length, 0.14 m wide, smooth tube (circular cross section), as outlined in [Figure 6.1](#).

The initial conditions can be declared in simple way, since the tube is not divided in different sections with different conditions: only a portion on the left extreme of the tube is assumed to be the initiation

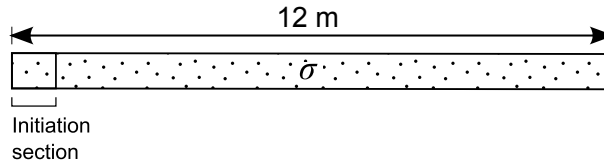


Figure 6.1: Smooth tube geometric model for Chen Test.

section, where a igniting spark is modelled. Pressure is set to 1 bar and  $T = 300$  K all along the tube. The solid phase consists of  $6 \mu\text{m}$  diameter Aluminum particles, and the initial concentration of particles in the mixture is  $\sigma = 500 \text{ g/m}^3$ . Aluminium ignition temperature is assumed to be  $T_{ig} = 1350$  K, though no details are given about this parameter in [20] nor in [19].

As the solid phase is considered to be initially composed by only Aluminium, we expect to get a mixture of Al and  $\text{Al}_2\text{O}_3$  as particles burn. Aluminium density is  $\rho_{\text{Al}} = 2.7 \times 10^3 \text{ kg/m}^3$  and alumina density,  $\rho_{\text{Al}_2\text{O}_3} = 3.97 \times 10^3 \text{ kg/m}^3$ , values which are taken from [83].

The kinetics of the oxidation process of Al dust, referred to as the *combustion model*, is modelled by means of a one-step heterogeneous reaction mechanism reported by Ogle et al. [85]. Some details of the kinetic parameters and the reaction rates were gathered in Section 3.4.2.3. The combustion model has proven to give valid data on aluminium particles oxidation. However, we did realise there is some inconsistency about the kinetic parameters in the original model by Ogle and the version found in Chen and Fan [19]. This last reported values for activation energy, pre-exponential factor, and released reaction heat respectively of:  $E = 8.2 \times 10^4 \text{ kJ/mol}$ ,  $A = 3.8 \times 10^5 (\text{m}^3/\text{kg})^{1/2}/\text{s}$  and  $Q_c = 3.7 \times 10^6 \text{ J/kg}$ . These values are referred to Ogle et al. [85], but if we take a look on this paper, the actual value given for activation energy is different:  $E = 100 \text{ kJ/mol}$ . The fact is, according to our calculations, the real values are  $E = 2 \times 10^5 \text{ kJ/mol}$  and  $Q_c = 1 \times 10^9 \text{ J/kg}$ , for Chen's results to be reproduced.

On other hand, regarding how the reaction is initiated, Chen states that, for achieving a planar flame propagating in the combustion tube, 6 igniters are mounted uniformly on the inner closed end (the left end for our geometric model in Figure 6.1). Each igniter consists of a small fusehead and 1 gram of black powder contained inside a paper capsule. The total ignition energy produced by 6 igniters is around 1.5 kJ [20]. In order to reproduce the effect of the igniters and start the flame propagation, several options can be implemented: first, an energy of ignition,  $Q_{ig}$  can be added to each phase in accordance to the void fraction, as an attempt to modelise the experiment conditions; also, a high temperature and pressure can be set at the initial time step (that is, reproducing a high-energy state in the system); a third option would be to calculate the ZN state at the initiation section. The

latter means to consider the adiabatic, isochore, complete combustion of the two-phase mixture in a small section of the tube. To do that, the limiting burning species must be determined (either Al or O<sub>2</sub>). Then, the combustion source terms are computed and added to the conserved variables.

Pressure transducers were placed in Chen's experiment on six different coordinates of the tube ( $x = 4.40, 5.25, 6.15, 7.00, 7.95$  and  $8.85$ ), so that pressure fluctuations were recorded as long as with the wave propagated. Then, the pressure evolution in time was reported for each position [19].

### 6.1.2 One-dimensional and multi dimensional grids for this test

A collection of structured grids have been developed for the geometry of this test, so that the finite volume method may be applicable. For the one dimensional solving, the standard mesh comprises a total of 608 uniform elements in a row. The element size is a critical parameter in this type of simulation as by Courant's stability condition (Equation 4.18), the time step is a function of  $\Delta t_x$ . Specifically, in this case the size of elements is calculated by dividing the total length between the number of tube elements, yielding a  $\Delta x = 0.02$  m.

Moreover, multi-dimensional meshes have been used for 2D y 3D simulations with the code Cast3M. The 2D mesh consists of  $1000 \times 20$  uniform elements. The tube, which is presented in [20] as a circular-cross-section duct with an inner diameter of 0.14 m, is modelled in two dimensions as a  $12 \times 0.14$  m rectangle. A detail of this mesh is shown in Figure 6.2 (left). Meanwhile, the three-dimensional domain is a  $12 \times 0.124 \times 0.124$  m parallelepiped (so that the tube's cross section is maintained with respect to that in Chen's experiment). This domain is discretised as a structured mesh with  $500 \times 12 \times 12$  cubic elements with sides of equal size, as depicted in Figure 6.2 (right).

Nevertheless, other grids have been used as well, with the aim of conducting a study on grid convergence. For 1D case, three meshes have been considered for the analysis (608, 1216 and 2432 elements). In the 2D study, they have, respectively, 500, 1000 and 2000 square elements in  $x$  direction. The corresponding outcomes of the study are discussed later.

### 6.1.3 Computational implementation

**Escribir brevemente sobre implementacion en Fortran y Castem. Diagramas de flujos.** Comentar tambien que se usa el esquema de AUSM (particulas) y AUSM+ (gases).

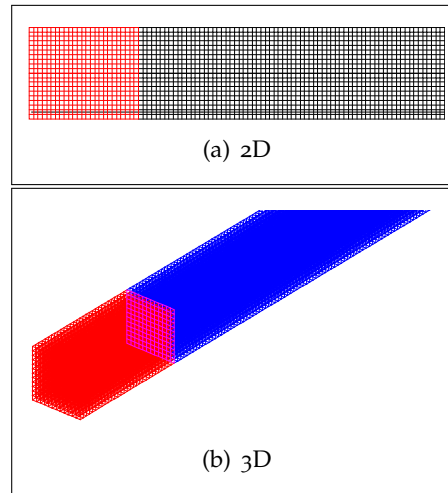


Figure 6.2: 2D and 3D grids for numerical resolution of Chen Test with multi-dimensional modelling (only the left end of the domain is represented).

#### 6.1.4 Numerical results

Here we turn to discuss the numerical results obtained by *DUST* code in 1D, implemented in Fortran 95, and results in 2D and 3D yielded by the version of *DUST* in Cast3M. The solution obtained from the 1D model shows the system initiation on the left side of the domain and the spread of flame along tube's length in the  $x$  direction. Figure 6.3 shows the typical evolution of pressure as a function of time for different  $x$  positions, corresponding with the location of pressure transducers in Chen's experiment [19]. In turn, Figure 6.4 gathers the distributions of the main variables inside the tube at three different times.

The pressure histories in Figure 6.3 match well with Chen's results. The interpretation thereof allows realizing the wave propagation, as one can see how the wave front reaches later and later further positions from the initiation section on the left. The average wave speed is 920 m/s near  $x = 4.40$  m. The wave front keeps accelerating until it reaches a sort of stationary speed, i.e., 1100 m/s at  $x = 7.0$  m and 1240 m/s at  $x = 8.85$  m (compared to 1300 m/s reported in [19]).

Regarding the peak pressures, according to Chen et al. [20], those depend on both the initial concentration of particles and its diameter. Then, for a  $\sigma = 500$  g/m<sup>3</sup> and 6  $\mu$ m particles, the peak pressure should range 2 - 2.5 MPa (Figure 3 in [20]). And indeed, the maximum pressures that we got are close to those values (Figure 6.3).

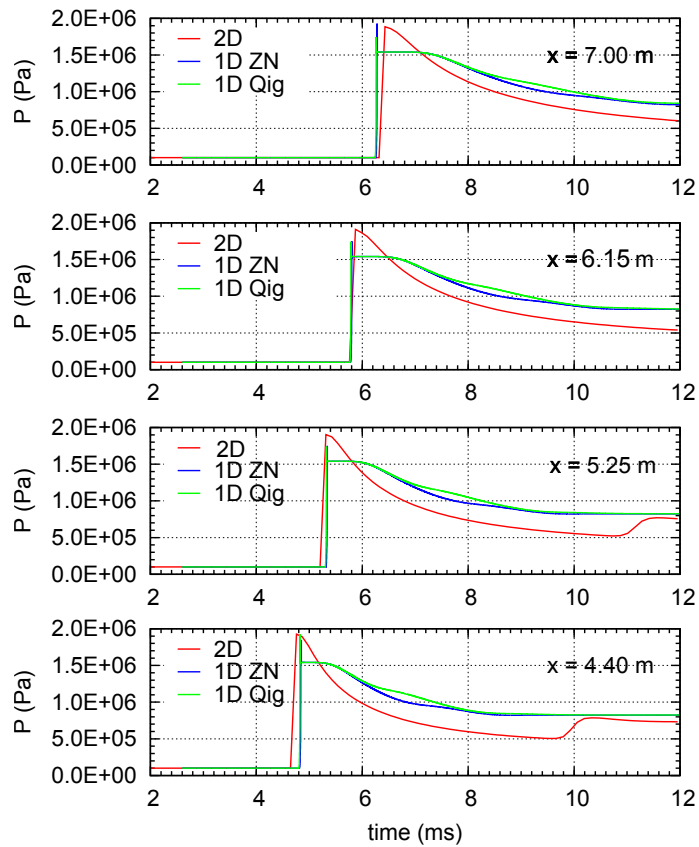


Figure 6.3: Chen Test: Pressure history over time, for the case of 1D computations (ZN and  $Q_{ig}$  initiation) and 2D simulation with Cast3M.

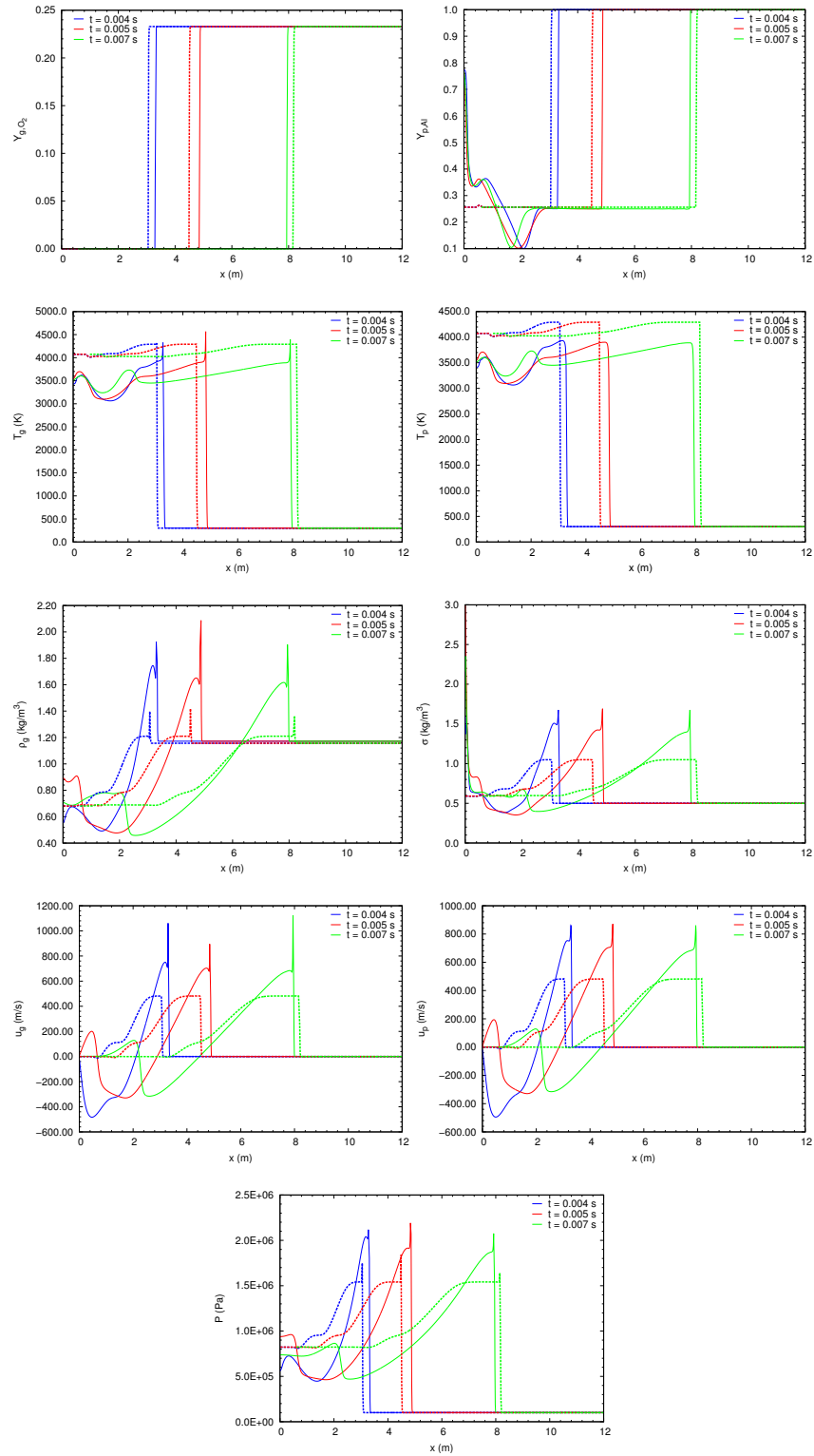


Figure 6.4: Chen test 1D and 2D-3D results. From top to bottom, left to right: distributions of gas  $O_2$  and particle Al mass fractions, temperature of gas and particle phases, density of gas, concentration of particles, gas velocity, particles velocity and pressure, at 4 ms, 5 ms and 7 ms. Dashed line: results from 1D model, continuous line: 2D and 3D model outcomes.

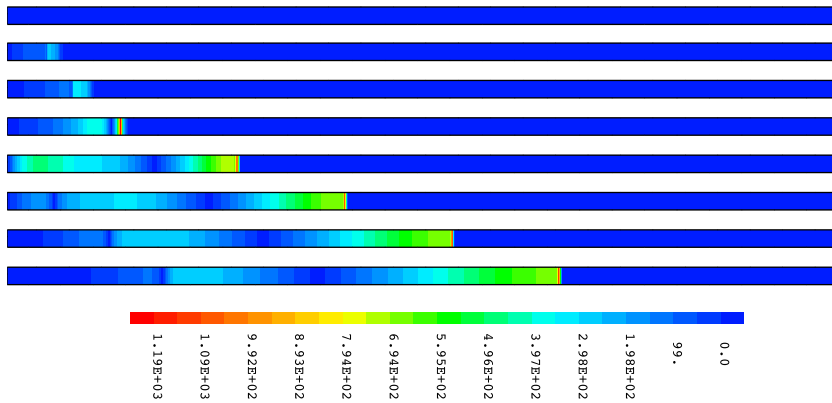


Figure 6.5: 2D Chen Test outcomes: Contours of particles velocity (m/s) at every 0.001 s.

### 6.1.5 Discussion of results for the multi-dimensional cases

Numerical solution of the two-dimensional version of the test is also depicted in both [Figure 6.3](#) and [Figure 6.4](#), where the evolution of variables in the 2D mesh is projected over a line across the computational domain.

As shown in pressure plots of [Figure 6.3](#), there is no big difference between the 1D and 2D approach. In fact, the wave speed is pretty similar for both cases. Peak pressures are clearly higher for 2D results, although the multi-dimensional solution avoids a spurious oscillation that is present in the 1D solution (even using TDV schemes).

The multi-dimensional solution is also represented together with the one-dimensional curves (dashed lines) in [Figure 6.4](#). Although temperatures remain around 500 K lower in the 2D tube, the velocities are by contrast 200 m/s higher in that case. Probably the main differences (in percentage terms) are found in gas densities and solid concentration. Contours of particles velocity are shown in [Figure 6.5](#) at each 1 ms from  $t = 0$ .

On other side, the 3D solution, computed with the same Cast3M code, is so similar to the 2D outcome, that curves appear in most cases overlapped. That is not strange, since wall friction is neglected in this test and, furthermore, the same solver and numerical schemes are used for 2D and 3D approaches. Contours of pressure ([Figure 6.6](#), top) and velocity of particles ([Figure 6.6](#), bottom) are included, in order to illustrate the flame spread through the descriptive outcome of 3D simulations.

#### 6.1.5.1 Heuristics research on the appropriate computational parameters

It is worth noting that some incertitude is found on the maximum pressures in Chen's experiments. In fact, the test conditions specified above are similar at both works ([\[20\]](#) and [\[19\]](#)), but pressure history

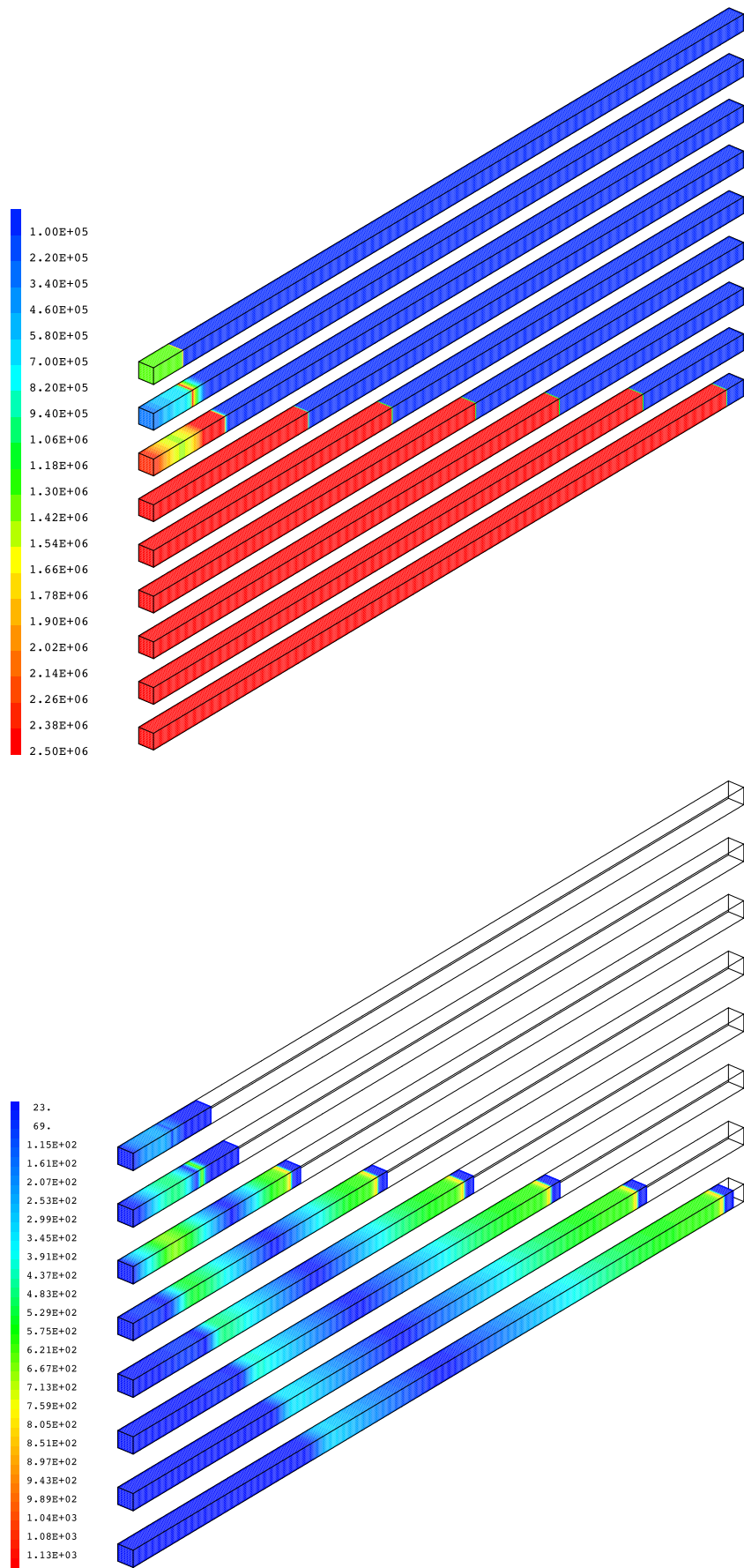


Figure 6.6: 3D Chen Test outcomes. Top: Contours of pressure (Pa), bottom: velocity of particles (m/s) at every 0.001 s.

plots showed they differ by an order of magnitude (5 MPa in the earlier work and 0.5 MPa in later).

With respect to our results, we can take them for validated, since we get numerical results that fit well with the flame speed in both papers [20] and [19]) and the maximum pressures match to those in the study of P versus  $\sigma$  [20]. Notwithstanding, we wanted to conduct a study on what conditions should be imposed to obtain similar results to those in the 2005 paper. Thus, a sensitivity study was executed over different parameters, such as, dust concentration, particle diameters, oxygen concentration and the kinetic model parameters (pre-exponential factor and activation energy). The results of this study — details of which are not of interest to be shown— conclude that certainly the most influential factor in the results is the activation energy  $E$  of the burning law. In particular, if  $E = 2.5 \times 10^5$  is set (SI units), results became much closer to those in [19], and then we find peak pressures of 0.5 MPa (Figure 6.7) and wave speed similar to the experiments.

The parameter  $E$  has also an influence on phase velocities, the burning velocity of particles behind the shock and, in general, in the structure of the flame front. High activation energies tend to counter the oxidation process and to make it weaker. If the value is high enough, flame detaches from the wave front, which travels faster. That would be deflagration as in Figure 6.7. On the contrary, with a lower activation energy, the reaction could be strong enough to maintain a stationary detonation, where the shock wave is fed by combustion energy. This is the case of results in Figure 6.4. Note that maximum velocities, pressures and propagation speed tend to become stable.

#### 6.1.6 Grid convergence study for dust combustion simulations

Finally, a grid convergence study is done for this test so we can get sure the number and size of elements we chose is not making a big influence on the results. For this, three different 1D meshes are considered with 608, 1216 and 2432 elements, each doubling the number of elements of the previous one.

The analysis is done with two sets of test parameters: the original Chen test configuration (see Section 6.1.1) and the test with  $E = 2.5E5$  (Section 6.1.5.1, obtaining similar conclusions for any case. For the first test (Figure 6.8) the typical pressure histories are found and even multiplying by four the number of elements, we do not find great changes (variation of peak pressure do not exceed 1.16 % for the extreme cases). What we actually watch is an increase of the spurious oscillation right at the wave front for the finest mesh. Then, for the second test with kinetic adapted parameters, a bigger influence is seen (Figure 6.9). There is a percentage variation of 3.50 % in peak pressure between the finest mesh and the medium one, whilst a 27.9

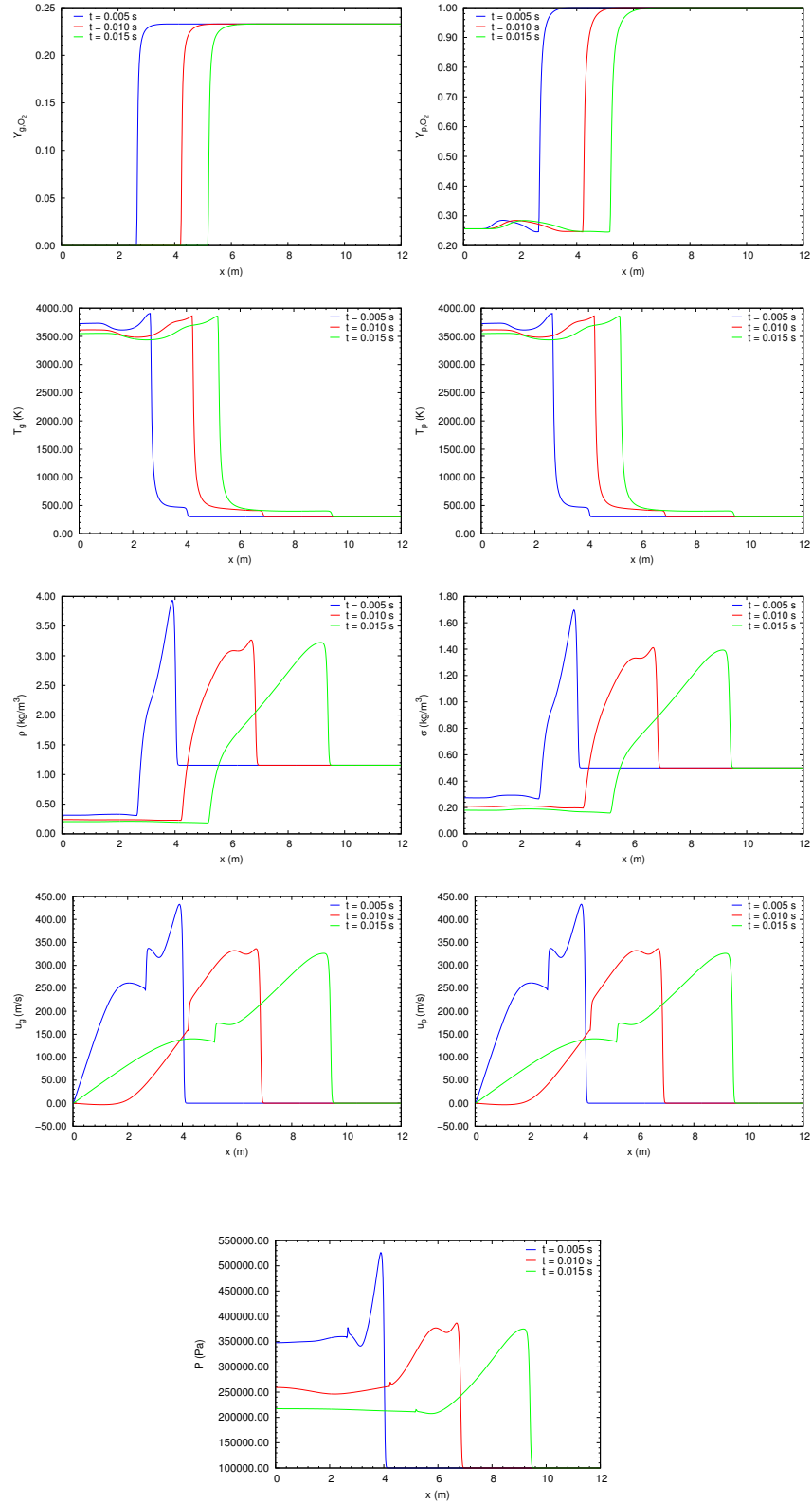


Figure 6.7: 1D Chen test with adapted kinetic parameters. From top to bottom, left to right: distributions of gas  $O_2$  and particle Al mass fractions, temperature of gas and particle phases, density of gas, concentration of particles, gas velocity, particles velocity and pressure, at 4 ms, 5 ms and 7 ms.

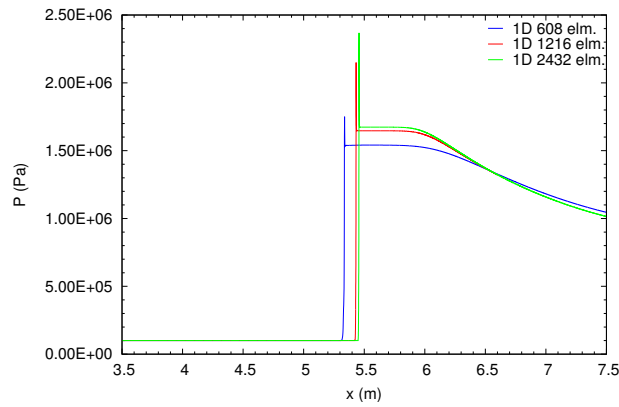


Figure 6.8: Pressure history for the 1D Chen test. Computations with varying grid resolutions.

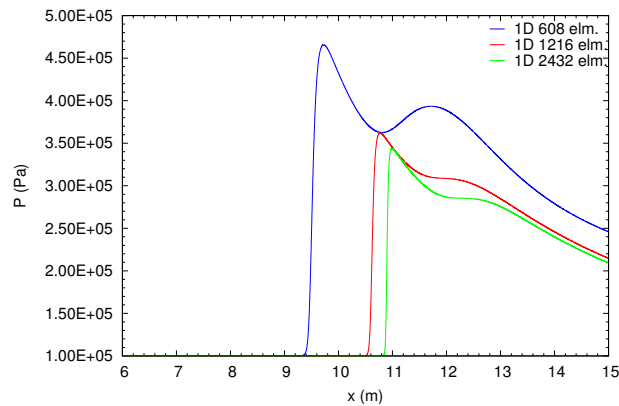


Figure 6.9: Pressure history for the 1D Chen test with adapted parameters. Computations with varying grid resolutions.

% is found between the medium and the coarser mesh. However, pressures tend to converge in a clear way when increasing the number of elements. The medium mesh, counting a number of 1216 elements, rises as a compromise solution to obtain a relatively accurate simulation in conjunction with an affordable computational cost.

## 6.2 DETONATION INDUCED BY COMBUSTION OF HYDROGEN AND SOLID PARTICLES

Unlike the test in the previous section, in which chemical reaction took place in the solid phase, a test is now proposed with a higher level of complexity, in which there is both a homogeneous and a heterogeneous reaction. That is, a detonation shock, led by a hydrogen oxidation reaction, is followed by explosion of Aluminium dust.

This test aims to reproduce that experimental study carried out by Veyssi re [130]. That paper addresses the detonation of gas-solid particles mixtures in a vertical detonation tube. Different experiments are reported with a wide variety of reactive gaseous components, such as,  $H_2$ ,  $C_2H_4$  or  $C_2H_2$ , with  $O_2/N_2$  mixtures. Aluminium particles are suspended within the gas phase. As mentioned in Chapter 2, focuses on the analysis of the double front detonation (DFD) structure obtained during the combustion those gases in the presence of the Al particles. Among these experiments, three of them are specially of interest for us, those tests with  $H_2$ , namely:

(H1) Mixture:  $H_2 + X O_2 + Z N_2$ , where  $Z/X = 3.76$  and  $r = 0.78$

(H2) Mixture:  $H_2 + X O_2 + Z N_2$ , where  $Z/X = 3.76$  and  $r = 1.06$

(H3) Mixture:  $H_2 + X O_2 + Z N_2$ , where  $Z/X = 2.2$  and  $r = 0.75$

All three tests have been successfully simulated with *DUST*. In the current Section, we proceed to reproduce the results given for experiment (H1). To that end, all the parameters that define the experiment are clearly determined. Also some attention is paid to different meshes that are used for spatial discretisation at one-dimensional resolution, as well as multi-dimensional modelling.

### 6.2.1 Veyssi re Test geometry and spatial discretisation

The test section is a 6 m long, vertical detonation tube (Figure 2.4). Details about the detonation tube are described in previous works by Veyssi re [133, 129]. The tube comprises two parts: the first one is 3.5 m long and includes several devices with various functions, such as a closing valve, ignition chamber and suspension generator. The initiation (at the ignition chamber) is carried out by a blasting cap generating a spark. The second part is about 2.5 m long and is provided with a valve that closes the tube. In all Veyssi re's works the tube internal diameter is 69 mm (constant cross section).

For our purposes, the tube is assumed as a 6 m long smooth duct. This will let us model the tube as a one-dimensional vertical domain, as well as a vertical plain rectangle. Ignition will be triggered at the initial section of the detonation tube (the lower section, where the origin of coordinates,  $x = 0$ , is set). Inside this section, adiabatic

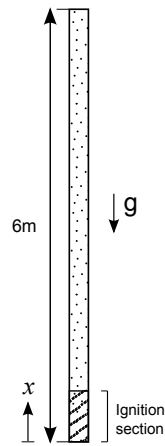


Figure 6.10: Smooth duct model for Veyssière Test.

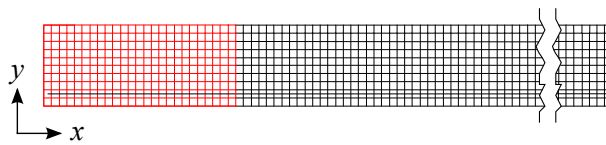


Figure 6.11: 2D grid for numerical resolution of Veyssière Test (only the lower end of the domain is represented).

complete combustion of  $H_2$  and Al particles will be forced. This simplified geometry is depicted in [Figure 6.10](#).

The grids used for this test to be resolved are similar to those previously described for Chen test, although they have been transformed into the new tube's dimensions. For 1D calculations, a 6 m long mesh is proposed with 608 uniform one-dimensional elements. Since in the grid convergence analysis taken for the last test ([Section 6.1.6](#)), the mesh of 1216 elements resulted as an accurate, reliable option to be chosen, the half number of elements (608) are now set for the resolution of a half-long duct. Then, elements are equally sized to those in the mesh of 1216 elements in the former test. Also 2D and 3D versions of the test have been studied for what multi-dimensional space discretisations were taken. For the resolution of the problem in 2D, the domain is divided into a set of  $1000 \times 10$  finite volumes in a structured mesh ([Figure 6.11](#)), whilst for the 3D calculations an equivalent  $1000 \times 10 \times 10$  grid is applied.

### 6.2.2 Test specifications

As discussed above, several tests can be studied by changing the particle and gas mixture concentrations. Provided that the parameters of each test are interpreted from the data reported by the author, three different sets of initial conditions will result respectively in tests (H1), (H2) and (H3).

Referring to the unburnt mixture, the equivalence ratio describes the ratio of fuel relative to the amount of fuel that potentially could be burnt with the available oxidiser. The equivalence ratio of a system is defined as the ratio of the fuel-to-oxidiser ratio to the stoichiometric fuel-to-oxidiser ratio), that is:

$$r = \frac{\text{fuel to oxidiser ratio}}{(\text{fuel to oxidiser ratio})_{st}} = \frac{m_{\text{fuel}}/m_{\text{ox}}}{(m_{\text{fuel}}/m_{\text{ox}})_{st}} = \frac{n_{\text{fuel}}/n_{\text{ox}}}{(n_{\text{fuel}}/n_{\text{ox}})_{st}} \quad (6.1)$$

where subscript st stands for stoichiometric conditions. The equivalent ratio is related to another important combustion parameter, the Air-fuel Equivalence Ratio,  $\lambda = 1/r$ . Following Veyssière [130], the equivalent ratio is  $r = 0.78$  for experiment (H1),  $r = 1.06$  for experiment (H2) and  $r = 0.75$  for experiment (H3). So initially, we have got the ratio  $Z/X$  and  $r$ . Let us recall the stoichiometric reaction of  $H_2$  combustion (R1); by using the two definitions just posed and a bit of common sense, we can calculate the molar fractions for each test from the data provided by Veyssière. As only for test (H1) numerical results are shown, the initial molar fractions for this test would be:

$$x_{H_2} = \frac{2 \times 0.78}{6.32} \left( \frac{\text{mol}_{H_2}}{\text{mol}_{gas}} \right); \quad (6.2)$$

$$x_{O_2} = \frac{1}{6.32} \left( \frac{\text{mol}_{O_2}}{\text{mol}_{gas}} \right); \quad x_{N_2} = \frac{3.76}{6.32} \left( \frac{\text{mol}_{N_2}}{\text{mol}_{gas}} \right). \quad (6.3)$$

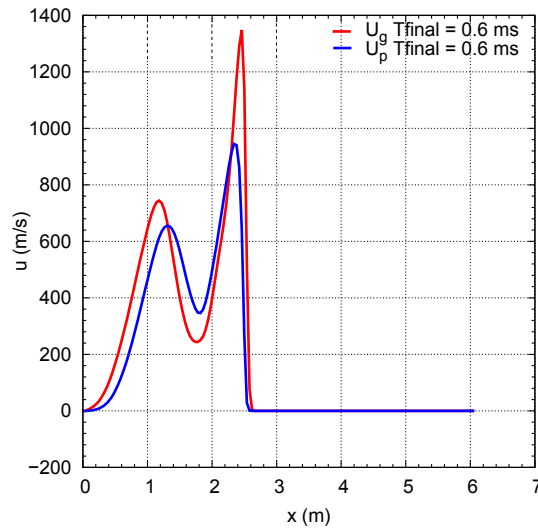
The initial conditions for this test are imposed over the whole domain, that means there are not different sections initially considered in the tube. Standard ambient temperature and pressure are set:  $293 \pm 5$  K and 1 bar. Solid phase consists on Aluminium homogeneous particles with  $10 \mu\text{m}$  average diameter. Particles concentration is  $65 \text{ g/m}^3$  for this test. Solid phase is incompressible and all gases are modelled as perfect gases. A quiescent atmosphere is found initially all along the tube.

### 6.2.3 Numerical results

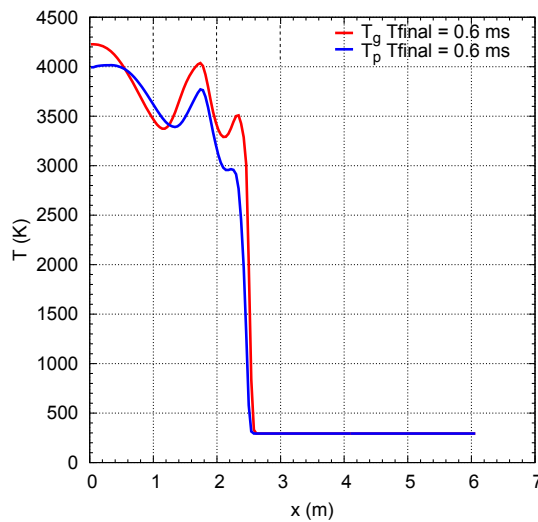
Test H1 (see Section 4.2.3) has been solved by using the 1D version of DUST code, implemented in Fortran language, and the 2D/3D version of DUST, based on the CEA platform Cast3M (see Appendix A about the implementation in Cast3M). In the case of the studies with Hydrogen mixtures, we would expect to obtain similar pressure profiles to those obtained experimentally in Veyssière (1984).

#### 6.2.3.1 Outcomes from the 1D test

The evolution of different variables has been depicted in Figure 6.12. These represent the propagation of the shock and progress of combustion. As shown, velocity in gas phase rapidly increases at the front



(a) Velocities of gas phase ( $U_g$ ) and particles ( $U_p$ ).



(b) Temperatures of gas ( $T_g$ ) and particles ( $T_p$ ).

Figure 6.12: Distribution of variables along the vertical combustion tube for Veyssière Test H1. Numerical results from 1D calculations.

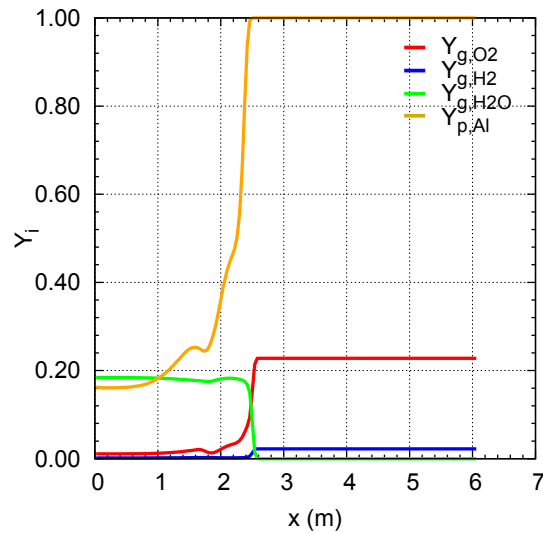


Figure 6.13: Mass fractions of species in Veyssière Test H1, at  $t = 0.6$  ms.

wave formation and it decreases gradually behind the shock. Note that velocity of particles reaches lower maximum values compared with the gas phase. A second maximum is found following to the detonation front, the peak value being roughly the half of the first one. This has been interpreted as the double front detonation described in [130]. The first maximum on particles velocity is slightly delayed with respect to the gas velocity first maximum, while the second maximum on gas velocity is a bit delayed with respect to particle's second maximum (note that the detonation propagates towards the right side).

A similar phenomenon can be observed in temperature graphics. Indeed, temperature of gas phase shows sharpened distributions in the combustion front, while temperatures in solid phase are slightly lower.

The propagation of the combustion front is stable as shown in the mass fraction curves of Figure 6.12. The combustion of Aluminium particles is not complete, unlike what happens with Hydrogen. The sudden  $H_2$  oxidation is occurring as the wave progresses, while the oxidation of Al takes place after a short delay. A relative increase in particles oxidation coincides with the second peak in the temperature profile of the particles.

Special interest must be paid to the history of the pressure variable in several locations in the tube (Figure 6.14), as it could be registered by a sensor on that location. There are no velocity or temperature distributions provided by Veyssière, so Figure 6.14 is used to compare our results with the benchmark set in [130]. Pressure history has been recorded at the point with coordinates  $x = 1.945$  m. The resulting maximum pressure value is around 25 bar, very similar to the experimental value recorded. Besides, a second maximum is reached at  $t = 0.6$  ms and it is delayed  $160 \times 10^{-4}$  s. The delay time of the dou-

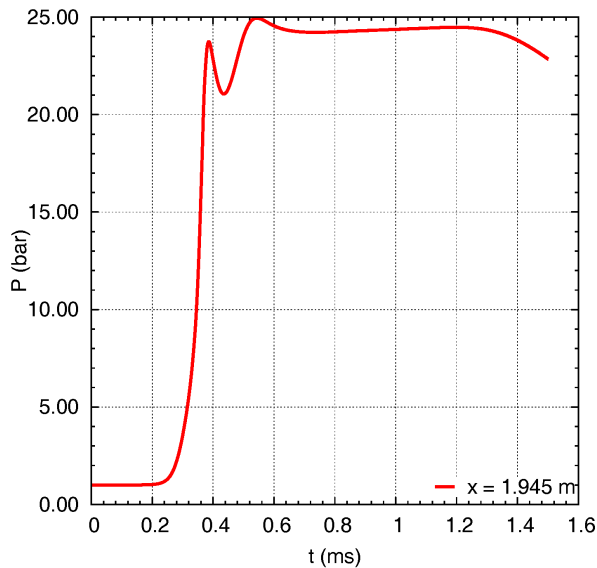


Figure 6.14: Pressure history of the detonation in Veyssière Test H1, at 1.195 m from the ignition point.

ble front detonation in Veyssière's work is  $150 \times 10^{-4}$  s, so it is pretty close to our prediction.

### 6.2.3.2 Veyssière Test 2D results

The same test has been also solved with *DUST* integrated in Cast3M. In Figure 6.15, distributions of gas-phase variables are depicted at many different times so that the flame development can be observed. Namely, gas velocity, temperature, pressure, Al mass fraction ( $Y_p$ ) and gas species mass fractions ( $Y - i$ ). The maximum velocities calculated are similar to those found in the one-dimensional test. Also gas-phase temperatures at the wave front, around 3500 K, are similar to those in the 1D results. Regarding pressures, the maximum value of 25 bar is coincident with the value in [130]. Let us recall that the solid phase, in the case of high diluted models, is not affected by the pressure term. Also, note that only two solid species are present in the system: Al and  $Al_2O_3$ . So, only the mass fraction for Aluminium is included in Figure 6.15. The mass fraction of the second species does not need to be calculated, for it is  $Y_{p,Al_2O_3} = 1 - Y_{p,Al}$ .

Results in Figure 6.16 are included in order to illustrate the differences between gas phase and solid phase, in velocity and temperature distributions.

Excluding the initial 0.3 ms, when the wave front is developing, the wave propagates at a constant burning velocity. This burning velocity, as measured from 2D calculations, is found to be  $S_c = 1840$  m/s. In Figure 6.17 the progression of the detonation wave is depicted versus time, and Figure 6.18 illustrates the progression with 2D contours of gas velocity at every 0.1176 ms from the initiation point.

The numerical results for this test, and its similarity to the experiments in the literature, validate the predictions generated by the code on detonation induced by combustion of particles and a reactive atmosphere. The following step, towards our goal of simulating the reactive atmosphere in ITER's vessel, involves the modelling of reactive mixtures with the solid species present in ITER (W, Be and C).

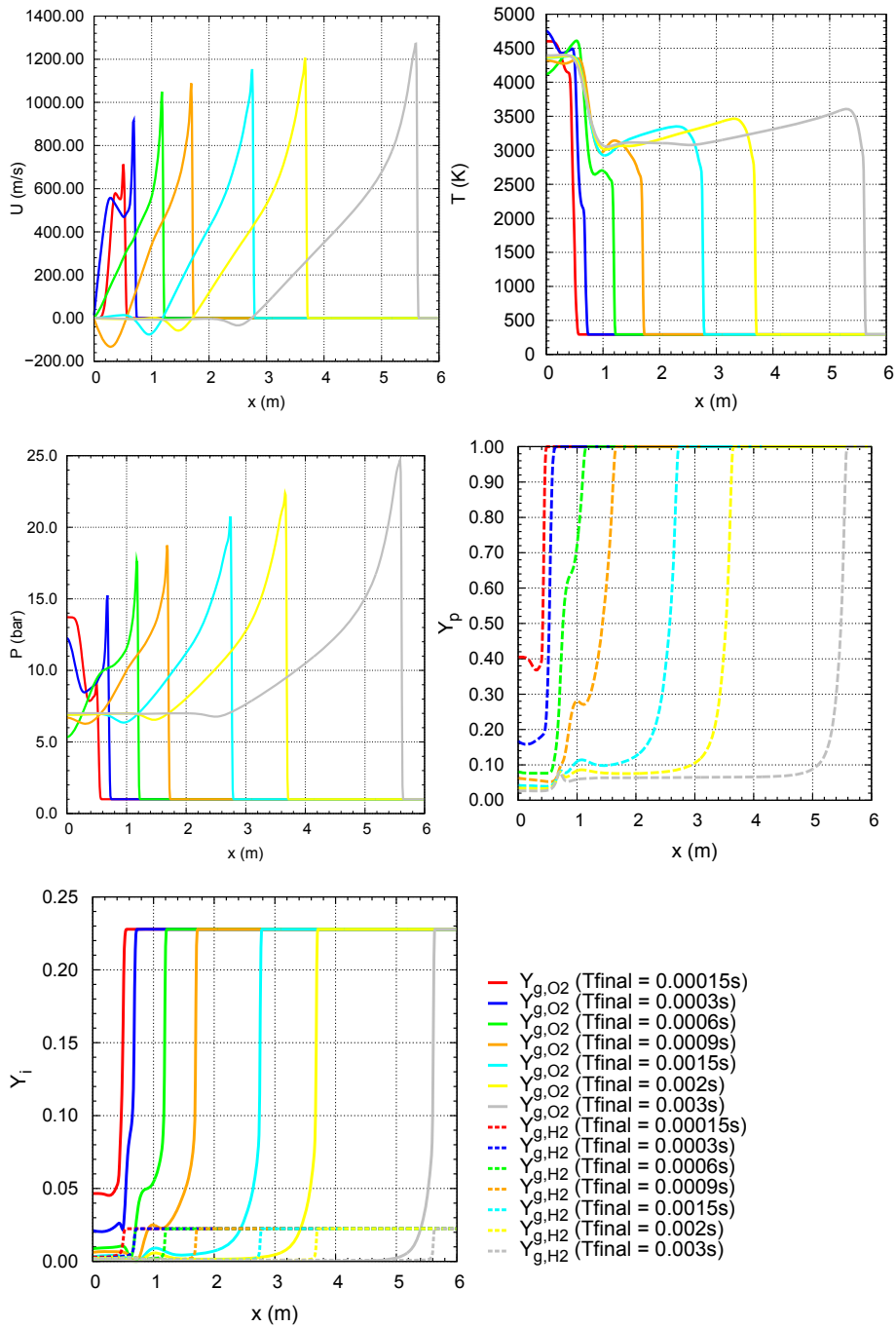


Figure 6.15: Distribution of variables along the vertical combustion tube for Veyssière Test H1. Numerical results from 2D calculations.

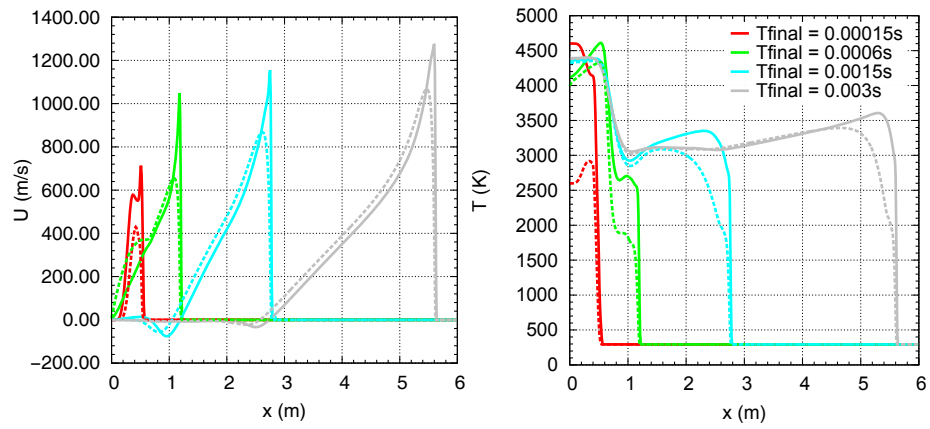


Figure 6.16: Distribution of variables along the vertical combustion tube for 2D Veyssière Test. Continuous line: gas phase, dashed line: solid phase.

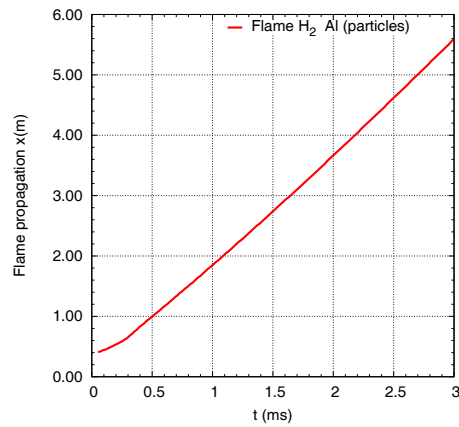


Figure 6.17: Flame propagation (m) vs. time (ms) for the H<sub>2</sub>-Al detonation. 2D Veyssière Test.

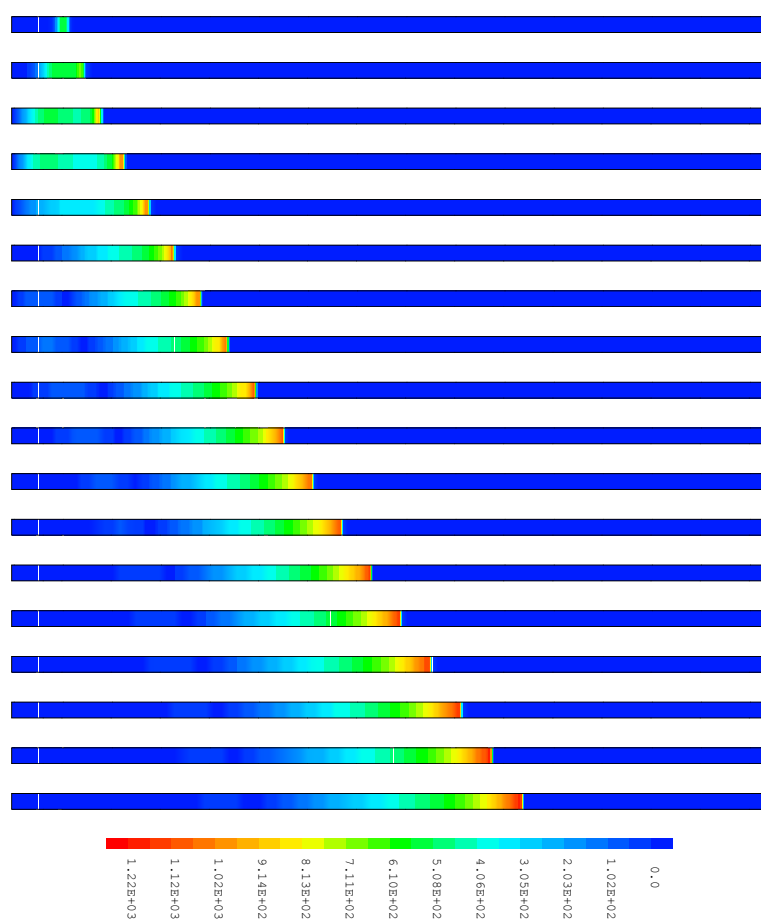


Figure 6.18: 2D Veyssière Test outcomes: Contours of gas velocity (m/s) at every 0.1176 ms.

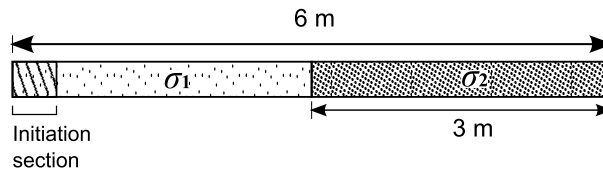


Figure 6.19: Smooth duct model for W-combustion Test.

### 6.3 W-DUST COMBUSTION IN A REACTING MULTICOMPONENT ATMOSPHERE

No references have been found in literature about experimental or numerical tests involving combustion of  $H_2$ , CO and W particles with air. The W-combustion test proposed here consists of a closed smooth tube filled with a two-phase mixture of particles and a gas reacting atmosphere ( $O_2$ ,  $H_2$ ,  $H_2O$ , CO,  $CO_2$  and  $N_2$ ). This combustion test will help to demonstrate that the new approach for source terms integration (ASTT) is valid also when combustion is modelled, which usually implies by itself a problem for stability.

#### 6.3.1 Description of the Test

The 6 m long tube is outlined in Figure 6.19. An initiation section is considered in the left end, where an ignition energy of 15 kJ is added. The walls are assumed to be smooth and to satisfy the flux adherence condition. The 1D domain of the tube is divided into two subsections: the left side with low dust concentration ( $\sigma_1$ ), and high concentration ( $\sigma_2$ ) on the right side. A one-dimensional mesh is constructed for this test with 1000 cells distributed along the tube's total length. Time step is computed with the *Courant's* condition by setting  $CFL = 0.45$ .

All dimensions, initial conditions and concentrations are listed in Table 2. Physical parameters (densities, specific heat capacities, formation enthalpies) of the various materials present in this test are found in the NIST data base [83].

#### 6.3.2 Results for low concentration test

Two different concentrations were used for the dust on the right side of the tube. First, a lower concentration  $\sigma_2 = 120 \text{ g/m}^3$  at right side, allows us to compare results given by both the conventional and the Advanced Source-Term Treatment (ASTT) methods, since concentrations are low enough to be resolved in DUST code by using both procedures. Results from the code are shown in Figure 6.20 and Figure 6.21. The step in dust concentrations at  $x = 3 \text{ m}$  is not a major obstacle for the propagation of the shock wave, as seen in  $\sigma$  and gas density distributions (Figure 6.20), but the initial low pressure in the tube promotes the rapid dissipation of the pressure wave. The first

VARIABLE	VALUE
Tube length L (m)	6.0
Internal diameter, D (m)	0.35
Initiation section length $L_1$ (m)	0.4
H <sub>2</sub> molar fraction	0.2468
H <sub>2</sub> O molar fraction	0.0
O <sub>2</sub> molar fraction	0.1582
CO molar fraction	0.015
CO <sub>2</sub> molar fraction	0.0
N <sub>2</sub> molar fraction	0.58
Left side particle concentration $\sigma_1$ (g/m <sup>3</sup> )	65
Right side particle concentration $\sigma_2$ (g/m <sup>3</sup> )	120,800.0
Particle diameter ( $\mu\text{m}$ )	1.0
Tungsten mass fraction, $Y_{p,W}$	1.0
Tungsten oxide mass fraction, $Y_{p,W\text{O}_3}$	0.0
Temperature of gas, $T_g$ (K)	490
Temperature of particles, $T_p$ (K)	490
Pressure (Pa)	4200
Velocity (both phases)	0.0

Table 6.1: Initial parameters for 1D W-combustion Tests.

impulse of the ignition energy gives a peak pressure of about 0.4 bar in 1 ms, whereas it is near 0.2 bar in 7 ms. The main differences between both integration methods lie in the solid phase solution. An important spurious oscillation is avoided in the distribution of the mass fraction of tungsten when using the advanced source term treatment (Figure 6.20). Under these conditions, because of the oxidation reaction of tungsten, hydrogen is generated when no free oxygen is available for its oxidation.

### 6.3.3 Results for high concentration test

In cases with a higher concentration ( $\sigma_2 = 8000 \text{ g/m}^3$ ), use of the source term treatment is mandatory for any real solution to be achieved. The results (Figure 6.22 and Figure 6.23) show that, on the left side of the tube, the wave propagation is similar to the case of low  $\sigma$ , whereas on the right side, the concentration step has a great influence on the wave speed and peak values of the variables. Distributions of  $\sigma$  show values near  $35 \text{ kg/m}^3$  and gas density round  $0.21 \text{ kg/m}^3$  at the moment when the front wave reaches the step at 4 ms (Figure 6.22), that means a rise rate of 10 compared with the initial state. Lower values are found in the subsequent time steps, as the dense cloud of particles exerts a restraining effect. The concentration step bounces part of the shock wave in the opposite direction, as one can realise by watching the pressure curve at 8 ms, in Figure 6.22. So, a new front begins that will be fed back by high temperatures in that section (see negative gas velocities in Figure 6.22). Relative velocity between phases is greatly reduced due to the small diameter of particles. Combustion takes place continuously in places where the temperature is high enough to allow ignition of hydrogen. The energy released by this reaction triggers the combustion of the solid phase. Let us note that the combustion wave progresses along the tube, as the temperature of both phases is sufficient to enable the reaction. This is shown in curves for species mass fractions,  $Y_p$  (Figure 6.23). The  $x$  coordinate position of the wave front increases as time progresses. From time 4ms and on, the pressure wave bounces back and the new shock induces transport of species in the opposite direction. That is why the distribution at 12 ms seems to be at a rearmost position.

Reported numerical results prove the code is able to solve fluxes with high concentration of particles by using the advanced source term integration proposed in this work. This test has been devised to show that the code is able to perform combustion simulations in a wide range of concentrations and pressures.

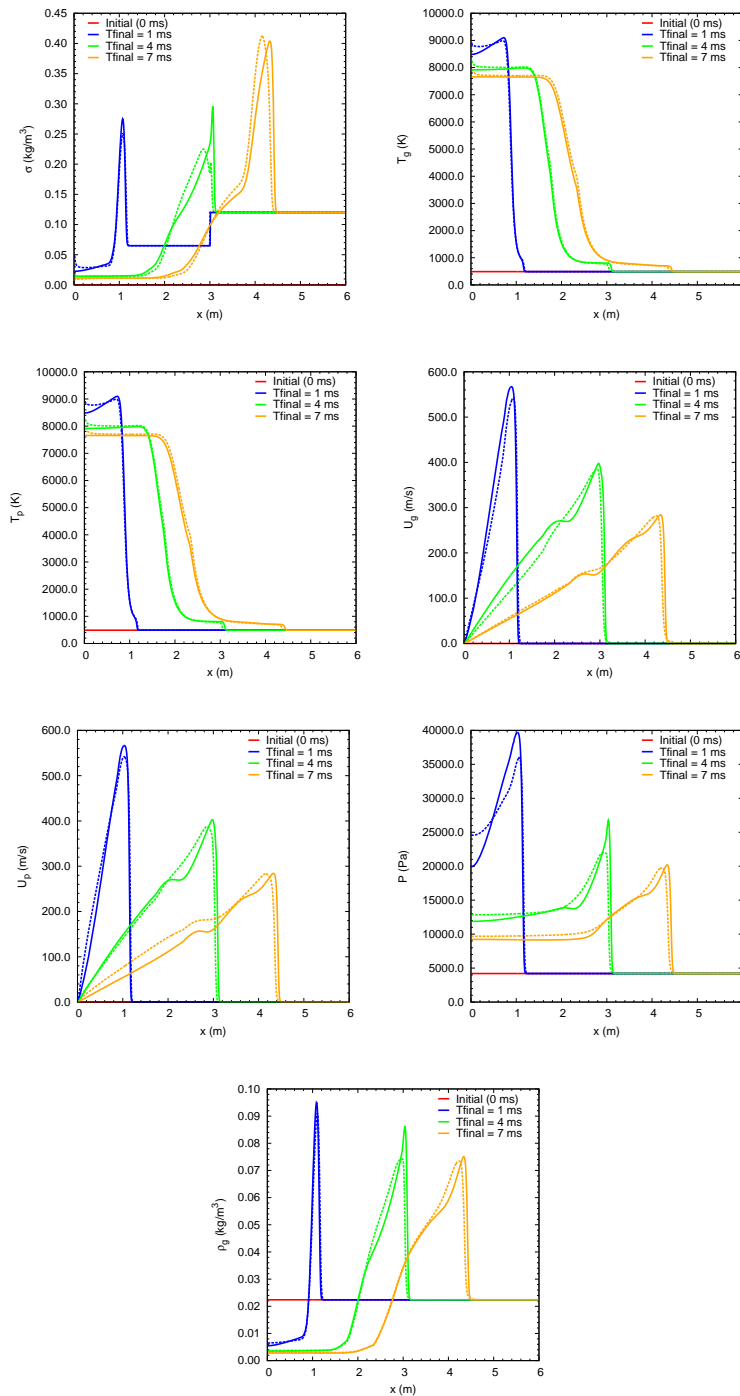


Figure 6.20: Results of W combustion Test for low concentration. From top to bottom, left to right: Distributions of concentration of particles, density of gas, pressure, particle velocity, gas velocity, temperature of particles and temperature of gas, at 1 ms, 4 ms and 7 ms. Dashed line: 1<sup>st</sup> order integration, continuous line: Advanced Source-Term Treatment.

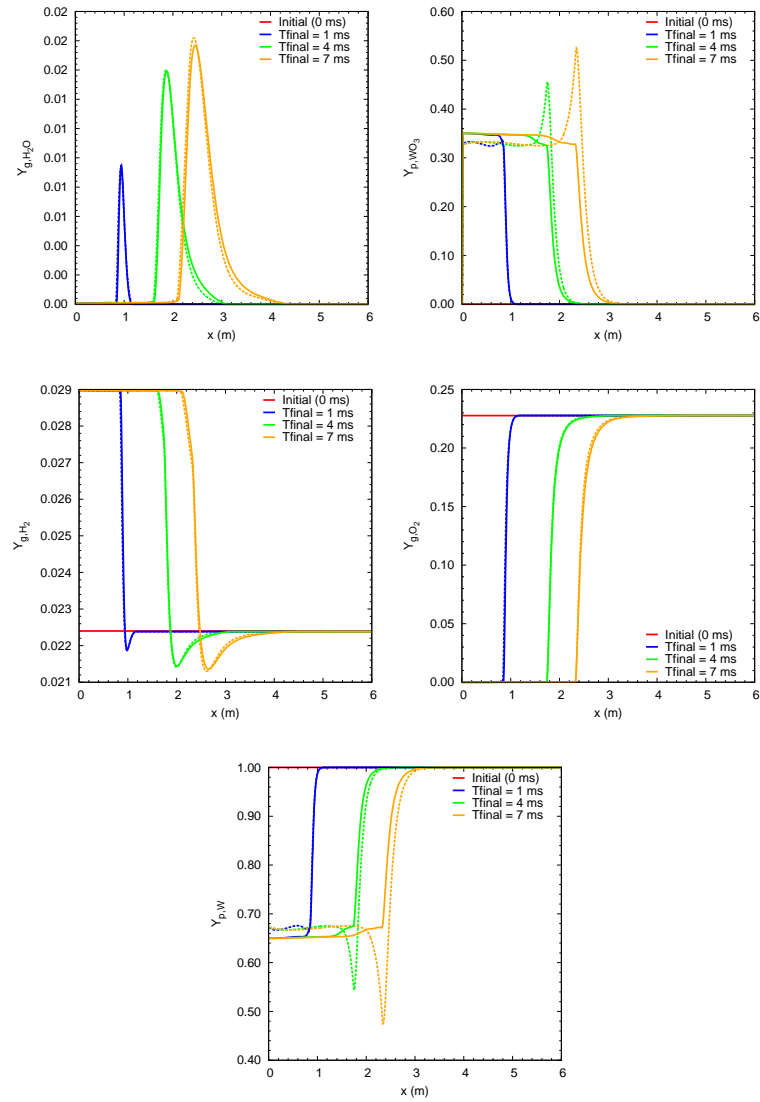


Figure 6.21: Results of W combustion Test for low concentration. From top to bottom, left to right: Distributions of  $O_2$  mass fraction,  $H_2$  mass fraction,  $H_2O$  mass fraction, W mass fraction and  $WO_3$  mass fraction, at 1 ms, 4 ms and 7 ms. Dashed line: 1<sup>st</sup> order integration, continuous line: Advanced Source-Term Treatment.

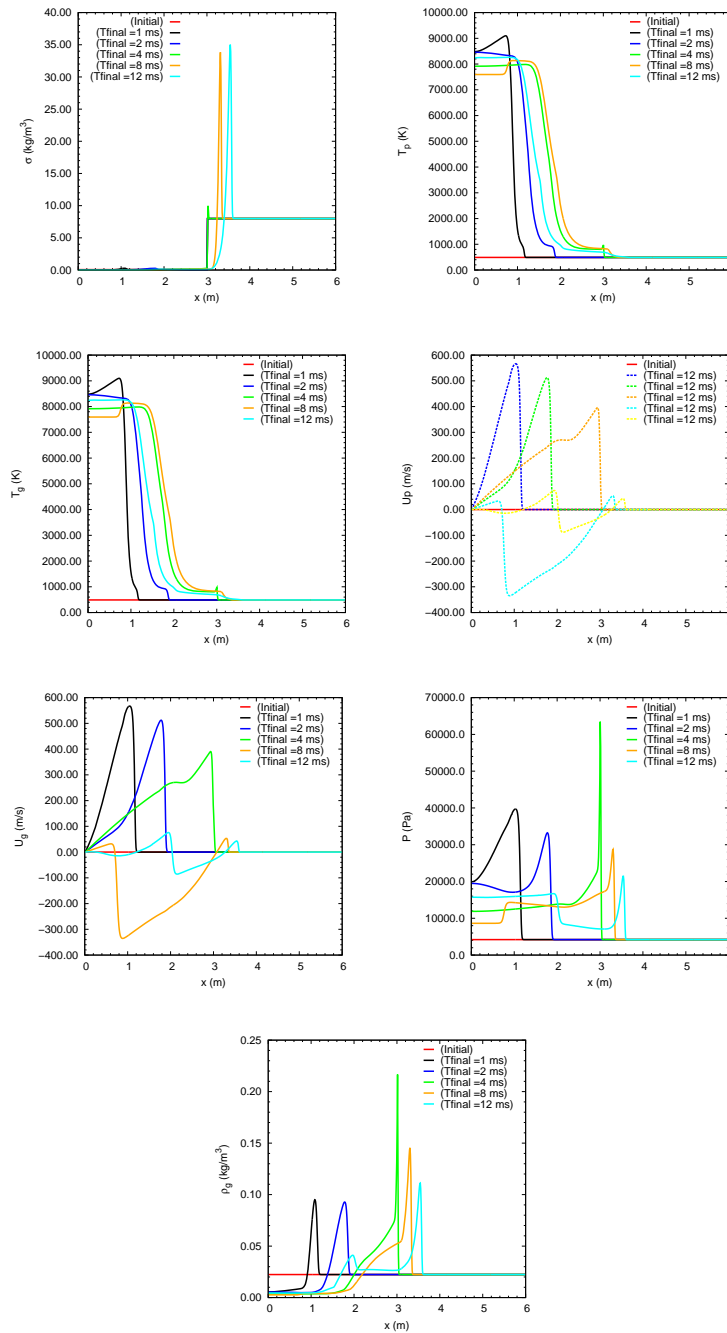


Figure 6.22: Results of W combustion Test for high concentration. From top to bottom, left to right: Distributions of concentration of particles, density of gas, pressure, gas velocity, particle velocity, temperature of gas and temperature of particles, at 1 ms, 2 ms, 4 ms, 8 ms and 12 ms.

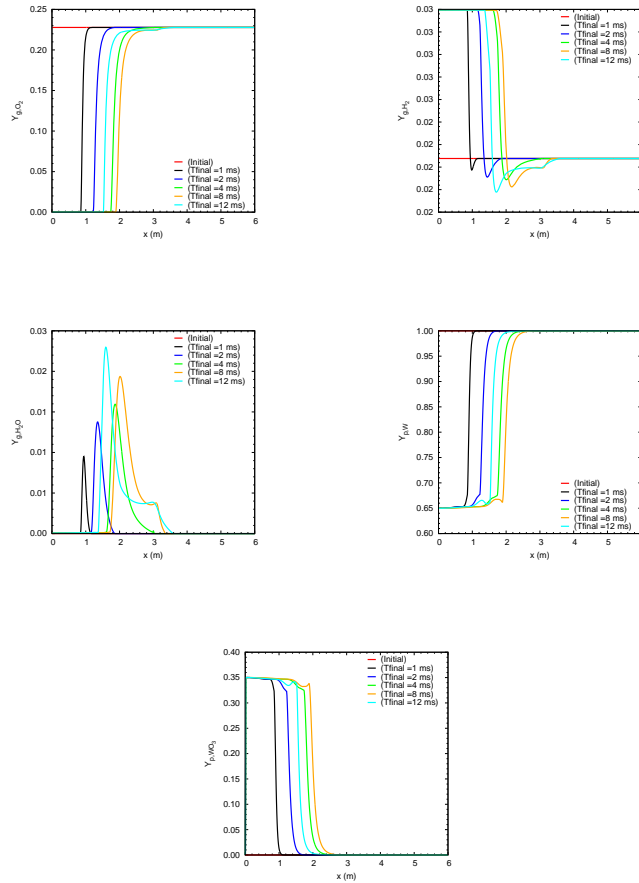


Figure 6.23: Results of W combustion Test for high concentration. From top to bottom, left to right: Distributions of  $O_2$  mass fraction,  $H_2$  mass fraction,  $H_2O$  mass fraction, W mass fraction and  $WO_3$  mass fraction, at 1 ms, 2 ms, 4 ms, 8 ms and 12 ms.

## 6.4 GRAPHITE COMBUSTION IN REACTIVE ATMOSPHERE. SIMULATION OF THE ORLEANS EXPERIMENTS

### 6.4.1 Implementation of graphite combustion models

Some of the combustion models for graphite particles found in literature (Section 2.4.6) have been implemented into the computational code, so that their particular effect in the solution can be assessed. Among the multiple combustion models, reaction schemes with no more than three steps have been selected: O'Brien et al. [84], Annamalai and Durbetaki [2], Libby and Blake [70], Vatikiotis [126], Phuoc and Annamalai [90] and Yang et al. [136]. Cast3M operator 'FUENTE' has been then modified so the 2D and 3D codes can allow the different combustion models, and CO<sub>2</sub> has been enabled as a reactive species, as considered by various approaches (i.e., [2, 70]).

In order to find out how different the wave speed is by using each reaction scheme, a 2D test is first here reported, consisting of a horizontal plain tube with  $L = 60$  m (geometry coming from the H<sub>2</sub> detonation test in [8]). As the gas and particle detonation is allowed to propagate through a very long, simple geometry, the differences in the solution are strengthened (see result comparison in Figure 6.24). Note that most approaches seem to give similar results, with the exception of two models (by Vatikiotis [126] and Yang et al. [136]) giving higher values of wave speed and peak pressure. Also big differences in temperature are found in these two models, rising up about to 3500 K, whereas the other options reach 2500 K as much. It is also worth noting the influence of the different reaction schemes in the curves for mass fractions. As Vatikiotis [126] and Yang et al. [136] predict faster reactions, combustion of C particles is more intense for the same time of reaction and complete depletion of O<sub>2</sub> is achieved, as shown in graphics for  $Y_{\text{O}_2}$  and  $\sigma$  (Figure 6.24), this last also causes, reversely, that combustion of H<sub>2</sub> takes place in a lesser extent. Initial conditions for this 2D study were taken from the specifications of a standard test usually adopted for DUST code checking ( $P = 1$  bar,  $T_k = 400$  K,  $u_g = u_p = 0$  and  $\sigma = 0.065$  kg/m<sup>3</sup>).

Not only the former 2D comparison is done, but we wanted also to check the behaviour of every combustion model under the conditions of a 3D test from experiments. Specifically, conditions from Experiment 2 (see Section 6.4.6) and a 3D grid featuring a spherical sector involving 36° of the total sphere. Distributions of variables along the radius of the sphere for these calculations at  $t = 2.5$  ms are presented in Figure 6.25 (the origin is set at the centre), while Figure 6.26 presents the history of pressure at a point placed near the wall of the sphere. One may wonder if the oscillations found at the beginning of the history of pressure are spurious, but a close watch to the

results prove that they actually are not. In fact, each fluctuation of pressure corresponds to a coming and going of the pressure wave in the sphere, as the radius is rather small (0.125 m) and the time scale in Figure 6.26 is quite wide. Thus, initial oscillations are caused by the way initiation is simulated in the sphere. Results show again an appreciable difference in pressure rise for both combustion models mentioned before: Vatikiotis [126] yields a final pressure near 9 bar at 12 ms and Yang et al. [136] stabilises at 8 bar, whilst the rest of models remain around 7 bar (absolute pressure). In order to make a decision, we just focus on the pressure, and a benchmark is set on the experimental results of Exp. 2 with Carbon (see Section 6.4.6). Then, as a conclusion to this previous study, we can state that any option is valid to model the C-graphite particle combustion, in terms of pressure, with the exception of two models giving excessive pressures. Among those valid options, the chemical scheme by O'Brien et al. [84] is selected, as it is also recommended by ITER technical basis ([95]).

#### 6.4.1.1 *Remarks on the modelling of graphite particles combustion*

Combustion of graphite particles involves some particularities with respect to the combustion of other solid species addressed up to date. Some modelling issues require a bit of attention, specially those related to the chemical model itself. That is, unlike the oxidation of tungsten, beryllium or aluminium, the combustion of carbon does not generate solid oxides. Indeed, according to the model selected for simulations (proposed by O'Brien et al. [84]), oxidation process is summarised in two main reactions:

- $C(s) + O_2(g) \rightarrow CO_2(g)$ ,
- $C(s) + H_2O(g) \rightarrow H_2(g) + CO(g)$ .

Meanwhile, hydrogen and carbon monoxide oxidise again, by other mechanisms, into gaseous species. Hence, carbon oxidation is assumed to generate only gaseous reaction products. The first implication of this fact into the computational code is about the species equation, as only one solid species is present in the problem and, then the resolution of the species equation makes no sense at all. Hence, the whole equation has been suppressed in the computational code which means multiple changes in every Cast3M operator as, for instance, in 'FUENTE' operator (see A). A later consequence in computations is the reduction of Random Access Memory to be allocated, and that leads into shorter computing times.

In the subsystem of balance equations for the solid phase, the mass transfer source term for graphite reactions,  $\dot{\omega}_{p,C}$ , is only applied into the equation for  $\sigma$ , although in the gas phase subsystem, the  $\dot{\omega}_{g,k}$  terms are applied both in the continuity equation and in the corresponding  $k$  species equations. Let us note there is no need to consider

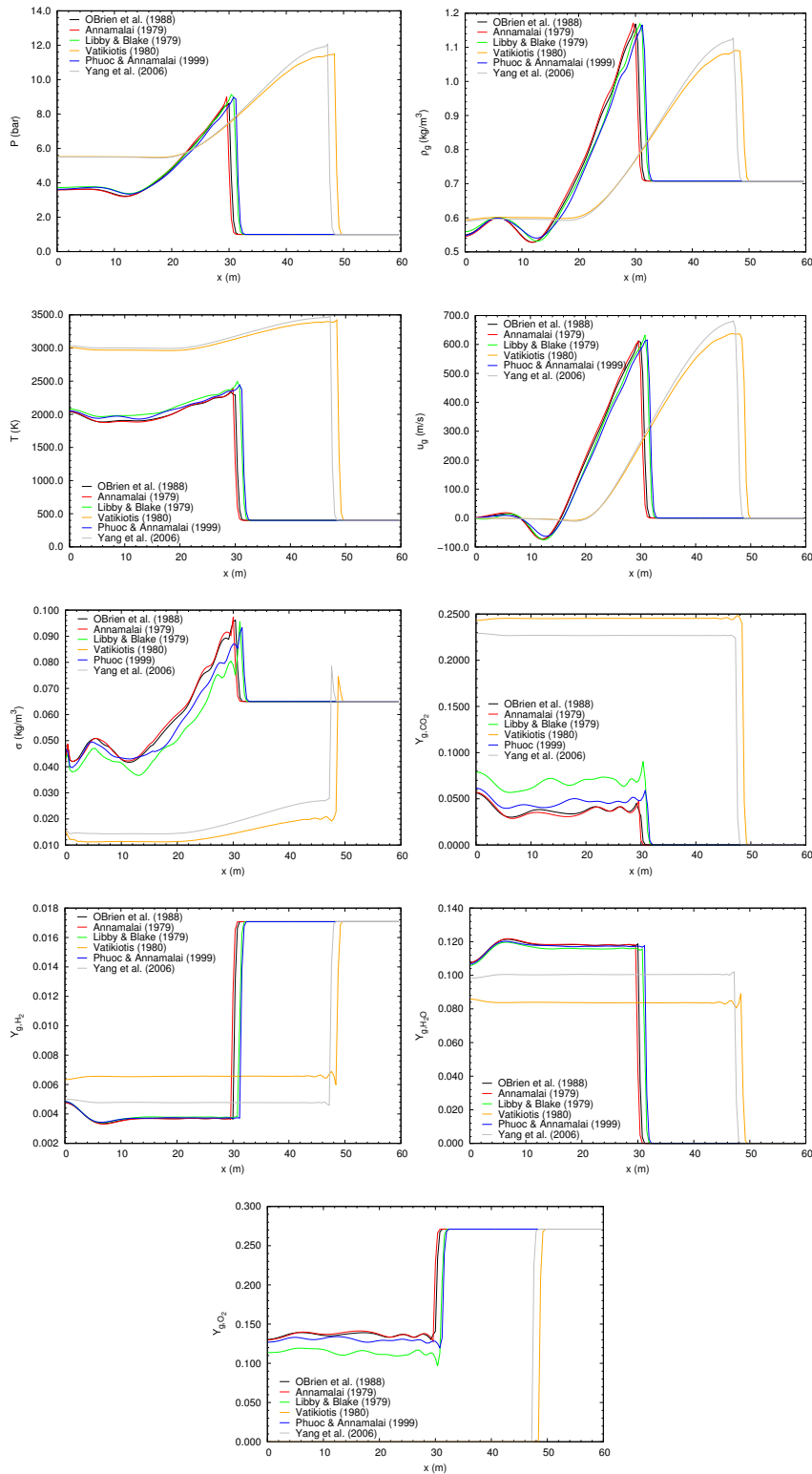


Figure 6.24: Implementation in 2D DUST code of combustion models from literature. The results correspond to a horizontal 2D tube at 24 ms.

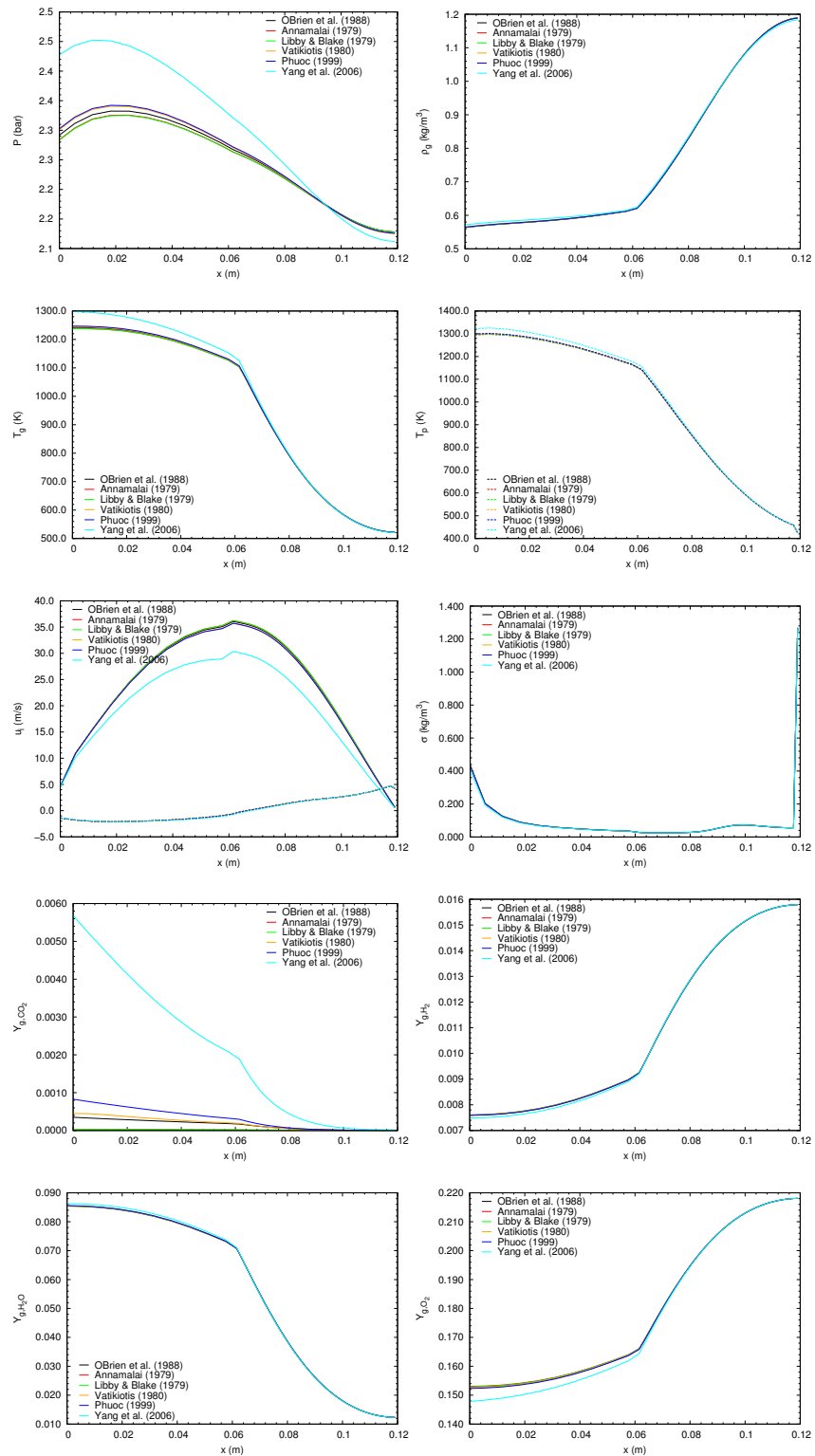


Figure 6.25: Spatial distributions at 2.5 ms in the CNRS Orleans sphere. Results by 3D *DUST* code with combustion models from literature. x coordinate seen as the distance from the centre of the sphere.

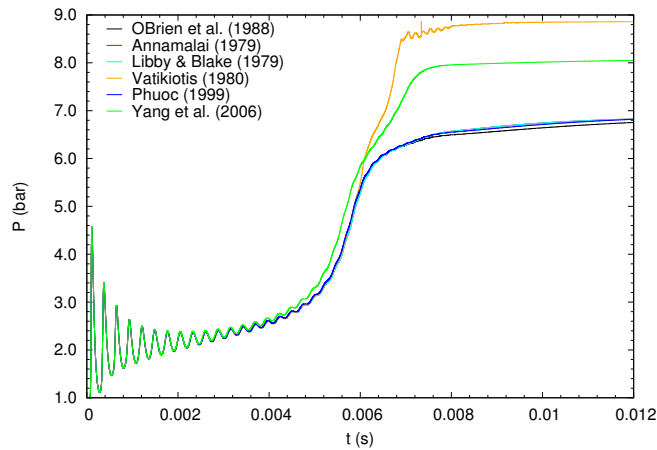


Figure 6.26: History of absolute pressure at the wall in the CNRS Orleans sphere. Graphite combustion laws from literature are compared.

CO<sub>2</sub> as a reacting species, but only as a product, if the reaction model by O'Brien et al. [84] is used.

#### 6.4.2 Definition of Orleans tests

The IRSN works on the development and performance of several experiments to study the combustion of solids in N<sub>2</sub>/O<sub>2</sub> atmospheres enriched with H<sub>2</sub>. Those are being performed in an experimental installation at the Centre National de la Recherche Scientifique (CNRS) in Orleans (France). The experiences are being conducted in the framework of the ITER project and the type of mixtures burnt so far are similar to those expected in prefigured accident scenarios inside the reactor. Some of these tests are reported by Sabard [104], including the following:

- Graphite tests: H<sub>2</sub>/N<sub>2</sub>/O<sub>2</sub> + C (dust),
- Tungsten tests: H<sub>2</sub>/N<sub>2</sub>/O<sub>2</sub> + W (dust).

The reactive two-phase mixtures are confined into a closed vessel acting as a combustion chamber. A sudden reaction is induced inside the vessel, leading into a explosion. Different experiences has been selected here to be used as a benchmark for a V&V study of DUST code.

##### 6.4.2.1 Test geometry

The geometry of the device employed for these tests is a 8-liter sphere filled inside with the reactive mixture. As the same apparatus is used for the different experiences selected, we will refer hereinafter

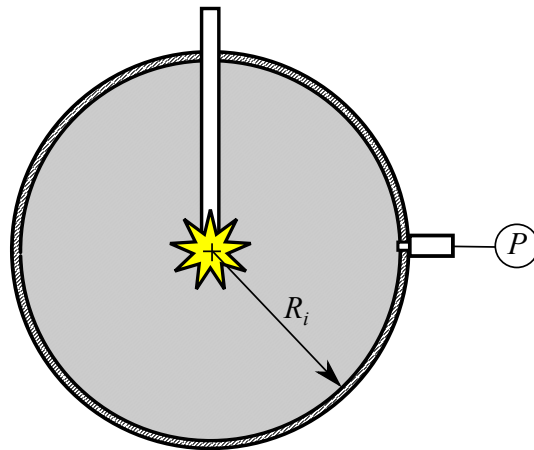


Figure 6.27: Simplified geometry of the CNRS Orleans experiment estimated for the modelling of this test.

as the *Orleans* tests for all those performed in this combustion chamber. Data from other equipment in the CNRS facility, e.g. the 56-litre sphere, are used here only for previous analysis.

In the geometric centre of the sphere, a weak electric spark provides the activation energy to initiate the chemical reaction. In the wall of the sphere, pressure is registered by means of a pressure transducer (see the outline in Figure 6.27), while the experiment is running, so that pressure-history plots are available for validation.

In what follows, experimental data on the Orleans tests, reported by Sabard [104], are used to validate the predictions on particle combustion by 3D *DUST* code. Before that, some aspects related to the modelling of the problem will be discussed.

#### 6.4.3 Mesh analysis

In this section, some aspects related to the mesh used in the numerical resolution of the three-dimensional problems are detailed. First of all a general description of the mesh is addressed, then, an analysis is performed on the use of different initiation conditions, and finally, a study is reported on the influence of grid resolution on the final results.

##### 6.4.3.1 3D grid of a sphere for Orleans tests

A three-dimensional grid comprising a spherical sector is used in order to model the geometry of the combustion chamber. Dimensions from the CNRS Orleans sphere are adopted. According to [104], experiments are performed into a combustion sphere with internal radius  $R_i = 0.125$  m.

Two different possibilities have been accounted for mesh generation: constant-thickness and constant-volume elements (both have

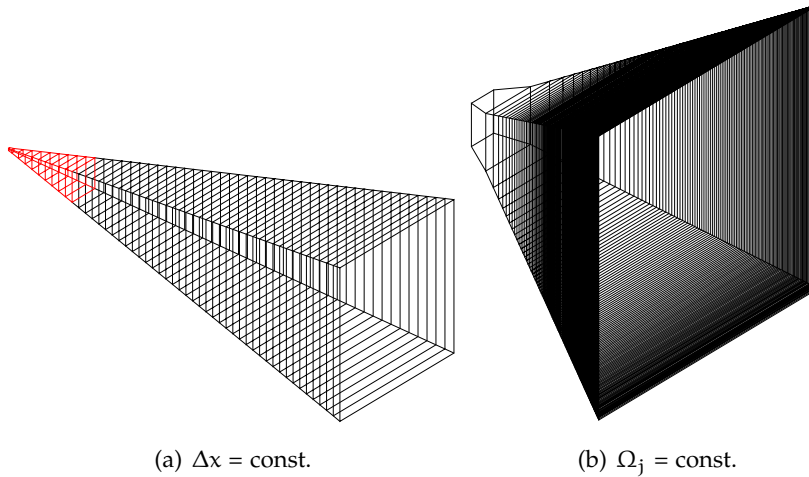


Figure 6.28: Two different approaches to mesh a spherical sector: constant thickness (left) and constant volumes (right).

been implemented into Cast3M). When the first approach is enabled, all elements are homogeneously defined in the  $x$  direction (being  $x$  the direction of the radius, with origin at the centre of the sphere). So, with a constant  $\Delta x$ , elements have a increasing volume as their nodes get closer to the sphere's wall (see Figure 6.28(a)). If the second method is preferred, then all elements in the spherical sector present a similar volume ( $\Omega_j = \Omega_{sect}/M$ , being  $M$  the number of cells), so that  $\Delta x$  becomes smaller for cells closer to the wall (see Figure 6.28(b)).

The selection of the initiation volume, where the ignition conditions are initially set, is not trivial. A small initiation volume will not allow to keep a maintained combustion, whereas a overdimensioned volume will exert a negative influence over the solution, which is then dominated by ignition. The smartest election seems to be that by which the stationary front wave is just strong enough to match with experiments. The criterion to that end is taken from Section 6.4.3.2.

Two additional parameters to look at in this kind of mesh are:

- The opening angle of the spherical sector,  $\alpha$ . If  $\theta$  is the polar and  $\phi$  the azimuthal spherical coordinate, the dimensions of the sector should be  $(R_i, \Delta\theta, \Delta\phi)$ . The fact is, for this case, we took  $\alpha = \Delta\theta = \Delta\phi$ . Different values are used in this study, from  $\alpha = 0.36^\circ$  (Figure 6.29) to  $\alpha = 30^\circ$ .
- The number of elements in the  $x$  direction. This parameter also ranges from 50 to 2500 cells for the studies presented in this document.

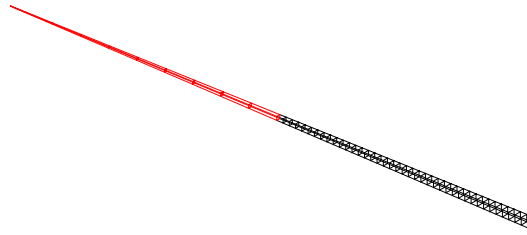


Figure 6.29: 3D grid of spherical sector with  $\alpha = 0.36^\circ$ .

#### 6.4.3.2 Some aspects related to grid generation on the simulation of combustion problems with Cast3M

On every CFD study, the mesh should account for certain minimum criteria. These criteria become more stringent in the case of compressible-flow combustion problems, and even more, according to our experience, when dealing with multiple Arrhenius models in FLAM operator (see Appendix A). Moreover, in the case of deflagration/detonation problems, the flame front speed would not be properly simulated, unless the mesh does meet these criteria. Also the expected raise in pressure due to combustion would not be obtained, and thus, non-physical solutions would be achieved.

Some best practice guidelines on grid design and grid quality for CFD, applied to nuclear reactor safety, can be found in [87]. With this motivation to create good quality grids, only structured mesh algorithms have been employed, with quadrangular (2D) or hexahedral elements (3D). Jumps in grid density, high aspect ratios in elements, and sharp grid angles have been avoided. The mesh requirements may also depend on the geometry of the problem studied, and thus, complex geometries can need the use of a finer and more regular grid in critical regions, e.g. regions with high gradients. For the spheric 3D grid, no refinements have been needed.

There are also other criteria more related to the modelling of the problem itself, as for instance the election of the geometry and size of the sub-domain where the effects of the initial spark are simulated. An *ad-hoc* study has been performed to assess the significance of these requirements for *DUST* code, under the scenario studied in this Section.

The study of the 3D sphere has permitted the definition of the optimal mesh for the simulation of the CNRS Orleans combustion experiments. The analysis includes both the 8-litre sphere aforementioned, and another sphere with a radius equal to the one of the CNRS Orleans 56-litre facility [104]. The simulations have been performed assuming  $H_2$  at 20% in the absence of particles,  $N_2/O_2 = 3.76$ , initial pressure of 99700 Pa, and initial temperature equal to 400 K. The combustion is assumed to be complete everywhere. For the initiation sequence, the von Neumann state is imposed together with the Arrhenius combustion model. That sequence makes allowance for

the hypothesis that the reactive matter within a volume considered for ignition is burnt instantaneously before the initial time ( $t = 0$  s). To this end, the thermodynamic conditions for the gas within the ignition volume are estimated to be those at the von Neumann state (i.e., 2000 K), and then chemical reaction is allowed so that the gas is brought into a burnt state through an isochoric combustion. These conditions are equivalent to the imposition, into the ignition volume, of an initial total enthalpy per unit of volume equal to  $2.15 \times 10^6$  J/m<sup>3</sup>.

The parametric study included the evaluation of the influence of the ignition volume, the number of cells in the whole domain and in the ignition volume, and the use of cells with equal volume and different thickness ( $\Delta x$ ) or with the same thickness and different volume (two approaches for mesh generation shown in [Figure 6.28](#)).

In both cases, it has been found that there is a minimum ratio of ignition volume with respect to the total volume of the system, required for a proper simulation of combustion. This ratio matches for the two geometries studied: the minimum ratio is 14%, for both spheric geometries, the sphere of 8 litres and the one of 56 litres. This result confirms this mesh requirement is not “scale dependent”. But is it “geometry dependent”?

To evaluate that, a 2D geometry has also been tested. This is a common rectangular, structured mesh modelling a smooth tube, similar to others in this work (see [Section 6.1.1](#)). Besides, the study of the 2D tube permitted the comparison of the results of the simulation with a standard combustion problem widely studied both theoretically and experimentally: the detonation inside a tube. We can use as a benchmark an experimental study by Teodorczyk [119] on direct detonation initiation and DDT in H<sub>2</sub>-air mixtures. The rectangular grid is 125 mm long, and the initial thermodynamic state and the von Neumann initiation sequence are imposed as we previously did at 3D. Now the parametric study included the analysis of the influence of the tube’s height, ignition volume, number of cells in the domain and in the ignition volume, and element aspect ratio  $\Delta x/\Delta y$ . Finally, for the 2D tube we found the minimum ratio of ignition volume with respect to the total volume of the system is 5% for the development of a combustion front, a different value to that found in the two spherical tests. Hence, the ignition volume ratio is scale independent, but geometry dependent.

The rest of parameters did not exert a big influence, with the exception of the grid resolution. The sensitivity of this parameter was already tackled in [Section 6.4.3.3](#), and it is an important factor in every simulation, but on detonation calculations this is crucial, as it depends on the structure of the detonation wave itself. Actually, even in 1D geometries, a detonation wave has a multidimensional structure, consisting of interacting reactive Mach waves. As reported by exper-

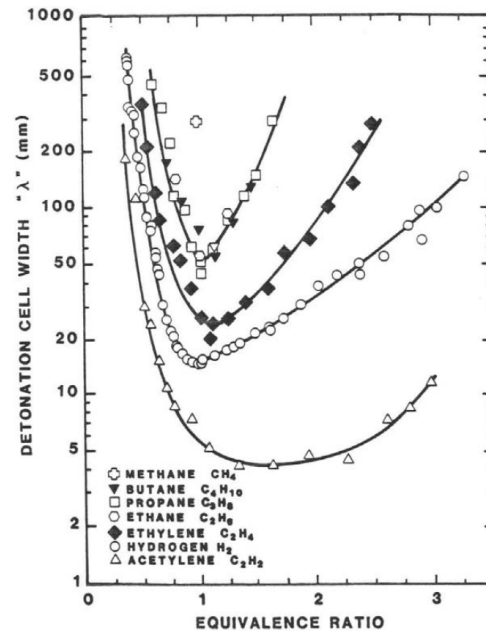


Figure 6.30: Cell detonation sizes for different fuel-air mixtures (source: Teodorczyk [119]).

iments [119], in a tube with rectangular section, a diamond-shaped cell pattern is left by a detonation wave. The regular pattern is typical of low pressure mixtures involving oxygen as oxidizer and inert gases as diluter. In the case of hydrogen-air mixtures at atmospheric conditions the structure is very irregular and the dimension of the principal diamond-shaped cell length  $\lambda$  varies from about  $\lambda = 15$  mm (stoichiometric mixtures, i.e.  $X_{\text{H}_2} \approx 0.296$ ) to  $\lambda = 1$  m ( $X_{\text{H}_2} \approx 0.136$ ). In general, the more reactive the mixture, the smaller the cell size [8]. In detonation tubes with  $\text{H}_2$ , the cell detonation size is experimentally known to be a function of the combustion equivalence ratio (see Figure 6.30). For the specific case of Orleans tests (see Section 6.4.6), we have that for a mixture 20%  $\text{H}_2$  and  $\text{N}_2/\text{O}_2 = 3.76$ , the cell detonation size  $\lambda$  would range 50 ~ 80 mm; and for a mixture 20%  $\text{H}_2$  and  $\text{N}_2/\text{O}_2 = 2.33$ , the cell detonation size would rise to 100 ~ 200 mm. Note this is based on a study on detonation in straight tube, but we can state a parallelism to the case of spherical sector with a small  $\alpha$ , to get an idea about the order of magnitude of the mesh size.

A detailed study of a detonation wave would require mesh of the order of the reaction length, which is about 1/100 - 1/10 the dimension of a detonation cell. In principle, the more grid elements are placed inside the detonation cell, the better the wave structure is reproduced. However, there are limits: as diffusive terms are not considered in the model of equations, the resolution at small length scales will not be realistic. We can only expect to solve the global physics of detonation, using an Arrhenius-type combustion model together with Euler equations, and ignoring the effects at diffusive scale.

Finally, there is another restriction, as concerning the solid phase, it would be meaningless to impose a cell size smaller than the average size of the particles, which in this particular problem is set to 35.0  $\mu\text{m}$ .

It is worth noting that the study by Teodorczyk [119] referenced here considers only monophasic mixtures, and no reliable information has been found about the cell detonation size when particles are present. The addition of these to the mix usually has the consequence of increasing the effects of turbulence by breaking the laminar flame front. This is expected to have a mixing effect that causes the characteristic size of the detonation cell is smaller.

#### 6.4.3.3 Mesh convergence analysis

The influence of the number of elements of the mesh for the case of the 3D sphere model have been assessed by analysing gauge pressure at the wall of the CNRS Orleans sphere of 8 litres during Graphite test. Four different simulations have been performed with  $N = 50, 500, 2500,$  and  $3500$  elements. Parameters for those simulations agree with the initial conditions of experiment EXP<sub>1</sub> in Section 6.4.6. Note that, according to what is exposed in Section 6.4.3.2, the detonation cell length for the monophasic detonation would be  $50 < \lambda < 80$  mm. Grid resolution should range  $5 \sim 8$  mm (if mesh elements are 1/10 the dimension of a detonation cell), and  $0.5 \sim 0.8$  mm (if they are 1/100 of its size). The four grids employed in this Section would meet the first condition,  $\Delta x < \lambda/10$ . For the second case ( $\lambda/100$ ), only the grid with  $N = 50$  elements ( $\Delta x = 2.5$  mm) is over the resolution required, while grids with  $N = 500, 2500,$  and  $3500$  elements, have  $\Delta x$  equal to 0.25, 0.05, and 0.035 mm, respectively.

As shown in Figure 6.31, when the number of elements increases, the combustion time also increases, and the initial fluctuations are reduced. Regarding the influence of solid angle used to model the 3D sphere it is found that over a certain angle, the results become grid independent, i.e. results for the case of  $20^\circ$  and  $30^\circ$  merge (Figure 6.32).

#### 6.4.4 Analysis of different initiation sequences

Different initiation strategies have been developed for *DUST* code. In this section some of them are enumerated, and their influence on predicted combustion times and maximum pressures is analysed.

Choosing a proper initiation sequence is a central issue for the sort of simulations undertaken in this Thesis. Focusing on the Orleans experiences, an initial spark releases enough ignition energy to start the combustion reaction, and that should be properly modelled for the simulations. Notwithstanding, the solution must not be artificially distorted by this effect.

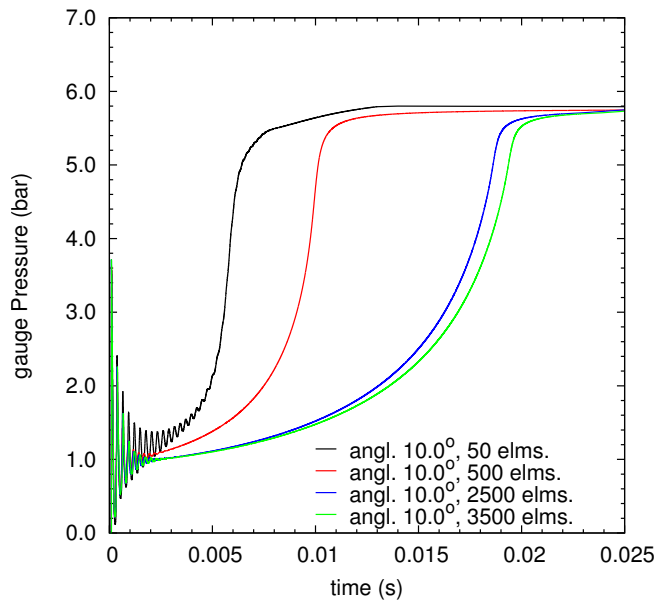


Figure 6.31: History of gauge pressure at the wall in the CNRS Orleans sphere. Four grids are employed in simulations with 50, 500, 2500, and 3500 elements, in order to study the grid convergence.

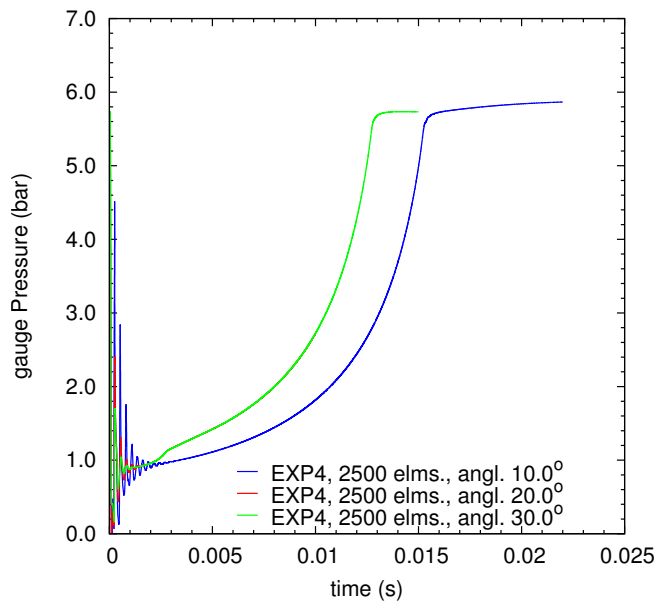


Figure 6.32: History of gauge pressure at the wall in the CNRS Orleans sphere. Three grids are employed in simulations with three different solid angles.

	Experience	Grid elements			
	EXP1	50	500	2500	3500
$P_{\max}$ (bar)	5.73	5.80	5.75	5.75	5.75
Error (%)		1.30	0.44	0.41	0.41
$t_{\text{comb}}$ (ms)	18.90	8.19	10.70	17.95	18.67
Error (%)		56.67	43.39	5.03	1.23

Table 6.2: Grid convergence analysis for Orleans tests. Errors in peak pressure and time of combustion, for every grid studied.

In the Orleans tests, as reported by Sabard [104], initiation takes place in the centre of the sphere so that they can study the spherical propagation of the flame. For the study they perform about two-phase mixtures inside the combustion chamber, two ignition systems are used: electric spark ignition and laser beam. The first method consists in two electrodes delivering around 20 mJ of ignition energy, which means a tiny amount of energy. Even when the ignition is triggered by a laser shorting (with beam diameter of 3.2 mm), the ignition energy is fairly limited. In the experiments, this energy allows the molecules of reactive matter, closest to the electrode, to ignite. Combustion then spreads out, in a higher length scale, and a flame front is gradually formed which could lead into a detonation front. By contrast, a stronger initial impulse should be given on simulations, then imposing jump conditions pertaining to a detonation.

Therefore, the ignition strategies implemented in *DUST* are intended to generate an intermediate state at  $t = 0$  in the activation domain, corresponding to a certain burnt state. This is modelled as:

- ACT1 Isochoric combustion as a result of solving the energy balance equation, after assuming complete combustion and, then, obtaining the adiabatic flame temperature. The new thermodynamic state is computed considering an isochoric process.
- ACT2 The von Neumann state is imposed in the whole activation domain and, then, the burnt state is computed for those conditions.
- ACT6 The electric spark is modelled as a release of energy  $Q_{ig}$ , added to the system inside the ignition volume.

At the end of the ignition sequence, these options define the total enthalpy per unit of volume and a total internal energy of the intermediate state. The volume where this energy is released in our model (i.e., the activation domain or ignition volume), is based on the

OPTION	$Q_T$ (J)	$Q_{ig}$ (J/m <sup>3</sup> )	$E_g$ (J/m <sup>3</sup> )
ACT2	–	–	$2.16 \times 10^6$
ACT6	$0.57 \times 10^3$	$0.5 \times 10^6$	$0.76 \times 10^6$
ACT6	$1.15 \times 10^3$	$1.0 \times 10^6$	$1.24 \times 10^6$
ACT6	$1.73 \times 10^3$	$1.5 \times 10^6$	$1.74 \times 10^6$

Table 6.3: Orleans tests. Energy parameters for different initiation strategies.

conclusions of the previous study in [Section 6.4.3.2](#): 14% of the total volume.

When the option ACT2 is selected, the total enthalpy per unit of volume of the intermediate state at  $t = 0$  is the sum of the total enthalpy per unit of volume associated to the initial conditions before combustion, plus the change of enthalpy corresponding to the new thermodynamic conditions (von Neumann state) and the change of enthalpy relative to the subsequent combustion. Conversely, when ACT6 is selected, the variation of the total enthalpy is given by the energy  $Q_{ig}$  (in J/m<sup>3</sup>) defined in the test.

A sensitivity study has been raised on the use of the different initiation strategies, in order to assess the influence of each one on the solution. Thus, various  $Q_{ig}$  have been considered for the case of ACT6, and several particle concentrations in the case of ACT2. The outcomes of this study are outlined in [Figure 6.33](#), which shows the pressure evolution with time at the sphere's wall for a 500-elements structured grid. The test parameters match with the experience EXP1 at the 8-litre sphere of CNRS Orleans. The figure shows the pressure evolution for ACT2 (von Neumann ignition sequence) with  $\sigma = 0, 94.1$  and  $200.0$  g/m<sup>3</sup>. Three different ignition energies have been tested ACT6 strategy, by the simulation three sparks: 0.57 kJ, 1.15 kJ, and 1.73 kJ. These correspond, respectively to ignition energies  $Q_{ig}$  of  $0.5$  MJ/m<sup>3</sup>,  $1.0$  MJ/m<sup>3</sup>, and  $1.5$  MJ/m<sup>3</sup>. Regarding the total internal energies per unit of volume, the case with  $Q_{ig} = 1.5$  MJ/m<sup>3</sup> results in a  $E_g$  a 20% lower than the one obtained with ACT2 and no particles, the one with  $1.0$  MJ/m<sup>3</sup> gives a 43% lower, and the third one,  $Q_{ig} = 0.5$  MJ/m<sup>3</sup>, results in a 66% lower, compared with the case of ACT2 and no particles. All these parameters are gathered in [Table 6.3](#).

Therefore, with respect to the option ACT2, the different ignition options result in a reduction of the initial total internal energy associated to the ignition volume, what generates an relative increment of the combustion time and a slight reduction of the maximum pressure achieved.

Another important output is found: we need a relatively high ignition energy, otherwise the initial combustion front wave is not prop-

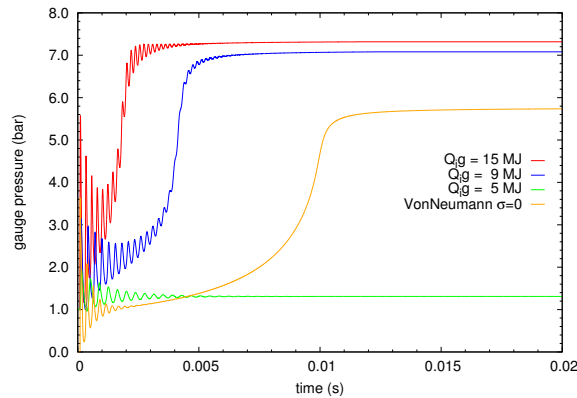


Figure 6.33: 3D Orleans with graphite. Overpressure (Pa) at the sphere's wall vs. time (s), for different ignition strategies (CNRS experimental conditions with the 8 litres sphere).

erly simulated and the results just show a weak deflagration where the combustion front and the pressure wave do not travel together. Moreover, in that case the flame slows down until it quenches. As a consequence, the quantity of mass burnt within the sphere does not fit with the experimental data and, therefore, the expected pressure rise is not obtained. We found, in fact, that the minimum value to run the problem is above  $Q_{ig} = 0.9 \text{ MJ/m}^3$ , and it performs a good simulation above  $Q_{ig} = 1.0 \text{ MJ/m}^3$ .

One may wonder how such a significant amount of energy could produce an effect that is comparable to that of a small spark (20 mJ) in the Orleans experiences. As a matter of fact, the focus must be on the energy by unit volume. If the energy released by the ignition system is expressed per unit volume, as for instance considering the diameter of the laser beam, a value of  $1.16 \text{ MJ/m}^3$  is obtained. And, opportunely, it closely approximates the value numerically estimated.

All things considered, the model responds in a suitable manner to an ignition energy per unit volume of the order of that provided by the spark and, as can be seen, to other initiation strategies (ACT2) intended to impose jump conditions pertaining to detonation.

#### 6.4.5 Analysis on the influence of particle concentration

As mentioned in the literature on graphite combustion (Section 2.4.6), flammable limits exist for suspensions of graphite particles in air and, in general, for any dispersion of dust. For the experiments involving graphite being modelled here (Orleans tests), the presence of a certain amount of hydrogen improves the flammability of the mixture and, consequently, of the particles. However, it has been observed that the

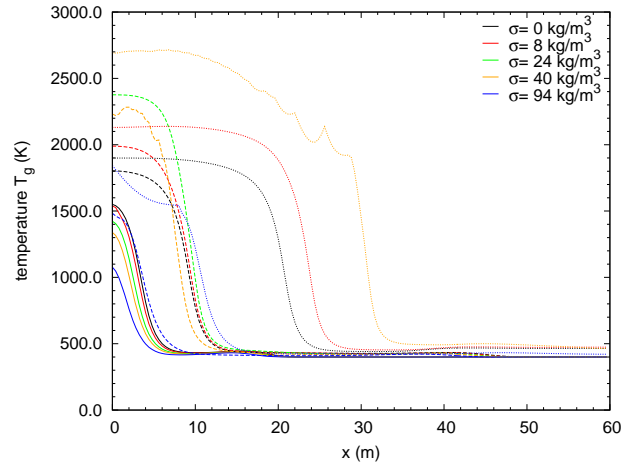


Figure 6.34: Influence of  $\sigma$  in the combustion. Transient evolution of temperature distributions for various particle concentrations.

concentration of particles have a visible effect on the reactivity of the biphasic system.

According to Sabard [104], flammability limits of the powders are between 50 and 100 g/m<sup>3</sup> for the lower limit, and between 2000 and 3000 g/m<sup>3</sup> for the upper limit. Given the concentration range covered by the Orleans experiments, closer to the lower flammability limit, the addition of particles should result in an increase of the reactivity of the mixture, which could lead to a more rapid combustion.

In this section the influence of the particle concentration on the simulated results is evaluated. First, an experience is reported in which the sensitivity of the flame propagation to  $\sigma$  is evaluated by means of a simple 2D grid, similar to that already used in the simulations of Section 6.4.1. This influence is represented by the temperature  $T_g$  in Figure 6.34. The initial conditions of the test agree with Orleans EXP1.

Regarding the 3D sphere, Figure 6.35 shows the influence of particle concentration in the case of a CNRS graphite experiment. As shown combustion time decreases as particle concentration increases.

#### 6.4.6 Simulation of graphite experiments at CNRS Orleans

The validation of DUST code under typical ITER combustion conditions have been performed with the simulation of the Orleans Experiments [104].

For the case of Graphite combustion, four experiments performed in the 8 litres sphere (0.25 m diameter) have been simulated. They have been named as EXP1, EXP2, EXP3, EXP4. The experimental conditions of those tests are:

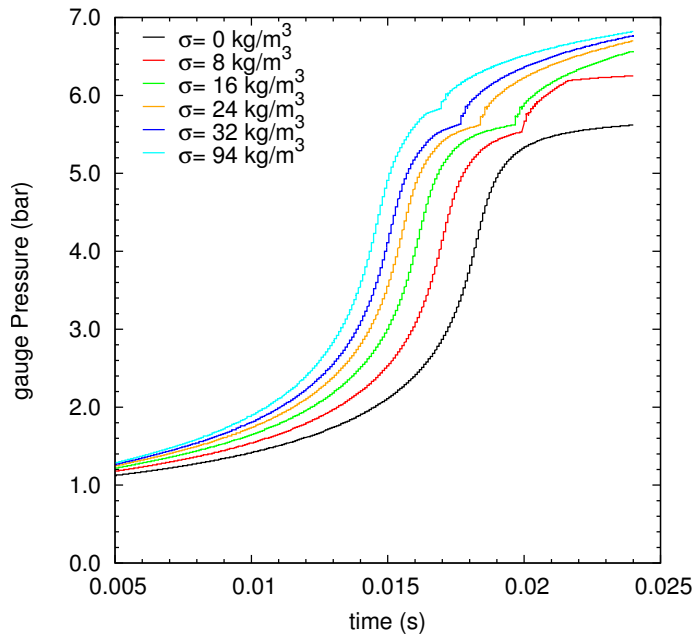


Figure 6.35: 3D Orleans with graphite. Overpressure (Pa) at the sphere's wall vs. time (s), for different particle concentrations (CNRS experimental conditions with the 8 liters sphere).

EXP1: 20% H<sub>2</sub> ( $X_{\text{H}_2} = 0.2$ ) and N<sub>2</sub>/O<sub>2</sub> = 3.76. Graphite powder concentration  $C(s) = 0 \text{ g/m}^3$ . No dust was present in this experiment.

EXP2: 20% H<sub>2</sub> ( $X_{\text{H}_2} = 0.2$ ) and N<sub>2</sub>/O<sub>2</sub> = 3.76. Graphite powder concentration  $C(s) = 94.1 \text{ g/m}^3$ .

EXP3: 20% H<sub>2</sub> ( $X_{\text{H}_2} = 0.2$ ) and N<sub>2</sub>/O<sub>2</sub> = 2.33. Graphite powder concentration  $C(s) = 0 \text{ g/m}^3$ . In this experiment no dust was present.

EXP4: 20% H<sub>2</sub> ( $X_{\text{H}_2} = 0.2$ ) and N<sub>2</sub>/O<sub>2</sub> = 2.33. Graphite powder concentration  $C(s) = 96.6 \text{ g/m}^3$ .

The experimental results, reported by Sabard [104], show the increase of pressure inside the combustion sphere as the H<sub>2</sub> and the graphite particles inside get burnt (see Figure 6.36). According to [104], the injection of particles in the reactive atmosphere leads to an increase of the time of combustion and also an increase of maximum pressures. It is also reported that the H<sub>2</sub> initially present inside of the sphere burns completely in all the experiments, whilst the combustion of graphite is not complete (the rate of graphite transformed into CO and CO<sub>2</sub> is 21.15 % for EXP2 and 28.17 % for EXP4). That is, for the cases under study, a reduction of the ratio N<sub>2</sub>/O<sub>2</sub> leads to a rise in the amount of graphite burnt into CO and CO<sub>2</sub>. For the cases with

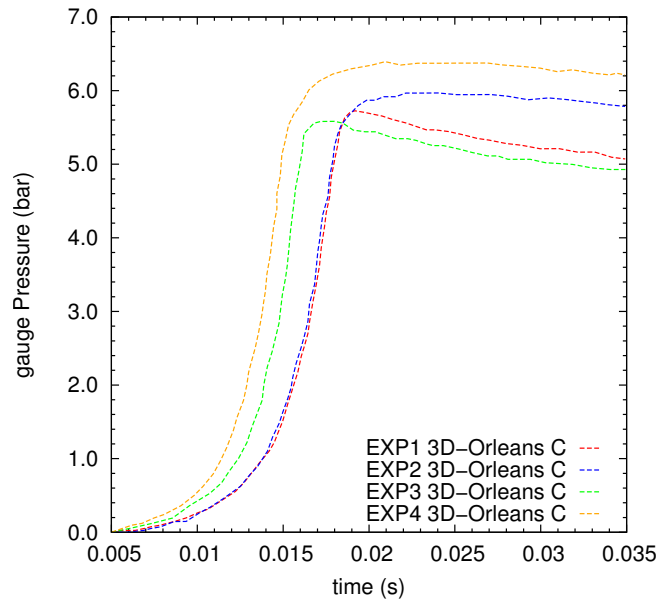


Figure 6.36: Experimental results. Gauge pressure (Pa) at the wall vs. time (s) for experiments with graphite in the CNRS Orleans sphere. Source: Sabard [104].

a ratio  $N_2/O_2 = 2.33$ , more oxygen is present in the initial mixtures and the combustion efficiency of the graphite particles is enhanced.

Also from the experimental results, we can deduce that combustion of powder takes longer than combustion in the case with a gaseous mixture, and it contributes to provide an additional pressure in the chamber. Although the pressure rise is faster in the cases with particles, due to turbulence and energy generated by particle combustion, the existence of particles in the mixture results in a different type of pressure curve: after the first increase, pressure keeps increasing as particle combustion is ongoing.

In addition, some conclusions can be outlined from results in Figure 6.36 regarding the maximum pressures. A diminishing of the ratio  $N_2/O_2$  entails a major reactivity of the mixture, because of a higher proportion of oxygen in the enclosure. This is seen in the experiments as a reduction of the combustion times. However, it has no influence on the maximum pressure for the cases without particles (EXP1 and EXP3) as the amount of reactive  $H_2$  is not affected. Indeed, the major proportion of oxygen leads to a higher pressure for a given concentration of particles, when  $N_2/O_2$  goes down from 3.76 to 2.33 (EXP2 and EXP4).

Concerning the simulations, the physical domain is a sphere of 250 mm of diameter. Due to its spherical symmetry it has been simulated only 3D portion of sphere. This portion has been modelled with a 3D mesh with the shape of a squared pyramid—as a approximation of a spheric sector—with  $10^\circ$  of angle (see Section 6.4.3 on mesh

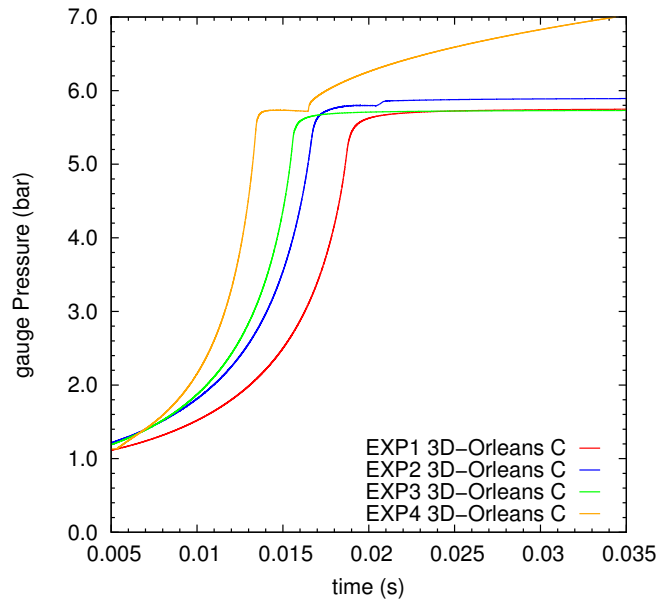


Figure 6.37: Result of 3D numerical simulations for graphite Orleans tests. Gauge pressure (Pascals) at the sphere's wall vs. time (seconds).

analysis). Simulations have been performed in Cast3M with a 3D two-phase Eulerian model.

The ignition procedure used for these tests is the *von Neumann* Strategy (ACT=2). The combustion model selected is the reaction scheme by O'Brien et al. [84] (eqs. 2.112, 2.114).

Results are shown in the following Figure (Figure 6.37). It shows the overpressure (i.e. gauge pressure:  $P_{abs} - P_{atm}$ ) evolution with time at the wall of the sphere for the four experiments simulated. As shown, final pressure at the wall is well predicted with the DUST code for the four experiments. It can be also seen that the combustion time (i.e. the time at which the maximum pressure is reached) is reasonably well predicted taken into account that no turbulence is modelled in this simulations. Let us recall that, according to Sabard [104], the flame propagation takes place in a smooth, spherical flame front, and the effect of turbulence into the burning speed is assumed into the Arrhenius law.

Regarding tendencies, the comparison between the simulations of EXP1 and EXP2 shows that the increase of the concentration of dust generates a reduction of the combustion time. That effect is found both in the experiments and the simulations.

Also, in light of Figures 6.36 and 6.37, the main difference between the pressure predicted and the actual one of the experiments is found at the initial 10 ms of the tests, where simulations shows a pressure fluctuation, caused by the ignition strategy, which is stabilised after 3 ms to a gauge pressure over 1 bar. These phenomena are somehow expected, and are due to the ignition procedure that is being used in the simulations (ACT2). As a matter of fact, by this pro-

	Experience			
	EXP1	EXP2	EXP3	EXP4
Experimental $P_{max}$ (bar)	5.72	5.96	5.58	6.39
Numerical $P_{max}$ (bar)	5.75	5.89	5.73	5.89
Error (%)	0.44	1.23	2.63	8.46
Experimental $t_{rp}$ (ms)	19.2	18.9	16.2	15.6
Numerical $t_{rp}$ (ms)	19.8	17.1	15.2	13.2
Error (%)	3.12	9.52	6.17	15.38

Table 6.4: Numerical errors in peak pressure and rise time of pressure for the Orleans Tests.

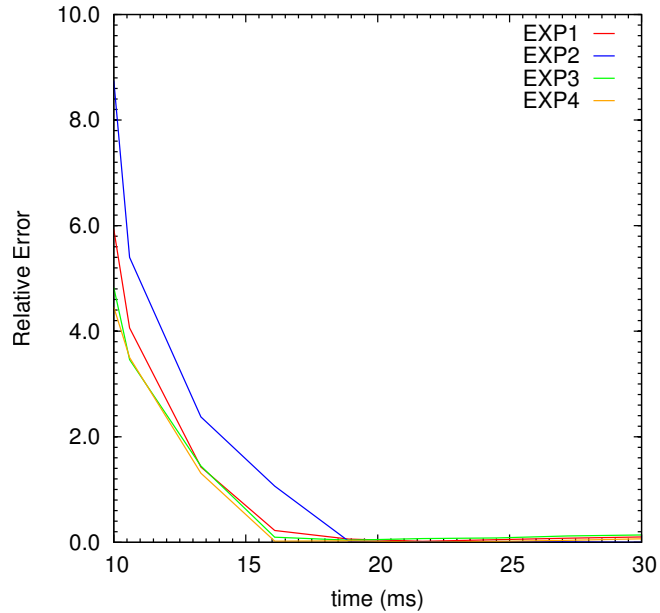


Figure 6.38: 3D Orleans tests with graphite. Numerical errors vs. time for every test simulated from EXP1 to EXP4.

cedure the VN conditions are fixed at  $t = 0$ , starting a going-and-coming flame front that gets stable around  $t = 3$  ms. This difference between the numerical and experimental pressures ( $\approx 1$  bar) generates considerable numerical error in the first instants of the simulation. When the simulation time progresses, however, the error drops until almost disappear in the area near the peak pressure. [Figure 6.38](#) shows the numerical error, which has been calculated as  $\delta P_E = |P_{exp}(t_n) - P_{num}(t_n)| / P_{exp}(t_n)$ , for every discrete time  $t_n$ . The remarkable fact is that, eventually, the numerical results provide acceptable predictions about the pressure rise time and very small errors in what refers to the maximum pressures (as shown in [Table 6.4](#)).

Finally, it is worth pointing out that the actual combustion of graphite and hydrogen in the experiments is being modelled with an Arrhenius model that constitutes a first level of approximation to the chemical phenomena that may be present within the experimental enclosure.

## 6.5 3D SIMULATION OF TUNGSTEN COMBUSTION INSIDE A SPHERE

### 6.5.1 *Simulation of tungsten experiments at CNRS Orleans*

Several tests have also been performed in order to validate the code in what concerns the tungsten reaction model.

In particular, four experiments of the sphere from the CNRS Orleans, reported by [\[104\]](#), are modelled. This is done after the wide study addressed on the combustion of graphite in the same combustion sphere, and taking advantage of the results previously obtained about mesh convergence, initiation volume and cell-detonation size.

All of the experiences selected for simulation are carried out in mixtures  $H_2/O_2/N_2/Tungsten$  with a 20% in volume of  $H_2$ , with respect to the gaseous mixture. Different  $N_2/O_2$  ratios and concentrations of tungsten ( $\sigma$ ) are considered though.

The four experiences modelled are:

EXP1:  $H_2$  20%,  $N_2/O_2 = 2.33$ ,  $\sigma = 0$  ;

EXP2:  $H_2$  20%,  $N_2/O_2 = 2.33$ ,  $\sigma = 119.9$  g/m<sup>3</sup>;

EXP3:  $H_2$  20%,  $N_2/O_2 = 3.76$ ,  $\sigma = 0$  ;

EXP4:  $H_2$  20%,  $N_2/O_2 = 3.76$ ,  $\sigma = 127.1$  g/m<sup>3</sup>.

The rest of the initial conditions assumed for the computational analyses are gathered in [Table 6.5](#).

The specific heats at constant pressure of the gas mixture are temperature dependent and are computed through [Equation 2.84](#). Coefficients of the polynomial are obtained from the NIST data base [\[83\]](#).

VARIABLE	VALUE
Sphere diameter $D_{\text{int}}$ (m)	0.25
Temperature of gas, $T_g$ (K)	273
Temperature of particles, $T_p$ (K)	273
Pressure (Pa)	$10^5$
Initial Velocity (both phases)	0.0
Particle diameter ( $\mu\text{m}$ )	0.5
Tungsten density, $\rho_W$ ( $\text{kg}/\text{m}^3$ )	19386.0
Tungsten trioxide density, $\rho_{W\text{O}_3}$ ( $\text{kg}/\text{m}^3$ )	7160.0
Specific heat of tungsten, $c_{p,W}$ ( $\text{J}/(\text{kg}\cdot\text{K})$ )	162.47
Specific heat of tungsten trioxide, $c_{p,W\text{O}_3}$ ( $\text{J}/(\text{kg}\cdot\text{K})$ )	568.48

Table 6.5: Initial parameters for tungsten combustion tests in CNRS Orleans sphere.

Because of the high density of tungsten, the use of a splitting method is advisable. For these simulations the splitting method described in Section 4.2 is adopted. The numerical schemes applied for the numerical fluxes evaluation are AUSM+ for the gas phase and Rusanov scheme for the solid. The Advanced Source-Term Treatment (Section 4.4) is applied for the resolution of the source-term ODE problem. Moreover, to ensure stability, mainly in the first milliseconds of computation, the CFL parameter is set to 0.55.

The combustion model of tungsten considered on the simulations is the two-reaction approach proposed by Topilski [120], that is, Equations 2.128 and 2.131. In the Arrhenius expression of the reaction rate of W reacting with air, the pressure in the equation is assumed to be the total pressure of the mixture, instead of the partial pressure of any species. Conversely, in the reaction rate of W reacting with steam, the pressure considered is the partial pressure of  $\text{H}_2\text{O}$ . No scale factor or reduction has been applied in this case.

Details about the experimental results for the four experiences can be found in [104]. Figure 6.39 shows the experimental pressure measured in the sphere. As one can expect, the mixture with more concentration of  $\text{O}_2$  burns faster: a reduction of the  $\text{N}_2/\text{O}_2$  ratio from 3.76 to 2.33 leads to lowering combustion time. For the gaseous mixtures of  $\text{H}_2/\text{O}_2/\text{N}_2$  without particles, the flame propagation takes place through a spheric and smooth flame front which becomes cellular over time [104].

The addition of particles in the mixture leads to a decrease of the combustion time. This is explained by the increase of turbulence generated by the burning particles, which enhances the reactivity of the mixture. Further, the presence of tungsten particles in the system

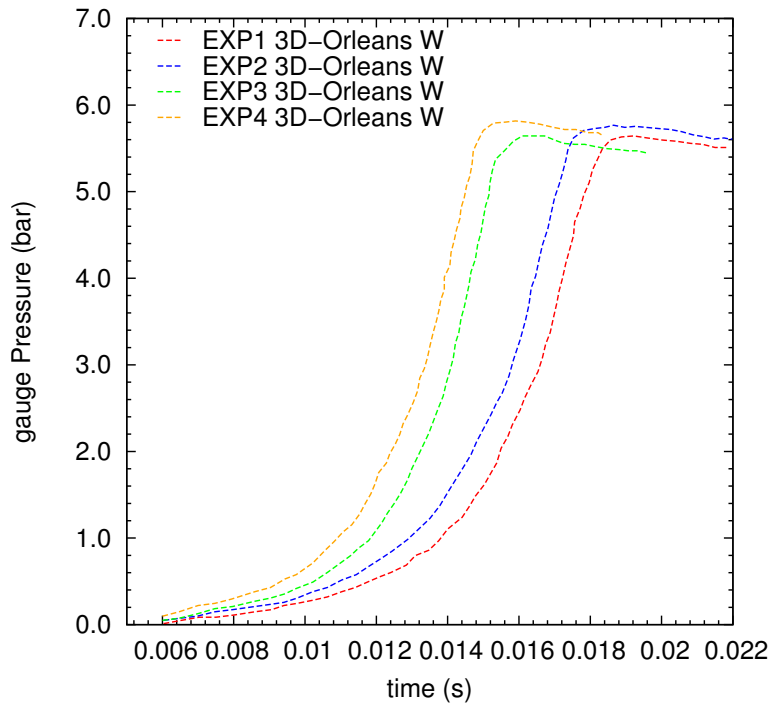


Figure 6.39: Experimental gauge pressure in the sphere vs. time for Tungsten Orleans tests.

induces a slight rise of the combustion maxima, compared with the mixtures without dust. However, there are similar shapes of pressure profiles, whatever the amount of tungsten in the system.

Numerical results obtained with *DUST* code, as shown in Figure 6.40 and 6.41, also exhibit this behaviour: combustion is faster in those cases with tungsten particles, as deduced from the curves for pressure history.

Results with two different meshes are presented. In fact, Figure 6.40 corresponds to a coarse mesh of 60 cells in the axial direction, whilst Figure 6.41 to a finer mesh with 600 cells. Meshes are structured and homogeneous, that is, the element width is constant across the sphere diameter. Thus, the grid density, in other words, the number of elements, seems to have a big influence on the burning velocity and, then, in the total combustion time. As shown in the figures, the numerical combustion times approach the experimental times when the mesh is refined.

Similar tendencies are observed between calculated and experimental pressures regarding the  $N_2/O_2$  ratio and combustion time. Predictions on maximum pressures match, in general, with the experimental values. In Figure 6.41 we see an overestimation of pressure which is important in the case of EXP2 (gas and particle mixture at high concentrations of  $O_2$ ). The other three cases give more accurate predictions on that respect.

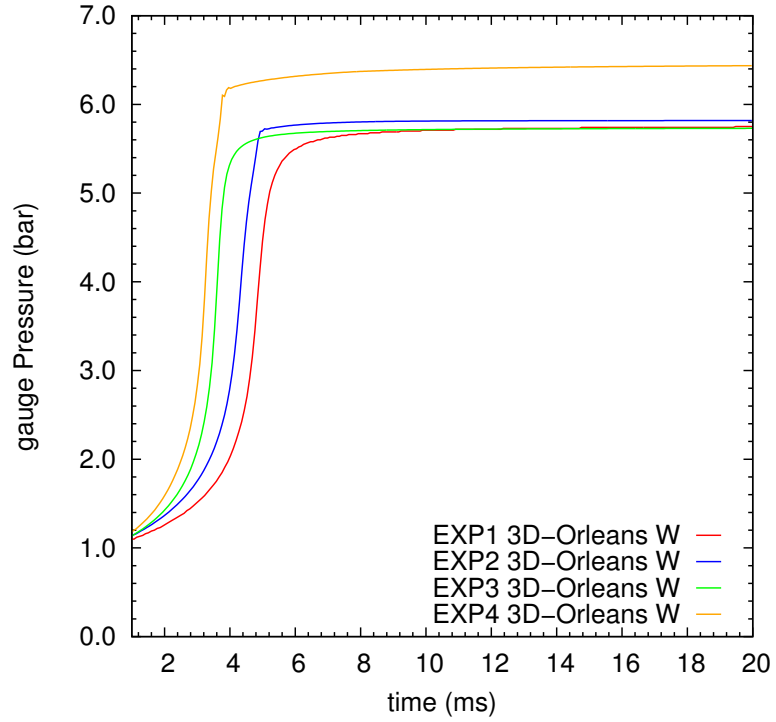


Figure 6.40: Gauge pressure at the wall vs. time for simulations. Mesh of 60 cells. Tungsten Orleans tests.

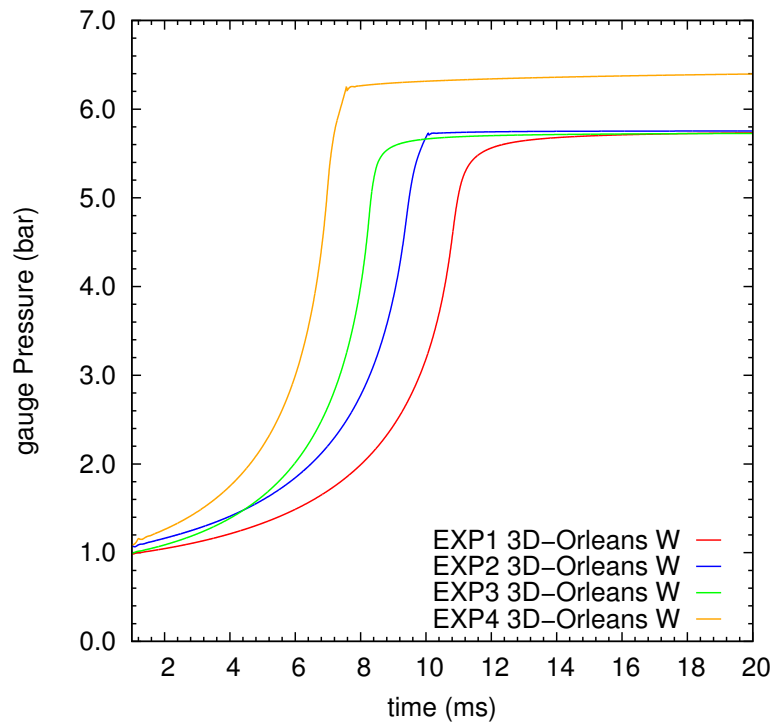


Figure 6.41: Gauge pressure at the wall vs. time for simulations. Mesh of 600 cells. Tungsten Orleans tests.

$\text{WO}_3$  is assumed to be solid in our calculations. This approximation might be responsible for the high levels of pressure obtained in EXP2 (about 1 bar of overestimation). Let us recall that Sabourin [105] mentions that above  $1250^\circ\text{C}$  no solid oxides are formed, and that the presence of steam favours the oxide vaporisation. The phase change of  $\text{WO}_3$  should be taken into account in future developments. Also, modelling the heat transfer through the chamber walls would mean an improvement on the results, particularly on the pressures curves after the maximum is reached and the effects of combustion tend to weaken.



## CONCLUSIONS AND PERSPECTIVES

---

In this Doctoral Thesis, the development and investigation of some Riemann solvers have been performed, aimed at solving an unsteady, reactive, two-phase problem, involving a mixture of particles and gases.

- An introductory chapter has presented and expounded on the subject under research, emphasising the underlying purpose of the investigation: the necessity to develop a new software to be employed as a prediction tool for dust explosion problems. This research topic has been motivated by the currently launched project to build and put into operation an experimental fusion reactor: the ITER project. This nuclear facility has been conceived as the necessary experimental step on the road to exploit the multiple advantages of nuclear fusion as a massive source of energy. Even though the fusion process is inherently safe, as an experimental reactor, the focus of the project is set on safety. On this regard, the new software would be useful in the previous analysis of hypothetical accident scenarios involving an ingress of air or coolant within the reactor's vacuum vessel, and a subsequent dust explosion. Thus, that code could help in the safety assessment by providing reliable predictions of the different transient phenomena in the problem: discontinuous flow (shock waves and rarefactions), low-pressure flow, dust mobilisation, heterogeneous chemical reaction and deflagration/ detonation. Consequently, it has been fixed as the main object of this Thesis to develop such tool, and a numerical code based on the Finite Volume method has been considered to be the most trustful option.
- To that end, a complete literature review has been addressed on mathematical models of governing equations for two-phase mixtures of gases and particles. In the search for different approaches, the state-of-the-art models of reactive two-phase mixtures most appropriate for each use have been pointed. It has been determined that, for our purposes, it is advisable to use an Eulerian-Eulerian two-phase approach. With regard to the type of mixture to which the model would be applied, it has been found that models for laden mixtures (mostly formulated from the model of conservation equations by Baer and Nunziato) are usually applied to numerical computation of solid propellant beds, detonation in solid granulated materials or de-

flagration to detonation transition, among other problems. Conversely, models for high-dilute mixtures are particularly suitable for numerical predictions about dispersed clouds of particles (namely, Veyssiere-Khasainov, Chen-Fan or Koribeinikov models). These have, indeed, some mathematical advantages: equations are not so tightly coupled, easing its resolution, and some non-conservative terms associated to partial derivatives of the void fraction  $\alpha$  vanish. Therefore, for the type of mixtures which are subject of this thesis, we can conclude that the mathematical model must be an Eulerian system of conservation equations for dispersed mixtures. The system is subdivided into two groups of equations (subsystems), one for each phase.

- The partial differential equations in the models remain coupled by the conserved variables, but also for the source terms related to combustion, drag of particles, heat transfer between phases, among other effects. Therefore, also a comprehensive literature review has been performed aiming at selecting suitable physical laws to model those effects and incorporating them into the equations.
- Once the model of equations has been presented, the strategy for the numerical resolution of the problem has been addressed. In this regard, after a brief introduction of conservative methods for hyperbolic systems of equations, the numerical approach that has been employed has been expounded. This consists in a splitting method, for which the convective part of the system is resolved by a first or second order finite-volume method, and then the inhomogeneous part of the system (including the source terms) is tackled by means of a numerical method for ODE resolution.
- With respect to the convective part, approximate Riemann solvers have been employed for the resolution of the numerical fluxes. In addition to some classical schemes (Roe scheme, Rusanov scheme and FVS methods such as the van Leer-Hanel scheme), hybrid methods (the AUSM family of schemes) have been implemented. Actually, these schemes can be readily used to compute shocks in mixtures of ideal gases with temperature-dependent specific heats. However, its application to the solid phase, with very particular characteristics, is not as immediate as in the case of gases.

As a matter of fact, a significant portion of the work performed for this Thesis have concerned the development and investigation on Riemann solvers for the subsystem belonging to the solid phase. The main differences in the implementation of these schemes to the solid phase compared to the gas phase,

lie on the speed of sound and on the assumption that the particles are incompressible. In fact, this is grounded on the underlying assumption of a highly-dilute mixture: it is considered that the terms of pressure does not affect the solid phase. As a result, two options have been developed and tested, including a version of the Rusanov scheme as well as an AUSM scheme for a particle phase. The performance of these schemes have been analysed together with the rest of Riemann solvers implemented in the computational code.

- Regarding the source terms, a splitting strategy has been successfully developed and applied to solve the inhomogeneous non-linear system of ODEs. We can draw on many classical methods to solve this problem (e.g., multi-step Euler method or Runge-Kutta). Nonetheless, a remarkable goal of this Thesis lies in the development and testing of an *Advanced Source-Term Treatment* (ASTT). The ASTT plays a key role in the successful computation of reactive gas-solid mixtures under numerically adverse conditions. That is, for the type of problems we are dealing with, a set of conditions can be identified for which the ODE problem becomes numerically stiff (i.e., low pressure, small particle diameters or high particle density). Consequently, the ASTT has been developed as a relaxation method which is able to make the splitting method to compute a prediction, even in those problems for which classical methods do not even give a solution.

The ASTT method is based on the integration of each source term separately. The friction terms are integrated by making use of the time derivatives of the relative speed between gas and particles. Likewise, the source terms for heat transfer are integrated by means of the time derivative of the temperature jump between phases. Then, an implicit integration is used for combustion source terms. Thus, a robust strategy has been elaborated and implemented into the code that makes possible the resolution of the problems we face in this Thesis.

- The resolution of the source terms has been completed with a newly developed algorithm for the dynamic time stepping, for those cases where multiple reactive species are modelled simultaneously. The time stepping device ensures stability for the different methods employed in the splitting strategy. It also satisfies the continuity equation by maintaining the positivity of the conserved variables even though some species act as both a product and a reactant by the reaction mechanism.

The outcomes of the research that has been performed on different mathematical models, closure laws and numerical methods, as well as

the new developed numerical approximations, have been duly tested and validated with numerical computations. The whole mathematical apparatus expounded in this Doctoral Thesis was implemented in a computer code called *DUST*, which has been programmed in Fortran for one-dimensional problems, and incorporated into the platform *Cast3M* for multidimensional problems. Thus, a collection of numerical tests-cases has been useful in order to:

- (i) Evaluate the suitability of the selected mathematical models.
- (ii) Verify the effectiveness of the numerical methods to cope with problems involving combustion, strong shock waves, low pressure and, in general, numerically adverse conditions, such as those described above.
- (iii) Observe the behaviour of the code in dealing with multidimensional flows with particles, and to assess its efficiency in relation to the phenomenon of dust mobilisation.
- (iv) Study the combustion of particles in closed domains.

In most cases, the validation of the model has been performed by comparing with reliable benchmarks, consisting of experimental data supported by related literature. The validation process has yielded the following conclusions:

- The application of the code to classic problems of mobilisation in shock tubes, caused by both shock waves and rarefactions, has provided successful results that largely match with the available experimental data.
- A detailed study of the influence of several variables on the analysis of mobilisation and combustion problems has been carried out. Special attention has been paid to the conditions expected in the VV of ITER. The test-cases that have been studied have resulted in numerically stiff problems, due to low pressure conditions, the high concentration and the high density of particles (e.g., the tungsten dust present in some of the mixtures). The numerical results have allowed us to prove the ability of the model to characterise the mobilisation of solids by means of the action of shocks and rarefactions also in the presence of demanding conditions. Thus, the numerical scheme proposed, based on splitting methods has been demonstrated to work quite well in conditions in which others fail. The positive features of this technique have been shown in terms of the absence of oscillations in the solution and of the lower computational time required to perform the calculations.
- Numerical results concerning a first study of a 3D dust mobilisation problem inside ITER are also provided. Pressurisation

of the reactor's Vacuum Vessel, caused by a breach beside the divertor, has been simulated. The reactor's geometry was faithfully reproduced in a three-dimensional grid, and the expected operation conditions inside the reactor were initially imposed in the domain. Thereby, numerical results have been presented on the transient air-ingress process, with consequent mobilisation of the dust cloud inside the reactor. The evolution of particle concentration has been reported for different internal points of the VV. Thus, the results prove the effectiveness of the ASTT when dealing with ITER initial conditions.

- Regarding the combustion models, simulations have shown that some of them are still somewhat simplified. All in all, they have been useful to demonstrate the success of the methodology described. In addition, they have provided good combustion predictions in those cases when the initiation strategy is properly adjusted. That is, the chemical schemes implemented can be well suited for detonation problems and, as a consequence, the code has provided reliable predictions for test-cases simulating detonation in different mixtures (aluminium particles, aluminium in a  $H_2/O_2/N_2$  reactive atmosphere, high concentrations of tungsten particles in multi-component reactive atmospheres, and graphite in  $H_2/air$ ).
- Experimental data from literature, regarding detonation in combustion tubes, have been used to validate the numerical results in essentially one-dimensional geometries. These problems have been modelled with 1D, 2D and 3D grids of a straight tube, in order to validate both the results from the Fortran code (1D) and the Cast3M code (2D and 3D), as a previous step before heading fully three-dimensional geometries. As shown, predictions on aluminium combustion within a horizontal tube filled in with air, and a vertical tube with  $H_2/O_2/N_2$ , have yielded values for maximum pressures and wave velocities very close to those reported in the experiments.
- Finally, some tests on the combustion of graphite and tungsten dust inside a detonation sphere have been addressed. Also experimental results are available from these tests to compare. A thorough analysis has been tackled on the mesh definition and the initiation strategy to be employed for simulations. Results have shown there is still a way to go in defining the perfect conditions for initiation, and on the implementation of more complex combustion models. Notwithstanding, pressure histories have shown a reasonably good agreement between experiments and numerical predictions, since peak pressures and combustion times have been accurately predicted. These favourable outcomes open the way towards the application of the code and

the models presented in this Thesis in future ITER assessment simulations.

The work carried out in the framework of this Doctoral Thesis lays the groundwork for a much broader investigation. The physical and mathematical models presented here, and the computer code (that is an expression of the applicability of these models) are just a tool that can be used in future studies of two-phase mixtures.

Future work should be directed towards the improvement and validation of the physical models in a wider variety of three-dimensional applications. These tests may reveal the need to implement more complex models of combustion or to improve the undertaken approximations for the ignition of particles.

However, an important breakthrough has yet to be achieved: the turbulence model, which is becoming a reality, but it has not been sufficiently validated and tested as part of this thesis. This will result in enhanced predictions, starting with the velocity of the turbulent flame front (up to date all we modelled was laminar flames), and continuing with the significant effects that turbulence has on multidimensional transport.

With those advances, final predictions on ITER reference events may be close at hand, and the simulations of the full problem may be directly addressed.

Part III

APPENDIX





## IMPLEMENTATION IN CAST<sub>3</sub>M

---

### A.1 THE CODE CAST<sub>3</sub>M AND ITS PHILOSOPHY

Cast<sub>3</sub>M is a computer code originally developed for the analysis of structures by the Finite Element method, which has been equipped with the mathematical tools that are needed to tackle simulations on Computational Fluids Dynamics.

At the beginning, this code was developed by the Department of Mechanics and Technology (DMT) of the French Atomic Energy Commission (CEA). Cast<sub>3</sub>M is the product of more than thirty years of development of computer codes for the method of Finite Elements (resolution of partial derivative equations in a finite domain). The code aims to incorporate all the tools that are needed to bring into fruition a study of finite elements, integrating not only the functions of calculation themselves, but also functions for the grid generation and post-processing of numerical results. His special field of application is the Mechanics, but also demonstrates a good performance with thermal calculations, Hydraulics and Electromagnetism.

Unlike many other codes, Cast<sub>3</sub>M does not work as a “black box” but gives to the user the knowledge of the problem that he actually treat and the methods used to solve it. Cast<sub>3</sub>M includes a set of elementary processes (library of operators) that the user can bind to define and solve problems. Arguably, Cast<sub>3</sub>M is based on a concept of OPERATOR-OPERAND, and that is indeed its main difference with respect to other classical Finite-Element codes. The operators are just tools acting on specific objects.

The program Cast<sub>3</sub>M is preferably run with UNIX systems and the user might have some knowledge on text-user-interface and command-line shell. The input data structure chosen in Cast<sub>3</sub>M development is “Data Flow Control” (similarly to the data input in Unix philosophy). That is, data entered by the user are guiding the sequence of actions, those having a priori no pre-established order. Thus, in order to run the code, a command supervisor is needed who should be able to:

- read a command line,
- recognise the action to do,
- interact with the operator, in order to understand the arguments it reclaims as well as to retrieve the results it generates,
- chain it with a new command.

Cast3M is a system designed and developed to exceed the limits of adaptability offered by the conventional codes. That is why it was selected, in the project in which this Doctoral Thesis is framed, as a base platform from which to construct Dust code. There are some specific features that are well suited to the aspirations of our code: the ease of creating new operators or modifying those previously existing and, in general, the independence between some operators and others. All these are a great advantage over other open source codes.

#### A.1.1 *Programming languages: Gibiane and Esope*

Cast3M is a computational code conceived as an object oriented language. This language is based on the idea that a computation is a succession of independent process communicating by means of information structures called objects. From the user's viewpoint, Cast3M can be seen as a combination of a language named Gibiane, and a set of objects.

Gibiane is high-level programming language allowing the user to communicate directly with the program by an exchange of data. Thus, the data of the problem to be resolved, as well as the specific instructions defined by the user, are introduced by the use of Gibiane language. The goal of an instruction is generally to create or modify a particular object which is build by the aid of previously defined operators. The typical syntax of an elementary operation can involve different objects, and can be presented in different ways:

```
RESULT = OPERATOR OBJECT1 OBJECT2 ... ;
```

```
DIRECTIVE OPERANDS ;
```

Operations are executed by the operators acting directly on the objects supplied as arguments (a brief description of the different types of object allowed is gathered in [Table A.1](#)). In that way, Gibiane can be described as a text-user-interface language managing objects. Some abstract types may contain just mathematical or computing data (*entier, reel, liste de mots...*), others have a more physical character and are adapted to a Finite-Element modelling or a Finite-Volume method (*chpoint, mchaml, rigidite...*). In addition to the formal definition of the information contained in a type, the computer description must be provided, including the access methods and the creation and suppression of types.

For the modelling of a problem by Finite-Volume methods, values are calculated at discrete places on a meshed geometry. The problem's domain is converted into a discrete collection of points: a mesh (see [Chapter 4](#)); in Cast3M this is structured in an object type MAILLAGE. Then variables are also discretised in on the mesh nodes. A field defined in the mesh nodes is named CHPOINT in Gibiane. A

field by points exists *a priori* on every node, but it is in vain to make it defined whereas its value is zero. Therefore, the best choice should be only to specify the field on those points directly concerned with calculations. So, a partition is done on the nodes of a CHPOINT with respect to the variables it contains. This information about the node partitions, and also other general data (the nature of the field, its components, the name, the numerical method under which the field is defined, and a type) are contained in the CHPOINT object. Conversely, the object supporting all the fields defined in the elements, instead of nodes, are named MCHAML. The fields supported for the MCHAML must be of real data type or pointers to other objects.

In calculations on fluid mechanics with Cast3M, the type TABLE is intensively employed. The main reasons that led to this are the simplification of programming and to ensure consistency of the indices associated with different objects that may be related to the same field. Unlike other objects, referring to a physical reality, the TABLE object belongs to the Gibiane syntax, to the extent that this object is treated in a particular way by the syntax parser. On the other hand, it can be used by programmers to gather information and thus plays the role of an auxiliary object.

Whilst the user of Cast3M is able to define his problem and the instructions oriented towards its resolution with Gibiane, the kernel of Cast3M is built by means of an object oriented language named ESOPE, developed as an extension of Fortran 77. The reason is to ease the management of information and to allow the notion of "object" by the structuring of data. To provide the code with an object oriented language it is necessary to associate a set of data to a variable. To this end, the entity named SEGMENT is added to ESOPE, which responds to the following requirements:

- It is a collection of Fortran variables defined by the programmer.
- It is referred by a only variable named POINTEUR. Knowing the pointer is enough to access all the variables in the structure of data.

For the manipulation of the structures of data, a few instructions are added to those from Fortran77. As in Fortran, a declaratory instruction must be added for each SEGMENT, followed by the instructions affecting it. Those comprise:

- to create a segment (or initialize it): SEGINI,
- to delete a segment: SEGSUP,
- to deactivate a segment: SEGDES,
- to activate a segment: SEGACT,
- to adjust the size of a segment: SEGADJ.

Main objects of interest	
ENTIER	Integer
FLOTTANT	Float
LISTENTI	List of integers
LISTREEL	List of floats
MOT	Word
LOGIQUE	Logic
LISTMOTS	List of words
TABLE	Group of objects indexed by objects
EVOLUTION	Representation of a numeric function
NUAGE	Set of n-tuples.
Meshing objects	
POINT	Coordinates of a point and density associated
MAILLAGE	Mesh
Objects for calculation	
CHPOINT	Field defined at the mesh nodes
LISTCHPO	List of CHPOINT
MMODEL	Type of material behaviour
MCHAML	Field defined at elements
RIGIDITE	Stiffness matrix, or matrices of mass, conductivity, convection, radiation or geometric stiffness
CHARGEMENT	Spatial/temporal description of a structural load.
SOLUTION	Set of natural modes and frequencies associated to a modal analysis
CONFIGURATION	Position of nodes
ATTACHE	Description of joint between sub-structures in view of a dynamic analysis
BASEMODA	Description of joints exerted over a structure and specification of the set of static solutions
ELEMSTRU	Description of joints between sub-structures with each structural element and associated geometry
STRUCTURE	Description of a structure with its stiffness and mass
Objects for post-treatment	
VECTEUR	Vectorial representation (arrows) allowing to visualize a CHPOINT or a MCHAML
DEFORME	Deformation

Table A.1: Succinct description of the different types of objects in Cast3M.

The source code, written in ESOPE, is at first translated into Fortran 77 before been sent to compilation. The translation into Fortran is done by the execution of a program named also ESOPE that includes a complete library of functions, so that the average user or even a developer rarely has to get involved into the translation.

#### A.1.2 *Operators and their structure*

In Cast3M, operators take the lead with respect to the sequence of actions the program performs. When the user undertakes the programming with Gibiane language, in order to give resolution to a problem, he defines the order of the operators to be executed and the objects been affected.

Operators are grouped together according to their function: operators of general interest, operators used for the preparation of the model, operators used for solving the problem and post-processing operators. There is no point to detail here the long list of operators available in Cast3M. The reader is referred to [67] for further information.

It is worth noting that a single operator can perform different functions depending on the *keyword* provided by the user in Gibiane. In the internal structure of Cast3M, the operator is branched into a set of source files of ESOPE code. Each of these source files represent a specific option selected by the user.

##### A.1.2.1 *Development of new Operators*

Cast3M special structure not only enables the user to elaborate procedures capable of solving new types of problems, but also to define operators different from those in existence. The program structure of Cast3M brings about the fact that it is not necessary to know the other operators to introduce a new one: new operators can actually be developed, tuned up and checked apart from the others. That is, those are in fact orthogonal to each others. One just needs to know the structure of the data contained in the objects handled by the new operator, and in the objects common to the whole program. This is especially useful when the analysis demands specific adaptations.

Of course, creating new operators implies that the developer masters the programming language ESOPE. Without going into details, the user just needs to specify that a computer entity such as a sub-program is written in ESOPE language, translated in standard FORTRAN, and compiled as usual.

When developing a new operator, it is useful to know that both the operators and the directives are defined by the first four characters, the next ones are not taken into account. If a new name is given, the sub-program PILOT is also modified. PILOT manages the list of

operators and enables one of them when the syntax parser detects its name in the command line.

## A.2 APPLICATION INTO FLUID DYNAMICS, COMPRESSIBLE FLOW SIMULATIONS

Despite his origin as a Finite-Element code for structural and mechanical studies, Cast3M has been widely applied and validated for computation of fluid mechanics problems [8, 9, 116, 117].

The models implemented in the code make Cast3M a suitable tool for the simulation of a vast range of cases. A summarised list of the most usual applications of Cast3M on Computational Fluid Dynamics is enumerated in [Table A.2](#).

Field	Problem	Cases
Scalar equation transport	Convection	2D rotational transport flow.
	Convection-diffusion	2D Smith-Hutton flow.
	Non-linear conservation law	2D Burgers equation.
	Diffusive transport	2D and 3D heat equation.
Radiation heat transfer	Transparent media	Square cavity, wedge, co-axial cylinders, co-centric spheres, cube.
	Radiation and conduction	Air-filled cylinder.
	Absorbing media	Absorbing gas in a sphere.
	Radiation and natural convection in absorbing media	2D square cavity.
Single Component Flow	Incompressible	Lid-driven cavity.
		Blasius flat plate.
		Backward-facing step.
	Boussinesq	Natural convection in zero Prandtl fluid. Rayleigh-Marangoni convection. Vahl Davis differentially heated cavity.
Low Mach Number	Differentially heated cavity with large temperature differences.	

		Pressurisation.
Compressible Flows		2D Laval-type nozzles or channel flow; 1D SOD shock tube; 1D double rarefaction wave; shock collisions; moving or steady contact waves; moving or steady shock waves; 1D blast wave; 2D shock reflection; 2D inviscid shear layer; 2D jet interaction; odd-even decoupling; “Carbuncle Test Case”; double Mach reflection; forward-facing step; shock diffraction over 90° corner.
Turbulence Modelling		Incompressible $k - \epsilon$ : grid turbulence; fully-developed channel flow; turbulent natural convection in a square cavity.  LES on specific experiments.  $k - \epsilon$ and Mixing-Length model for low Mach number NS Equations with condensation.  $k - \epsilon$ for low Mach number reactive flows (EBU modelling).
Multi-Component Flows	Low Mach and compressible approaches.	
	Shock tube	Shear layer; non-reactive shock tube; reactive shock tube.
	Multidimensional two-phase flow.	

Table A.2: A variety of CFD tests already studied with Cast3M by other authors. Source: CEA Nuclear Safety NEA/CSNI/R(2007)13.

When modelling a fluids problem with Cast3M, first of all, we ought to choose the most appropriate physical model, so that the information about the model is taken into account at the definition of the different objects (type MAILLAGE, CHPOINT, MCHAML). Accordingly, the purpose of MODE (MODELISER) operator is to associate a formulation, a model of material behaviour, a type of finite element or finite volume to be used, and possibly a name of constituent, with a mesh. In the current version of the program, there are several formulations to be chosen, namely: simple formulations as “MECANIQUE”, “LIQUIDE”, “POREUX”, “CONTACT”, “THERMIQUE”, “DARCY”, “MAGNETODYNAMIQUE”, “NAVIER-STOKES”, “EULER”, “MELANGE”, “FISSURE”, “THERMOHYDRIQUE”, “LIAISON”, and “DIFFUSION”.

Finite elements for the "NAVIER-STOKES" formulation					
Geometrical support	Finite element	Description	Degree	Option for calculation	Nodal unknowns
QUAF	LINE		1 U 0 P		
TRI7 QUA9	TRF3 QUF4	TRI3 QUA4		PLAN AXI	UX UY
CU27 PR21	CUF8 PRF6	CUB8 PRI6		TRID	UX UY UZ
TE15 PR19	TEF4 PYF5	TET4 PYR5		TRID	UX UY UZ
QUAF	MACR		1 U 0 P		
TRI7 QUA9	MTR6 MQU9	4xTRI3 4xQUA4		PLAN AXI	UX UY
CU27 PR21	MC27 MP18	8xCUB8 8xPRI6		TRID	UX UY UZ
TE15 PR19	MT10 MP14	8xTET4		TRID	UX UY UZ
QUAF	QUAF		2 U 1 P		
TRI7 QUA9	TRF7 QUF9	TRI7 QUA9		PLAN AXI	UX UY
CU27 PR21	CF27 PF21	CU27 PR21		TRID	UX UY UZ
TE15 PR19	TF15 PF19	TE15 PR19		TRID	UX UY UZ
Finite volumes for the "EULER" formulation					
	TRI3 QUA4			PLAN	
	CUB8 PRI6			TRID	
	TET4 PYR5			TRID	

Table A.3: Finite elements and finite volumes allowed in Cast3M for the Navier-Stokes and Euler formulations, respectively (QUAF LINE and MACR are generic names for elements family listed below in the corresponding column).

The type of model needed for the problem will determine some of the object characteristics, including, at a first place, the sort of finite elements or finite volumes to be chosen. Table A.3 shows the possible options for the specific cases of Navier-Stokes or Euler model. The choice must be made according to the geometric description of the problem (plane or three-dimensional) and to numerical reasons, as the order of discretisation.

The Navier-Stokes model allows to compute incompressible or near incompressible flows. The flow regimes can be either transient or steady state, laminar or turbulent, and including forced, free or mixed convection. Near incompressible flows have proven to be useful to model the Boussinesq approximation or low Mach number flows, among many other applications. Turbulence models implemented within this option are the  $k - \varepsilon$  model and the RNG  $k - \varepsilon$  model. The spatial discretisation is obtained by a multidimensional Finite-Element method, 2D (in Cartesian or cylindrical coordinates) or 3D. Only a few special elements are allowed for the mixed velocity-pressure formulation. One can distinguish two classes of elements: continuous pressure elements and discontinuous ones. In the current version of Cast3M, only discontinuous pressure elements are available.

Similarly, the Euler model was specifically implemented in Cast3M with the object of simulating compressible-flow problems. This is in fact the model employed in the multi-dimensional simulations presented in this dissertation. The model, as it is implemented, allows for the calculation of:

- the Finite-Volume (FV) “cell-centred” discretisation of the Euler equations of gas dynamics for perfect, mono-component, poly-tropic gas (keyword “PERFMONO”);
- the FV “cell-centred” discretisation of the Euler equations for a multi-component mixture of perfect gases with temperature-dependent specific heat capacities (keyword “PERFTEMP”);
- the FV “cell-centred” discretisation of the Euler equations when using the Free Matrix method of implicitation. In that case, the conservative variables are computed in the  $i$ -th cell by:

$$(\mathbf{U}_i^{n+1} - \mathbf{U}_i^n) \times A_{N,i}(\mathbf{U}^n) = \text{RES}_i(\mathbf{U}^n) + B_{N,i}(\mathbf{U}^n) - B_{N,i}(\mathbf{U}_i^{n+1}) \quad (\text{A.1})$$

where  $A_{N,i}$  contains the contributions linked to inverse of the local time step and to the interfacial Rusanov diffusivities;  $\text{RES}_i$  is the residual computed with any numerical scheme;  $B_{N,i}$  contains the interfacial contributions linked to the centred flux and to the Rusanov diffusivity multiplied by the neighboring state;

- the VF “cell-centred” discretisation of the Euler equations for low Mach flows, by the Free Matrix method of implicitation.

Here, in the  $i$ -th cell we have to compute  $(u_i^{n+1} - u_i^n) = \Delta u_N$  by the use of the keyword "PMON1FMM";

- the discretisation of the Euler equations for a multi-component mixture of perfect gases with constant specific heats (keyword "PERFMULT");
- the Finite-Volume "cell-centred" discretisation of the one-pressure six-equation two-fluid model, only for water and air mixtures (with the keyword "TWOFLUID");
- the Finite-Volume discretisation of Euler equation describing a flow of multi-component thermally perfect gas, and the Discrete Equation Method is used to determine the flux (keyword "DEM");
- the "Ghost fluid method for the poor", that is, the VF "cell-centred" discretisation of two fluid Euler Equations for interface transport (by keyword "GFMP").

For the user of Cast3M, in Gibiane language, all this range of Finite-Volume discretisations are undertaken in a simple form by the aid of the operator KONV (this operator also offers many other functionalities, including transport of scalars and Finite-Element formulations, but we will focus here in the options concerning the Euler equations). A standard syntax to call KONV operator, in order to compute the residuals of at a determined time step for the method of Finite Volumes, would be the following:

```
RESID DELTAT = 'KONV' 'VF' 'PERFTEMP' 'RESI' METO
              DOMTOT PGAZ LISTINC RGF VGF PF YGF ;
```

For this specific case where the keyword "PERFTEMP" is been called, two objects are given as a result: RESID is the name of the CHPOINT containing the residuals of the system (it has as many components as equations in the model), DELTAT is a float whose value is the characteristic time of the fastest wave. Among the arguments we have METO, a MOT object with the name of the numerical scheme for the numerical flux vector, DOMTOT, which is an object type MMODEL with the information about the mesh and the formulation (Euler equations). PGAZ is a table object that contains the name of the species non-explicitly treated in Euler equations, the names of the species explicitly treated (to specify in the multicomponent case only), the degree of the polynomial for the heat capacities as a function of temperature, the properties of each gas, the constant of the gas, and the enthalpy of formation at  $T = 0$  K. Later, LISTINC is a list of MOT objects with the names of the residual components, RGF is an

MCHAML object containing the density and has a geometrical support in the faces of the finite volumes, VGF is also a MCHAML object with the velocity and the director cosines of the local frame (n,t) with respect to the global one (x,y), PF is a one-component MCHAML containing the total pressure, and YGF is the MCHAML with the mass fractions of every species in the mixture of gases.

These MCHAML objects providing information about the gas density, velocities, pressure and mass fractions can be obtained in Cast3M by means of the PRET operator, another genuine Cast3M operator for applications on compressible flow. This also admits the keywords "PERFMONO", "PERFMULT", "PERFTEMP", "TWOFLUID", "DEM", and "GFMP". For the three first keywords, this operator provides the evaluation of the primitive variables at the interfaces in the modelling of the Euler equations for the "cell-centred" Finite-Volume formulation. The corresponding syntax to call PRET operator in Gibiane with the option "PERFTEMP" is:

```
RGF VGF PF YGF = 'PRET' 'PERFTEMP' N1 N2
                DOMTOT PGAZ RG VG P YG ;
```

where N1 and N2 are the desired orders of discretisation in space and time, respectively; RG, VG, P, and YG are CHPOINT objects containing, respectively, the density, velocities, pressure and mass fractions, in the fluid field, at the centre of each finite volume.

The primitive variables, in turn, are computed by another operator: PRIM. This converts the CHMPOINTS with the conserved variables of the system into other objects with the primitive variables, with the exception of density which is already a primitive variable. The syntax of PRIM operator, for the case above, is as follows:

```
VG PP TG YG GAMG = 'PRIM' 'PERFTEMP' PGAZ RG GG RETG RYG ;
```

where RG, GG, RETG and RYG are for CHPOINT objects which contain the values of the conserved variables in the fluid field, that is, respectively, conservation of mass, momentum, total energy and species.

#### A.2.1 *Different approaches for numerical flux evaluation (implemented schemes)*

We can see by the experience in Cast3M that, in general, the available numerical schemes, intended to compute the numerical flux vector in Cast3M, depend on the model option previously selected. If the Euler model is chosen altogether with the method of Finite Volumes, one can choose a numerical scheme from the list:

'GODUNOV'	: exact solver
'VANLEER'	: Van Leer's solver
'VLH'	: Van Leer Hanel's solver
'HUSVL'	: HUS (van Leer + Osher)
'HUSVLH'	: HUS (van Leer Hanel + Osher)
'AUSMPLUS'	: AUSM+
'ROE'	: Roe' solver
'SS'	: shock-shock solver
'AUSMPLM'	: AUSM+ low Mach solver
'RUSANOV'	: Rusanov scheme
'RUSANOLM'	: Rusanov scheme for low-Mach
'CENTERED'	: Centered scheme
'ROELM'	: Roe-Turkel scheme for low-Mach
'HLLC'	: solver HLLC
'HLLCLM'	: solver HLLC-Turkel for low-Mach
'AUSMPUP'	: solver AUSM+up low Mach

In the standard Cast3M release, there is no numerical scheme available which allows for the resolution of a discrete solid phase. However, the program structure facilitates the introduction of new options in the existing operators, or even new operators, if necessary, to allow the resolution of equations for the second solid phase.

#### A.2.2 Detonations in Cast3M. FLAM and DETO operators.

Hydrogen detonations in Cast3M have been successfully simulated so far by the application of Euler equations together with FLAM operator [8, 9]. This operator integrates from time  $t_n$  to time  $t_{n+1} = t_n + \Delta t$  a system of ordinary differential equations which model the time evolution of mass fractions of hydrogen, oxygen, nitrogen and water vapour following the global reaction for  $H_2$  oxidation:



Thus, FLAM solves from  $t_n$  and  $t_{n+1}$ , the ODEs:

$$\begin{aligned}\frac{dY_{H_2}}{dt} &= C_{H_2} \omega_{H_2}, \\ \frac{dY_{O_2}}{dt} &= C_{O_2} \omega_{H_2}, \\ \frac{dY_{H_2O}}{dt} &= C_{H_2O} \omega_{H_2},\end{aligned}$$

where  $C_{H_2}$ ,  $C_{O_2}$ ,  $C_{H_2O}$  are constants which depend on the stoichiometric coefficients of the reaction and the molar masses of the constituents, and  $\omega_{H_2}$  the reaction rate. Note that nitrogen is a neutral

species. Depending on the option, the reaction rate is given by a kinetic rate adapted to combustion in the laminar regime ('LAMINAR'), or for turbulent regime by an Eddy Break-Up model ('EBU'), or by a general Arrhenius law adapted to the detonation regime by user defined coefficients ('ARRHENIU'), or for a burning velocity model to follow the flame front ('CREBCOM'), or by a infinitely fast combustion if temperature is greater than a threshold temperature ('HEAVY-SIDE').

As in [8], the reaction model employed here for H<sub>2</sub> detonations is provided by **FLAM** operator, and the keyword 'ARRHENIU'.

The fact that Cast3M is provided with numerous operators sometimes entails a drawback: the sets of data may be long and complex; one will soon realise, though, that some sequences of instructions are used several times in the same set of data or by several users. Hence the idea of gathering these instructions together into a specific structure: the procedure.

In this sense, a procedure is usually employed in Cast3M when dealing with H<sub>2</sub> detonation. It is aimed at setting a proper initial condition which may trigger the detonation phenomenon. It was named 'DETO' and it sets the Zeldovitch- von Neuman and Doringt state (ZND) within a selected sub-domain.

Later, a new operator was developed (and incorporated to the official Cast3M release) following the objective of the DETO procedure and adding a new functionality. As such, the DETO operator evaluates the Chapman-Jouguet state (CJ), the Adiabatic Isochore Complete Combustion state (AICC) and the ZND state for a mixture O<sub>2</sub> / N<sub>2</sub> / H<sub>2</sub> / H<sub>2</sub>O. The CJ velocity and the progress variable for the stable combustion are also evaluated.

In order to implement the combustion of carbon monoxide in Cast3M, FLAM operator has been modified. As mentioned before, the objective of FLAM operator in Cast3M is the computation of H<sub>2</sub> combustion under different models and assumptions. The model for CO combustion chosen in this work (see Section 3.4.2) is given by Dryer and Glassman [30] and Yetter et al. [137]. Therefore, it is an Arrhenius model with a kinetic law similar to the model previously defined for H<sub>2</sub> combustion, so the same ESOPE file structure has been imitated for the new option, as shown in Figure A.1. The keyword to call the operator is 'ARRHENIC'.

### A.3 IMPLEMENTATION OF THE SOLID PHASE

In order to implement in the code the two-phase model described in Section 3.3, and the numerical methods in Section 4.2, with the goal to perform the numerical simulations presented in this Thesis, some operators have had to be modified.

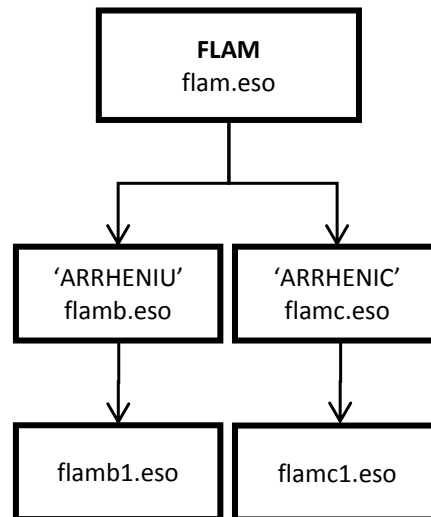


Figure A.1: File structure of FLAM operator including the keywords 'ARRHENIU', for  $H_2$  oxidation, and 'ARRHENIC' for CO oxidation.

Before describing the changes in those operators, let us have a look at the way we have adopted to address the resolution of a case with Cast3M. In fact, the sequence of operations is inherited from the code in 1D programmed entirely in Fortran language. In the [Figure A.2](#), we can find a flow diagram describing the algorithm followed in the analysis of a standar fluid problem with Cast3M, involving gas-phase combustion. The procedure begins with the mesh construction. This will generate a series of MAILLAGE objects and variables with all the information about the finite volumes or cells (forms, coordinates, volumes, faces, centroids, sub-domains, models, etc.). Then, as required for a transient calculation, the initial conditions defined by the user are imposed in the total domain. These conditions are translated into the conserved variables of the problem, defined in the centres of each cell. By means of PRET operator the values at the faces are generated (this will also give the information about the gradients). This information is later provided to KONV operator for the calculation of the numerical fluxes and the time stepping although, actually, the result generated by KONV is the convective residuals, that is, the quantities which should be added to the conserved variables at  $t_n$  in order to get the new values at  $t_{n+1}$ . In this moment, despite the residuals are known, the conserved variables remain unchanged. Making use of them, FLAM operator would calculate the combustion rate of  $H_2$  oxidation. In case we are dealing with a two-phase problem, a new operator should be used, as described later.

Let us introduce at this point FUEN operator. It was originally developed by the Department of Thermal and Fluid Engineering of UPCT to account for the source terms related to the coupling between phases, namely, particle drag, heat transfer and phase transition. In

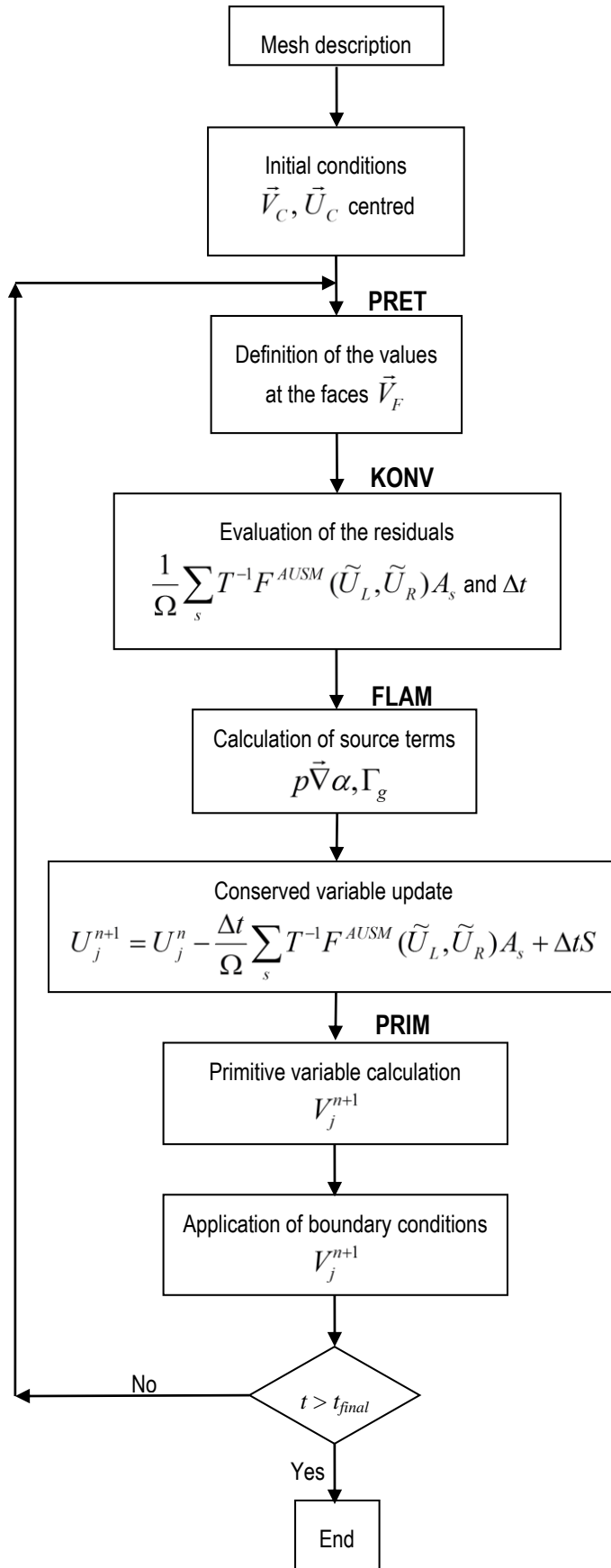


Figure A.2: Flow chart of a general solution strategy in Cast3M, for VF approach applied to a transient, compressible-flow problem.

the course of the present work, the operator was modified with a new structure and contents, to update the models and allow calculation of combustion source terms for a set of multiple reactions.

Getting back to the flow chart, when all the source terms at  $t_n$  are known, it is time to update the values of the conserved variables. This updating is done according to the scheme of the conservative method of [Section 4.2](#). What remains now is for the boundary conditions to be imposed in the ghost cells, but these conditions are defined over the primitive variables. Hence, PRIM operator is called to compute the primitives from the new conserved variables at  $t_{n+1}$ .

After that, there is only a decision concerning the final time. If the simulation has reached that point, the program will save the computation for the post-processing of the results. Otherwise, if  $t < t_{\text{final}}$ , the current time is updated ( $t = t_n + \Delta t = t_{n+1}$ ) and a new loop is started.

As one might expect, the Cast3M operators to modify are PRET, KONV and PRIM, and a new operator FUEN to be developed.

#### A.3.1 *Operators being modified*

As mentioned, KONV performs the Finite-Volume cell-centred discretisation of Euler equations of gas dynamics under various assumptions. Because of the features of the problems in which we have focused (mixtures of gases and combustion problems, for which the variation of specific heats with temperature is dramatically influential), the option 'PERFTEMP' has been normally adopted. Not surprisingly, this option was taken as a reference when developing a new functionality the use of KONV with particles. However, it is proven that heat capacities of metal particles are not so influenced by temperature, as compared to gases, and this backs the possibility of assuming constant heat capacities for the solid as a simplification. On other hand, only one solid species is being considered at a time, along with a solid combustion product. As a result, a new option was first enabled by the keyword 'PARTMONO' for the Finite-Volume discretisation of the Euler sub-system of equations for a discrete solid phase with constant heat capacities.

Also by the option 'PARTMONO', the operator KONV can yield either an evaluation of the residuals, or the components of the numerical flux. This is done by a secondary Gibiane keyword: 'RESI' for the residuals and 'FLUX' for the numerical flux. When these instructions are interpreted by the ESOPE code, each keyword will enable a source file in the operator's structure. For instead, the file structure of KONV operator, in what refers to particles, is organised as outlined in [Figure A.3](#).

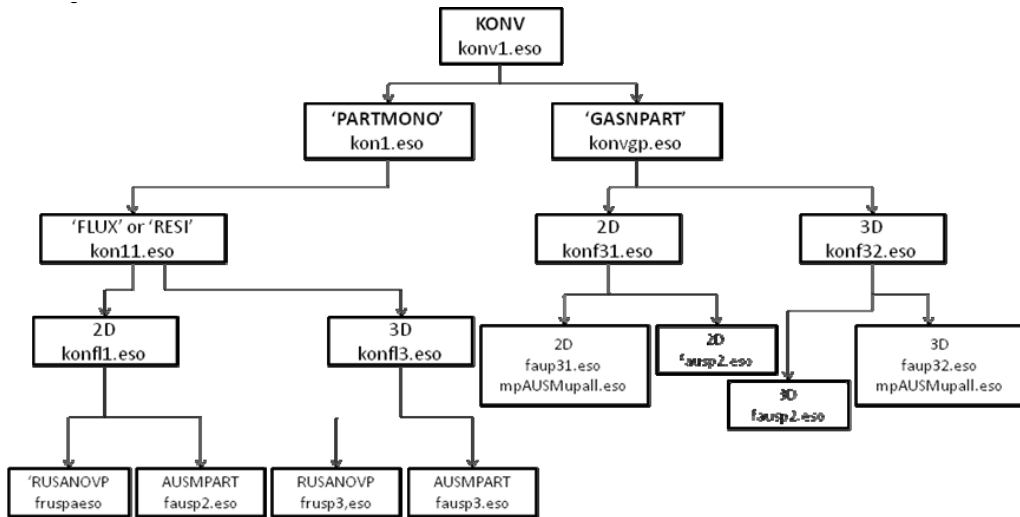


Figure A.3: Diagram on the structure of KONV operator in Cast3M.

The syntax for this operator to compute the residuals, or the numerical flux, under the option 'PARTMONO' (a solid discrete phase with constant heat capacities) is the following:

```

RCHPO1 RFL0T1 = 'KONV' 'VF' 'PARTMONO' MOT1 MOT2
MOD1 LMOT1 MCHAM1 MCHAM2 MCHAM3 MCHAM4 ;
    
```

- MOT<sub>1</sub> : object type MOT, possible values:
  - 'RESI' to compute the Residual,
  - 'FLUX' to compute the numerical Flux;
- MOT<sub>2</sub> : object type MOT, indicating the numerical method:
  - 'RUSANOVP',
  - 'AUSMPART';
- MOD<sub>1</sub> : MODEL object;
- LMOT<sub>1</sub> : object type LISTMOTS with the names of the components of the resultant vector (RCHPO<sub>1</sub>). They are named in the following order:
  - name of the density,
  - name of the momentum,
  - name of the total energy per unit volume;
- MCHAM<sub>1</sub> : MCHAML containing the particle concentration, and it has as SPG (geometric support) 'DOMA' MOD<sub>1</sub> 'FACEL' (one component, 'SCAL');

- MCHAM<sub>2</sub> : MCHAML containing the velocity components and the components of the local basis (n,t) with respect to the global basis (x,y) (in the 2D case there are 6 components):
- 'UN' = normal component of velocity (SPG = 'DOMA' MOD<sub>1</sub> 'FACEL')
  - 'UT' = tangential component of velocity (SPG = 'DOMA' MOD<sub>1</sub> 'FACEL')
  - 'NX' = n.x (SPG = 'FACE')
  - 'NY' = n.y (SPG = 'FACE')
  - 'TX' = t.x (SPG = 'FACE')
  - 'TY' = t.y (SPG = 'FACE')
- (see the description of the operator PRET);
- MCHAM<sub>3</sub> : MCHAML containing the temperature of the particles;
- MCHAM<sub>4</sub> : MCHAML containing the heat capacity of the particles (operator PRET with keyword 'PARTMONO');
- RCHPO<sub>1</sub> : object of the type CHPOINT (components = LMOT<sub>1</sub>) with the residual if MOT<sub>1</sub> = 'RESI' (SPG = 'DOMA' MOD<sub>1</sub> 'CENTRE'), or the numerical flux if MOT<sub>1</sub> = 'FLUX' (SPG = 'DOMA' MOD<sub>1</sub> 'FACE');
- RFLOT<sub>1</sub> : object of the type FLOTTANT with the value of the characteristic time associated with the fastest wave (even in the case of low Mach flow, one considers the non-preconditioned system).

Later, the option '**PARTTEMP**' was implemented in **KONV** operator. This allows to compute the residual by the VF method, for a solid phase with temperature-dependent heat capacities. This option is added to those aforementioned, in an ESOPE file structure as shown in [Figure A.4](#). Let us recall that, if a new option is enabled in the operator, it is possible to add a new structure with no setback to the rest. Now, the syntax for the '**PARTTEMP**' option should be the following:

```
RCHP01 RFL0T1 = 'KONV' 'VF' 'PARTTEMP' 'RESI' MOT1
                MOD1 TAB1 LMOT1 MCHAM1 MCHAM2 MCHAM3 MCHAM4 ;
```

where all the results and arguments are similar to those in **PARTMONO** option, except for:

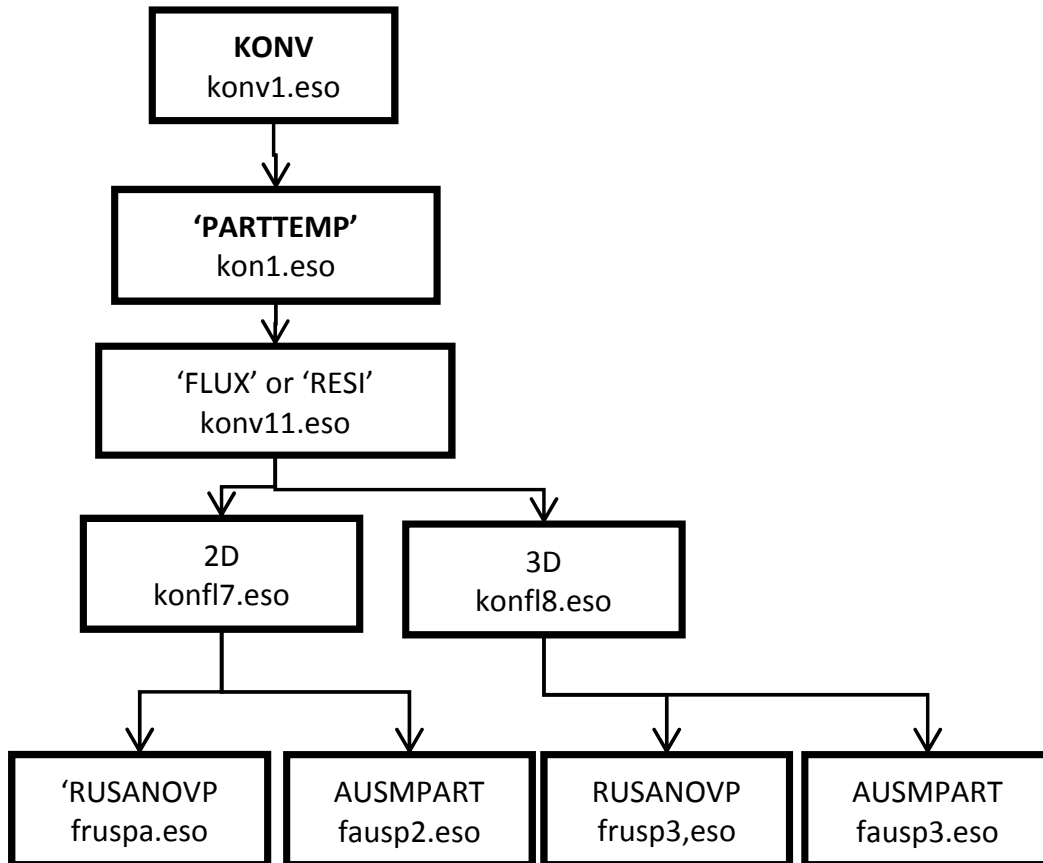


Figure A.4: Diagram on the structure of KONV operator in Cast3M.

- TAB<sub>1</sub> : TABLE object that contains:
- the name of the solid species non-explicitly treated in Euler's Equations in TAB<sub>2</sub> . 'ESPNEULE' (MOT object);
  - the names of the species explicitly treated in TAB<sub>2</sub> . 'ESPEULE' (LISTMOTS object; to specify in the multicomponent case only);
  - the degree of the polynomial  $c_v = c_v(T)$ , in TAB<sub>2</sub> . 'NORD' (ENTIER object,  $\geq 0$ );
  - the properties of each type of particles, in TAB<sub>2</sub> . 'ESPI' (TABLE object);
- MCHAM<sub>4</sub> : MCHAML containing the mass fractions for each species (the objects must contain as many components as  $NSSP - 1$ , being NSSP the number of solid species).

However, most of the arguments provided in KONV operator are MCHAML objects that need to be computed from the CHPOINT objects containing the primitive variables. This is done by means of PRET operator. As mentioned above, PRET is in charge of the eval-

uation of the primitive variables at the faces of the finite volumes in our control volume. The file structure is schematically described in the diagrams of [Figure A.5](#) and [Figure A.6](#).

Concerning the solid phase computation, this operator admits different keywords: 'GASNPART' for dense mixtures of gases and particles (the hypothesis of  $\alpha \approx 1$  is not assumed), 'PARTMONO' for mono-component solid phase with constant heat capacity, and 'PARTTEMP' for the multi-component case, with heat capacities variable with temperature. Let us take a glance on the syntax. In the case of 'PARTMONO' option, the syntax of **PRET** operator depends on the discretisation order. That is, for second order in space:

```
MCHAM1 MCHAM2 MCHAM3 MCHAM4 = 'PRET' 'PARTMONO' ENT1 ENT2
                                MOD1 CHP01 (CHP02) (CHP03)
                                CHP04 (CHP05) (CHP06) CHP07
                                (CHP08) (CHP09) CHP010 ;
```

where:

- ENT1 : ENTIER object; space order (=2);
- ENT2 : ENTIER object; time order (=1 or 2);
- MOD1 : MODELE Object;
- CHPO1 : CHPOINT "CENTRE" that contains the solid concentration  $\sigma$  ( $\text{kg}/\text{m}^3$ ), with just one 'SCAL' component;
- CHPO2 : CHPOINT "CENTRE" that contains the gradient of the solid concentration ( $\text{kg}/\text{m}^4$ ), 2 components in 2D: 'P1DX', 'P1DY');
- CHPO3 : CHPOINT "CENTRE" that contains the limiter of solid concentration gradient (one component, 'P1');
- CHPO4 : CHPOINT "CENTRE" that contains the velocity of particles ( $\text{m}/\text{s}$ ), containing two components in 2D: 'UX' and 'UY';
- CHPO5 : CHPOINT "CENTRE" that contains the velocity gradient ( $\text{s}^{-1}$ ), 4 components in 2D ('P1DX', 'P1DY', 'P2DX', 'P2DY');
- CHPO6 : CHPOINT "CENTRE" that contains the limiter of the velocity gradient (2 components in 2D, 'P1', 'P2');
- CHPO7 : CHPOINT "CENTRE" that contains the temperature of particles (K), with one 'SCAL' component;
- CHPO8 : CHPOINT "CENTRE" that contains the temperature gradient ( $\text{K}/\text{m}$ ), 2 components in 2D ('P1DX', 'P1DY');
- CHPO9 : CHPOINT "CENTRE" that contains the limiter of temperature gradient (one component, 'P1');
- CHPO10 : CHPOINT "CENTRE" containing the specific heat of the particles ( $\text{J}\cdot\text{kg}^{-1}\cdot\text{K}^{-1}$ ), one component 'SCAL';

- MCHAM<sub>1</sub> : MCHAML that contains the solid concentration (kg/m<sup>3</sup>) and has as underlying space (SPG) 'DOMA' MOD<sub>1</sub> 'FACEL';
- MCHAM<sub>2</sub> : MCHAML that contains the velocity (m/s) and the direction cosines of the local frame (n,t) in the global frame (x,y), with 6 components in 2D ('UN', 'UT', 'NX', 'NY', 'TX', 'TY');
- MCHAM<sub>3</sub> : MCHAML (SPG = 'FACEL') containing the temperature of particles (K);
- MCHAM<sub>4</sub> : MCHAML (SPG = 'FACEL') containing the specific heat of particles (J·kg<sup>-1</sup>·K<sup>-1</sup>).

In the simpler case when the discretisation order in space is ENT<sub>1</sub> = 1, there is no need to provide the information regarding the gradients, so that the syntax would be like this:

```
MCHAM1 MCHAM2 MCHAM3 MCHAM4 = 'PRET' 'PARTMONO' 1 1 MOD1
                                CHP01 CHP04 CHP07 CHP010 ;
```

Now, regarding the keyword '**PARTTEMP**' which was explained before, by this option **PRET** operator can provide the fields defined in the elements by the following syntax:

```
MCHAM1 MCHAM2 MCHAM3 MCHAM4 = 'PRET' 'PARTTEMP' ENT1 ENT2
                                MOD1 TAB1 CHP01 (CHP02) (CHP03)
                                CHP04 (CHP05) (CHP06) CHP07
                                (CHP08) (CHP09) CHP010 (CHP011)
                                (CHP012) (FLOT1) ;
```

where, in this case, we have the following list of arguments and results (note that the parenthesis denote objects that should be introduced as arguments only in case ENT<sub>1</sub> = 2, that is, only if second-order space discretisation is considered):

- ENT<sub>1</sub> : ENTIER object; space order (=1 or 2);
- ENT<sub>2</sub> : ENTIER object; time order (=1 or 2);
- MOD<sub>1</sub> : MODELE Object;
- CHPO<sub>1</sub> : CHPOINT "CENTRE" that contains the solid concentration  $\sigma$  (kg/m<sup>3</sup>), with just one 'SCAL' component;
- CHPO<sub>2</sub> : CHPOINT "CENTRE" that contains the gradient of the solid concentration (kg/m<sup>4</sup>), 2 components in 2D: 'P<sub>1DX</sub>', 'P<sub>1DY</sub>');
- CHPO<sub>3</sub> : CHPOINT "CENTRE" that contains the limiter of solid concentration gradient (one component, 'P<sub>1</sub>');
- CHPO<sub>4</sub> : CHPOINT "CENTRE" that contains the velocity of particles (m/s), containing two components in 2D: 'UX' and 'UY';

- CHPO<sub>5</sub> : CHPOINT "CENTRE" that contains the velocity gradient ( $s^{-1}$ ), 4 components in 2D ('P1DX', 'P1DY', 'P2DX', 'P2DY');
- CHPO<sub>6</sub> : CHPOINT "CENTRE" that contains the limiter of the velocity gradient (2 components in 2D, 'P1', 'P2');
- CHPO<sub>7</sub> : CHPOINT "CENTRE" that contains the temperature of particles (K), with one 'SCAL' component;
- CHPO<sub>8</sub> : CHPOINT "CENTRE" that contains the temperature gradient (K/m), 2 components in 2D ('T1DX', 'T1DY');
- CHPO<sub>9</sub> : CHPOINT "CENTRE" that contains the limiter of temperature gradient (one component, 'T1');
- CHPO<sub>10</sub> : CHPOINT "CENTRE" containing the mass fractions of the different species (only in the case of a mixture of Nssp - 1 components);
- CHPO<sub>11</sub> : CHPOINT "CENTRE" with the gradient of the mass fractions ( $m^{-1}$ ), only in the case of a mixture;
- CHPO<sub>12</sub> : CHPOINT "CENTRE" that contains the limiter of the gradient of the mass fractions;
- FLOT<sub>1</sub> : FLOTTANT object containing the time increment (in s) for the prediction step (only in the case ENT2 = 2; suggested value:  $\Delta t/2$ );
- MCHAM<sub>1</sub> : MCHAML that contains the solid concentration ( $kg/m^3$ ) and has as underlying space (SPG) 'DOMA' MOD<sub>1</sub> 'FACEL';
- MCHAM<sub>2</sub> : MCHAML that contains the velocity (m/s) and the direction cosines of the local frame (n,t) in the global frame (x,y), with 6 components in 2D ('UN', 'UT', 'NX', 'NY', 'TX', 'TY');
- MCHAM<sub>3</sub> : MCHAML (SPG = 'FACEL') containing the temperature of particles (K);
- MCHAM<sub>4</sub> : MCHAML (SPG = 'FACEL') containing the mass fractions of each species (the same components as CHPO<sub>10</sub>).

Meanwhile, the CHPOINTS of the primitive variables, defined in the centres of the finite volumes, which must be an input for PRET operator, have to be updated at every discrete time during computation. According to the flowchart depicted in [Figure A.2](#), this update is undertaken after the computation of the conserved variables for  $t^{n+1}$ , and before the application of the boundary conditions. Therefore, the primitive variables are re-calculated for each time step by calling PRIM operator. Again, this operator features some options conditioned by the sort of solid phase and, thus, the model of equations.

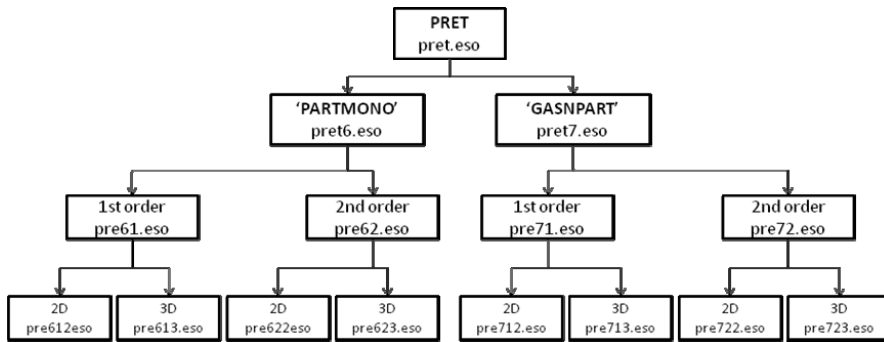


Figure A.5: Diagram on the structure of PRET operator in Cast3M.

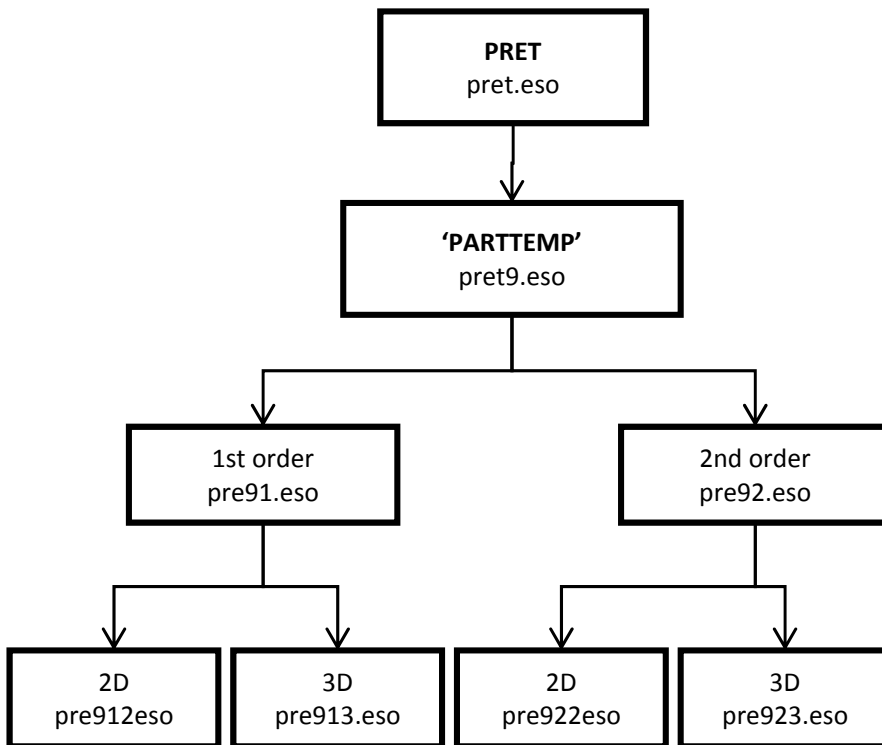


Figure A.6: Diagram on the structure of PRET operator in Cast3M.

Depending on the case, we use the 'GASNPART' keyword for laden mixtures, or the 'PARTMONO' keyword for a solid phase of a high-dilute mixture of particles. The underlying file structure for these two options is described in [Figure A.7](#). Also, for multi-component, diluted mixtures with temperature-dependent heat capacities, we can choose the keyword 'PARTTEMP', whose file structure has been depicted in [Figure A.8](#). The standard syntax in Gibiane language for the two last options is as follows:

```
RCHPO1 RCHPO3 = 'PRIM' 'PARTMONO' CHP01 CHP02 CHP03 CHP04 ;
```

```
RCHPO1 RCHPO2 RCHPO3 RCHPO4 RCHPO5 = 'PRIM' 'PARTTEMP' TAB1
      CHP01 CHP02 CHP03 CHP05 ;
```

with a number of objects involved:

- TAB1 : TABLE object that contains: (i) the name of the species non-explicitly treated in Euler's Equations for the solid phase: TAB1 . 'ESPNEULE' (MOT object); (ii) the names of the species explicitly treated in TAB1 . 'ESPEULE' (LISTMOTS object); (iii) the degree of the polynomial  $c_v = c_v(T)$ , in TAB1 . 'NORD' (ENTIER object,  $\geq 0$ ); (iv) the properties of each gas 'ESPI', in TAB1 . 'ESPI' (TABLE object);
- CHPO1 : CHPOINT that contains the solid concentration  $\sigma$  ( $\text{kg}/\text{m}^3$ ) with just one 'SCAL' component;
- CHPO2 : CHPOINT containing the momentum of the particle phase ( $\text{kg}/\text{s}/\text{m}^2$ ), two components in 2D, 'UX ', 'UY ', and three components in 3D, 'UX ', 'UY ', 'UZ ';
- CHPO3 : CHPOINT containing the total energy of particles  $\sigma E_{t,p}$  ( $\text{J}/\text{m}^3$ ), with one 'SCAL' component.
- CHPO4 : CHPOINT containing the specific heat of the solid ( $\text{J}\cdot\text{kg}^{-1}\cdot\text{K}^{-1}$ ), as an input for the case with 'PARTMONO' keyword;
- CHPO5 : CHPOINT that contains the quantity of each species  $\sigma Y_{p,i}$ ; the object must include Nssp - 1 components;
- RCHPO1 : CHPOINT with results from the operator, including the solid concentration  $\sigma$  ( $\text{kg}/\text{m}^3$ );
- RCHPO2 : CHPOINT that contains the density of the solid  $\rho_p$  ( $\text{kg}/\text{m}^3$ ), with just one 'SCAL' component;
- RCHPO3 : CHPOINT containing the temperature of the particles (in K), with a single 'SCAL' component;
- RCHPO4 : CHPOINT containing the mass fractions of the different solid species (only in the case of a mixture of Nssp components);

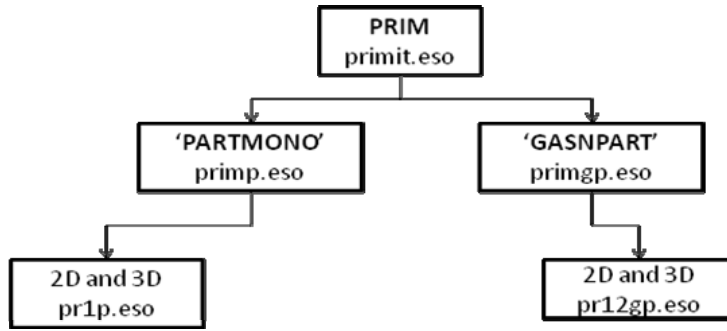


Figure A.7: Diagram on the structure of PRIM operator in Cast3M.

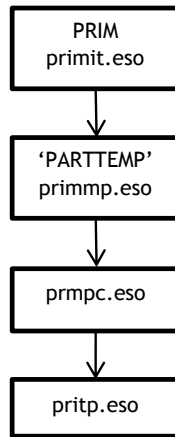


Figure A.8: Diagram on the structure of PRIM operator in Cast3M for the 'PARTTEMP' keyword.

RCHPO<sub>5</sub> : CHPOINT containing the specific heat of particles ( $\text{J}\cdot\text{kg}^{-1}\cdot\text{K}^{-1}$ ), one component 'SCAL'.

### A.3.2 FUENTE operator: friction and heat transfer

The system of conservation equations described in [Section 3.3](#) incorporated a series of physical effect by the addition of source terms. Thus, the vector of source terms included the effect of external forces (like gravitational force), particle-gas interaction (heat exchange, drag force, etc.) and chemical reaction (homogeneous and heterogeneous reactions).

When, at a first stage of development, the mobilisation of particles was implemented in Cast3M, we denoted the lack of an operator being able to compute the values of the source terms for particle-gas interaction, or even to compute the new updated values of the conserved variables, once the source terms were added. So, the goal was to enable in Cast3M the possibility to choose some of the physical laws detailed in [Section 3.4](#).

In order to implement these physical laws in Cast3M, FUEN operator (FUENTE) was created . In this case, the operator structure in ESOPE was entirely developed from scratch. Options for laden mixtures, as well as highly diluted models, were considered. These are the options currently implemented in FUEN operator:

- 'PHASEIN1' considers drag force and interfacial heat transfer 2D and 3D. Source file: fnt1p.eso.
- 'PHASEIN2' considers drag force, interfacial heat transfer and Magnus' force only valid for 3D problems. Source file: fnt2p.eso (if 2D it is equivalent to fnt1p.eso).
- 'PHASEIN3' considers drag force, interfacial heat transfer and includes turbulent source terms for the gas-particles mixture (2D and 3D). The source file is fnt3p.eso.
- 'PHASEIN4' all previously considered plus particle wall interaction. Source file: fnt4p.eso.
- 'PHASEIN5' considers a drag force law for the case of the dense model (Rogue et al. expressions). Source file: fnt5p.eso.
- 'PHASEIN6' is suited for a dense model. This option considers the drag force and heat transfer for the Combe and Herard expression [23]. Source file: fnt6p.eso.
- 'PHASEIN8' computes the source terms (drag force and interfacial heat transfer), similar to 'PHASEIN1', but it does by means of an implicit treatment. Source file: fnt8p.eso.
- 'PHASEIN9' has implemented a model that considers drag force, interfacial heat transfer, turbulent source terms and complete wall functions for both gas and particles. Source file: fnt9p.eso.
- 'PHASEIN10' This model considers drag force, interfacial heat transfer, turbulent source terms, and the wall function is enabled only for gases. Source file: fnt10p.eso.
- 'PHASEIN12' considers gravity, turbulent source terms and complete wall functions for the gas phase. This case differs from 'PHASEIN10' just in the gravity source terms. The source file is: fnt12p.eso.
- 'PHASEIN13' is similar to 'PHASEIN12', but in this case both phases are affected by gravity and wall functions. Source file: fnt13p.eso.

In [Figure A.9](#), the ESOPE file structure developed for FUEN operator is shown. Let us have a look on to the syntax for FUEN operator with the keyword 'PHASEIN1', by far the most repeatedly used in

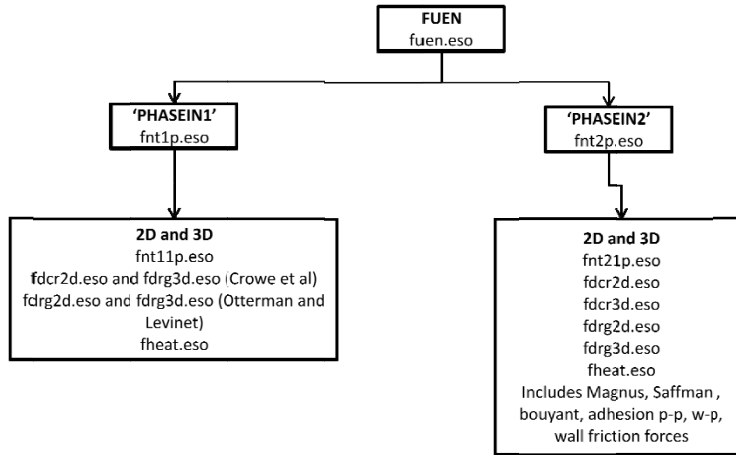


Figure A.9: File structure concept constructed for the evaluation of coupling source terms (drag and heat transfer) with FUEN operator. Two options are shown: 'PHASEIN1' and 'PHASEIN2'.

this Thesis, specially under the secondary keyword 'MIURA' which enables the closure laws by Miura and Glass [81].

```
ST7 ST6 ST3 ST2 = 'FUEN' 'PHASEIN1' MCLE1
                  CHP01 CHP02 CHP03 CHP04 CHP05 CHP06
                  CHP07 CHP08 CHP09 CHP010 FL01 (FL02);
```

where

- MCLE1 : MOT object intended to select a set of laws for drag force and heat transfer (options: 'MIURA', 'CROWE', 'FZK', 'ENEA', 'ROGUE', 'COMBE');
- CHPO1 : CHPOINT which contains the density of the mixture of gases (kg/m<sup>3</sup>) with just one 'SCAL' component;
- CHPO2 : CHPOINT containing the velocity of the gas phase (m/s), two components in 2D, 'UX ', 'UY ', and three components in 3D, 'UX ', 'UY ', 'UZ ';
- CHPO3 : CHPOINT containing the field of pressures (Pa), one component 'SCAL';
- CHPO4 : CHPOINT which contains the temperature of the gas (K); one component 'SCAL';
- CHPO5 : CHPOINT containing the specific heat at constant pressure of the gas  $(c_p)_g = R_g + (c_v)_g$  (J·kg<sup>-1</sup>·K<sup>-1</sup>), one component 'SCAL';
- CHPO6 : CHPOINT that contains the solid concentration  $\sigma$  (kg/m<sup>3</sup>) with just one 'SCAL' component;
- CHPO7 : CHPOINT containing the velocity of the particle phase (m/s), two components in 2D, 'UX ', 'UY ', and three components in 3D, 'UX ', 'UY ', 'UZ ';

- CHPO8 : CHPOINT which contains the temperature of particles (K), with one 'SCAL' component;
- CHPO9 : CHPOINT containing the specific heat of particles ( $\text{J}\cdot\text{kg}^{-1}\cdot\text{K}^{-1}$ ), one component 'SCAL';
- CHPO10 : CHPOINT containing the weighted average of the density of the material from which the solid phase is formed ( $\text{kg}/\text{m}^3$ ), with one 'SCAL' component;
- FLO1 : FLOTTANT object containing the initial average diameter of particles (m);
- FLO2 : FLOTTANT object containing the value of the constant of gravity acceleration, if considered ( $\text{m}/\text{s}^2$ );
- ST2 : CHPOINT object which contains the values of the source term (including drag force and heat transfer) for the momentum conservation equation (gas phase);
- ST3 : CHPOINT containing the values of the source term (including drag force and heat transfer) for the energy conservation equation (gas phase);
- ST6 : CHPOINT containing the values of the source term (including drag force and heat transfer) for the momentum conservation equation (particle phase);
- ST7 : CHPOINT containing the values of the source term (including drag force and heat transfer) for the energy conservation equation (particle phase).

Note that FUEN operator under the option 'PHASEIN1' gives as a result the values of the source terms (the sum of those for friction and for heat transfer) and those terms must be integrated in time to give the updated values of the conserved variables. In this version of FUEN operator, this must be done in Gibiane language and outside the operator.

There is another version ('PHASEIN8') where the integration is done by an "Advanced Source-Term Treatment". In that case, the integration takes place inside the operator. This implicitation method allows the code to provide successful results even in case of numerically-adverse conditions, that is, some specific values of the test conditions which make the source terms become numerically stiff (see [Section 4.4](#) or results in [Chapter 5](#) for further details about this method). Since this is an implicit method, the syntax should appear in Gibiane simplified. In addition, there is no secondary keyword to choose the closure laws for drag and heat transfer (by this option only the laws by Miura and Glass [81] were implemented). However, in this case the result objects are the primitive variables and, consequently, the conserved variables must be recalculated after the operator is called.

The standard syntax for **FUEN** operator under the '**PHASEIN8**' keyword is as follows:

```
RCHP05 RCHP04 RCHP03 RCHP02 RCHP01 = 'FUEN' 'PHASEIN8'
      CHP01 CHP02 CHP03 CHP04 CHP05 CHP06
      CHP07 CHP08 CHP09 CHP010 CHP011
      FLOT1 FLOT2 FLOT3;
```

where

- CHPO<sub>1</sub> : CHPOINT which contains the density of the mixture of gases (kg/m<sup>3</sup>) with just one 'SCAL' component;
- CHPO<sub>2</sub> : CHPOINT containing the velocity of the gas phase (m/s), two components in 2D, 'UX ', 'UY ', and three components in 3D, 'UX ', 'UY ', 'UZ ';
- CHPO<sub>3</sub> : CHPOINT containing the field of pressures (Pa), one component 'SCAL';
- CHPO<sub>4</sub> : CHPOINT which contains the temperature of the gas (K); one component 'SCAL';
- CHPO<sub>5</sub> : CHPOINT containing the specific heat at constant pressure of the gas  $(c_p)_g = R_g + (c_v)_g$  (J·kg<sup>-1</sup>·K<sup>-1</sup>), one component 'SCAL';
- CHPO<sub>6</sub> : CHPOINT that contains the solid concentration  $\sigma$  (kg/m<sup>3</sup>) with just one 'SCAL' component;
- CHPO<sub>7</sub> : CHPOINT containing the velocity of the particle phase (m/s), two components in 2D, 'UX ', 'UY ', and three components in 3D, 'UX ', 'UY ', 'UZ ';
- CHPO<sub>8</sub> : CHPOINT which contains the temperature of particles (K), with one 'SCAL' component;
- CHPO<sub>9</sub> : CHPOINT containing the specific heat of particles (J·kg<sup>-1</sup>·K<sup>-1</sup>), one component 'SCAL';
- CHPO<sub>10</sub> : CHPOINT containing the weighted-average density of the material from which the solid phase is formed (kg/m<sup>3</sup>), with one 'SCAL' component;
- CHPO<sub>11</sub> : CHPOINT containing the values of the adiabatic index or heat capacity ratio,  $\gamma = C_{p,gas}/C_{v,gas}$ , of the mixture of gases in the fluid field, with one component 'SCAL';
- FLOT<sub>1</sub> : FLOTTANT object containing the initial average diameter of particles (m);
- FLOT<sub>2</sub> : FLOTTANT object containing the value of the characteristic time,  $\Delta t$ , associated with the fastest wave;
- FLOT<sub>3</sub> : FLOTTANT object containing the value of the constant of gravity acceleration, if considered (m/s<sup>2</sup>);

- CHPO<sub>1</sub> : CHPOINT object which contains the updated values of the gas velocity in m/s (components = CHPO<sub>2</sub>);
- CHPO<sub>2</sub> : CHPOINT containing the updated values of the gas temperature in K (one component 'SCAL');
- CHPO<sub>3</sub> : CHPOINT containing the updated values of pressure in Pa (one component 'SCAL');
- CHPO<sub>4</sub> : CHPOINT object which contains the updated values of the velocity of the particle phase in m/s (components = CHPO<sub>7</sub>);
- CHPO<sub>5</sub> : CHPOINT containing the updated values of the temperature of particles in K (one component 'SCAL').

#### A.4 MODIFICATIONS UNDERTAKEN FOR COMBUSTION

Further modification of FUEN operator have been tackled in order to enable the combustion effects, modelled in the system of equations by the combustion source terms (see [Section 3.4.2](#)). The first step when computing these terms is the calculation of the reaction rates. Then, the values of the source terms for each equation are obtained. The updated values of the conserved variables after combustion can be calculated through time integration inside the operator (ESOPE) or in the Gibiane code, depending on the preferences of the developer. Presumably, an operator giving the updated conserved variables, instead of the source terms, should be easier to understand for the user. However, in the last case, the user would have a simpler access to the integration process.

Meanwhile, we ought to take into consideration the issue of the “Time stepping strategy” for the case of multiple reactive species, some of which may be either consumed or generated. To this regard, a robust solution has been implemented in FUEN operator consisting in a time-step combustion loop, in which the different species are allowed to gradually react until one of them is consumed and, then, it is excluded from the loop (see [Section 4.4.5](#) for a detailed explanation).

Different options are enabled in FUEN operator regarding combustion, at the time of writing. These can be invoked through the following keywords:

- 'COMBUST1' includes an Arrhenius model for the combustion of Al particles with O<sub>2</sub> following Chen et al. [20] and Ogle et al. [85]. The source file is fnt7p.eso.
- 'PRPLLANT' This model considers drag force, interfacial heat and combustion in the case of a burning propellant (this option is under development as of the date of publication of this document).

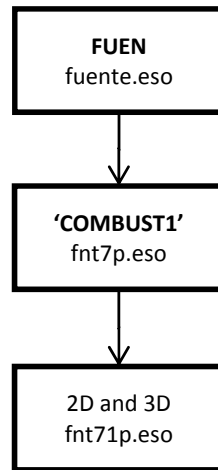


Figure A.10: File structure of FUEN operator under the keyword “COMBUST1”.

- ‘COMBUSTW’ computes the source terms for the combustion of tungsten particles. It considers, simultaneously, the reactions: (i)  $W + 3/2 O_2 \rightarrow WO_3$ , (ii)  $W + 3H_2O \rightarrow WO_3 + 3H_2$ , and (iii)  $H_2 + 1/2 O_2 \rightarrow H_2O$ . Source file: fnt14p.eso.
- ‘COMBUSTC’ computes the source terms for the combustion of graphite particles, considering the reaction scheme: (i)  $C + O_2 \rightarrow CO_2$ , (ii)  $C + H_2O \rightarrow CO + H_2$ , (iii)  $H_2 + 1/2 O_2 \rightarrow H_2O$ , and (iv)  $CO + 1/2 O_2 \rightarrow CO_2$ . The source file is fnt15p.eso.

The simplest of these options is ‘COMBUST1’. It has been employed in the simulation of several tests: Chen Tests (Section 6.1.1) and Veysiere Tests (sec:veysiere-test). Figure A.10 describes schematically the file structure of the operator just under the keyword “COMBUST1”. And the syntax in Gibiane of this operator should be as follows:

```

RFL01 CST8 CST7 CST6 CST5 CST4 CST3 CST2 CST1 = 'FUEN' 'COMBUST1'
      CHP01 CHP02 CHP03 CHP04 CHP05 CHP06 CHP07 CHP08
      FL01 FL02 FL03 FL04 FL05 FL06;
  
```

where:

- CHPO1 : CHPOINT containing the density of the mixture of gases ( $kg/m^3$ ) with just one ‘SCAL’ component;
- CHPO2 : CHPOINT containing the weighted average of the density of the material from which the solid phase is formed ( $kg/m^3$ ), with one ‘SCAL’ component;
- CHPO3 : CHPOINT containing the concentration of particles  $\sigma$  ( $kg/m^3$ ), one componen ‘SCAL’;

- CHPO4 : CHPOINT containing the velocity of the particle phase (m/s), two components in 2D, 'UX', 'UY', and three components in 3D, 'UX', 'UY', 'UZ';
- CHPO5 : CHPOINT containing the temperature of particles (K), one component 'SCAL';
- CHPO6 : CHPOINT containing the specific heat of particles ( $\text{J}\cdot\text{kg}^{-1}\cdot\text{K}^{-1}$ ), one component 'SCAL';
- CHPO7 : CHPOINT containing the amount of  $\text{O}_2$  per unit volume, that is, the conserved variable  $\rho_g Y_{g,\text{O}_2}$  ( $\text{kg}_{\text{O}_2}/\text{m}^3$ ); with one component 'O2';
- CHPO8 : CHPOINT containing the amount of reactive particle species (aluminium), that is,  $\sigma Y_{p,\text{Al}}$  ( $\text{kg}_{\text{Al}} / \text{m}^3$ ); with one component 'Al';
- FLO1 : FLOTTANT containing the initial average diameter of particles (m);
- FLO2 : FLOTTANT containing the reference density considered for aluminium ( $\text{kg}/\text{m}^3$ ), with one 'SCAL' component;
- FLO3 : FLOTTANT with a kinetic constant of the reaction model by Ogle et al. [85], the activation energy  $E_{\text{Al}}$  (kJ/mol);
- FLO4 : FLOTTANT with the second kinetic constant of the reaction model by Ogle et al. [85], the pre-exponential factor,  $A$ , in SI units  $(\text{m}^3/\text{kg})^1/2\cdot\text{s}^{-1}$ ;
- FLO5 : FLOTTANT containing the threshold temperature for the combustion of particles (K);
- FLO6 : object type FLOTTANT with the value of the characteristic time  $\Delta t_n$  (in seconds) associated with the fastest wave (see operator KONV);
- CST1 : CHPOINT object which contains the values of the source term modelling the combustion of particles, corresponding to the mass conservation equation (gas phase);
- CST2 : CHPOINT containing the combustion source terms corresponding to the momentum conservation equation (gas phase);
- CST3 : CHPOINT containing the combustion source terms corresponding to the energy conservation equation (gas phase);
- CST4 : CHPOINT containing the combustion source terms corresponding to the equation for the conservation of the gaseous species (gas phase);

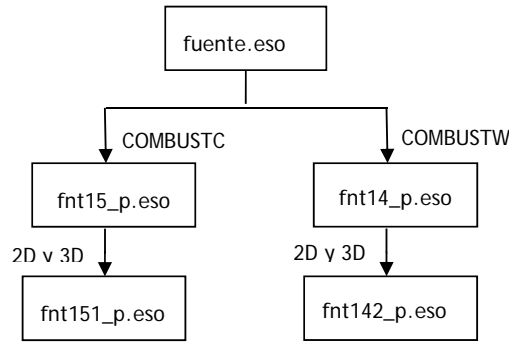


Figure A.11: File structure constructed in CAST<sub>3</sub>M for the evaluation of the combustion source terms, for the case of multiple gaseous species and reactive particles (graphite = 'COMBUSTC', tungsten = 'COMBUSTW').

- CST<sub>5</sub> : CHPOINT containing the combustion source terms corresponding to the mass conservation equation (discrete phase);
- CST<sub>6</sub> : CHPOINT containing the combustion source terms corresponding to the momentum conservation equation (discrete phase);
- CST<sub>7</sub> : CHPOINT containing the combustion source terms corresponding to the energy conservation equation (discrete phase);
- CST<sub>8</sub> : CHPOINT containing the combustion source terms corresponding to the equation for the conservation of the solid species (discrete phase);
- RFLO<sub>1</sub> : object type FLOTTANT with the new value of the time step (in seconds) associated with the time of combustion  $\Delta t_c$  on each finite volume (only if  $\Delta t_c < \Delta t_n$ ; otherwise, RFLO<sub>1</sub> = FLO<sub>6</sub>).

With respect to the other FUEN options developed for combustion, 'PRPLLANT' is used for ballistic simulations, which is not the aim of this Thesis. Conversely, 'COMBUSTC' and 'COMBUSTW' are particularly suited for the simulation of combustion problems with multiple species, as those in [Section 6.4.6](#) and [Section 6.5](#).

In particular, the keyword 'COMBUSTC' of FUEN operator is specially aimed to compute the combustion source terms for the case of the multiple-species heterogeneous reaction, including O<sub>2</sub>, H<sub>2</sub>, H<sub>2</sub>O, CO, CO<sub>2</sub> and C (graphite). More species can be introduced in the arguments but none of them would be considered for the reaction model. Thus, only four reactions are considered, as mentioned be-

fore. Alternatively, the 'COMBUSTW' option considers a reactive mixture of  $O_2$ ,  $H_2$ ,  $H_2O$ ,  $CO$ ,  $CO_2$ ,  $W$  (tungsten particles), and  $WO_3$ . More species can be included to the calculations, but they will not be considered for the reaction model. The ESOPE file structure developed for the integration in Cast3M of these two options is outlined in [Figure A.11](#). Therefore, to call FUEN operator we can now employ the following syntax:

```
RCHP7 RCHP6 RCHP5 RCHP4 RCHP3 RCHP2 RCHP1 = 'FUEN' MCLE1
          CHP01 CHP02 CHP03 CHP04 CHP05 CHP06
          CHP07 CHP08 CHP09 CHP010 CHP011 CHP012
          CHP013 FLOT1 FLOT2;
```

where:

- MCLE1 : MOT object to select the reaction scheme ('COMBUSTC' or 'COMBUSTW');
- CHPO1 : CHPOINT containing the density of the mixture of gases ( $kg/m^3$ ) with just one 'SCAL' component;
- CHPO2 : CHPOINT containing the momentum of the gas phase ( $kg/s/m^2$ ), two components in 2D, 'UX ', 'UY ', and three components in 3D, 'UX ', 'UY ', 'UZ ';
- CHPO3 : CHPOINT containing the total energy of the gas phase  $\rho_g E_{t,g}$  ( $J/m^3$ ), with one 'SCAL' component);
- CHPO4 : CHPOINT containing the weighted average of the density of the material from which the solid phase is formed ( $kg/m^3$ ), with one 'SCAL' component;
- CHPO5 : CHPOINT containing concentration of particles  $\sigma$  ( $kg/m^3$ ), one component 'SCAL';
- CHPO6 : CHPOINT containing the momentum of the particle phase ( $kg/s/m^2$ ), two components in 2D, 'UX ', 'UY ', and three components in 3D, 'UX ', 'UY ', 'UZ ';
- CHPO7 : CHPOINT containing the total energy of particles  $\sigma E_{t,p}$  ( $J/m^3$ ), with one 'SCAL' component.
- CHPO8 : CHPOINT containing the field of pressures (Pa), one component 'SCAL';
- CHPO9 : CHPOINT containing the temperature of the gas mixture (K), one component 'SCAL';
- CHPO10 : CHPOINT containing the temperature of particles (K), one component 'SCAL';
- CHPO11 : CHPOINT containing the the specific heat of particles ( $J \cdot kg^{-1} \cdot K^{-1}$ ), one component 'SCAL';
- CHPO12 : CHPOINT containing the amount of gaseous species, that is,  $\rho_g Y_g$  ( $kg / m^3$ ); NGSP components with the symbol of each species ('O2' 'H2' 'H2O' 'CO' 'CO2');

- CHPO<sub>13</sub> : CHPOINT containing the amount of reactive particle species (graphite), that is,  $\sigma Y_p$  (kg / m<sup>3</sup>); with one component 'C' (if MCLE<sub>1</sub> = 'COMBUSTC') or 'W' (if MCLE<sub>1</sub> = 'COMBUSTW');
- FLOT<sub>1</sub> : FLOTTANT containing the initial average diameter of particles (m);
- FLOT<sub>2</sub> : object type FLOTTANT with the value of the characteristic time  $\Delta t_n$  (in seconds) associated with the fastest wave (see operator KONV);
- RCHP<sub>1</sub> : CHPOINT that contains the updated values of the gas density (kg/m<sup>3</sup>) after the integration of the source terms for combustion (one 'SCAL' component);
- RCHP<sub>2</sub> : CHPOINT that contains the updated values of the momentum (gas phase) in SI units (kg/s/m<sup>2</sup>), with the same components as CHPO<sub>2</sub>;
- RCHP<sub>3</sub> : CHPOINT that contains the updated values of total energy (gas phase) in J/m<sup>3</sup>, with one component 'SCAL';
- RCHP<sub>4</sub> : CHPOINT that contains the updated values of species conserved variable for the gas phase  $\rho_g Y_g$  (kg / m<sup>3</sup>); same components as CHPO<sub>12</sub>;
- RCHP<sub>5</sub> : CHPOINT that contains the updated values of concentration of particles in kg/m<sup>3</sup> (one component 'SCAL');
- RCHP<sub>6</sub> : CHPOINT that contains the updated values of the momentum (particle phase) in SI units (kg/s/m<sup>2</sup>), with the same components as CHPO<sub>6</sub>;
- RCHP<sub>7</sub> : CHPOINT that contains the updated values of total energy in the particle phase  $\sigma E_{t,p}$  (J/m<sup>3</sup>), with one 'SCAL' component.

Hence, following this, the structure of a Gibiane case for a two-phase problem has undergone some changes from the standard fluid problem without particles. The general flowchart of a two-phase problem in Cast3M with the FUEN operator has been depicted in [Figure A.12](#).

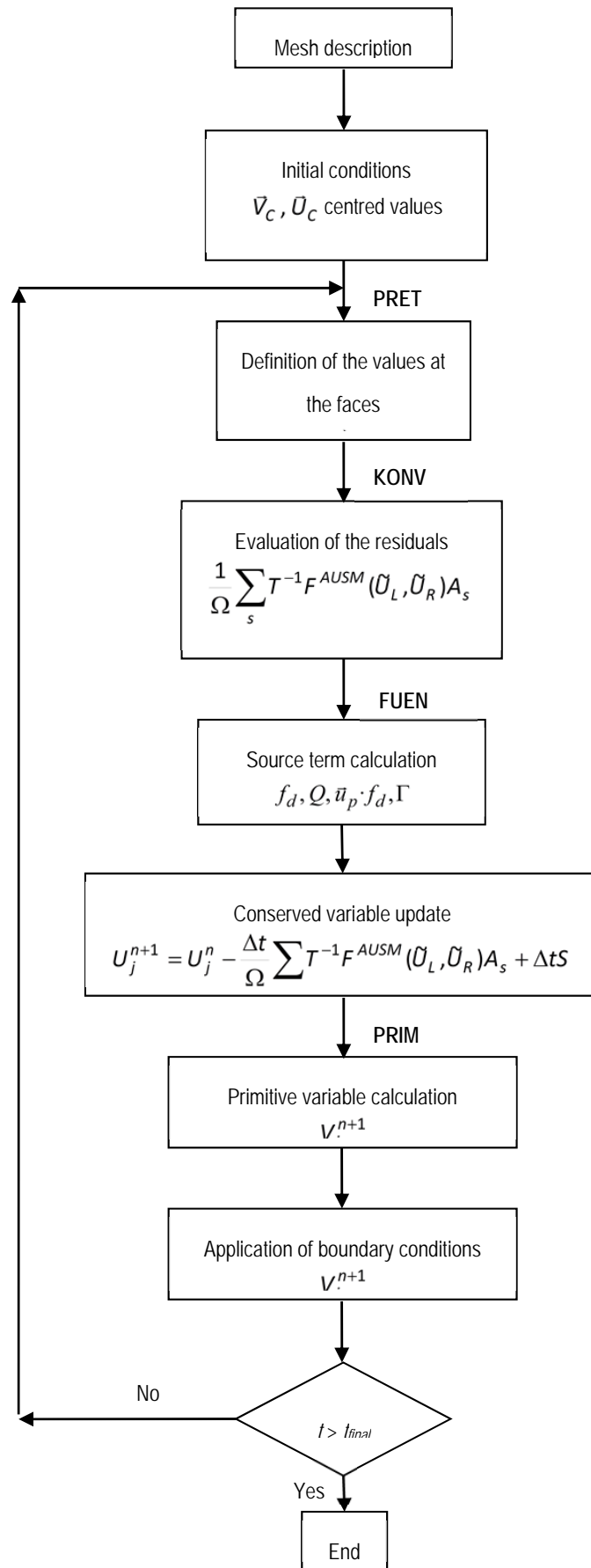


Figure A.12: General flowchart of a two-phase problem in Cast3M with FUEN operator.

## BIBLIOGRAPHY

---

- [1] K. Annamalai. Critical regimes of coal ignition. *Engineering for Power*, 101(4):576–583, 1979.
- [2] K. Annamalai and P. Durbetaki. Combustion behavior of char/-carbon particles. In *17th Symp. Int. on Combustion*, Leeds, England, 1979.
- [3] S.R. Aspinall. Principles governing the behavior of solid materials in severe high temperature environments. Technical Report AD466458, Union Carbide Research Institute, Tarrytown, NY, 2008.
- [4] M. R. Baer and J. W. Nunziato. A two-phase mixture theory for the deflagration-to-detonation transition (ddt) in reactive granular materials. *International Journal on Multiphase Flow*, 12(6): 861–889, 1986.
- [5] G.M. Barrow. *Química física*. Editorial Reverté, Barcelona, Spain, 1988.
- [6] R.V. Bartlett. Tungsten and molybdenum oxidation kinetics at extremely high temperatures, us air force. *Documentary report ML-TDR-64-290*, 1964.
- [7] J.B. Bdzil, R. Menikoff, S.F. Son, A.K. Kapila, and D.S. Stewart. Two-phase modeling of ddt in granular materials: A critical examination of modeling issues. *Physics Of Fluids*, 11:378–402, 1999.
- [8] A. Beccantini. Upwind splitting schemes for ideal gases mixtures with temperature-dependent specific heat capacities. Doctoral thesis, Université d'Evry val d'Essonne, 2000.
- [9] A. Beccantini and H. Paillère. Modeling of hydrogen detonation for application to reactor safety. In *Proc. ICONE-6*, San Diego, USA, 1998.
- [10] V.M. Boiko, A.V. Fedorov, V.M. Fomin, A.N. Papyrin, and R.I. Soloukhin. Ignition of small particles behind shock waves. *Progress in Astronautics and Aeronautics*, 87:71–87, 1983.
- [11] P. Boivin, C. Jiménez, A.L. Sánchez, and F.A. Williams. A four-step reduced mechanism for syngas combustion. *Combustion and Flame*, 158:1059–1063, 2011.

- [12] P.B. Butler, M.F. Lembeck, and H. Krier. Modeling of shock development and transition to detonation initiated by burning in porous propellant beds. *Combustion and Flame*, 46:75–93, 1982.
- [13] CEA France. Cast3m website, 2013. URL <http://www-cast3m.cea.fr>.
- [14] C. H. Chang and M. S. Liou. A new approach to the simulation of compressible multifluid flows with aum+ scheme. *AIAA J.*, 38:1624–1633, 2000.
- [15] S. Chapman and T.G. Cowling. *The mathematical theory of non-uniform gases*. Cambridge University Press, 1961.
- [16] P. Chappuis, E. Tsitrone, M. Mayne, X. Armand, H. Linke, H. Bolt, D. Pett, and J. P. Sharpe. Dust characterization and analysis in tore-supra. *J. Nucl. Mater.*, 293(293):245–249, 2001.
- [17] H.K. Chelliah. The influence of heterogeneous kinetics and thermal radiation on the oxidation of graphite particles. *Combustion and Flame*, 104:81–94, 1996.
- [18] H.K. Chelliah and F.J. Miller. Heterogeneous combustion of porous graphite particles in microgravity. In *4th International Microgravity Combustion Workshop*, Cleveland USA, 1979.
- [19] Z. Chen and B. Fan. Flame propagation through aluminum particle cloud in a combustion tube. *Journal of Loss Prevention in the Process Industries*, 18:13–19, 2005.
- [20] Z. Chen, B. Fan, Q. Liu, and H. Li. Shock wave induced by turbulent combustion in suspension. In *Dust Explosions (Int. Colloquium)*, Bergen, Norway, 1996.
- [21] D.P. Clark and Smoot L.D. Model of accelerating coal dust flames. *Combustion and Flame*, 62:255–269, 1985.
- [22] R. Clift and W.H. Gauvin. The motion of particles in turbulent gas streams. *Proc. Chemeca*, 70:1–14, 1970.
- [23] L. Combe and J.M. Hérard. Un schéma volumes-finis pour la simulation d'un modèle bi-fluide d'écoulements diphasiques compressibles gaz-solide. *Revue Européenne des Éléments Finis*, 6:197–231, 1997.
- [24] C.T. Crowe, M. Sommerfeld, and Y. Tsuji. *Multiphase flows with droplets and particles*. CRC Press LLC, Boca Raton, Florida, USA, 1998.
- [25] W. Cybulski. Explosibility of coal dust of very high fineness. In *7th International Conference of Directors of Safety in Mines Research*, Buxton, England, 1952.

- [26] S.F. Davis. Simplified second-order godunov-tupe methods. *SIAM J. Sci. Stat. Comput.*, 9:445–473, 1988.
- [27] S.G. Davis, A.V. Joshi, H. Wang, and F. Egolfopoulos. Testing a small detailed chemical-kinetic mechanism for the combustion of hydrogen and carbon monoxide. *Proceedings of the Combustion Institute*, 30:1283–1292, 2005.
- [28] A. J. Delisle, F.J. Miller, and H.K. Chelliah. Combustion of porous graphite particles in oxygen enriched air. In *7th International Workshop on Microgravity Combustion and Chemically Reacting Systems*, pages 9–12, 2003.
- [29] E. Desroches-Ducarne, J.C. Dolignier, E. Marty, G. Martin, and L. Delfosse. Modelling of gaseous pollutants emissions in circulating fluidized bed combustion of municipal refuse. *Fuel*, 77(13):1399–1410, 1998.
- [30] F. Dryer and I. Glassman. High-temperature oxidation of co and ch<sub>4</sub>. In *Fourteenth Symposium (Int.) on Combustion*, pages 987–1003, 1973.
- [31] R.K. Eckhoff. Current status and expected future trends in dust explosion research. *Journal of Loss Prevention in the Process Industries*, 18:225–237, 2005.
- [32] J. R. Edwards, R. Franklin, and M. S. Liou. Low-diffusion flux-splitting methods for real fluid flows with phase transitions. In *16th AIAA CFD Conference, Orlando, FL*, 2003.
- [33] T. E. Evans, R. A. Moyer, K. H. Burrell, M. E. Fenstermacher, I. Joseph, A. W. Leonard, T. H. Osborne, G. D. Porter, M. J. Schaffer, P. B. Snyder, P. R. Thomas, J. G. Watkins, and W. P. West. Edge stability and transport control with resonant magnetic perturbations in collisionless tokamak plasmas. *Nature Physics*, 2:419–423, 2006.
- [34] M. Farber. High-temperature reaction rates of several metals with hydrogen chloride and water vapor. *Journal of the Electrochemical Society*, 106:751–754, 1959.
- [35] J. R. García-Cascales and H. Paillere. Application of ausr schemes to multi-dimensional compressible two-phase flow problems. *Nuclear Engineering and Design*, 236:1225–1239, 2006.
- [36] J. R. García-Cascales, J. Mulas Pérez, and H. Paillere. Advances in the characterization of two-phase mixtures. *AIAA Journal*, 45:2579–2584, 2007.
- [37] J. R. García-Cascales, J. Mulas Pérez, and H. Paillere. Extension of some numerical schemes to the analysis of gas and particle

- mixtures. *Int. Jou. for Numerical Methods in Fluids*, 56:845–875, 2008.
- [38] J. R. García-Cascales, F. Vera-García, J. Zueco-Jordán, A. Bentaib, N. Meynetb, J. Vendel, and D. Perrault. Development of an irsn code for dust mobilisation problems in iter. *Fus. Eng. Des.*, 85:2274–2281, 2010.
- [39] S. K. Godunov. A finite difference method for the computation of discontinuous solutions of the equations of fluid dynamics. *Matematicheskii Sbornik*, 47:357–393, 1959.
- [40] K.A. Gonthier and J.M. Powers. A numerical investigation of transient detonation in granulated material. *Shock Waves*, 6:183–195, 1996.
- [41] P.S. Gough and F.J. Zwarts. Modeling heterogeneous two-phase reacting flow. *AIAA Journal*, 17(1):17–25, 1979.
- [42] J.M. Heikkinen, B.C.H. Venneker, G. d Nola, W. de Jong, and H. Spliethoff. Cfd simulation and experimental validation of co-combustion of chicken litter and mbm with pulverized coal in a flow reactor. *Fuel Processing Technology*, 89:874–889, 2008.
- [43] W. Hinds. *Aerosol Technology: Properties, behavior, and measurement of airborne particles*. JohnWiley & Sons, New York, USA, 1982.
- [44] S.J. Hoffman and H. Krier. Fluid mechanics of deflagration-to-detonation transition in porous explosives and propellants. *AIAA Journal*, 19:1571–1579, 1981.
- [45] J. B. Howard, G. C. Williams, and D. H Fine. Kinetics of carbon monoxide oxidation in postflame gases. In *Symposium (International) on Combustion 14*, pages 975–986, 1973.
- [46] E. Hutchinson. *Los Elementos y sus Reacciones*. Editorial Reverté, Barcelona, Spain, 1973.
- [47] R.D. Ingebo. Drag coefficients for droplets and solids spheres in clouds accelerating in airstreams. *NACA TN*, 3765, 1956.
- [48] ITER Project. Iter: The way to energy, 2013. URL <http://www.iter.org>.
- [49] G. V. Ivanov, A. A. Reshetov, V. G. Surkov A. M. Viktorenko, and L. N. Karmadonov. Powdered tungsten combustion in pyrotechnic mixtures. *Combustion, Explosion and Shock Waves*, 18:142–145, 1982.

- [50] Jr. J. N. Ong. Oxidation of refractory metals as a function of pressure, temperature, and time: Tungsten in oxygen. *Journal of the Electrochemical Society*, 109:284–288, 1962.
- [51] A. Jensen and J. E. Johnsson. In *Proceedings of the Finnish and Swedish Flame Days*, Naantali, 1996.
- [52] A.K. Kapila, R. Menikoff, J.B. Bdzil, S.F. Son, and D.S. Stewart. Two-phase modeling of deflagration-to-detonation transition in granular materials: Reduced equations. *Physics Of Fluids*, 13: 3002–3024, 2001.
- [53] A.R. Kasimov and H.K. Chelliah. Numerical modelling of quasi-steady combustion of porous graphite particles. In *1997 Fall Technical Meeting on Chemical and Physical Processes in Combustion*, Hartford, 1997.
- [54] J L. Kassebaum and H.K. Chelliah. Oxidation of isolated porous carbon particles: Comprehensive numerical model. *Combustion Theory and Modelling*, 13(1):143–166, 2009.
- [55] C. Kauffman, M. Sichel, and P. Wolanski. Reserach on dust explosions at the university of michigan. *Powder Technology*, 71: 119–134, 1992.
- [56] B.A. Khasainov and B. Veyssière. Analysis of the steady double-front detonation structure for a detonable gas, laden with aluminium particles. *Archivum Combustionis*, 7:333–352, 1987.
- [57] M. Kilpatrick and S.K. Lott. Reaction of flowing steam with the refractory metals. iii tungsten (1000 deg - 1700 deg c). 1966.
- [58] T. Kim, R. Yetter, and F. Dryer. New results on moist co oxidation: high pressure, high temperature experiments and comprehensive kinetic modeling. In *Twenty-Fifth Symposium (International) on Combustion*, pages 759–766, 1994.
- [59] L. Kjaldman. Numerical simulation of dust explosions. Technical report, Technical Research Centre of Finland. Presented at the 2nd International PHOENICS User Conference, November 1987.
- [60] J. Klammer, R. Klemens, V. P. Korobeinikov, V.V Markov, I.S. Men'Shov, and P. Wolanski. On ignition and unsteady flows of dusty gases with combustion reactions. *Combustion Science and Technology*, 142:81–90, 1999.
- [61] R. Klemens and P. Kosinski. Numerical simulation of dust layer dispersion due to rarefaction waves. In *18th International Colloquium on the Dynamics of Explosions and Reactive Systems*, Seattle, Washington, USA, 2001.

- [62] R. Klemens, P. Kosinski, and P. Oleszczak. Mathematical modelling of dust layer dispersion due to rarefaction waves. *Archivum Combustionis*, 22, 1/2:3–12, 2002.
- [63] R. Klemens, P. Zydak, M. Kaluzny, D. Litwin, and P. Wolanski. Dynamics of dust dispersion from the layer behind the propagating shock wave. *Journal of Loss Prevention in the Process Industries*, 19:200–209, 2006.
- [64] J.G. Knudsen and D.L.V. Katz. *Fluid dynamics and heat transfer*. McGraw-Hill, New York, USA, 1958.
- [65] V.P. Korobeinikov, R. Klemens, P. Wolanski, and V.V. Markov. Models and numerical methods for coal mine explosion development. *Computational Fluid Dynamics Journal*, 9:110–115, 2000.
- [66] P. Kosinski and A.C. Hoffmann. A eulerian-lagrangian model for dense particle clouds. *Comput. Fluids*, 36:714–723, 2007.
- [67] CEA / DMT / LAMS. Castem2000 user's guide. Technical report, Saclay, France, 1993.
- [68] P. D. Lax and B. Wendroff. Difference schemes for hyperbolic equations with high order accuracy. *Comm. on Pure and Applied Mathematics*, 13:217–237, 1960.
- [69] R.J. LeVeque. *Finite Volume Methods for Hyperbolic Problems*. Cambridge Texts in Applied Mathematics, Cambridge, 2002.
- [70] P.A. Libby and T.R. Blake. Theoretical study of burning carbon particles. *Combustion and Flame*, 36:139–169, 1979.
- [71] M. S. Liou. A sequel to ausm: Ausm+. *Journal of Comput. Physics*, 129:364–382, 1996.
- [72] M. S. Liou. A sequel to ausm, part ii: Ausm<sup>+</sup>-up. *J. Comput. Phys*, 214:137–170, 2006.
- [73] M. S. Liou and C. J. Steffen. A new flux splitting scheme. *Journal of Comput. Physics*, 107:23–39, 1993.
- [74] E. A. Fedorin M. E. Derevyaga, L. N. Stesik. Ignition and combustion of high-melting metals (tungsten, molybdenum, boron) combustion. *Explosion and Shock Waves*, 15:438–446, 1979.
- [75] G. H. Markstein. Heterogeneous reaction processes in metal combustion. In *11th Symp. (Intl.) on Combustion*, pages 219–234, Pittsburg, 1966. The Combustion Institute.
- [76] K.A. McCarthy, D.A. Petti, W.J. Carmack, and Smolik G.R. The safety implications of tokamak dust size and surface area. *Fusion Eng & Des*, 42:45–52, 1998.

- [77] A.E. Medvedev, A.V. Fedorov, and V.M. Fomin. Mathematical modeling of metal particle ignition in the high-temperature flow behind a shock. *Combustion, Explosion, and Shock Waves*, 18(3):261–265, 1982.
- [78] S.P. Medvedev, J.H. Geng, and H. Gronig. Shock tube study of dust layer dispersion by rarefaction wave. In *Proceedings of the fifth international colloquium on dust explosions*, Pultusk, 1993.
- [79] B.J. Merrill. Recent updates to the melcor 1.8.2 code for iter applications, idaho national laboratory, inl/ext-07-12493. 2007.
- [80] B.J. Merrill, R.L. Moore, S.T. Polkinghorne, and D.A. Petti. Modifications to the melcor code for application in fusion accident analyses. *Fusion Engineering and Design*, 51-52:555–563, 2000.
- [81] H. Miura and I.I. Glass. On dusty-gas shock tube. *Proceeding of the Royal Society of London*, 382:373–388, 1982.
- [82] M.J. Moran and H.N. Shapiro. *Fundamentals of Engineering Thermodynamics, 5th Ed.* John Wiley & Sons, 2006.
- [83] National Institute of Standards and Technology. Nist: Web book of chemistry, 2012. URL <http://webbook.nist.gov>.
- [84] M.H. O'Brien, B.J. Merrill, and S.N. Ugaki. Combustion testing and thermal modeling of proposed cit graphite tile materials. Technical Report EGG-FSP-8255, INEEL, 1988.
- [85] R. A. Ogle, J. K. Beddow, L. D. Chen, and P. B. Butler. An investigation of aluminum dust explosions. *Combustion Science and Technology*, 61:75–99, 1988.
- [86] P. Oleszczak and R. Klemens. Mathematical modelling of dust-air mixture explosion suppression. *Journal of Loss Prevention in the Process Industries*, 19:187–193, 2006.
- [87] Committee on the Safety of Nuclear Installations. Best practice guidelines for the use of cfd in nuclear reactor safety applications. Technical Report NEA/CSNI/R(2007)5, OCDE Nuclear Energy Agency, 2007.
- [88] S. Osher and F. Salomon. Upwind schemes for hyperbolic systems of conservation laws. *Math. Comput.*, 38:339–374, 1982.
- [89] B. Otterman and A. Levine. Analysis of gas-solid particles in shock tubes. *AIAA Journal*, 12:579, 1974.
- [90] T.X. Phuoc and K. Annamalai. A heat and mass transfer analysis of the ignition and extinction of solid char particles. *Transactions of the ASME*, 121:886–893, 1999.

- [91] J.H. Pickles. A model for coal dust duct explosions. *Combustion and Flame*, 44:153–168, 1982.
- [92] J. M. Powers, D. S. Stewart, and H. Krier. Theory of two-phase detonation- part i: Modeling. *Combustion and Flame*, 80:264–279, 1990.
- [93] J. M. Powers, D. S. Stewart, and H. Krier. Theory of two-phase detonation- part ii: Structure. *Combustion and Flame*, 80:280–303, 1990.
- [94] ITER Project. Technical basis. engineering design activities documentation series no. 24. Technical Report IAEA ITER EDA DS 24, Vienna, 2002.
- [95] ITER Project. Safety analysis data list- version 5.2.6. Technical Report ITER D 24LSAE v. 5.2.6, Environment, Safety & Health group, Vienna, 2008.
- [96] A. Putnam. Integrable form of a droplet drag coefficient. *ARS Jou.*, 31:1467, 1961.
- [97] M.W. Reeks and D. Hall. Kinetic models for the particles resuspension in turbulent flows: theory and measurement. *Journal of Aerosol Science*, 32(1):1–31, 2001.
- [98] P. L. Roe and J. Pike. Efficient construction and utilisation of approximate riemann solutions. *Computing Methods in Applied Science and Engineering*, 1984.
- [99] P.L. Roe. Approximate riemann solvers, parameter vectors & difference schemes. *Jou. Comput. Phys.*, 43(2):357–371, 1981.
- [100] X. Rogue, G. Rodríguez, J.F. Hass, and R. Saurel. Experimental and numerical investigation of the shock-induced fluidization of a particles bed. *Shock Waves*, 8:29–45, 1998.
- [101] M. Rubel, J. von Seggern, P. Karduck, V. Philipps, and A. Vevecka-Priftaj. Analysis and oxidation of thick deposits on textor plasma facing components. *J. Nucl. Mater.*, 266:1185, 1999.
- [102] M. Rubel, M. Cecconello, J.A. Malmberg, G. Sergienko, W. Biel, J. R. Drake, A. Hedqvist, A. Huberb, and V. Philipps. Dust particles in controlled fusion devices: morphology, observations in the plasma and influence on the plasma performance. *Nucl. Fus.*, 41:1087–1099, 2001.
- [103] V. V. Rusanov. Calculation of interaction of non-steady shock waves with obstacles. *J. Comput. Math. Phys.*, 1:267–279, 1961.

- [104] J. Sabard. Etude de l'explosion de mélanges diphasiques: hydrogène et poussières. Doctoral thesis, Université d'Orléans, 2013.
- [105] J.L. Sabourin. High temperature heterogeneous reaction kinetics and mechanisms of tungsten oxidation, phd thesis, pennsylvania state university. 2010.
- [106] M. Sami, K. Annamalai, and M. Wooldridge. Co-firing of coal and biomass fuel blends. *Progress in Energy and Combustion Science*, 27:171–214, 2001.
- [107] R. Saurel and R. Abgrall. A multiphase godunov method for compressible multifluid and multiphase flows. *Journal of Computational Physics*, 150:425–467, 1999.
- [108] P. Saxena and F.A. Williams. Testing a small detailed chemical-kinetic mechanism for the combustion of hydrogen and carbon monoxide. *Combustion and Flame*, 145:316–323, 2006.
- [109] L. Schiller and A. Neumann. Über die grundlegenden berechnungen bei der schwerkraftaufbereitung. *Ver. Deut. Ing.*, 77:318, 1933.
- [110] J.P. Shapre, D.A. Petti, and H-W. Bartels. A review of dust in fusion devices: implications for safety and operational performance. *Fusion Eng & Des*, 63:153–163, 2002.
- [111] T.W. Sheu and S.M. Lee. Analysis of combustion processes in a gun interior ballistics. *Comp. Fluid Dyn.*, 4:57–71, 1995.
- [112] R. Sivaramakrishnan, A. Comandiniand R.S. Tranter, K. Brezinsky, S.G. Davis, and H. Wang. Combustion of co/h<sub>2</sub> mixtures at elevated pressures. *Proceedings of the Combustion Institute*, 31: 429–437, 2007.
- [113] G. Smolik. Tungsten alloy oxidation behavior in air and steam. Technical report, Idaho National Engineering Laboratory, 1992.
- [114] G. Smolik, K. McCarthy, and D. Petti. Hydrogen generation from steam reaction with tungsten. *Journal of Nuclear Materials*, 258-263:1979–1984, 1998.
- [115] G. Strang. On the construction and comparison of difference schemes. *SIAM J. Numer. Anal.*, 5:506–517, 1968.
- [116] E. Studer, N. Coulon, A. Stietel, F. Damian, H. Golfier, and X. Raepsaet. Gas-cooled reactor thermal-hydraulics using cast3m and cronos2 codes. In *Proceedings 10th Int. Topical Meeting on Nuclear Thermal-Hydraulics (NURETH-10)*, Seoul, Korea, 2003.

- [117] E. Studer, A. Beccatini, S. Gounand, F. Dabbene, J.P. Magnaud, H. Paillere, I. Limaïem, F. Damian, H. Golfier, C. Bassi, and J.C. Garnier. Cast3m/arcturus: A coupled heat transfer cfd code for thermal-hydraulic analyzes of gas cooled reactors. In *Proceedings 11th Int. Topical Meeting on Nuclear Thermal-Hydraulics (NURETH-11)*, Avignon, France, 2005.
- [118] T. Tanaka and Y. Tsuji. Numerical simulation of gas-solid two-phase flow in a vertical pipe: On the effect of inter-particle collision. Technical Report FED-Vol. 121, Gas-Solid Flows, ASME, 1991.
- [119] Andrzej Teodorczyk. Fast deflagrations, deflagration to detonation transition (ddt) and direct detonation initiation in hydrogen - air mixtures. In *First European Summer School on Hydrogen Safety, Belfast, 15-24 August 2006*, pages 987–1003, Ireland, 2006.
- [120] L. Topilski. Iter documentation, safety analysis data list, version 5.2.6, iter d 24lsae v.5.2.6. 2008.
- [121] L. Topilski and S. Reyes. Accident analysis report- vol. iii: Hypothetical event analysis. Technical Report ITER-D-2E2XAMv4.1, ITER Project, May 2009.
- [122] E.F. Toro. *Riemann Solvers and Numerical Methods for Fluid Dynamics, A Practical Introduction*. Springer-Verlag, Berlin Heidelberg, 1997.
- [123] J.Y. Tu and C.A.J. Fletcher. Numerical modelling of three-dimensional fly-ash flow in power utility boilers. *Int. J. Num. Meth. Fluids*, 24:787–807, 1997.
- [124] Bohl Unal, C., W.R., and K.O. Pasamehmetoglu. Modeling of heat and mass transfer in accelerator targets during postulated accidents. *Nuclear Engineering and Design*, 196:185–200, 2000.
- [125] B. van Leer. Flux-vector splitting for the euler equations. Technical Report ICASE 82-30, NASA Langley Research Center, USA, 1982.
- [126] C. S. Vatikiotis. Analysis of combustion and heat transfer in a porous graphite medium. Master's thesis, Naval Postgraduate School, Monterey, CA., 1980.
- [127] F.J.S. Velasco, C. López del Prá, and L.E. Herranz. Aerosol retention in the vicinity of a breach in a tube bundle: an experimental investigation. *Aerosol Sci. & Tech*, 44:1–13, 2010.
- [128] H. Versteeg and W. Malalasekera. *An Introduction to Computational Fluid Dynamics: The Finite Volume Method*. Addison Wesley Longman Limited, 1995.

- [129] B. Veyssi re. Ignition of aluminum particles in a gaseous detonation. *AIAA Progress in Astronautics and Aeronautics*, pages 362–375, 1983.
- [130] B. Veyssi re. Double-front detonations in gas-solid particle mixtures. *Progress in Astronautics and Aeronautics*, 94:264–276, 1984.
- [131] B. Veyssi re and B.A. Khasainov. A model for steady, plane, double-front detonations (dfd) in gaseous explosive mixtures with aluminum particles in suspension. *Combustion and Flame*, 85:241–253, 1991.
- [132] B. Veyssi re and B.A. Khasainov. Structure and multiplicity of detonation regimes in heterogeneous hybrid mixtures. *Shock Waves*, 4:171–186, 1995.
- [133] B. Veyssi re, R. Bourianne, and N. Manson. Detonation characteristics of two ethylene-oxygen-nitrogen mixtures containing aluminum particles in suspension. *Progress in astronautics and aeronautics*, pages 423–438, 1981.
- [134] F.A. Williams. *Combustion Theory: Second Edition*. Addison-Wesley Publishing Company, 1985.
- [135] H. Xien and W. Xuejun. Combustion kinetics model for htgr spherical graphite fuel element. *Tsinghua Science and Technology*, 1(4), 1996.
- [136] H.C. Yang, H.C. Eun, D.G. Lee, C.H. Jung, and K.W. Lee. Analysis of combustion kinetics of powdered nuclear graphite by using a non-isothermal thermogravimetric method. *Journal of Nuclear Science and Technology*, 43(11):1436–1439, 2006.
- [137] R. Yetter, F. Dryer, and H. Rabitz. Complications of one-step kinetics for moist co oxidation. In *Twenty-first Symposium (Int.) on Combustion*, pages 749–760. The Combustion Institute, 1986.